Co-evolution of Rock Strength, Erosion, and Steep Topography

by

Kirk F. Townsend

A dissertation submitted in partial fulfillment
of the requirements for the degree of
Doctor of Philosophy
(Earth and Environmental Sciences)
in the University of Michigan
2021

Doctoral Committee:

Professor Marin K. Clark, Chair
Associate Professor Andrew D. Gronewold
Associate Professor Eric A. Hetland
Associate Professor Naomi E. Levin
Professor Nathan A. Niemi

Kirk F. Townsend

kirkft@umich.edu

ORCID iD: 0000-0002-0655-857X

Acknowledgements

The work presented in this dissertation would have been possible without my advisor, Marin Clark, whom I cannot thank enough for her support, encouragement, and mentorship over these last five years. Marin taught me to critically examine previous studies, creatively apply existing and new methodologies, patiently and thoughtfully examine my own datasets, and always seek the bigger picture. I would also like to thank my committee member, Nathan Niemi, for guidance and mentorship in the components of my dissertation that lean heavily into tectonics and structural geology. I would like to extend thanks to my other committee members, Eric Heltand, Naomi Levin, and Drew Gronewold, for their insight and feedback on my work. I owe a lot of gratitude to my NSF-INTERNSHIP mentor at the U.S. Geological Survey, Francis Rengers, who patiently helped me navigate a pivot towards research in post-wildfire erosion near the end of my dissertation. Additional thanks to coauthors and collaborators, including Tim Stahl, Dimitrios Zekkos, Sean Gallen, and Josh West, as well as to earlier mentors including Tammy Rittenour, Joel Pederson, and Tony García.

My close friends and lab mates were key to my happiness and well-being during graduate school. Discussions with fellow incoming-2016 cohort member and SCALE lab member William Medwedeff were instrumental in refining the rock strength methods presented in this dissertation, as well as bouncing around ideas and frustrations. Becca Dzombak and Nikolas Middtun could always be relied upon for wine and cheese nights, walks around Kerrytown, discussion of weathering and faulting, and overexcitement over road-side cobbles on long road trips. The two UM Earth-and-friends ‘bike gangs’ were a much-needed source of community: Maddie Hille, Julia Kelson, and Chrissie Nims for mountain and gravel bike adventures during the latter part of my time in Michigan, and William Medwedeff, Bekah Stein, Alyssa Abbey, Erin Lynch, Alex Tye, and Sophie Macarewich for bikes-and-beers road rides during the earlier years. I would be remiss to not also mention the excellent orthopaedic and plastic surgery groups at Michigan Medicine, as well as multiple occupational therapists, who enabled my recovery when my biking adventures went awry. SCALE lab members Alyssa Abbey and Alex Tye were a source of guidance in tectonics and thermochronometry early on in my studies. There are many others, too numerous to list here, who have helped make my time in Michigan both a fun and productive experience.

Many friends and colleagues contributed to collecting and processing the samples and data presented in this dissertation, including Abra Atwood, Max Dahlquist, Sean Gallen, Logan Knoper, Amanda Maslyn, William Medwedeff, Nikolas Midttun, Eric Portenga, Stuart Thomson, Bian Wang, Josh West, and Wing Yee Winnie Woo. From carrying bags of rocks down mountains in the heat of summer around Ojai, to cruising the Channel Islands by UTV looking for outcrop, I greatly appreciate the effort of everyone who chipped in.

The work presented here would not have been possible without the cooperation and support of government land agencies, oil field operators, and private landowners in southern California. Denise Kamradt and Laura Shaskey with the U.S. Park Service, Yonni Schwartz with the U.S. Forest Service, and Kurt White with the United Water Conservation District aided with field access and permitting. Salvador Dominguez, Tim Cohen (Rancho Temescal), Gordon Kimball, and Jim Lynn allowed access to private properties, and Seneca Resources, Carbon Energy Corporation, and Aera Energy allowed access to oil fields.

Funding for this dissertation was provided by a National Science Foundation division of Earth Science, Geomorphology and Land Use Dynamics award (EAR-1528576) to Marin Clark. Additional funding was provided by the National Science Foundation through an INTERNSHIP supplement to NSF EAR-1640797, as well as an Award in Geochronology Student Research (AGeS2, supported by NSF awards EAR-1759200 and EAR-1759353). This dissertation research was further supported by an Evolving Earth Foundation grant, a Geological Society of America grant, four Turner Research Awards from the Department of Earth and Environmental Sciences, two graduate student research grants from the Rackham Graduate School, and a Rackham International Research Award. Additionally, the National Center for Airborne Laser Mapping (NCALM) enabled the research that became Chapter 6 of this dissertation by acquiring and providing the post-wildfire airborne-LiDAR dataset free-of-charge through a successful seed proposal. Funding from the Rackham Graduate Student Emergency Fund for occupational therapy following three wrist surgeries greatly reduced my financial and emotional stress during the first two years of my graduate studies.

Finally, I would like to thank my family for their continuous support, encouragement, patience, and understanding.

Table of Contents

List of Tables

List of Figures

List of Appendices

Abstract

Rock-mass strength is recognized as an important control in geomorphology that influences the morphology of landscapes and modulates feedbacks between surface processes, tectonics, and climate. Despite this general recognition, many of the factors controlling rock-mass strength in the near-surface are not widely understood, largely due to challenges in quantifying strength over the appropriate spatial scales. Although the strength of small rock samples can be readily measured with laboratory techniques, fractures and weathering gradients at progressively larger spatial scales dramatically reduce the strength of rock masses compared to their intact (unfractured) counterparts. Due to a lack of approaches that incorporate discontinuities into strength estimates, the contribution of rock-mass properties to geomorphic processes and topographic relief remains unquantified. In this dissertation, I address gaps in our understanding of the role of rock mass strength in geomorphology by testing new methods for quantifying scale-dependent rock mass strength, using these new tools to quantify gradients in strength across environmental variables, and assessing the contribution of rock strength to topographic form and erosion. Research activities focus on an inverted sedimentary basin within the Western Transverse Ranges of southern California, USA, where differences in fault activity have exposed sedimentary rocks with variable burial histories. With Chapters 2 and 3, I test new approaches to quantifying outcrop- and hillslope-scale near-surface rock-mass strength using slope-stability models and field methods. With these new techniques, I resolve order-of-magnitude differences in strength that appear to be related to diagenetic changes associated with the maximum burial depth of young clastic sedimentary rocks. I resolve smaller differences in strength (300 kPa – 1.5 MPa) that are positively correlated with mean erosion rates, which I hypothesize reflects decreased weathering extents with increasing erosion rates for mountain ranges experiencing faster fault slip rates.

Assessing the contribution of rock-mass properties to the evolution of landscapes requires recognizing patterns of long-term fault activity and erosion. In Chapter 4, I resolve differences in the timing of reverse fault localization, initiation, and propagation, as well as long-term erosion

rates, using low-temperature thermochronometry. Inverse thermal modelling of Miocene to Pleistocene apatite (U-Th-Sm)/He cooling ages and partially reset zircon (U-Th)/He cooling ages on eleven vertical transects reveal that deformation localization was likely driven by contrasts in the rheology and strength of the lithosphere, rather than by restraining bend tectonism.

With estimates of near-surface rock-mass strength and long-term erosion rates mapped across the landscape in Chapters 2-4, I evaluate the contribution of rock-mass strength to topography in Chapter 5. Where erosion rates and climate are spatially uniform, I find a non-linear relationship between topographic metrics and rock-mass shear strength, implying that rock-mass strength sets the topographic structure of the mountain range. Chapter 6 builds on this observation, and I find that post-wildfire erosion as quantified from repeat airborne-LiDAR surveys is positively correlated with local slope and the strength of the underlying bedrock. Rather than setting the erodibility of earth materials directly, I hypothesize that rock-mass strength controls event-driven erosion by setting the steepness of the overlying landscape. Collectively, interpretations put forward in this dissertation highlight the complex interplay between tectonics, erosion, topography, and the mechanical evolution of rock to transportable, erodible materials.

Chapter 1: Introduction

1.1 Motivation

The strength of near-surface earth materials has long been hypothesized to be an important contribution to landscape morphology and evolution (Gilbert, 1877; Hack, 1975; Schmidt & Montgomery, 1995). The strength of soils, mobile to immobile regolith, and weathered to intact rock exert a control on the evolution of mountainous landscapes by governing the ability of material to be dislodged and transported by surface processes, as well as modulating feedbacks between tectonics, climate, and surface processes (Montgomery & Brandon, 2002; Selby, 1980, 1993). The processes and rates by which landscapes evolve are likely sensitive to the properties of the underlying rock mass, which contribute to hillslope stability and failure mechanisms (Collins & Sitar, 2008; Gallen et al., 2015; Hoek & Brown, 1980; Selby, 1980), the architecture of the critical zone (St. Clair et al., 2015; Riebe et al., 2017), and the mechanisms of bedrock erosion in channels (Bursztyn et al., 2015; Forte et al., 2016; Gallen, 2018; Roy et al., 2015; Sklar & Dietrich, 2001). Rock mass strength is also expected to be expressed in the local relief structure of mountain ranges by controlling the critically-stable morphology of hillslopes and setting relief on the fluvial network (Montgomery & Brandon, 2002; Schmidt & Montgomery, 1995; Whipple & Tucker, 1999). Despite this general recognition, many of the factors controlling rock strength are not widely understood, and the contribution of rock mass properties to geomorphic processes and topographic relief remain unquantified.

Lithologic type is widely recognized to contribute to the strength of intact (i.e. unfractured) rock pieces (e.g. Sklar & Dietrich, 2001), but recent work has focused on identifying the effect of other environmental controls on fracture density and weathering, which influence rock mass strength at the broader spatial scales relevant to geomorphology. Fracture generation and weathering profiles are influenced by environmental factors including climate (Gabet et al., 2010; Gallen et al., 2015; Goudie, 2016), tectonic inheritance and active deformation (DiBiase et al., 2018; Kirkpatrick et al., 2020; Molnar et al., 2007; Neely et al., 2019), burial of sedimentary rocks (Collins & Sitar, 2008; Worden & Burley, 2003), and topographic stresses due to geomorphic position on the landscape (St. Clair et al., 2015; Gabet et al., 2015; Leone et al., 2020; Slim et al., 2015). However, most landscape evolution models continue to incorporate rock strength as an erodibility coefficient (e.g. 'K' in the stream power erosion model) that is typically estimated or assigned solely by lithologic type (Bursztyn et al., 2015; Stock & Montgomery, 1999). Quantitatively constraining the relationships between environmental variables, fracturing, weathering, and the resultant scale-dependent rock mass strength will further geomorphologists' ability to accurately model the evolution of landscapes with respect to strength.

Identifying environmental controls on rock strength, and untangling the signal of rock strength from other tectonic and climatic variables that influence topographic form, has been challenged by the difficulties in the quantification of material properties at the appropriate spatial scale (Hoek & Brown, 1980, 1997; Schmidt & Montgomery, 1995). "Strength", defined here as the maximum shear stress a material can sustain before failure, is commonly described using Mohr-Coulomb failure criteria (cohesion and angle of internal friction) for properties on the sliding plane of a failure mass. While laboratory tests of rock strength are conducted on intact hand-sized samples, we recognize that fractures and weathering dramatically reduce strength at the spatial scales relevant to geomorphic processes compared to their intact counterparts (Gallen et al., 2015; Hoek & Brown, 1980, 1997; Schmidt & Montgomery, 1995). Laboratory approaches may overestimate near-surface rock strength at outcrop, hillslope, or regional spatial scales by an order of magnitude or more (Bunn et al., 2020; Gallen et al., 2015; Schmidt & Montgomery, 1995), yet adequately accounting for variability of rock mass strength in landscape evolution is challenged by the paucity of approaches for quantifying in-situ strength at the relevant spatial scales (Gallen et al., 2015; Schmidt & Montgomery, 1995; Townsend et al., 2020).

In this dissertation, I address gaps in our understanding of the role of rock mass strength in geomorphology by testing new approaches for quantifying scale-dependent rock mass strength, using these new tools to quantify gradients in strength across environmental variables, and assessing the contribution of rock strength to topographic form and erosion. I test two approaches for quantifying strength properties remotely using hillslope stability models, digital topography and coseismic landslide inventories, and I complement these techniques with a novel field-based approach for evaluating near-surface strength profiles (up to 30 m depth) from surface and subsurface measurements (Culmann, 1875; Gallen et al., 2015; Hoek et al., 2002; Hoek & Brown, 1997; Schmidt & Montgomery, 1995). The spatial distribution afforded by these methods allowed me to quantify rock strength across tectonic and stratigraphic gradients, where differences in fault motion have exposed sedimentary rocks with variable burial and exhumation histories. Stratigraphic gradients were inferred from published geologic maps (Dibblee, 1982), and I used low-temperature thermochronometry and thermal modelling to constrain the timing and rates of erosion and fault motion within the inverted sedimentary basins (Ehlers, 2005). Finally, I leveraged the rock strength and erosion rate datasets to assess the influence of rock strength on landscape morphology and spatial patterns of erosion.

1.2 Basin Inversion Study Area

This dissertation focusses on geologic settings with a simple history of basin inversion, which offers several advantages to understanding how rock strength evolves with burial and time. Inversion is marked by a transition from an extensional setting where sediments are deposited and buried in basins to form sedimentary rocks, to a subsequent stage in which crustal shortening drives reverse faulting. These settings commonly contain stratigraphic sequences that are well-dated, and monotonic exhumation histories suggest that these sedimentary rocks lack inherited deformation from previous tectonic events (e.g. Molnar et al., 2007; DiBiase et al., 2018). This simple geologic history enables an assessment of variability of strength with respect to stratigraphic depth and active upper crustal structures.

The evolution of rock mass strength in an inverted basin is likely dramatic, which makes this geologic setting ideal for understanding and quantifying the interplay between exhumation, rock mass strength, and topography. During burial, increasing temperatures and pressures drive an increase in grain packing and decrease in porosity through both physical and chemical compaction. Chemical compaction enriches pore water with dissolved silica though partial dissolution of minerals, and precipitation of this silica in pore spaces further reduces porosity while adding cements, leading to lithification of the sediments (Boggs Jr., 2011; Worden & Burley, 2003). Gradients in these physical and chemical changes with burial occur from the surface to at least 5 km depth, and we expect that this lithification gradient will produce a similar gradient in strength (Worden & Burley, 2003). Subsequent inversion of sedimentary basins with slip along range-bounding faults incrementally exposes sedimentary rocks from increasing stratigraphic depth at the surface, which should be associated with a concurrent increase in rock mass strength. This evolving distribution of rock mass strength may in turn impart a signal on the relief structure of the overlying landscapes, all other variables being constant.

The work presented in this dissertation is conducted within the Western Transverse Ranges (WTR) of southern California, USA (Figure 1.1). Here, active shortening drives reverse faulting, causing inversion of a ~13 km thick section of late-Cretaceous through Plio-Pleistocene marine and non-marine clastic sedimentary rocks that were deposited during multiple stages of regional extension and basin formation (Dibblee, 1982; Namson & Davis, 1988). During Cretaceous and early Cenozoic time, the WTR accumulated sediments derived from the continent in the forearc above the subducting Farallon Plate (Atwater, 1998). Shallow-marine to terrestrial sandstones and conglomerates were deposited in Oligocene time as the Pacific Plate first made contact with the North American Plate and the boundary transitioned from subduction to predominantly transform (Crowell, 1979). During Miocene time, thick sections of marine siliceous mudstones, marine sandstones, and volcaniclastic rocks locally accumulated in extensional basins as the region underwent rotation and left-lateral shearing in a predominantly transtensional tectonic regime (Atwater, 1998; Namson & Davis, 1988; Nicholson et al., 1994; Wright, 1991). Reverse faulting and shortening of the WTR is conventionally thought to have initiated at 5-6 Ma due to eastward migration of the North American-Pacific plate boundary, which lead to development of the transpressional ~160 km Big Bend in the San Andreas Fault, although later chapters of this dissertation call the timing and mechanism into question (Crowell, 1979, 1982; Link, 1982; Link & Osborne, 1978). The late-Mesozoic through Cenozoic sedimentary and volcaniclastic rocks sequences are now being inverted along east-west trending oblique-reverse faults, forming the modern mountainous topography (Figure 1.1).

In the WTR, I leverage a space-for-time substitution to quantify how rock strength evolves as a function of burial depth and stratigraphic age. Differential fault motion, driven by differences in the timing of fault initiation and fault slip rates, have exhumed sedimentary rocks with varying burial histories (Dibblee, 1982; Rockwell, 1988). It is therefore possible to measure and sample different depth intervals of the late-Mesozoic through Plio-Pleistocene section by moving along-strike of the principal structures. This space-for-time substitution allows us to assess how these gradients in the magnitude of rock exhumation influence rock strength, erosion, and topographic relief.

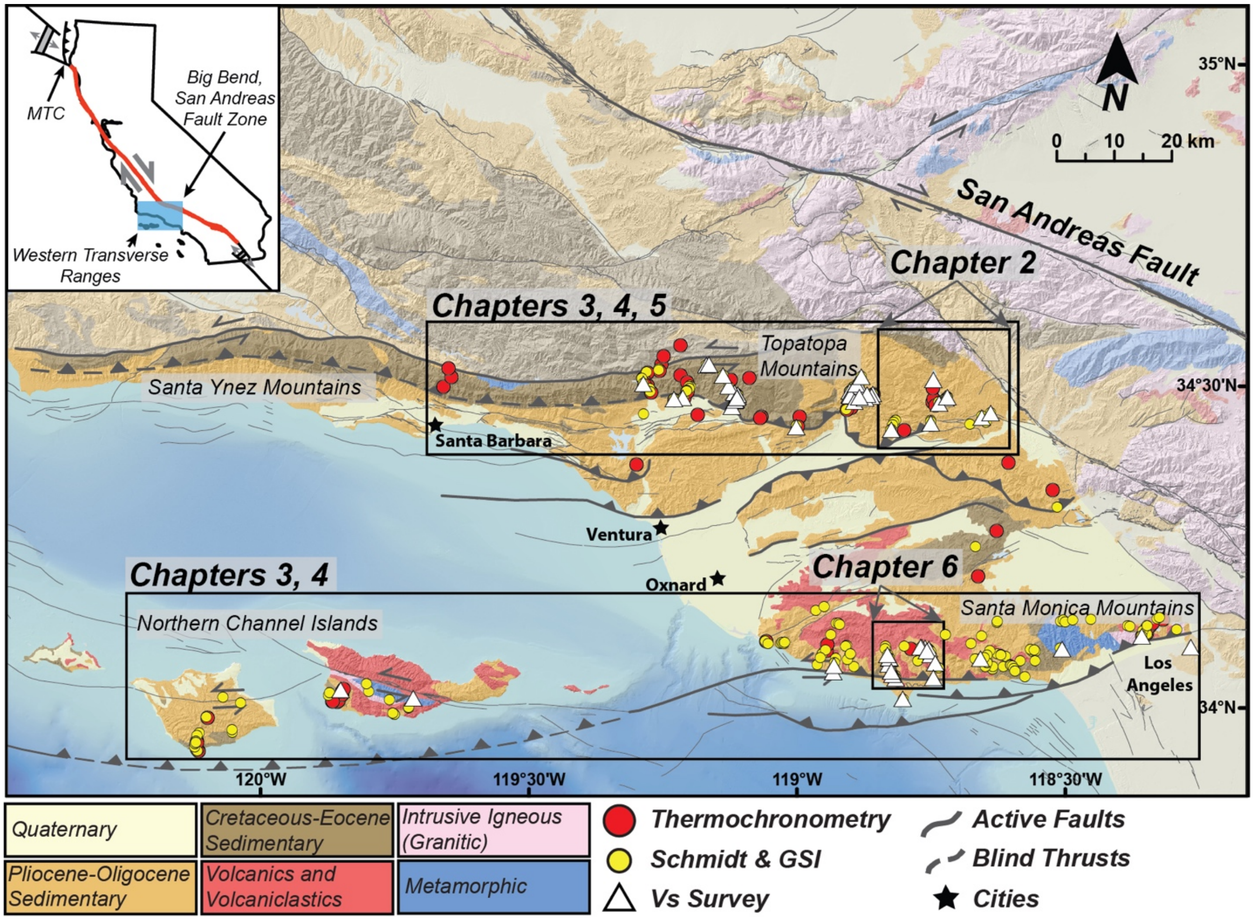

Figure 1.1: Simplified geology and structure of the Western Transverse Ranges (WTR), southern California, USA. Black boxes indicate the locations of detailed studies along the northern and southern boundaries of the WTR (Chapter 2-6). Sites from which thermochronometry samples were collected for this dissertation are shown as red circles (n = 67), sites from which Schmidt hammer rebound values and GSI observations were collected are shown as yellow circles (n = 226), and locations surveyed for S-wave velocities are shown as white rectangles (n = 60). Inset map shows location of the WTR in southern California, USA, relative to the San Andreas Fault (red). Shortening across the WTR is conventionally thought to be driven by convergence associated with the Big Bend in the San Andreas Fault Zone. MTC–Mendocino Triple Junction.

1.3 Thesis Outline

The following chapters address three areas of inquiry regarding the role of rock strength in the evolution of mountainous landscapes: 1) development and application of novel approaches for quantifying scale-dependent rock mass strength across the broad spatial scales necessary for understanding the contribution of strength to geomorphic processes; 2) investigating the localization, initiation, propagation, and rates of reverse faulting within the WTR, which must be recognized and accounted for in order to resolve signals of rock strength in topography; and 3) assessing the role of landscape-scale rock strength in setting the morphology and evolution of the overlying landscape.

Chapters 2 and 3 focus on the development of new model and field techniques for quantifying scale-dependent rock mass strength. In Chapter 2, I test two approaches for quantifying rock mass cohesion and friction angles averaged over the hillslope-scale using hillslope-stability models. In the first of these approaches, I use the Culmann finite-slope stability model to calculate apparent cohesion and friction angle of hillslope materials from measurements of hillslope heights and gradients extracted from a digital elevation model at the pixel-scale (Culmann, 1875; Schmidt & Montgomery, 1995). In the second approach, we invert the simplified Newmark infinite-slope stability model using local slope, modelled peak ground accelerations, and a co-seismic landslide inventory to quantify strength (Gallen et al., 2015; Jibson, 2007). To directly compare the resulting strength estimates, we fix the friction angle estimates for the Newmark inversion with the Culmann model estimates. Model cohesion results are broadly similar, with cohesion increasing with increasing stratigraphic age and depth in Plio-Pleistocene through Miocene clastic sedimentary rocks. This work was published in the July 2020 issue of *Journal of Geophysical Research Earth Surface* (Townsend et al., 2020).

Chapter 3 builds on the methodology explored in Chapter 2 by quantifying scale-dependent near-surface material properties from field measurements, which are likely more exportable to other field settings than the remote approaches. I present a novel technique for quantifying outcrop-scale shear strength on depth profiles from surface measures of intact (unfractured) rock strength as measured from a Schmidt hammer, and assessment of outcrop-scale structure and weathering from Geological Strength Index observations (Hoek & Brown, 1980, 1997; Hoek & Marinos, 2000). At select sites, I pair the surface measures of rock properties with shallow S-wave velocity profiles measured from short geophysical arrays. I apply these techniques across the full late-Mesozoic to Plio-Pleistocene sedimentary sequence exposed in the WTR, and I find that stratigraphic age and inferred burial depth exert the strongest apparent control on strength. Shear strength varies by over an order of magnitude from 200 kPa to ~5 MPa, and subsurface S-wave velocities range from ~300 m/s to ~1400 m/s as a function of stratigraphic formation. Collectively, Chapters 2 and 3 provide quantitative constraints on the relationship between the burial depth and strength of clastic sedimentary rocks while also furthering development of approaches for quantifying strength at spatial scales relevant to geomorphology. Chapter 3 was published in the April 2021 issue of *Journal of Geophysical Research Earth Surface* (Townsend et al., 2021).

As landscape form reflects a balance between the tectonic forces that uplift mountains, rock strength, and erosional forces (including gravity), knowledge of fault activity and tectonically-driven erosion rates are required to isolate the contribution of strength to landscape form (Hovius et al., 1998; Montgomery, 2001; Willett & Brandon, 2002. Chapter 4 investigates the localization, initiation, and propagation of reverse faulting within the WTR using low-temperature thermochronometers, which are sensitive to upper-crustal tectonic and surface processes. Active shortening within the WTR is inferred to have initiated at ~5 Ma, coeval with development of the Big Bend of the San Andreas fault (Crowell, 1979; Link, 1982), but spatiotemporal data directly constraining the timing of reverse fault initiation had not been previously produced. New apatite and zircon (U-Th-[Sm]) thermochronometry data presented in this chapter suggest that reverse faulting initiated at ~8 and ~10 Ma on the northern and southern boundaries of the WTR, respectively, well before development of the Big Bend. Further, reverse faulting along both boundaries of the WTR propagates towards the Big Bend, rather than outwards from it, suggesting that restraining bend tectonism is not the primary source of shortening within the WTR. The implications of these spatiotemporal patterns for our current understanding of the controls on deformation along the continental transform plate boundary in southern California are discussed further in this chapter. This work was submitted to *Tectonics* for peer review in May 2021 (Townsend et al., *in review*).

Chapters 5 and 6 build on the preceding chapters to reveal how landscape-scale gradients in rock-mass strength are expressed in the topographic structure and geomorphic processes in the overlying landscape. In the Topatopa Mountains on the northern boundary of the WTR (Figure 1.1), thermochronometry data from Chapter 4 suggest that long-term erosion rates and inferred bedrock uplift rates are consistent along-strike of the range. As climate also varies little across the range, topographic differences are likely to be driven by differences in rock mass strength. I document a positive and non-linear relationship between rock mass shear strength and topographic metrics in the Topatopa Mountains. This relationship suggests that rock strength is important in setting the relief structure during the early stages of mountain building, but that rock strength progressively becomes less important with the exhumation of stronger rocks. In Chapter 6, I explore the contribution of rock strength to the volume of material eroded following the 2018 Woolsey Fire in the Santa Monica Mountains on the southern boundary of the WTR. I find a positive relationship between rock strength and post-wildfire erosion, wherein erosion appears to increase linearly with strength. This paradoxical result suggests that the gradient in rock strength is not manifest as differences in the erodibility of near-surface materials. Instead, it appears that the gradient in rock strength is expressed as differences in the local topographic slope, which controls stream power of channels and thus the susceptibility of near-surface materials to erosion following wildfire (Staley et al., 2016). Chapters 5 and 6 are in preparation for publication in the journals *Geology* and *Geophysical Research Letters*, respectively.

Chapter 7 summarizes the interpretations and conclusions of the preceding chapters. The summary highlights the key contributions of this thesis to furthering methods for quantifying scale-dependent near-surface rock strength, recognizing controls on the regional distribution of strength, and understanding the role of rock strength on topography. Outstanding problems and directions for future research are discussed. Each chapter includes an appendix with additional figures, data tables, or explanation of methods utilized.

1.4 References

Atwater, T. (1998). Plate tectonic history of southern California with emphasis on the Western Transverse Ranges and northern Channel Islands. In P. W. Weigand (Ed.), *Contributions to the geology of the Northern Channel Islands, Southern California* (pp. 1–8). American Association of Petroleum Geologists, Pacific Section.

Boggs Jr., S. (2011). *Principles of Sedimentology and Stratigraphy*. Pearson.

Bunn, M., Leshchinsky, B., & Olsen, M. J. (2020). Geologic Trends in Shear Strength Properties Inferred Through Three-Dimensional Back Analysis of Landslide Inventories. *Journal of Geophysical Research: Earth Surface*, *125*(9), 1–25. https://doi.org/10.1029/2019jf005461

Bursztyn, N., Pederson, J. L., Tressler, C., Mackley, R. D., & Mitchell, K. J. (2015). Rock strength along a fluvial transect of the Colorado Plateau - quantifying a fundamental control on geomorphology. *Earth and Planetary Science Letters*, *429*, 90–100. https://doi.org/10.1016/j.epsl.2015.07.042

St. Clair, J., Moon, S., Holbrook, W. S., Perron, J. T., Riebe, C. S., Martel, S. J., et al. (2015). Geophysical imaging reveals topographic stress control of bedrock weathering. *Science*, *350*(6260), 534–539. https://doi.org/10.1126/science.aab2210

Collins, B. D., & Sitar, N. (2008). Processes of coastal bluff erosion in weakly lithified sands, Pacifica, California, USA. *Geomorphology*, *97*(3–4), 483–501. https://doi.org/10.1016/j.geomorph.2007.09.004

Crowell, J. C. (1979). The San Andreas fault system through time. *Journal of the Geological Society*, *136*, 293–302. https://doi.org/10.1144/gsjgs.136.3.0293

Crowell, J. C. (1982). The tectonics of Ridge Basin, southern California. In J. C. Crowell & M. H. Link (Eds.), *Geologic History of Ridge Basin, Southern California* (pp. 25–42). Society of Economic Paleontologists and Mineralogists.

Culmann, C. (1875). *Die Graphische Statik*. Zurich: Meyer and Zeller.

Dibblee, T. W. (1982). Regional geology of the Transverse Ranges Province of southern California. In D. L. Fefe & J. A. Minch (Eds.), *Geology and Mineral Wealth of the Califrnia Transverse Ranges* (pp. 7–26). Santa Ana, California: South Coast Geological

Society, Inc.

DiBiase, R. A., Rossi, M. W., & Neely, A. B. (2018). Fracture density and grain size controls on the relief structure of bedrock landscapes. *Geology*, *46*(5), 399–402. https://doi.org/10.1130/G40006.1

Ehlers, T. A. (2005). Crustal Thermal Processes and the Interpretation of Thermochronometer Data. *Reviews in Mineralogy and Geochemistry*, *58*(1), 315–350. https://doi.org/10.2138/rmg.2005.58.12

Forte, A. M., Yanites, B. J., & Whipple, K. X. (2016). Complexities of landscape evolution during incision through layered stratigraphy with contrasts in rock strength. *Earth Surface Processes and Landforms*, *41*(12), 1736–1757. https://doi.org/10.1002/esp.3947

Gabet, E. J., Wolff-Boenisch, D., Langner, H., Burbank, D. W., & Putkonen, J. (2010). Geomorphic and climatic controls on chemical weathering in the High Himalayas of Nepal. *Geomorphology*, *122*(1–2), 205–210. https://doi.org/10.1016/j.geomorph.2010.06.016

Gabet, E. J., Mudd, S. M., Milodowski, D. T., Yoo, K., Hurst, M. D., & Dosseto, A. (2015). Local topography and erosion rate control regolith thickness along a ridgeline in the Sierra Nevada, California. *Earth Surface Processes and Landforms*, *40*(13), 1779–1790. https://doi.org/10.1002/esp.3754

Gallen, S. F. (2018). Lithologic controls on landscape dynamics and aquatic species evolution in post-orogenic mountains. *Earth and Planetary Science Letters*, *493*, 150–160. https://doi.org/10.1016/j.epsl.2018.04.029

Gallen, S. F., Clark, M. K., & Godt, J. W. (2015). Coseismic landslides reveal near-surface rock strength in a highrelief, tectonically active setting. *Geology*, *43*(1), 11–14. https://doi.org/10.1130/G36080.1

Gilbert, G. K. (1877). *Report on the geology of the Henry Mountains: Geographical and geological survey of the Rocky Mountain region*. Washington. D.C.

Goudie, A. S. (2016). Quantification of rock control in geomorphology. *Earth-Science Reviews*, *159*, 374–387. https://doi.org/10.1016/j.earscirev.2016.06.012

Hack, J. T. (1975). Dynamic equilibrium and landscape evolution. *Theories of Landform Development: Publications in Geomorphology*. Retrieved from http://geomorphology.sese.asu.edu/Papers/Hack_1975.pdf

Hoek, E., & Brown, E. (1980). Empirical Strength Criterion for Rock Masses. *Journal of the Geotechnical Engineering Division*. https://doi.org/10.1016/0148-9062(81)90766-X

Hoek, E., & Brown, E. (1997). Practical estimates of rock mass strength. *International Journal of Rock Mechanics and Mining Sciences*, *34*(8), 1165–1186. https://doi.org/10.1016/S1365-1609(97)80069-X

Hoek, E., & Marinos, P. (2000). Predicting tunnel squeezing problems in weak heterogeneous rock masses. *Tunnels and Tunnelling International*, *Part 1-2*(November), 1–20. Retrieved from https://www.rocscience.com/documents/hoek/references/H2000d.pdf%0Ahttp://www.rocscience.com/hoek/references/H2000d.pdf

Hoek, E., Carranza, C., & Corkum, B. (2002). Hoek-brown failure criterion – 2002 edition. *Narms-Tac*, 267–273. https://doi.org/10.1016/0148-9062(74)91782-3

Jibson, R. W. (2007). Regression models for estimating coseismic landslide displacement. *Engineering Geology*, *91*(2–4), 209–218. https://doi.org/10.1016/j.enggeo.2007.01.013

Kirkpatrick, H. M., Moon, S., Yin, A., & Harrison, T. M. (2020). Impact of fault damage on eastern Tibet topography. *Geology*, *48*.

https://doi.org/10.1130/G48179.1/5137742/g48179.pdf

Leone, J. D., Holbrook, W. S., Riebe, C. S., Chorover, J., Ferré, T. P. A., Carr, B. J., & Callahan, R. P. (2020). Strong slope-aspect control of regolith thickness by bedrock foliation. *Earth Surface Processes and Landforms*, *3010*(July), 2998–3010. https://doi.org/10.1002/esp.4947

Link, M. H. (1982). Stratigraphic Nomenclature and Age of Miocene Strata, Ridge Basin, Southern California. In J. C. Crowell & M. H. Link (Eds.), *Geologic History of Ridge Basin, Southern California* (pp. 5–12). Pacific Section, Society of Economic Paleontologists and Mineralogists.

Link, M. H., & Osborne, R. H. (1978). Lacustrine facies in the Pliocene Ridge Basin Group: Ridge Basin, California. *Modern and Ancient Lake Sediments*, *Special Pu*, 169–187.

Molnar, P., Anderson, R. S., & Anderson, S. P. (2007). Tectonics, fracturing of rock, and erosion. *Journal of Geophysical Research: Earth Surface*, *112*(3), 1–12. https://doi.org/10.1029/2005JF000433

Montgomery, D. R., & Brandon, M. T. (2002). Topographic controls on erosion rates in tectonically active mountain ranges. *Earth and Planetary Science Letters*, *201*(3–4), 481–489. https://doi.org/10.1016/S0012-821X(02)00725-2

Namson, J. S., & Davis, T. L. (1988). Structural transect of the western Transverse Rances, California: Implications for lithospheric kinematics and seismic risk evaluation. *Geology*, *16*, 675–679.

Neely, A. B., DiBiase, R. A., Corbett, L. B., Bierman, P. R., & Caffee, M. W. (2019). Bedrock fracture density controls on hillslope erodibility in steep, rocky landscapes with patchy soil cover, southern California, USA. *Earth and Planetary Science Letters*, *522*, 186–197. https://doi.org/10.1016/j.epsl.2019.06.011

Nicholson, C., Sorlien, C. C., Atwater, T., Crowell, J. C., & Luyendyk, B. P. (1994). Microplate capture, rotation of the western Transverse Ranges, and initiation of the San Andreas transform as a low-angle fault system. *Geology*, *22*(6), 491–495.

Riebe, C. S., Hahm, W. J., & Brantley, S. L. (2017). Controls on deep critical zone architecture: a historical review and four testable hypotheses. *Earth Surface Processes and Landforms*, *42*(1), 128–156. https://doi.org/10.1002/esp.4052

Rockwell, T. K. (1988). Neotectonics of the San Cayetano fault, Transverse Ranges, California. *Geological Society of America Bulletin*, *100*, 500–513.

Roy, S. G., Koons, P. O., Upton, P., & Tucker, G. E. (2015). The influence of crustal strength fields on the patterns and rates of fluvial incision. *Journal of Geophysical Research : Earth Surface*, *120*, 275–299. https://doi.org/10.1002/2015JF003602.Received

Schmidt, K. M., & Montgomery, D. R. (1995). Limits to Relief. *Science*, *270*(5236), 617–620.

Selby, M. J. (1980). A rock mass strength classification for geomorphic purposes: With tests from Antarctica and New Zealand. *Z. Geomorphol*, *24*, 31–51.

Selby, M. J. (1993). *Hillslope materials and processes*. Oxford University Press.

Sklar, L. S., & Dietrich, W. E. (2001). Sediment and rock strength controls on river incision into bedrock. *Geology*, *29*(12), 1087–1090. https://doi.org/10.1130/0091-7613(2001)029<1087:SARSCO>2.0.CO

Slim, M., Perron, J. T., Martel, S. J., & Singha, K. (2015). Topographic stress and rock fracture: A two-dimensional numerical model for arbitrary topography and preliminary comparison with borehole observations. *Earth Surface Processes and Landforms*, *40*(4), 512–529. https://doi.org/10.1002/esp.3646

Staley, D. M., Negri, J. A., Kean, J. W., Laber, J. L., Tillery, A. C., & Youberg, A. M. (2016).

Updated logistic regression equations for the calculation of post-fire debris-flow likelihood in the western United States. U.S. Geological Survey Open-File Report 2016–1106. https://doi.org/10.3133/ofr20161106

Stock, J. D., & Montgomery, D. R. (1999). Geologic constraints on bedrock river incision using the stream power law. *Journal of Geophysical Research: Solid Earth*, *104*(B3), 4983–4993. https://doi.org/10.1029/98JB02139

Townsend, K. F., Clark, M. K., & Niemi, N.A. (*in review*). Reverse faulting within a continental plate boundary transform system. *Tectonics*.

Townsend, K. F., Clark, M. K., & Zekkos, D. (2021). Profiles of near-surface rock mass strength across gradients in burial, erosion, and time. *Journal of Geophysical Research: Earth Surface*, *126*(4). https://doi.org/10.1029/2020JF005694

Townsend, K. F., Gallen, S. F., & Clark, M. K. (2020). Quantifying Near-Surface Rock Strength on a Regional Scale From Hillslope Stability Models. *Journal of Geophysical Research: Earth Surface*, *125*(7). https://doi.org/10.1029/2020JF005665

Whipple, K. X., & Tucker, G. E. (1999). Dynamics of the stream-power river incision model: Implications for height limits of mountain ranges, landscape response timescales, and research needs. *Journal of Geophysical Research*, *104*(B8), 17661. https://doi.org/10.1029/1999JB900120

Worden, R. H., & Burley, S. D. (2003). Sandstone Diagenesis: The Evolution of Sand to Stone. In *Sandstone Diagenesis: Recent and Ancient* (pp. 3–44). Malden, MA: Blackwell Publishing. https://doi.org/10.1002/9781444304459.ch

Wright, T. L. (1991). Structural Geology and Tectonic Evolution of the Los Angeles Basin, California. In K. T. Biddle (Ed.), *Active Margins Basins* (pp. 35–135). American Association of Petroleum Geologists Memoir 52. https://doi.org/10.1306/9488784D-1704-11D7-8645000102C1865D

Chapter 2: Quantifying Near-Surface Rock Strength on a Regional Scale from Hillslope Stability Models[1]

2.1 Abstract

Rock strength is a fundamental property of earth materials that influences the morphology of landscapes and modulates feedbacks between surface processes, tectonics, and climate. However, rock strength remains challenging to quantify over the broad spatial scales necessary for geomorphic investigations. Consequently, the factors that control rock strength in the near-surface environment (i.e. the “critical zone”) remain poorly understood. Here we quantify near-surface rock strength on a regional scale by exploiting two hillslope-stability models, which explicitly relate the balance of forces within a hillslope to Mohr-Coulomb strength parameters. We first use the Culmann finite-slope stability model to back-calculate static rock strength with high-density measurements of ridge-to-channel hillslope height and gradient. Second, we invert the Newmark infinite-slope stability model for strength using an earthquake peak ground acceleration model and coseismic landslide inventory. We apply these two model approaches to a recently inverted sedimentary basin in the eastern Topatopa Mountains of southern California, USA, where a tectonic gradient has exposed stratigraphic units with variable burial histories. Results show similar trends in strength with respect to stratigraphic position and have comparable strength estimates to the lowest values of published direct-shear test data. Cohesion estimates are low, with Culmann results ranging from 3 to 60 kPa and Newmark results from 6 to 30 kPa, while friction angle estimates range from 24 to 44 degrees from the Culmann model. We find that maximum burial depth exerts the strongest control on the strength of these young sedimentary rocks, likely through diagenetic changes in porosity, cementation, and ultimately, lithification.

2.2 Introduction

Rock mass strength has long been recognized as a major control on landscape morphology and evolution (Gilbert, 1877; Hack, 1975). Rock strength governs the ability of material to be dislodged and transported by surface processes and modulates feedbacks between

---

[1] Published as: Townsend, K.F., Gallen, S.F., and Clark, M.K., 2020, Quantifying near-surface rock strength on a regional scale from hillslope stability models: Journal of Geophysical Research: Earth Surface, *125*, e2020JF005665. https://doi.org/10.1029/2020JF005665

tectonics, climate, and surface processes in mountain belts (Montgomery & Brandon, 2002; Selby, 1980, 1993). Despite this general recognition, many of the factors controlling rock strength are less widely appreciated or quantified. Understanding the interdependences of factors that control rock strength is of broad interest because it is applicable to geotechnical analyses of hillslope stability (Frattini & Crosta, 2013; Hoek & Brown, 1980; Selby, 1980), process models of weathering (Riebe et al., 2017), erosion and sediment transport on hillslopes (Larsen et al., 2010) and in channels (Bursztyn et al., 2015; Sklar & Dietrich, 2001), and overall landscape evolution rates (Gallen, 2018; Forte et al., 2016; Molnar et al., 2007; Roy et al., 2015). Rock strength is also expected to exert a control on the local relief structure of mountain ranges (Montgomery & Brandon, 2002; Schmidt & Montgomery, 1995; Whipple et al., 1999), but untangling the role of rock strength from tectonic and climatic drivers is inhibited by the difficulties in the quantification of this property at the appropriate spatial scale.

Measuring rock strength at spatial scales relevant for geomorphic investigations remains an outstanding challenge due to the scale-dependent nature of strength (Hoek & Brown, 1980, 1997; Schmidt & Montgomery, 1995). “Strength”, defined here as the maximum shear stress a material can sustain before failure, is commonly described using Mohr-Coulomb failure criteria (cohesion and angle of internal friction) for properties on the sliding plane of a failure mass. While laboratory tests of rock strength are conducted on intact hand-sized samples, we know that fractures and discontinuities in a rock mass set the upper limit on strength at the hillslope-scale (Gallen et al., 2015; Hoek & Brown, 1997; 1980). Consequently, laboratory tests can overestimate hillslope-scale strength by an order of magnitude (Schmidt & Montgomery, 1995). The effect and behavior of discontinuities on rock mass strength can be effectively captured at the outcrop-scale using field observations coupled with ranked classification schemes (e.g. GSI, RMC, etc.) that penalize intact rock strength by the density, orientation, and surface conditions of fractures (e.g. Hoek and Brown, 1997). However, such classifications require detailed field investigations, and we lack a general, theoretical basis for relating weakening and discontinuity characteristics to rock mass strength that can be applied to a regional scale. Consequently, these approaches are not scalable to entire watersheds or mountain belts, nor are they easily applied to areas that lack observational data.

In this study, we test two approaches to quantifying rock mass strength at regional scales based on slope stability models, digital topography and coseismic landslide inventories. One approach uses static properties of hillslopes extracted from digital elevation models (DEMs) to estimate minimum strength (Culmann, 1875; Schmidt & Montgomery, 1995). This approach may be generally exportable to other settings as a way to quantify rock strength from DEMs. The second approach leverages earthquake-driven landslide inventories as a means to invert for rock strength properties using a dynamic model in which the forces from strong ground motion cause landsliding (Gallen et al., 2015). Because resisting and driving forces are estimated rather than assumed, the latter may be a more robust measure of rock strength but is only applicable where requisite data exist. Using these two techniques in concert allows us to assess the reproducibility of strength values and confidence in our results. The spatial distribution afforded by these methods allows us to quantify rock strength across a tectonic gradient, where differences in fault motion have exposed sedimentary rocks with variable burial and exhumation histories.

2.3 Field Setting

2.3.1 Basin Inversion in the Western Transverse Ranges

A setting with a simple tectonic inversion offers several advantages to understanding how rock strength evolves through time. Inversion is marked by a transition from an extensional setting where sediments are deposited and subsequently buried in basins to form sedimentary rocks, followed by a subsequent stage where normal faults are re-activated as reverse faults due to crustal shortening. Slip on reverse faults exposes sedimentary rocks deposited in former basins to form incipient mountain ranges. These settings commonly contain stratigraphic sequences that are well-dated, and monotonic exhumation histories suggest that these sedimentary rocks lack inherited deformation from previous tectonic events, which can dominate the spatial distribution of rock strength in some regions (i.e. Molnar et al., 2007; DiBiase et al., 2018). This simple history enables us to assess the variability of strength with respect to stratigraphic depth and active upper crustal structures. Furthermore, inversion is a common process in the geological record, so findings here are likely broadly applicable.

The Western Transverse Ranges of southern California, USA, represent an example of an inverted basin (Figure 2.1). These ranges are composed predominately of late-Cretaceous through Plio-Pleistocene marine and non-marine clastic sedimentary rocks that were deposited during multiple stages of regional extension and basin formation (Namson & Davis, 1988). Cretaceous through Eocene marine sandstones and shales, followed by Oligocene sandstones and conglomerates were deposited in an extensional setting, with specific facies dependent on

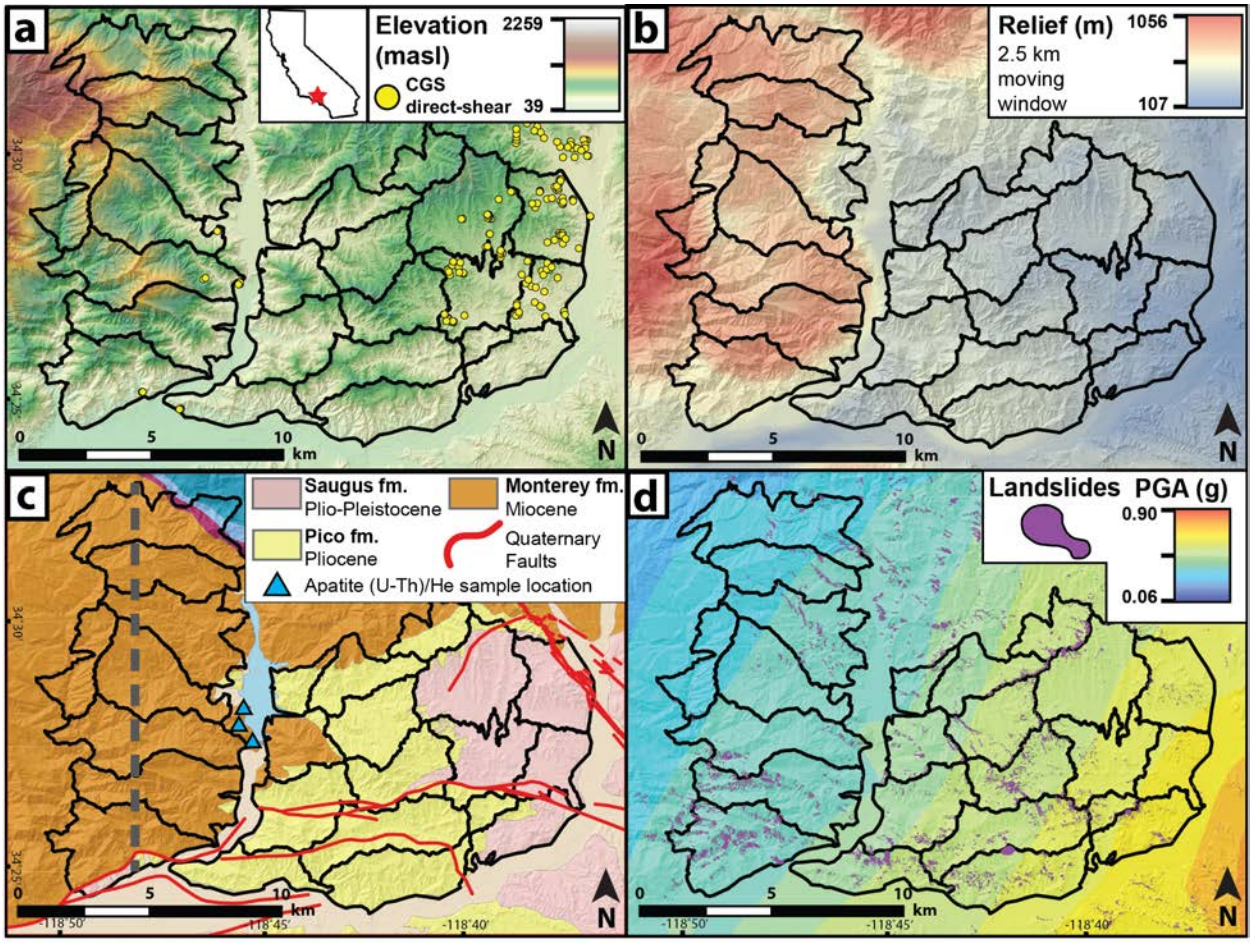

Figure 2.1: Measurement regions (black polygons) for rock strength estimates from the Culmann and Newmark models in the eastern Topatopa Mountains, southern California. (a) Elevation. Locations sampled for direct-shear tests in the California Geological Geological Survey (CGS) borehole inventory are shown (yellow). Note that samples were typically collected from multiple depth intervals in each borehole, and that multiple samples have the same map-view location. See Figure A.2 for the complete map of rock samples used to calculate average strength estimates reported in Table 2.1. (b) Relief calculated within a 2.5 km moving window. (c) Mapped geologic units, which include the Miocene Monterey Formation, the Pliocene Pico Formation, and the Pliocene/Pleistocene Saugus Formation (Dibblee, 1991; 1993; 1996; Dibblee and Ehrenspeck,1996; U.S. Geological Survey, 2006). Dashed gray line shows location of the geologic cross section in Figure 2.9. (d) Shakemap PGA raster (U.S. Geological Survey, 1994; Earle et al., 2009) and coseismic landslides produced during the 1994 M_w 6.7 Northridge Earthquake.

relative sea level (Atwater, 1998; Prothero & Vance, 1996). The region transitioned to a transtensional tectonic regime as it underwent over 90° of clockwise rotation following complete subduction of the Farallon Plate in early Miocene time (Nicholson et al., 1994; Hornafius et al., 1986). Thick sections of marine siliceous mudstones, sandstones, conglomerates, and volcaniclastic rocks produced by syn-tectonic volcanism accumulated in fault-bounded extensional basins, which continued through Pliocene time (Namson & Davis, 1988; Wright, 1991). Eastward migration of the North American-Pacific plate boundary at 5-6 Ma lead to development of a transpressional ~160 km "Big Bend" in the San Andreas Fault, which drives the modern regional shortening in the Western Transverse ranges and caused many normal faults to re-activate as high-angle reverse faults (Dolan et al., 1995; Hornafius et al., 1986; Huftile & Yeats, 1996; Wright, 1991). The late-Mesozoic through Cenozoic sedimentary and volcaniclastic rocks sequences are now being inverted along east-west trending oblique-reverse faults forming the modern mountainous topography.

2.3.2 Eastern Topatopa Mountains Study Site

We focus our study on the easternmost Topatopa Mountains, along the northeast margin of the Western Transverse Ranges (Figure 2.1). Here the mountains expose a section of young (Miocene to Plio-Pleistocene) and variably lithified sedimentary rocks in a broad homocline that dips to the east with strike perpendicular to the range front (Dibblee, 1991, 1993; Dibblee & Ehrenspeck, 1996). Stratigraphic units have similar lithology (primarily clastic rocks) and a simple tectonic history of basin inversion with no inherited deformation, allowing us to assess the variability of strength with respect to stratigraphic depth and active structures. These rocks are being uplifted due to active reverse faulting along the San Cayetano Fault, which initiated during Pliocene time (Dolan & Rockwell, 2001; Huftile & Yeats, 1996; Rockwell, 1988). These stratigraphic units are faulted and folded proximal to the San Cayetano Fault, allowing us to assess how strength varies with stratigraphic depth and exhumation within individual formations. Here a high-resolution (3 m pixel resolution) digital topographic dataset has already been produced by the National Oceanographic and Atmospheric Administration (NOAA) (Office for Coastal Management, 2016), and an inventory of coseismic landslides produced during the 1994 M_w 6.7 Northridge Earthquake is available (Harp & Jibson, 1995, 1996). The geologic setting and existing coseismic landslide inventory allow us to leverage both static and dynamic properties of slope stability to evaluate rock strength.

In the study area, surface rock exposures consist of an east to west gradient of progressively older stratigraphic units of a paleo-extensional basin (Figure 2.1c) (Dibblee, 1991, 1993; Dibblee & Ehrenspeck, 1996). The age of the exposed strata is, therefore, a proxy for maximum burial depth, and each stratigraphic unit can be viewed as exhumational time steps in the evolution of an inverted basin sequence. The weakly-consolidated, shallow-marine to terrestrial Plio-Pleistocene Saugus Formation is predominately a sandstone and pebble conglomerate with clasts sourced from the San Gabriel Mountains, indicating deposition by an ancestral Santa Clara River (DeVecchio et al., 2012; Levi & Yeats, 1993). This unit represents the initial phase of basin inversion and growth of a nascent mountain range. The Pliocene Pico Formation consists of conglomerate, sandstone, and siltstone members deposited in a shallow marine environment (Dibblee, 1993; Yeats et al., 1986). This unit is exhumed from greater depths and represents an intermediate step in the rise of a fault-bounded block. The Monterey (locally known as Modelo) Formation is a deep marine siliceous shale that was deposited throughout much of present-day Southern California during Miocene time (Bramlette, 1946). Within the eastern Topatopa Mountains, this formation was deposited at the paleo-basin margin proximal to its source, resulting in predominately sandstone lithology (Gordon, 2014; Yeats et al., 1994). This unit is exhumed from greater depth and is more strongly lithified than the overlying units, representing the most mature time step in our framework.

Additional constraints on burial histories come from new low-temperature (U-Th)/He thermochronology data. These thermal ages yield constraints on the timing and magnitude of rock exhumation in the eastern Topatopa Mountains because apatite crystals begin retaining radiogenically-produced helium after cooling between ~40-80°C (Farley, 2002; Flowers et al., 2009). Assuming a typical geothermal gradient (~15°C/km for sedimentary basins; Ehlers, 2005), the system is sensitive to tectonic and geomorphic processes affecting the upper ~3-5 km of the crust. For detrital grains, such as those preserved in sandstone rocks, the closure temperature must be exceeded during burial in order to release the inherited helium from a previous cooling event and reset the apatite age. Cooling ages that are younger than the stratigraphic age of the rock are assumed to be reset and record a thermal event related to burial and exhumation, whereas cooling ages older than the age of the rock do not record a thermal event related to burial and exhumation. A sample collected from the lowest member of the Monterey fm. in the core of an anticline yielded an apatite cooling age of 3.9 ± 1.2 Ma, which is younger than the stratigraphic age of the rock (Figures 2.1 and A.3, Tables A.1 and A.2). A sample from the highest member of the Monterey fm. in the core of a syncline yielded an apatite cooling age that is older than the stratigraphic age of the rock, and a sample collected from an intermediate member yielded grains that are both younger and older than the age of the rock. These data indicate that only the deepest section of the Monterey fm. experienced complete thermal resetting and thus at least 3 km of burial prior to exhumation. As the Pico and Saugus fms. are stratigraphically higher than the Monterey fm., these must have experienced less burial prior to being exhumed.

2.3.3 Hillslope Soils and Weathered Rock Profile

Hillslopes in the eastern Topatopa Mountains are partially soil mantled, with soil map regions classified as up to fifty percent exposed bedrock (Natural Resources Conservation Service, 2019). Where present, soils on these hillslopes are predominately entisols with thin A horizons directly above residuum parent material (Calleguas and Saugus soil series) or inceptisols with weakly developed B horizons (Castaic soil series). Coseismic landslides produced during the 1994 M_w 6.7 Northridge Earthquake predominately originated from ridge tops, where soils and the collective mobile regolith layer were likely thinner than is indicated by type-location profiles for each soil series. Field observations and data from the Natural Resources Conservation Service (2019) suggest that depth to non-mobile regolith (weathered to intact bedrock) in C or Cr horizons beneath these soils is typically ~0.2 to 0.8 m (Figure 2.3d). Landslides during the Northridge Earthquake were typically 1-5m deep (Harp & Jibson, 1996), indicating that bedrock beneath the shallow mobile regolith layer must have been mobilized in these hillslope failures in addition to the thin soil mantle.

2.4 Methods

Here we measured apparent near-surface rock strength using two models that relate Mohr-Coulomb strength parameters to hillslope stability. We first back-calculated strength under static conditions using the Culmann limit-equilibrium, two-dimensional, finite-slope model with 2D hillslope morphology measured from a DEM (e.g. Schmidt and Montgomery, 1995). We then inverted the Newmark limit-equilibrium, one-dimensional, infinite-slope stability analysis for strength under dynamic conditions using 1D hillslope morphology (slope) measured from a DEM, peak ground accelerations estimated for the 1994 M_w 6.7 Northridge Earthquake (U.S. Geological Survey, 1994; Earle et al., 2009) and a coseismic landslide inventory (Gallen et al., 2015, 2017). We applied these two models to 24 regions in the eastern Topatopa Mountains to produce measures of apparent cohesive and frictional strength, and also compared the results to a dataset of direct-shear test results on the relevant stratigraphic units (California Department of Conservation, 2002a, 2002b).

2.4.1 Estimating Hillslope-Scale Rock Strength using the Culmann Analysis

A common concept in geomorphology is to assume that landscape form (i.e. topography) reflects a steady-state condition, that is, reflecting a balance between forces that uplift mountains, rock strength, and the erosional forces (including gravity) that act to lower the land surface

(Hovius et al., 1998; Montgomery, 2001; Willett & Brandon, 2002). Inherent in this view is the idea that the shape of the land surface represents a limit-equilibrium or "critical" state where the driving forces that change topography are in balance with the resistance to such change provided by rock strength. Applied to individual hillslopes and the formation of landslides, one can imagine that the distribution of hillslope heights and gradients throughout a landscape reflect such a balance, in this case, between gravity acting to destabilize the slope and the resistance provided by the rock, regolith, and soil cover (Hovius et al., 1998; Roering et al., 1999; Schmidt & Montgomery, 1995). Although the concept of criticality is a theoretical one, such an assumption allows us to extract features from digital topography that can be interpreted as estimates for minimum strength parameters related to landsliding processes.

Here we applied a static two-dimensional, finite-slope stability model or 'Culmann analysis' (Culmann, 1875; Schmidt & Montgomery, 1995) to digital topography to estimate near-surface rock strength from hillslope morphology over small fluvial catchments (~10 km^2). The Culmann analysis predicts slope failure for a simple hillslope of a given height and constant gradient, assuming a planar geometry that intersects the ground surface at the toe of the slope in a wedge-shaped geometry (Figure 2.2a). The analysis produces thin wedge geometries for steep, planar slopes (> ~40°), which are similar to observed failures in steep topography during earthquakes (Keefer, 1984) and also matches predictions from more rigorous approaches using log-spiral mechanisms (Ling et al., 1999). We note that our study area in the eastern Topatopa Mountains is dominated by short, steep, planar hillslopes, where the Culmann criteria is most likely to replicate observed landslides. Failure, or slip on the landslide surface, occurs when the ratio of the weight of the landslide mass exceeds the shear resistance of the slip surface (Factor of Safety = 1), expressed in terms of Mohr-Coulomb strength parameters (cohesion and angle of internal friction). Thus the Culmann analysis can predict the maximum hillslope height for a given slope that is critically stable for a given measure of cohesion (C) and angle of internal friction (ϕ). For values of hillslope gradient (β) that exceed the friction angle ϕ (typically gradients greater than 25-30 degrees), the Culmann model predicts an exponential-like decay in the maximum height of hillslopes as a function of β. In landscape terms, this criterion predicts

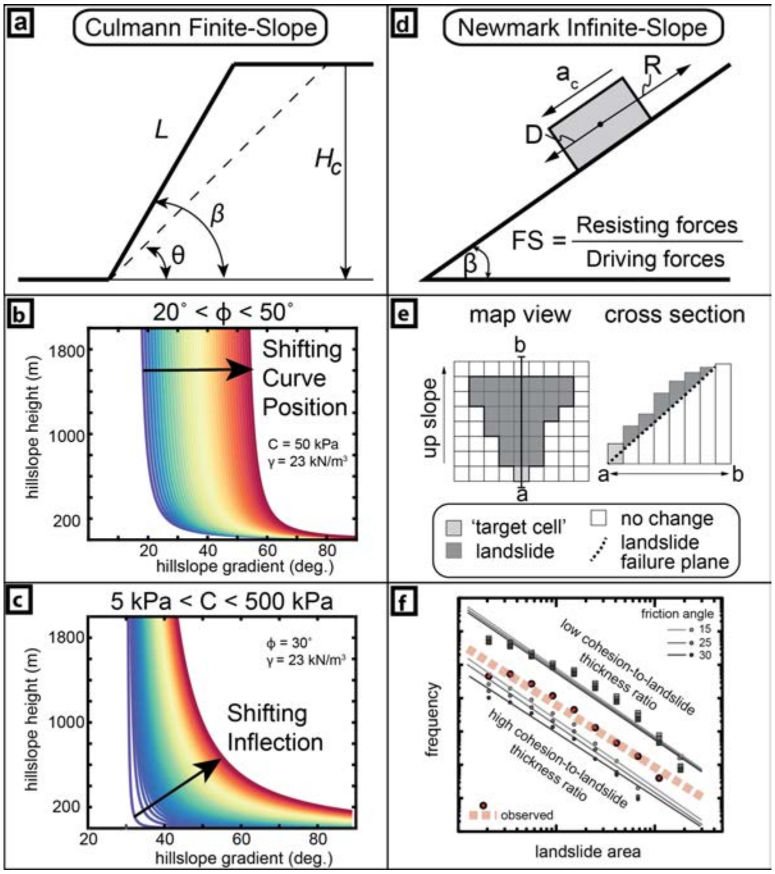

Figure 2.2: Culmann and Newmark model inputs for strength. (a) Simplified hillslope cross-section with length (L), gradient (β), and critical height (H_c) shown. (b) Theoretical Culmann curves of critically stable hillslope gradients and heights plotted with ϕ increasing in increments of one degree from 20 to 50 degrees while holding c = 50 kPa. (c) Culmann curves plotted with cohesion values increasing in increments of 5 kPa from 5 to 500 kPa while holding ϕ = 30 degrees. (d) Schematic force balance for the factor of safety infinite slope stability solution used on the simplified Newmark method. a_c is the critical acceleration required to overcome basal shear resistance and initiate motion during an earthquake. (e) Illustration of the synthetic landslide geometry used in our simplified Newmark landslide model (after Gallen et al., 2017). (f) An example model result showing the influence of selected cohesion (circles and squares) and internal angle of friction (different shades of gray) on synthetic landslide populations generated by our simplified Newmark landslide model (after Gallen et al., 2015). Solid lines represent best-fit regressions through landslide populations.

that the tallest hillslopes of a particular gradient represent a critical state under static conditions, which then can be interpreted in terms of strength parameters of the near-surface (mean depth of 3.7 m, Appendix A) profile subject to shallow landsliding. As strength parameters are determined solely from hillslope morphology, the Culmann approach requires only an input DEM, making it advantageous to other hillslope stability approaches and more broadly exportable to other landscapes. Further, the computational efficiency of this approach permits application at spatial scales as large as entire mountain ranges.

2.4.1.1 Culmann Finite-Slope Stability Model

The Culmann (1875) limit-equilibrium finite-slope stability model assumes wedge-shaped landslides with planar failure surfaces not parallel to the slope face such that the height of the critical hillslope is given by Equation 1 (Figure 2.2a).

(1) $$\boldsymbol{H_c = \left(\frac{4C}{\gamma}\right)\left(\frac{\sin(\beta)\cos(\phi)}{1-\cos(\beta-\phi)}\right)}$$

The derivation of the Culmann equation yields a second expression (Equation 2) wherein the angle of modeled landslide failure planes is equal to the arithmetic mean of the angle of internal friction and average hillslope gradient (Lu & Godt, 2013).

(2) $$\boldsymbol{\theta = \frac{\beta+\phi}{2}}$$

Thus the range of hillslope heights for slope values where $90 > \beta > \phi$ defines a critical relationship between hillslope relief, gradient, and Mohr-Coulomb strength parameters.

Mountainous topography can be parsed into a collection of 2D hillslope segments that extend from a drainage divide to the nearest adjacent channel (Figure 2.3). We extracted height (H) and average slope (β) for each of these segments within a drainage basin, assumed to be underlain by material of constant strength. This analysis produces a scatter plot of H vs β values from which we assert that the envelope encompassing the tallest slopes of various gradients represent the most critical parts of the landscape (the H_c vs β relationship). Defining this limit requires measuring the height and gradient of many individual hillslope segments (Figure 2.3).

The Culmann model predicts that threshold hillslope heights exponentially decrease with increasing hillslope gradient; the friction angle estimate is most sensitive to the gradient of the tallest hillslopes while the estimate of apparent cohesion is sensitive to the rate of the exponential decrease in hillslope height with increasing gradient (Figure 2.2b and 2c). For each measurement region (average of 8.3 km^2), one estimate of C and ϕ is produced, which necessarily assumes that materials characterized by the same strength underlie every hillslope segment within a sampled region. While constant strength is likely not a reality, such an assumption effectively averages

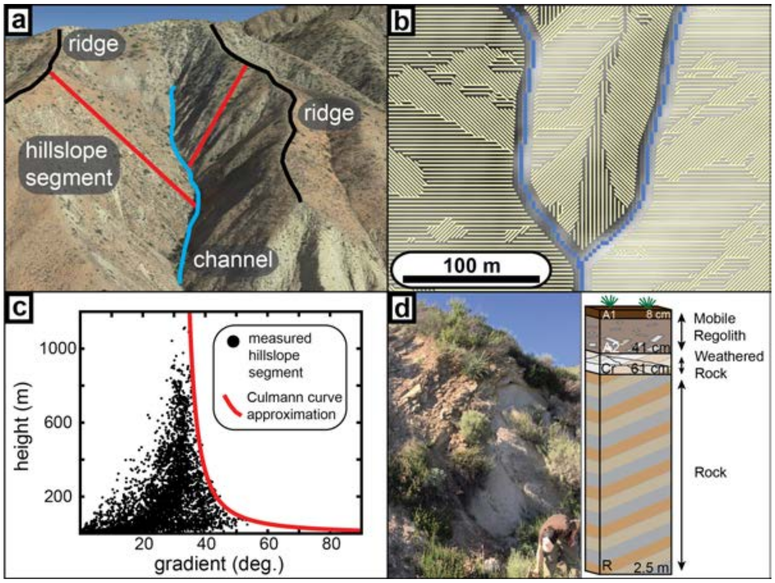

Figure 2.3: Hillslope flow paths (red) are routed from ridge crests (black) to channels (blue). Imagery from Google Earth. (b) Plan view of modeled hillslope flow paths above the fluvial network produced using GIS workflow. The spacing between flow path centerlines is three meters. (c) Scatter plot of measured hillslope segment gradient (β) vs. height (H_C) for a given measurement region. Approximating the threshold of data with the Culmann model results in estimates of cohesion (C) and friction angle (ϕ). (d) Typical profile for hillslope soils in the eastern Topatopa Mountains. Hillslopes are partially mantled by soils, with bedrock commonly exposed at the surface (image). Diagram shows near-surface profile depth over the average thickness of the Northridge coseismic landslides (2.5m). Where soils are present, depth to weathered bedrock beneath the mobile regolith layer is typically 0.2 to 0.8 meters.

strength differences at spatial scales smaller than the measurement region and also likely contributes to some degree of scatter about the H_c vs β relationship.

2.4.1.2 Hillslope geometry and scatter plots

Here we established a technique to automatically extract hillslope gradient (β) and height (H_c) at intervals equal to the pixel resolution of the input DEM. Standard hydrology raster datasets, including flow direction, flow accumulation, and flow length, were first generated using a NOAA Interferometric Synthetic Aperture Radar (IfSAR) DEM with 3 m pixel resolution (Office for Coastal Management, 2016). We used the D8 algorithm to determine flow direction, in which flow is distributed in 45 degree azimuth angles to the lowest elevation of the adjoining eight cells (Tarboton et al., 1991). Although it has been argued that the resulting flow paths do not reflect the dispersive nature of overland flow on hillslopes (Tarboton et al., 1991), this approach allowed us to isolate ridge-to-channel segments into 2D profiles (Figure 2.3a and 2.3b). From these raster datasets, flow lines initiating on ridge tops were produced. Hillslope flow lines were isolated from the fluvial network with slope-area analysis, using the contributing area at which the relationship between slope and area switches from a positive to negative trend as a proxy for the transition between hillslope and channelized (debris flows) process domains

(Dietrich et al., 2003; Grieve et al., 2016; Montgomery, 2001; Montgomery & Foufoula-Georgiou, 1993; Roering et al., 2007). Although it has been argued by other authors (e.g. Stock & Dietrich, 2003) that the rollover in slope-area space may instead reflect the transition from debris-flow dominated channels to fluvial channels, thereby potentially masking the hillslope-to-channel transition, changing this value by a few tens of square meters does not significantly change the distributions of hillslope geometries. Individual hillslope flow lines were amalgamated at intersections to produce segments that span the entire ridge-to-channel distance. Horizontal flow length and relief across each hillslope segment were extracted, from which the average gradient of the hillslope segment was calculated. In reality, not every hillslope in the landscape is planar, and this approach produces lower gradients for hillslopes with convex profiles than would be identified on a pixel-by-pixel basis. However, as these hillslopes plot at gradients below the threshold in hillslope height vs. gradient space, they do not change the strength results.

We sought to create measurement regions small enough to analyze spatial variability in material strength, but just large enough to generate sufficient data to populate the threshold and fit the Culmann curve. We defined regions of 3 to 10 km^2 for high-resolution (3-meter or finer) DEMs based on trial and error. To avoid truncating hillslope segments, measurement region boundaries were defined by watershed boundaries. Scatter plots containing hundreds to thousands of (β, H_c) pairs representing individual hillslope segments were created for each measurement region (Figures A.5-A.28).

2.4.1.3 Calculating apparent cohesion and friction angle from the Culmann model

Assuming uniform strength for small catchment areas, we approximated the threshold in hillslope height vs. gradient data with the Culmann model. This analysis produces an estimate of hillslope-scale C and ϕ for each small catchment while holding unit weight (γ) constant at 23 kN/m^3 (Figure 2.3c). For typical values of γ for a sandstone (20-25 kN/m^3), the resultant C varies by <15%, and ϕ varies by up to one degree, but in the absence of local data, we hold this variable constant. The vast majority of hillslope data plot at relatively low heights and gradients, and each threshold is typically defined by less than five percent of hillslope segments within each catchment. Hillslope data from several basins produced thresholds that are variably well-defined with respect to the Culmann model (i.e. the height of the tallest hillslope regularly decreases with increasing slope angle), with some regions yielding data with a larger number of tall moderately steep hillslopes than anticipated by a Culmann model. Curve fitting routines that minimize misfit by eliminating or penalizing static failures (points to the right of the curve) tend to systematically produce unrealistically high friction values because of the relatively few data points for the tallest hillslopes and the large scatter at moderately steep slopes (50-70°) (Figure A.31). Instead, the data were fit by inspection by first prioritizing fit to the tallest hillslopes (typically at intermediate gradients of ~30°-50°) followed by fitting the steepest hillslopes, which are typically short (> 70° and < ~20 m height) in order to minimize the number of points to the right of the model curve. By such an approach, nearly every basin has some hillslope data which falls to the right of the model curve. As such, estimated uncertainty in apparent cohesion is estimated to be as high as a few tens of kPa in basins with high C, whereas it may only be a few kPa in basins with low C.

2.4.2 Newmark Infinite-Slope Stability Inversion for Strength

Following the approach of Gallen et al. (2015), we estimated near-surface material strength under dynamic conditions by inverting a one-dimensional infinite slope stability model that predicts hillslope failure during seismic shaking (simplified Newmark model) with peak ground accelerations, pixel slope, and a coseismic landslide inventory (Jibson, 2007). The simplified Newmark model assumes an infinitely-long, planar hillslope and predicts landslide failure cells given local topographic slope, PGA, and rock strength. To turn the resultant distribution of landslide failure cells into a synthetic landslide inventory, we coupled the simplified Newmark analysis with a three-dimensional model of landslide geometry to produce area and volume estimates for each landslide failure. Using an observed landslide distribution during an earthquake event, we inverted these seismic landslide models for near-surface material strength over a spatial window defined from tributary drainage basins (Figure 2.1) (Gallen et al., 2015).

2.4.2.1 Seismic Slope Stability and Synthetic Landslide Geometries

The simplified Newmark seismic slope stability analysis is based on the effect of horizontal accelerations during an earthquake acting on a hillslope with static properties (inclination or slope, and the sub-surface material properties of soil and rock). Although seismic slope stability analyses have been developed assuming rotational failure planes (e.g. Sarma, 1981), here we applied the simplified Newmark rigid block approach, as coseismic landslides produced during the Northridge earthquake were generally shallow and planar (e.g. Jibson, 2007). Initially, we calculated the static factor of safety of a rigid block with finite thickness using local topographic slope, shear strength (cohesion and the angle of internal friction), density of hillslope material (assumed 2300 kg m^{-3}) and landslide thickness (Jibson, 1993; Jibson et al., 2000) (Figure 2.2d). Following Jibson et al. (2000) and Dreyfus et al. (2013), we neglected pore water pressure because the Northridge earthquake occurred during an abnormally dry period, when the transient effects of an elevated water table were likely negligible (Los Angeles Almanac; Parise & Jibson, 2000). The static factor of safety was calculated for each grid cell in the digital elevation model, as was the horizontal acceleration needed to overcome shear resistance to produce displacement of that block (critical acceleration, or ac). Using the simplified Newmark analysis, the ratio of peak ground acceleration to the critical acceleration was used to calculate permanent displacements (DN) experienced over an earthquake based on an empirical relationship (Jibson, 2007), where threshold displacements in excess of 5 cm in the model are identified as slope failure (Wieczorek et al., 1985; Godt et al., 2008).

A simplified Newmark analysis alone is one-dimensional and produces a binary map of grid cells that are identified as either stable or unstable based on an assigned threshold displacement (DN). To synthesize individual landslide geometries, we assumed that Newmark failure cells (DN ≥ 5 cm) are incipient failure points (unstable cells) from which we applied a set of geometric rules to calculate the location and 3D volume of each landslide. From a failure grid cell, we projected a failure plane upslope from a point at depth assuming the slope of the failure plane to be equal to the topographic gradient of the failure grid cell and for the full 3D landslide geometry to be defined from the failure plane projection that daylights at the Earth's surface (Figure 2.2e, Figure A.30) (Gallen et al., 2015). We tested initial point depths ranging from 1.0 to 2.5 m but found that this had little effect on the final strength results (< 4 kPa difference). Here we report results using an initial point depth of 2.5 m as this approximates the mean thickness of the 1994 Mw 6.7 Northridge Earthquake coseismic landslides (Harp & Jibson, 1996). From these landslide geometries, we generated synthetic landslide frequency-area distributions (Figure 2.2f). While lacking a mechanical basis, this simple geometric approximation applied to digital topography produces synthetic landslide distributions that closely match observed power-law scaling of landslide frequency-area statistical distributions for intermediate to large landslides (Gallen et al., 2015).

2.4.2.2 Inverse approach

We used a Markov-Chain Monte Carlo routine to invert models generating synthetic landslide populations compared to mapped landslide inventory in order to determine the best-fit strength parameters. For model inputs, we use the local topographic slope (derived from a DEM), and PGA (U.S. Geological Survey, 1994; Earle et al., 2009). Because landslide thickness, cohesion and friction angle collectively contribute to the one-dimensional infinite slope stability factor of safety, we cannot independently solve for these variables. For comparison with results produced with the finite-slope approximation, we set the friction angle using values determined from the Culmann method for each sub-basin. Thus, we varied the cohesion-to-thickness ratio (c/t) for each successive model run and then used the modeled landslide geometry to determine the average landslide thickness and express our modeling results in terms of apparent cohesion. The inversion works by maximizing the goodness-of-fit between observed and modeled landside frequency-area statistics over a predefined area (Figure 2.2f).

2.4.2.3 Landslide Inventory Remapping

The earthquake-triggered landslide model used in this study is sensitive to the total frequency and size (e.g., area) statistics of landslide populations, and therefore is sensitive to mapping artifacts such as amalgamation (Marc & Hovius, 2015). We remapped a portion of the original Northridge coseismic landslide inventory (Harp & Jibson, 1995) to remove the effects of amalgamation, to relocate misplaced landslides, and to remove anomalously large landslide polygons that contained a mix of disturbed and undisturbed regions (Figure 2.4; Marc and Hovius, 2015). Further descriptions of our landslide mapping approaches are given Appendix A. Through this effort, we identified 5,064 landslides in the eastern Topatopa Mountains in the region where the original Northridge coseismic landslide inventory contained 3,428 landslides. The re-mapped inventory has a power-law exponent of -2.65, compared to the original -2.29, effectively steepening the power-law tail of the frequency-area distribution (Figure 2.4c). Landslide polygons include both scar and runout areas, as the resolution of the historical imagery is too coarse to differentiate between the two.

2.5 Results

2.5.1 Modelled Landslide Depths

Landslide depths were calculated as the average distance between the failure plane and landslide surface, normal to the failure plane. The mean landslide depth as predicted by the

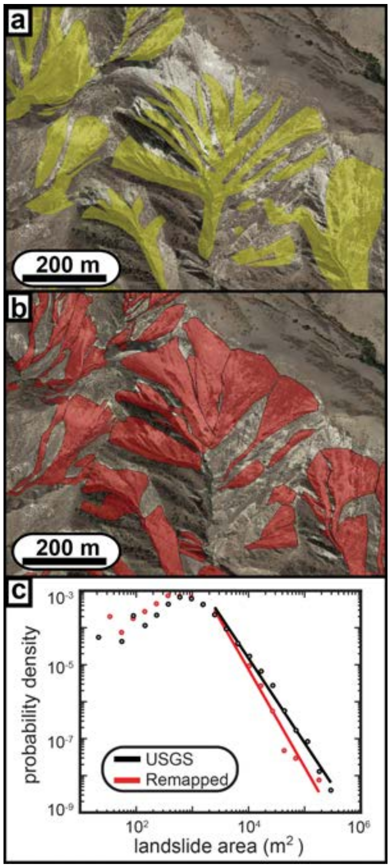

Figure 2.4: (a) Amalgamated landslide polygons in the original USGS 1994 M_w 6.7 Northridge Earthquake coseismic landslide inventory (Harp and Jibson, 1995, 1996). (b) Remapped landslides in the same extent as 'A'. (c) Frequency-area scaling of original USGS (black) and remapped (red) landslides. Remapping steepened the regression in loglog space.

Culmann model for critically-stable hillslopes is 3.7m (Appendix A), and the mean landslide depth of synthetic landslides produced using the Newmark approach is 3.0m (excluding outliers >20m thick). These values are within the range of failure plane depths for landslides produced by the 1994 M_w 6.7 Northridge Earthquake, which were typically 1-5m deep (Harp & Jibson, 1996). Despite the shallow depths of these failures, soil depth on hillslopes in the eastern Topatopa Mountains is generally thin (0.4 – 0.8 m, Natural Resources Conservation Service, 2019), indicating that bedrock must have been detached in these failures. We therefore expect a direct relationship between the strength of the failed material and the underlying rock mass properties, and we cast our strength results in terms of the strength of the rock mass rather than the thin overlying mobile regolith layer. We recognize that the failure plane of landslides assumed by the Culmann model would pass through the mobile regolith zone at the uppermost of lowermost

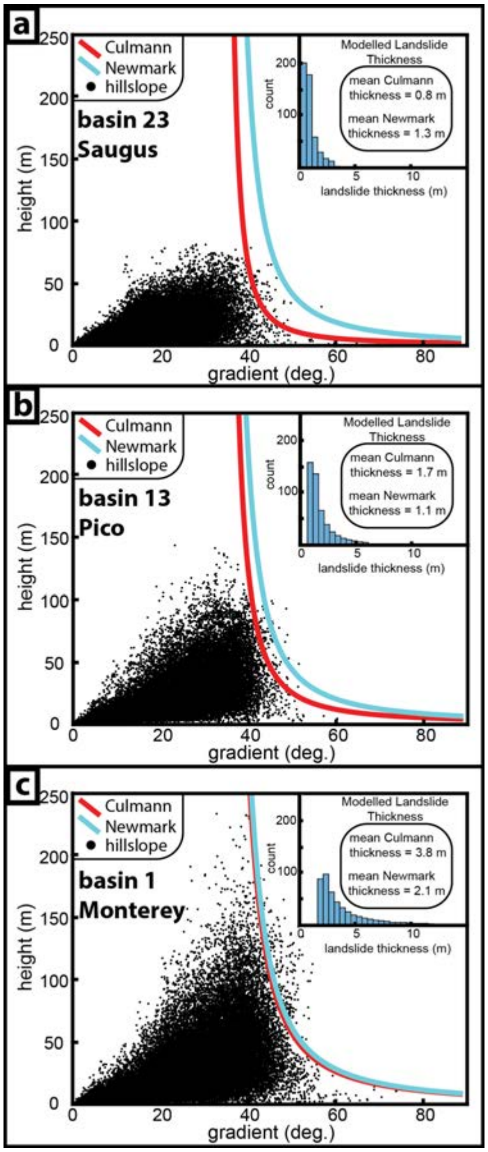

Figure 2.5: Hillslope segment gradient and height pairs from (a) the Saugus Formation, (b) the Pico Formation, and (c) the Monterey Formation. An exponential decay in hillslope height with gradient from the tallest hillslopes was used to infer strength with the Culmann model (red line). Culmann model curves with cohesive strength set by the Newmark model results are shown in blue. Newmark cohesion values were obtained using friction angle estimates derived from the Culmann analysis from each basin. Inset figure in each panel shows distribution of modeled Culmann landslide thicknesses for hillslope segments that fall along the threshold.

portions of the wedge, but these constitute a minor component of the landslide failure plane. We take results from the Culmann analysis to reflect the average strength of the material underlying each hillslope, which is predominately shallow bedrock.

2.5.2 Hillslope Data and Culmann Strength Estimates

Scatter plots of hillslope gradient and hillslope height for most watersheds produced a maximum value of slope height/gradient beyond which no hillslopes are measured (Figures 2.3 and 2.5). Maximum hillslope heights decrease exponentially with increasing hillslope gradient at

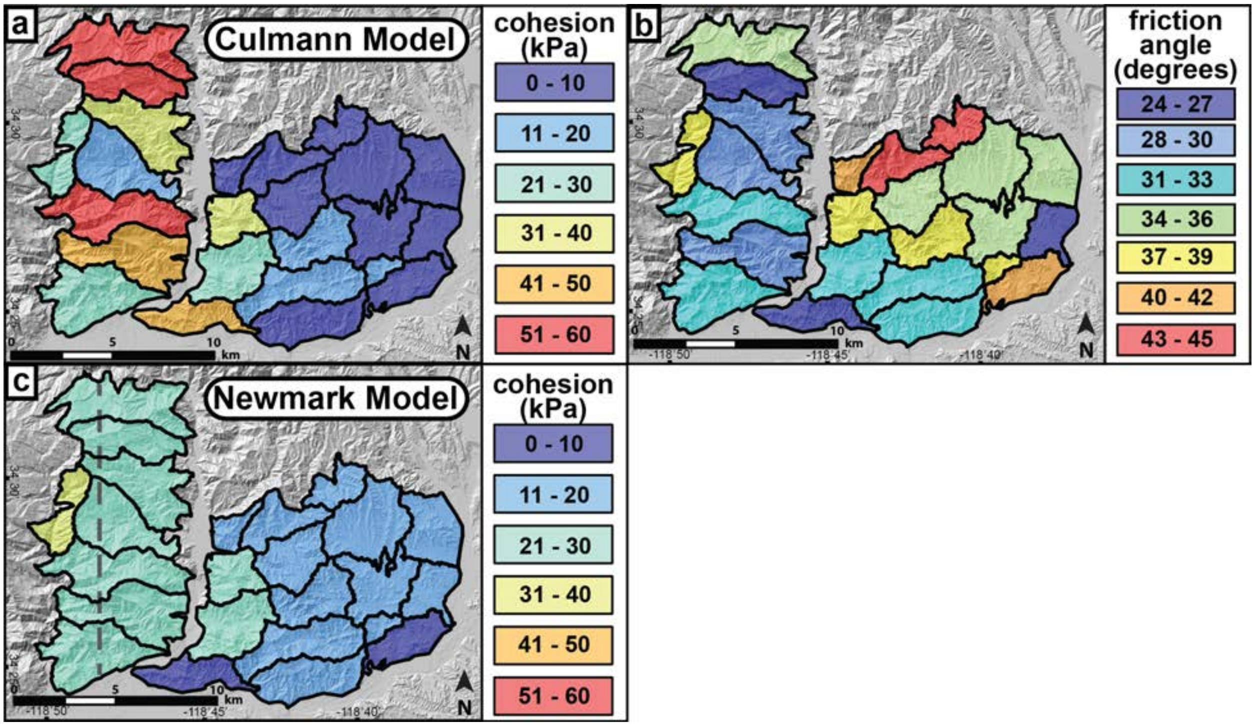

Figure 2.6: Map view of strength results. (a) Cohesion (kPa) produced from the Culmann finite-slope stability model, (b) friction angle (degrees) produced from the Culmann model, and (c) cohesion produced from inversion of the Newmark infinite-slope stability model. Cohesion results from the Newmark model were calculated using friction angle estimates derived from the Culmann analysis for each basin. Dashed line shows location of strength transects and geologic cross section in Figure 2.9.

angles greater than the tallest hillslope segment, which is consistent with the concept of critical hillslopes predicted by the Culmann failure criterion. Threshold hillslope segments appear distributed throughout most watersheds, but generally, the shorter, steeper critical hillslopes are located above low stream-order channels at the highest elevations, and the tallest critical hillslopes are located above higher stream-order channels at lower elevations (Figure A.29). We observe that the density of hillslope segments is typically highest at low gradients and heights, well below the threshold (Figures A.5-A.28).

Apparent cohesion estimates from individual basins produced by the Culmann model range from 3 to 60 kPa, while friction angle estimates range from 24 to 44 degrees (Figure 2.5, Figure 2.6a and 2.6c; Table A.3). These values are low but consistent with other measurements of hillslope-scale strength (Schmidt & Montgomery, 1995; Gallen et al., 2015). When divided into respective stratigraphic units, we observe that mean friction values overlap within one standard deviation, whereas apparent cohesion values increase with increasing stratigraphic age (Table 2.1). The Pliocene/Pleistocene Saugus fm. underlying the easternmost basins is the stratigraphically-highest unit in the Topatopa Mountains, and these regions produce a mean cohesion estimate of 6 ± 3 kPa (weighted by area, with one standard deviation uncertainty) and friction angle of 34 ± 3 degrees. Mean cohesion and friction angle of regions overlying the Pliocene Pico fm. to the west of the Saugus fm. basins is 17 ± 13 kPa and 35 ± 6 degrees. The Miocene Monterey fm. exposed in the westernmost basins is the stratigraphically lowest unit, and mean cohesion and friction angle estimates are 40 ± 16 kPa and 31 ± 3 degrees, respectively (Tables 2.1 and A.3). Taken collectively, estimates of apparent cohesion across the three transects increase from east to west as stratigraphically lower units are progressively exposed at the surface due to recent movement on the San Cayetano fault (Figures 2.1c and 2.6a). Friction angle estimates for individual basins generally decrease from east to west with exposure of progressively deeper strata (Tables 2.1 and A.3).

2.5.3 Newmark Inversion

For the same individual tributary basins used in the Culmann analysis, we considered the frequency-area relationship for the remapped Northridge landslides and compare these to our modified Newmark analysis. We did not apply a scar area correction to the remapped landslides (e.g. Marc et al., 2018) because the minimum size landslide we can model is controlled by the DEM resolution, and applying a scar correction therefore reduces the number of landslides that we can model. Our inverse approach is sensitive to the total number of landslides in each basin, and because full landslide areas were used, recovered strength estimates represent conservative values. For each sub-basin, we used the friction value from the Culmann results for that same basin and determine a best-fit C/t value (Figure 2.2f). We then used the median model thickness for the whole dataset (2.2 m) to determine apparent cohesion values for individual basins. These results suggest apparent cohesion from 6 to 30 kPa for friction angles of 24 to 44 degrees (Figure 2.6b, Table A.3) for the entire study area. The mean of cohesion estimates for the Monterey fm.

Table 2.1: Average estimates of cohesion and friction angle (± one standard deviation) from the Culmann model, Newmark model inversion, and direct-shear tests on hand samples. Culmann and Newmark averages are weighted by basin area.

	Monterey Formation		Pico Formation		Saugus Formation	
	C (kPa)	*ϕ* (degrees)	*C* (kPa)	*ϕ* (degrees)	*C* (kPa)	*ϕ* (degrees)
Culmann Model	40 ± 16	31 ± 3	17 ± 13	35 ± 6	6 ± 3	34 ± 3
Newmark Model	26 ± 3	-	16 ± 5	-	15 ± 3	-
Direct-Shear Test[1]	51 ± 32	33 ± 3	27 ± 15	34 ± 7	30 ± 26	34 ± 7

[1] Source: California Department of Conservation seismic hazard reports, 2002a, 2002b

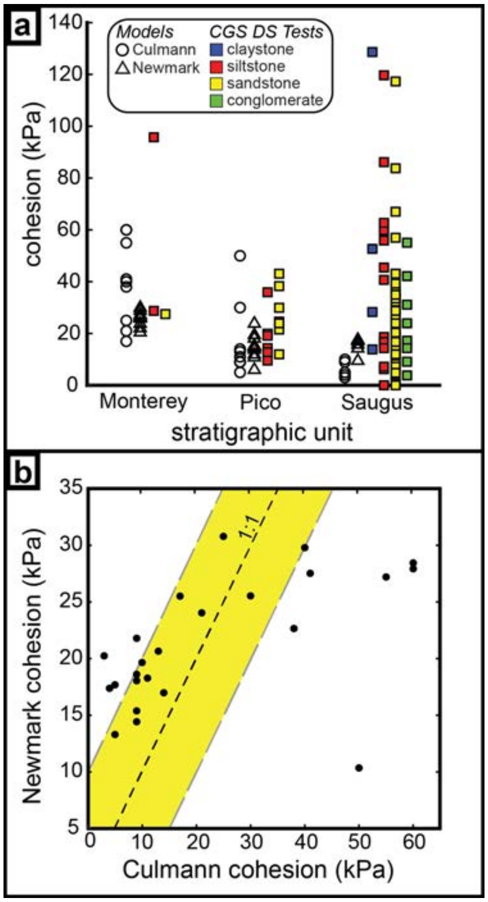

Figure 2.7: (a) Cohesive strength of the Saugus, Pico, and Monterey Formations from each basin by the Culmann and Newmark models. California Geological Survey (CGS) direct-shear (DS) test data are separated by lithology within each unit. (b) Newmark model cohesion results plotted against Culmann model cohesion results. Yellow shaded region shows ±10 kPa from one-to-one relationship (black dashed line).

is 26 ± 3 kPa, the Pico fm. is 16 ± 5 kPa and the Saugus fm. is 15 ± 3 kPa (Tables 2.1 and A.3). Variability in the quality of fits between synthetic and observed frequency-area distributions is likely driven by a mismatch between the topography that is predicted to landslide and the topography that actually failed in landslides during the earthquake (Appendix A).

Overall, the Newmark and Culmann estimates both produced low values of apparent cohesion (tens to several tens of kPa) and differ by up to ~10 kPa for averages within the same stratigraphic units (Figure 2.7, Table 2.1). The Newmark results produced a correlation between apparent cohesion and stratigraphic age between the Monterey and Pico fms., but did not distinguish values between the Pico and Saugus fms. The Newmark results estimated higher (+9 kPa) mean cohesive strength of the Saugus fm. compared to the Culmann model, while Newmark and Culmann mean estimates of cohesive strength are identical for the Pico fm. (within 1 kPa) (Table 2.1). The Newmark model produced a lower mean (-14 kPa) estimate of cohesion for the Monterey fm. compared to the Culmann model (Table 2.1). The basins with the greatest disagreement in cohesion estimates do not appear to be a result of either poor Newmark fits and poorly-defined thresholds for the Culmann curve (Appendix A).

2.5.4 Laboratory Strength Estimates

We compared laboratory direct-shear tests published by the California Geological Survey to our model results in order to evaluate the difference between hand-sized samples and more integrative estimates provided by the stability models. Notably, we expect that laboratory-based measurements do not capture fractures and other discontinuities that may penalize strength values at the hillslope scale; thus, we generally should expect the stability-based models to yield lower strength estimates compared to direct-shear tests. Samples were collected from boreholes and excavations, and direct-shear tests were conducted on unconsolidated, saturated samples under drained conditions. Reported cohesion and friction angles reflect peak strength required to induce failure of the sample. Data were filtered to remove samples collected from soils or landslide deposits. Direct-shear tests of three samples from the Monterey fm. yield a mean cohesion of 51 ± 32 kPa and mean friction angle of 33 ± 3 degrees (Figure 2.7, Table 2.1) (California Department of Conservation, 2002a, 2002b, 2018). Direct-shear tests from 14 samples in the Pico fm. yield a mean cohesion of 27 ± 15 kPa and friction angle of 34 ± 7 degrees, and direct-shear tests from 79 Saugus fm. samples yield mean cohesion of 30 ± 26 kPa and friction angle of 34 ± 7 degrees (Figure 2.7, Table 2.1). It should be noted that the samples for direct-shear tests were collected from the associated stratigraphic units in the vicinity of our 24 study regions for model strength estimates, but not necessarily from within them (Figure A.2).

In comparison between model-driven and direct shear tests, there is consistency across both methods and stratigraphic units around a friction value of ~32 ± 5 degrees. Variability in cohesion is greater, although still within a fairly narrow range of values (several tens of kPa, Figure 2.7). Direct shear tests are on average higher for all three formations compared to the Culmann and Newmark values. Despite the large range in direct-shear test results, the cohesive strength of the weakest rocks from each unit systematically decreases from ~28 kPa in the Monterey fm., to ~10 kPa in the Pico fm., to 0 kPa in the Saugus fm. (Figure 2.7a). These values are similar to mean results produced from the slope stability model approaches.

2.5.5 Burial Depth

The three stratigraphic units in the eastern Topatopa Mountains exhibit a gradient in maximum burial depth from east to west. The Saugus fm. is the stratigraphically highest unit in much of the Western Transverse Ranges, and with the exception of minor latest-Pleistocene to Holocene alluvial fills, has not been buried by overlying section (DeVecchio et al., 2012). Subsurface data suggest that the maximum thickness of the Saugus fm is ~2,040 m in the easternmost Topatopa Mountains (Dibblee, 1996), the maximum thickness of the Pico fm. is ~2,000 m (Dibblee, 1993, 1996), and the maximum thickness of the Monterey fm. is ~2,500m (Gordon, 2014; Yeats et al., 1994). Using these thicknesses and structural data in published geologic maps (Dibblee, 1991, 1993, 1996; Dibblee & Ehrenspeck, 1996, 1997), we estimated the minimum and maximum burial depth of rocks exposed within each measurement region (Table A.4), assuming that the thickness of each unit was originally constant. We recognize that there is significant variability in the thickness of the Saugus fm. where preserved elsewhere (e.g. DeVecchio et al., 2012), but an assumption of constant thickness over our study area is appropriate in the absence of local data. As expected, burial depth generally increases from east to west (Table A.4). Cohesive strength results from both the Newmark and Culmann models increase with increasing burial depth, both within and between formations (Figure 2.8).

2.6 Discussion

2.6.1 Difference in model strength results

Strength results from the Newmark and Culmann approaches are generally in good agreement, with 60% of the basins producing results within 10 kPa for comparative apparent cohesion values (recall that the Newmark method does not produce independent cohesion/friction results) (Figure 2.7b). When comparing Newmark fits against the height-slope data used to fit the Culmann model, the Newmark values still fall within the scatter of height-gradient values despite being independent of these data (Figures A.5-A.28). However, these fits variably hug the outliers of the height-slope data or lie within a scatter of low-density data (Figure 2.5). Here we notice two particular trends. First, at cohesion below 25 kPa, the Newmark model predicts higher estimates than the Culmann model (following the most extreme height-slope values), while at cohesion > ~ 25 kPa, the Newmark model produces estimates that are lower than the Culmann model and lie within the low-density region of height-gradient data (Figure 2.7b). The low cohesion basins have substantially lower mean slope median values

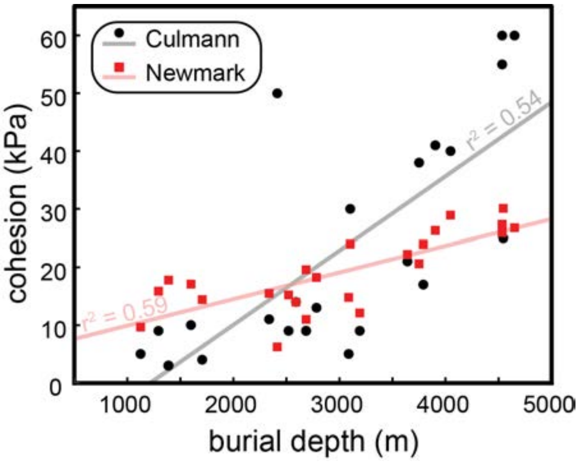

Figure 2.8: Culmann and Newmark cohesion results against average burial depth of sedimentary rocks within each measurement region. Solid lines show best-fit regressions.

compared to the higher cohesion values, reflecting the influence of strength on hillslope morphology (Korup, 2008). Also, these lower modal values for average hillslope gradient are associated with a less-defined peak in height-gradient values (Figure 2.5a vs. Figure 2.5c) (Figures A.5-A.28). Certainly, values within 10 kPa may be considered well within error of our curve-fitting approach for the Culmann method, given the relatively high scatter in the hillslope distributions for some basins. The fact that the Newmark method produces such similar results supports the hypothesis that near-surface rock strength may be faithfully recorded in the topographic structure, but we acknowledge that a statistical measure to quantify uncertainty would further support this interpretation.

The alternative explanation for some of the higher scatter (~ 10-30 kPa difference) is that the differences in strength instead reflect a difference in model assumptions or hillslope processes. Basins with the highest disagreement overly the Monterey fm., which commonly consists of alternating beds of massive sandstone and shale. We observe that sandstone beds are often undercut and protrude out of steep anti-dip slopes relative to shale beds, and shallow coseismic landslides and rockfalls during the 1994 Mw 6.7 Northridge Earthquake were common on these hillslopes. However, these hillslopes are also generally taller and steeper than hillslopes underlain by the Pico and Saugus fms. These observations imply that the general morphology of these hillslopes is supported by the stronger sandstone beds, resulting in relatively high apparent cohesion estimates from the Culmann model, but the instability of the overhanging blocks results in lower apparent cohesion values from the Newmark model. Alternatively, we also recognize that a 1D stability model will be more conservative than its 2D counterpart due to a lack of consideration of resisting forces in the second dimension.

The Culmann and Newmark model strength results from each stratigraphic unit are lower than mean direct-shear test results (Table 2.1). We interpret the lower strength at the hillslope scale as being driven by discontinuity sets within the rock mass that are not captured at the small scale of the laboratory tests (e.g. Hoek and Brown, 1997). However, we also observe that hillslope-scale strength results are similar to the weakest direct-shear test results within each stratigraphic unit (Figure 2.7a). An alternative explanation is that hillslope-scale strength is instead limited by the strength of the weakest member of a formation within a hillslope (e.g. Schmidt and Montgomery, 1995). A potential mechanism that may be responsible for this pattern is that landslide failure planes localize on the weakest rocks in a hillslope, and strength calculated using hillslope stability models would, therefore, reflect the strength of these units. In this framework, intact rock strength from individual laboratory-sized samples can greatly exceed hillslope-scale strength estimates (e.g. the Saugus fm., Figure 2.7a), but hillslope-scale strength can generally not exceed the strength of the weakest rocks within a formation.

2.6.2 Rock Strength Controlled by Burial Depth

Collectively, model and direct-shear tests show increasing cohesion across an east to west gradient with increasing formation age and stratigraphic depth, suggesting the inter-unit differences in strength may be attributed to maximum burial depth of these units prior to exhumation. Support for the control of burial depth on strength also arises from Culmann estimates of apparent cohesion within the Monterey fm. Variability within this unit can be explained by exposed stratigraphic position within the Temescal anticline and Santa Felica syncline – two multi-kilometer scale folds developed parallel to the main thrust front (Dibblee, 1991; Figure 2.9). Although the pattern is more subdued in the Newmark apparent cohesion estimates, these also mimic the broad-scale folding and variation in stratigraphic interval (Figure 2.9). Cohesive strength is highest where the deepest members of the Monterey fm. are exposed in anticlines, and strength is lowest where the highest members are exposed. Low-temperature apatite (U-Th/He) thermochronology data from the Monterey fm. show complete thermal resetting of apatite from the core of the Temescal Anticline, cooling ages older than the formation age of the Monterey fm. near the Santa Felicia Syncline, and partial resetting from intermediate samples (Figure 2.9, Table A.1 and A.2), suggesting that the deepest members of

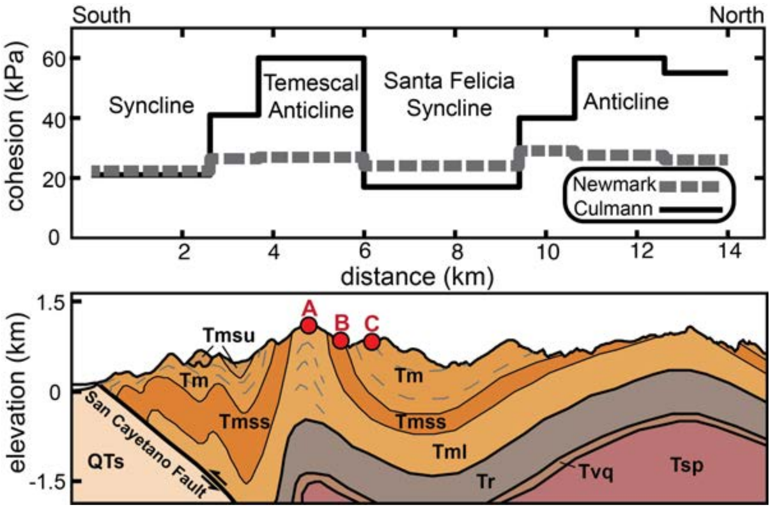

Figure 2.9: Transect across the Miocene Monterey Formation. Transect location shown in Figure 2.1a and 2.6c. Plot shows Culmann and Newmark model cohesion estimates against distance from the range front (south to north). Lower panel shows a geologic cross section through the Monterey and underlying fms. Modified from Dibblee (1991) and Dibble and Ehrenspeck (1996). Strength estimates are highest over structural anticlines, where rock exposed at the surface has been exhumed from greater depth. 'A' shows location of apatite (U-Th)/He sample 16-PC-4, which was collected from the core of the Temescal Anticline and had been buried deep enough to be thermally reset. 'B' and 'C' show location of unreset or partially reset ages indicating shallow burial. Geologic unit abbreviations: QTs (Saugus Formation), Tmsu (Monterey Formation, upper sandstone member), Tm (Monterey Formation, lower sandstone members), Tmss (Monterey Formation, sandstone), Tml (Monterey Formation, lower shale unit), Tr (Rincon Shale), Tvq (Vaqueros Sandstone), Tsp (Sespe Formation).

the unit reached a maximum burial depth of at least three kilometers before being exhumed (assuming a geothermal gradient of ~15 °C/km for sedimentary basins). These results suggest that maximum burial depth and associated vertical exhumation likely exert a first-order control on the strength of these geologically young stratigraphic units. The lower estimates of strength from the Pico and Saugus fms. are also consistent with this interpretation; although no thermochronology data from these formations have been produced, these units are stratigraphically higher than the old, non-reset apatite grains from the upper members of the Monterey fm., suggesting less than three kilometers of burial and exhumation.

The gradient in rock strength with stratigraphic age is likely a consequence of differing degrees of lithification and diagenesis associated with burial depth. Young, recently deposited sediments are loosely packed, have high porosity, and are generally uncemented. Continued sediment deposition in a subsiding basin progressively buries older sediments, which experience a concurrent increase in pressure and temperature. Elevated pressures caused by loading drive a significant increase in grain packing and reduction in pore space due to both physical and chemical compaction, which can continue to depths of at least 5 km (Worden & Burley, 2003). Chemical compaction results in the partial dissolution of minerals, which enrich pore water with dissolved silica. Precipitation of this silica and other minerals within the pore space results in cementation, which further reduces pore space and brings about lithification of the sediments (Boggs Jr., 2011). The degree of compaction and cementation associated with varying burial depth exert a strong control on the cohesive strength of sedimentary rocks (Collins & Sitar, 2008). In the Topatopa Mountains, the friable, poorly-consolidated condition of the Pico and Saugus fms. is likely a result of minimal compaction due to these units' shallow burial depth. The Monterey fm., by contrast, experienced higher temperatures and pressures due to burial beneath the Pico and Saugus fms. Therefore, the higher degree of diagenesis associated with deeper burial is likely responsible for the higher cohesive strength of the Monterey fm. While these findings are perhaps unsurprising, they remain some of the first to provide quantitative constraints on the potential effects of lithification and diagenesis on landscape-scale strength.

2.6.3 Other Controls on Hillslope-Scale Rock Strength

Off-fault deformation associated with slip along active faults has been proposed to weaken the surrounding rock mass and potentially influence the distribution of landsliding (Korup, 2004; Scheingross et al., 2013). Along the San Andreas Fault in central California, landslides not otherwise triggered by earthquakes have been observed to cluster within a couple of kilometers of the fault due to a reduction in rock strength associated with fault-proximal deformation of the surrounding rock mass (Scheingross et al., 2013). If the distribution of rock strength in the Topatopa Mountains were similarly controlled by fault-induced deformation, we should expect a north-south gradient in strength associated with proximity to the range-bounding San Cayetano Fault, which is oriented east-west (Figure 2.1c). While we cannot discount fracturing due to fault proximity as a control, we clearly see a dominant east-west gradient in strength that mirrors the exposure of sedimentary rocks, suggesting that original burial depth is a stronger control on the distribution of rock strength than deformation driven by local tectonism. Further, variability from north to south also closely mimics anticlinal structure rather than fault proximity within the Monterey Fm (Figure 2.9).

Other potential factors that influence slope failure or rock mass strength may be correlated with lithologic unit and original burial depth. Given the currently available datasets, we observe a correlation between rock strength and the original burial depth of these young sedimentary rocks, but other variables including porosity, mineralogy, and composition of interstitial cements, weathering controls, hydraulic conductivity, tectonic deformation rate, timing of rock exhumation initiation, and erosion rate may also vary in a systematic way that mirrors the distribution of rock strength. These datasets are currently unavailable in the eastern Topatopa Mountains, so we offer burial depth as a likely dominant control in this unique field setting but acknowledge that these other variables may contribute to the variability in rock mass strength.

2.7 Conclusions

Here we provide a methodology to quantify rock strength, which is an important control on topographic relief and supports conceptual models for landscape evolution posed by some of the earliest geomorphologists (Davis, 1899; Gilbert, 1877). We estimate hillslope-scale rock strength in the Eastern Topatopa Mountains using the Culmann finite-slope and Newmark infinite-slope stability models. With the Culmann model, we calculate the apparent cohesion and friction angle of hillslope materials by measuring the gradient and height of hillslope segments from a high-resolution (3m) DEM. By extracting these measurements over a defined measurement region, we estimate strength assuming that the limit in height vs. gradient space represents the critical, strength-limited components of the landscape. We invert the Newmark model for strength using local topographic slope, PGA model for the 1994 M_w 6.7 Northridge Earthquake, and the inventory of Northridge coseismic landslide polygons re-mapped to reduce amalgamation. To directly compare the resulting strength estimates, we fix the friction angle estimates for the Newmark inversion with the Culmann model estimates. Cohesive and frictional strength results from the Saugus fm. using the Culmann approach are 6 ± 3 kPa and 34 ± 3°, respectively, where the Newmark predicts a cohesion of 15 ± 3 kPa using the friction angle results from the Culmann. The Culmann model predicts a mean cohesion of 17 ± 13 kPa and friction angle of 35 ± 5° from the Pico fm., where the Newmark approach predicts a mean cohesion of 16 ± 5 kPa. Mean results for the Monterey fm. from the Culmann approach are 40 ± 16 kPa for cohesion and 31 ± 3° for the friction angle, where the Newmark predicts cohesion of 26 ± 3 kPa. The patterns in cohesive strength across the eastern Topatopa Mountains are similar, with strength increasing from east to west with increasing stratigraphic age and depth in Plio-Pleistocene to Miocene clastic sedimentary rocks. Within the Monterey fm., the stratigraphically lowest unit, near-surface strength is highest over the cores of anticlines and lowest over synclines, suggesting that maximum burial depth is a major control on strength in these geologically young, poorly-lithified sedimentary rocks.

2.8 References

Atwater, T. M. (1998). Plate tectonic history of southern California with emphasis on the Western Transverse Ranges and northern Channel Islands. In P. W. Weigand (Ed.), Contributions to the geology of the Northern Channel Islands, Southern California (pp. 1–8). American Association of Petroleum Geologists, Pacific Section.

Boggs Jr., S. (2011). Principles of Sedimentology and Stratigraphy. Pearson.

Bramlette, M. N. (1946). The Monterey Formation of California and the origin of its siliceous rocks (Report 212). US Government Printing Office.

Bursztyn, N., Pederson, J. L., Tressler, C., Mackley, R. D., & Mitchell, K. J. (2015). Rock strength along a fluvial transect of the Colorado Plateau - quantifying a fundamental control on geomorphology. Earth and Planetary Science Letters, 429, 90–100. https://doi.org/10.1016/j.epsl.2015.07.042

California Department of Conservation. (2002a). Seismic hazard zone report for the Piru 7.5-minute quadrangle, Ventura County, California. California Division of Mines and Geology Seismic Hazard Zone Report 074, 54.

California Department of Conservation. (2002b). Seismic hazard zone report for the Val Verde 7.5-minute quadrangle, Los Angeles and Ventura Counties, California. California Division of Mines and Geology Seismic Hazard Zone Report 076, 52.

California Department of Conservation. (2018). California Geological Survey Borehole Database. https://www.conservation.ca.gov/cgs/maps-data/borehole-database.

Collins, B. D., & Sitar, N. (2008). Processes of coastal bluff erosion in weakly lithified sands, Pacifica, California, USA. Geomorphology, 97(3–4), 483–501. https://doi.org/10.1016/j.geomorph.2007.09.004

Culmann, C. (1875). Die Graphische Statik. Zurich: Meyer and Zeller.

Davis, W. M. (1899). The Geographical Cycle. The Geographical Journal, 14(5), 481–504.

DeVecchio, D. E., Heermance, R. V., Fuchs, M., & Owen, L. a. (2012). Climate-controlled landscape evolution in the Western Transverse Ranges, California: Insights from Quaternary geochronology of the Saugus Formation and strath terrace flights. Lithosphere, 4, 110–130. https://doi.org/10.1130/L176.1

Dibblee, T. W. (1991). Geologic Map of the Piru Quadrangle, Ventura County, California (Map no. DF-34, scale 1:24,000). Santa Barbara, California: Dibblee Geological Foundation.

Dibblee, T. W. (1993). Geologic Map of the Val Verde Quadrangle, Los Angeles and Ventura Counties, California (Map no. DF-50, scale 1:24,000). Santa Barbara, California: Dibblee Geological Foundation.

Dibblee, T. W. (1996). Geologic Map of the Newhall Quadrangle (Map no. DF-56, scale 1:24,000). Santa Barbara, CA: Dibblee Geological Foundation.

Dibblee, T. W., & Ehrenspeck, H. E. (1996). Geologic Map of the Cobblestone Mountain Quadrangle, Ventura and Los Angeles Counties, California (Map no. DF-62, scale 1:24,000). Santa Barbara, California: Dibblee Geological Foundation.

Dibblee, T. W., & Ehrenspeck, H. E. (1997). Geologic map of the Whitaker Peak quadrangle, Los Angeles and Ventura Counties, California (Map no. DF-63, scale 1:24,000). Santa Barbara, CA: Dibblee Geological Foundation.

DiBiase, R. A., Whipple, K. X., Heimsath, A. M., & Ouimet, W. B. (2010). Landscape form and millennial erosion rates in the San Gabriel Mountains, CA. Earth and Planetary Science Letters, 289(1–2), 134–144. https://doi.org/10.1016/j.epsl.2009.10.036

DiBiase, R. A., Rossi, M. W., & Neely, A. B. (2018). Fracture density and grain size controls on the relief structure of bedrock landscapes. Geology, 46(5), 399–402. https://doi.org/10.1130/G40006.1

Dietrich, W. E., Bellugi, D. G., Heimsath, A. M., Roering, J. J., Sklar, L. S., & Stock, J. D. (2003). Geomorphic Transport Laws for Predicting Landscape Form and Dynamics. Geophysical Monograph, 135(D24), 1–30. https://doi.org/10.1029/135GM09

Dolan, J. F., & Rockwell, T. K. (2001). Paleoseismologic evidence for a very large (Mw >7), Post-A.D. 1660 surface rupture on the Eastern San Cayetano fault, Ventura county, California: Was this the elusive source of the damaging 21 December 1812 earthquake? Bulletin of the Seismological Society of America, 91(6), 1417–1432. https://doi.org/10.1785/0120000602

Dolan, J. F., Sieh, K., Rockwell, T. K., Yeats, R. S., Shaw, J. H., Suppe, J., et al. (1995). Prospects for Larger or More Frequent Earthquakes in the Los Angeles Metropolitan Region. Science, 267(5195), 199–205. https://doi.org/10.1126/science.267.5195.199

Dreyfus, D., Rathje, E.M., & Jibson, R.W. (2013). The influence of different simplified sliding-block models and input parameters on regional predictions of seismic landslides triggered by the Northridge earthquake. Engineering Geology, 163, 41-54. https://doi.org/10.1016/j.enggeo.2013.05.015

Earle, P.S., Wald, D.J., Jaiswal, K.S., Allen, T.I., Marano, K.D., Hotovec, A.J., Hearne, M.G., & Fee, J.M. (2009). Prompt Assessment of Global Earthquakes for Response (PAGER): a system for rapidly determining the impact of global earthquakes worldwide (U.S. Geological Survey Open-File Report 2009-1131). Reston, VA.

Ehlers, T. A. (2005). Crustal Thermal Processes and the Interpretation of Thermochronometer Data. Reviews in Mineralogy and Geochemistry, 58(1), 315–350. https://doi.org/10.2138/rmg.2005.58.12

Farley, K. A. (2002). (U-Th)/He Dating: Techniques, Calibrations, and Applications. Reviews in Mineralogy and Geochemistry, 47(1), 819–844. https://doi.org/10.2138/rmg.2002.47.18

Flowers, R. M., Ketcham, R. A., Shuster, D. L., & Farley, K. A. (2009). Apatite (U-Th)/He thermochronometry using a radiation damage accumulation and annealing model. Geochimica et Cosmochimica Acta, 73(8), 2347–2365. https://doi.org/10.1016/j.gca.2009.01.015

Forte, A. M., Yanites, B. J., & Whipple, K. X. (2016). Complexities of landscape evolution during incision through layered stratigraphy with contrasts in rock strength. Earth Surface Processes and Landforms, 41(12), 1736–1757. https://doi.org/10.1002/esp.3947

Frattini, P., & Crosta, G. B. (2013). The role of material properties and landscape morphology on landslide size distributions. Earth and Planetary Science Letters, 361, 310-319.

Gallen, S. F. (2018). Lithologic controls on landscape dynamics and aquatic species evolution in post-orogenic mountains. Earth and Planetary Science Letters, 493, 150–160. https://doi.org/10.1016/j.epsl.2018.04.029

Gallen, S. F., Clark, M. K., & Godt, J. W. (2015). Coseismic landslides reveal near-surface rock strength in a high relief, tectonically active setting. Geology, 43(1), 11–14. https://doi.org/10.1130/G36080.1

Gallen, S. F., Clark, M. K., Godt, J. W., Roback, K., & Niemi, N. A. (2017). Application and evaluation of a rapid response earthquake-triggered landslide model to the 25 April 2015 Mw 7.8 Gorkha earthquake, Nepal. Tectonophysics, 714, 173–187. https://doi.org/10.1016/j.tecto.2016.10.031

Gilbert, G. K. (1877). Report on the geology of the Henry Mountains: Geographical and geological survey of the Rocky Mountain region. U.S. Government Printing Office.

Godt, J. W., Baum, R. L., Savage, W. Z., Salciarini, D., Schulz, W. H., & Harp, E. L. (2008). Transient deterministic shallow landslide modeling: requirements for susceptibility and hazard assessments in a GIS framework. Engineering Geology, 102(3-4), 214-226. https://doi.org/10.1016/j. enggeo.2008.03.019

Gordon, G. (2014). Stratigraphic evolution and architectural analysis of structurally confined submarine fans: A tripartite outcrop-based study (Doctoral dissertation). Retrieved from Mountain Scholar (https://mountainscholar.org/handle/11124/278). Golden, CO: Colorado School of Mines.

Grieve, S. W. D., Mudd, S. M., & Hurst, M. D. (2016). How long is a hillslope? Earth Surface Processes and Landforms, 41(8), 1039–1054. https://doi.org/10.1002/esp.3884

Hack, J. T. (1975). Dynamic equilibrium and landscape evolution. In W. N. Melhorn and R. C. Flemal (Eds.), Theories of Landscape Evolution. Boston, MA.

Harp, E. L., & Jibson, R. W. (1995). Inventory of landslides triggered by the 1994 Northridge, California earthquake (U.S. Geological Survey Open-File Report 95-213). Reston, VA.

Harp, E. L., & Jibson, R. W. (1996). Landslides Triggered by the 1994 Northridge, California, Earthquake. Bulletin of the Seismological Society of America, 86(1B), 319–332.

Hoek, E., & Brown, E. (1997). Practical estimates of rock mass strength. International Journal of Rock Mechanics and Mining Sciences, 34(8), 1165–1186. https://doi.org/10.1016/S1365-1609(97)80069-X

Hoek, E., & Brown, E. (1980). Empirical Strength Criterion for Rock Masses. Journal of the Geotechnical Engineering Division, 106(ASCE 15715). https://doi.org/10.1016/0148-9062(81)90766-X

Hornafius, J. S., Luyendyk, B. P., Terres, R. R., & Kamerling, M. J. (1986). Timing and extent of Neogene tectonic rotation in the western Transverse Ranges, California (USA). Geological Society of America Bulletin, 97(12), 1476–1487. https://doi.org/10.1130/0016-7606(1986)97<1476:TAEONT>2.0.CO;2

Hovius, N., Stark, C. P., Tutton, M. A., & Abbott, L. D. (1998). Landslide-driven drainage network evolution in a pre-steady-state mountain belt: Finisterre Mountains, Papua New Guinea. Geology, 26(12), 1071–1074. https://doi.org/10.1130/0091-7613(1998)026<1071:LDDNEI>2.3.CO;2

Hudson, J. A., & Harrison, J. P. (1997). Engineering Rock Mechanics: An Introduction to the Principles. Oxford, UK: Elsevier Science. https://doi.org/https://doi.org/10.1016/B978-0-08-043864-1.X5000-9

Huftile, G. J., & Yeats, R. S. (1996). Deformation rates across the Placerita (Northridge Mw =

6.7 Aftershock Zone) and Hopper Canyon segments of the western transverse ranges deformation belt. Bulletin of the Seismological Society of America, 86, 3–18.

Jibson, R. W. (1993). Predicting earthquake-induced landslide displacements using Newmark's sliding block analysis. Transportation Research Record, 1411, 9-17.

Jibson, R. W., Harp, E. L., & Michael, J. A. (2000). A method for producing digital probabilistic seismic landslide hazard maps. Engineering Geology, 58(3–4), 271-289. https://doi.org/10.1016/S0013-7952(00)00039-9.

Jibson, R. W. (2007). Regression models for estimating coseismic landslide displacement. Engineering Geology, 91(2–4), 209–218. https://doi.org/10.1016/j.enggeo.2007.01.013

Keefer, D. K. (1994). Landslides caused by earthquakes. Bulletin of the Seismological Society of America, 95, 406-421.

Korup, O. (2004). Geomorphic implications of fault zone weakening: Slope instability along the alpine fault, South Westland to Fiordland. New Zealand Journal of Geology and Geophysics, 47, 257-267. https://doi.org/10.1080/00288306.2004.9515052

Korup, O. (2008). Rock type leaves topographic signature in landslide-dominated mountain ranges. Geophysical Research Letters, 35(11), 1-5. https://doi.org/10.1029/2008GL034157

Larsen, I. J., Montgomery, D. R., & Korup, O. (2010). Landslide erosion controlled by hillslope material. Nature Geoscience, 3(4), 247–251. https://doi.org/10.1038/ngeo776

Levi, S., & Yeats, R. S. (1993). Paleomagnetic constraints on the initiation of uplift on the Santa Susana Fault, Western Transverse Ranges, California. Tectonics 12(3), 688–702.

Ling, H. I., Mohri, Y., & Kawabata, T. (1999). Seismic analysis of sliding wedge: extended Francais – Culmann's analysis. Soil Dynamics and Earthquake Engineering, 18, 387–393.

Los Angeles Almanac. Monthly Precipitation. http://www.laalmanac.com/weather/we08aa.php. Accessed [22/09/2019].

Lu, N., & Godt, J. W. (2013). Hillslope Hydrology and Stability (1st ed.). Cambridge, U.K.: Cambridge University Press.

Marc, O., & Hovius, N. (2015). Amalgamation in landslide maps: Effects and automatic detection. Natural Hazards and Earth System Sciences, 15(4), 723–733. https://doi.org/10.5194/nhess-15-723-2015

Marc, O., Stumpf, A., Malet, J.-P., Gosset, M., Uchida, T., & Chiang, S.-H. (2018). Initial insights from a global database of rainfall-induced landslide inventories: the weak influence of slope and strong influence of total storm rainfall. Earth Surface Dynamics, 6(4), 903–922. https://doi.org/10.5194/esurf-6-903-2018

Molnar, P., Anderson, R. S., & Anderson, S. P. (2007). Tectonics, fracturing of rock, and erosion. Journal of Geophysical Research: Earth Surface, 112(3), 1–12. https://doi.org/10.1029/2005JF000433

Montgomery, D. R. (2001). Slope distributions, threshold hillslopes, and steady-state topography. American Journal of Science, 301, 432–454. https://doi.org/10.2475/ajs.301.4-5.432

Montgomery, D. R., & Brandon, M. T. (2002). Topographic controls on erosion rates in tectonically active mountain ranges. Earth and Planetary Science Letters, 201(3–4), 481–489. https://doi.org/10.1016/S0012-821X(02)00725-2

Montgomery, D. R., & Foufoula-Georgiou, E. (1993). Channel Network Source Representation Using Digital Elevation Models. Water Resources Research, 29(12), 3925–3934. https://doi.org/10.1029/93WR02463

Namson, J. S., & Davis, T. L. (1988). Structural transect of the western Transverse Ranges, California: Implications for lithospheric kinematics and seismic risk evaluation. Geology, 16, 675–679.

Natural Resources Conservation Service, United States Department of Agriculture. Web Soil Survey. https://websoilsurvey.sc.egov.usda.gov/. Accessed [20/09/2019]

Nicholson, C., Sorlien, C. C., Atwater, T., Crowell, J. C., & Luyendyk, B. P. (1994). Microplate capture, rotation of the western Transverse Ranges, and initiation of the San Andreas transform as a low-angle fault system. Geology, 22(6), 491–495. doi: https://doi.org/10.1130/0091-7613(1994)022<0491:MCROTW>2.3.CO;2

Office for Coastal Management, 2016: 2002/2003 IfSAR data for Southern California: Digital Elevation Model (NAVD88). NOAA National Centers for Environmental Information, https://inport.nmfs.noaa.gov/inport/item/48381.

Parise, M., & Jibson, R. (2000). A seismic landslide susceptibility rating of geologic units based on analysis of characterstics of landslides triggered by the 17 January, 1994 Northridge, California earthquake. Engineering Geology 58(3-4), 251-270. https://doi.org/10.1016/S0013-7952(00)00038-7

Prothero, D., & Vance, E. (1996). Magnetostratigraphy of the upper middle Eocene Coldwater Sandstone, central Ventura County, California. In D. Protherno & R. Emry (Eds.), The Terrestrial Eocene-Oligocene Transition in North America (pp. 155–170). Cambridge, U.K.: Cambridge University Press. https://doi.org/10.1017/CBO9780511665431.008

Reiners, P. W., & Farley, K. A. (2001). Influence of crystal size on apatite (U-Th)/He thermochronology: An example from the Bighorn Mountains, Wyoming. Earth and Planetary Science Letters, 188(3–4), 413–420. https://doi.org/10.1016/S0012-821X(01)00341-7

Reiners, P. W., & Nicolescu, S. (2006). Measurement of parent nuclides for (U-Th)/He chronometry by solution sector ICP-Ms. ARDHL Report 1, (December 2006), 1–33. Retrieved from http://www.geo.arizona.edu/~reiners/arhdl/arhdl.html

Riebe, C. S., Hahm, W. J., & Brantley, S. L. (2017). Controls on deep critical zone architecture: a historical review and four testable hypotheses. Earth Surface Processes and Landforms, 42(1), 128–156. https://doi.org/10.1002/esp.4052

Rockwell, T. (1988). Neotectonics of the San Cayetano fault, Transverse Ranges, California. Geological Society of America Bulletin, 100, 500–513.

Roering, J. J., Kirchner, J. W., & Dietrich, W. E. (1999). Evidence for nonlinear, diffusive sediment transport on hillslopes and implications for landscape morphology. Water Resources Research, 35(3), 853–870. https://doi.org/10.1029/1998WR900090

Roering, J. J., Perron, J. T., & Kirchner, J. W. (2007). Functional relationships between denudation and hillslope form and relief. Earth and Planetary Science Letters, 264(1–2), 245–258. https://doi.org/10.1016/j.epsl.2007.09.035

Roy, S. G., Koons, P. O., Upton, P., & Tucker, G. E. (2015). The influence of crustal strength fields on the patterns and rates of fluvial incision. Journal of Geophysical Research: Earth Surface, 120, 275–299. https://doi.org/10.1002/2015JF003602.

Scheingross, J. S., Minchew, B. M., Mackey, B. H., Simons, M., Lamb, M. P., & Hensley, S. (2013). Fault-zone controls on the spatial distribution of slow-moving landslides. Geological Society of America Bulletin, 125(3/4), 473-489. https://doi.org/10.1130/B30719.1

Schmidt, K. M., & Montgomery, D. R. (1995). Limits to Relief. Science, 270(5236), 617–620.

Selby, M. J. (1980). A rock mass strength classification for geomorphic purposes: With tests from Antarctica and New Zealand. Z. Geomorphol, 24, 31–51.

Selby, M. J. (1993). Hillslope materials and processes. Oxford University Press, Oxford.

Sklar, L. S., & Dietrich, W. E. (2001). Sediment and rock strength controls on river incision into bedrock. Geology, 29(12), 1087–1090. https://doi.org/10.1130/0091-7613(2001)029<1087:SARSCO>2.0.CO

Spiegel, C., Kohn, B., Belton, D., Berner, Z., & Gleadow, A. (2009). Apatite (U-Th-Sm)/He thermochronology of rapidly cooled samples: The effect of He implantation. Earth and Planetary Science Letters, 285(1–2), 105–114. https://doi.org/10.1016/j.epsl.2009.05.045

Stock, J., & Dietrich, W. E. (2003). Valley incision by debris flows: Evidence of a topographic signature. Water Resources Research, 39(4). https://doi.org/10.1029/2001WR001057

Tarboton, D., Bras, R., & Rodriguez-Iturbe, I. (1991). On the extraction of channel networks from digital elevation data. Hydrological Processes, 5(1), 81–100. https://doi.org/10.1002/hyp.3360050107

U.S. Geological Survey. (1994). Advanced National Seismic System (ANSS), ShakeMap, Global Region, Maps of ground shaking and intensity for event 19940117123055, Northridge, California, v1. https://earthquake.usgs.gov/earthquakes/eventpage/ci3144585/shakemap/intensity

U.S. Geological Survey (and California Geological Survey). (2006). Quaternary fault and fold database for the United States, from USGS web site: http//earthquake.usgs.gov/hazards/qfaults/.

Whipple, K. X., Kirby, E., & Brocklehurst, S. H. (1999). Geomorphic limits to climate-induced increases in topographic relief. Nature, 401, 39–43. https://doi.org/10.1038/43375

Wieczorek, G. F., Wilson, R. C., & Harp, E. L. (1985). Map showing slope stability during earthquakes in San Mateo County, California (Map no. 1257-E, scale 1:62,500). Reston, VA: U.S. Geological Survey.

Willett, S. D., & Brandon, M. T. (2002). On steady state in mountain belts. Geology, 30(2), 175–178. https://doi.org/10.1130/0091-7613(2002)030<0175

Worden, R. H., & Burley, S. D. (2003). Sandstone Diagenesis: The Evolution of Sand to Stone. In Sandstone Diagenesis: Recent and Ancient (pp. 3–44). Malden, MA: Blackwell Publishing. https://doi.org/10.1002/9781444304459.ch

Wright, T. L. (1991). Structural Geology and Tectonic Evolution of the Los Angeles Basin, California. In K. T. Biddle (Ed.), Active Margins Basins (pp. 35–135). American Association of Petroleum Geologists Memoir 52. https://doi.org/10.1306/9488784D-1704-11D7-8645000102C1865D

Yeats, R. S., Mcdougal, J. W., & Stitt, L. T. (1986). Cenozoic structure of the Val Verde 7 1/2-minute quadrangle and south half of the Whitaker Peak 7 1/2-minute quadrangle California (United States Geological Survey Open File Report 85-587, 24). Reston, VA.

Yeats, R. S., Huftile, G. J., & Stitt, L. T. (1994). Late Cenozoic tectonics of the east Ventura Basin, Transverse Ranges, California. American Association of Petroleum Geologists Bulletin, 78. https://doi.org/10.1306/A25FE42D-171B-11D7-8645000102C1865D

Data Availability Statement

Our remapped landslide inventory is available at the USGS Open Repository of Earthquake-Triggered Ground-Failure Inventories (https://doi.org/10.5066/F7H70DB4). Thermochronometry sample data and the California Geological Survey direct-shear test data used in this study are available at the Deep Blue data repository (https://doi.org/ 10.7302/9bj1-q884). The digital elevation model used in this study is available from the U.S. National Oceanic and Atmospheric Administration at coast.noaa.gov/dataviewer, the original inventory of coseismic landslides produced during the 1994 Mw 6.7 Northridge Earthquake is available from the U.S. Geological Survey at catalog.data.gov, and the Shakemap of peak ground accelerations during the Northridge Earthquake is available from the U.S. Geological Survey (https://earthquake.usgs.gov/). A summary of laboratory and analytical protocols for apatite (U–Th)/Hethermochronometry, landslide mapping methods, Culmann model methods, tables with thermochronometry sample information, and supplemental figures is included in Appendix A.

Acknowledgments

This work was supported by a National Science Foundation division of Earth Science, Geomorphology and Land Use Dynamics award (EAR-1528576) to M. K. Clark, a Turner Postdoctoral Fellowship and a Turner Graduate Research Award from the Department of Earth and Environmental Sciences at the University of Michigan to S. F. Gallen and K. F. Townsend, respectively, and a research grant from the Rackham Graduate School at the University of Michigan to K. F. Townsend. We thank Eric Hetland, A. Joshua West, Nathan Niemi, and Dimitrios Zekkos for discussions that helped strengthen the arguments and data interpretation put forward in this manuscript, Logan Knoper for assistance in remapping the landslide inventory, and Michael Silva for compiling the direct-shear test data. We further acknowledge Odin Marc and four anonymous reviewers for constructive comments that greatly improved this manuscript.

Chapter 3: Profiles of Near-Surface Rock Mass Strength Across Gradients in Burial, Erosion, and Time[2]

3.1 Abstract

Rock mass strength is recognized as an important control on landscape morphology and evolution. However, the controls on rock strength in mountainous topography remain poorly characterized, in part because strength remains challenging to quantify at spatial scales relevant to geomorphology. Here we quantify the mechanical properties of rock masses using subsurface S-wave velocities, Schmidt hammer hardness values, and Geological Strength Index (GSI) observations. We produce shallow depth profiles of rock mass shear strength using intact rock hardness as measured from a Schmidt hammer, and assessment of the structure and surface conditions of fractures using GSI. We apply these techniques to the Western Transverse Ranges, southern California, USA, where gradients in stratigraphic age and erosion rate allow us to evaluate our methodology. We resolve strength differences of 200 kPa to ~5 MPa that appear to be related to diagenetic changes associated with the maximum burial depth of young clastic sedimentary rocks. For rocks of the same lithologic type, stratigraphic age, and inferred burial histories, we resolve smaller differences in strength (300 kPa – 1.5 MPa) that appear to be positively correlated with mean erosion rates. We suggest that the increase in strength with increasing erosion rate reflects decreased residence time in the weathering zone for ranges experiencing faster fault slip rates. These findings demonstrate up to an order of magnitude variability in strength with respect to burial, erosion, and time for lithologically similar rocks. As such, lithology alone is unlikely to adequately capture the role of rock strength in landscape evolution.

3.2 Introduction

Near-surface rock strength is fundamental to topographic form and the erosive processes responsible for landscape evolution (Davis, 1899; Gilbert, 1877). Encompassing soil, weathered and intact rock, the rock mass strength profile extends from the surface to tens of meters depth and exerts a control on the evolution of mountainous landscapes by resisting erosion and

---

[2] Published as: Townsend, K.F., Clark, M.K., and Zekkos, D., 2021, Profiles of near-surface rock mass strength across gradients in burial, erosion, and time: Journal of Geophysical Research: Earth Surface, *126*, e2021JF005694. https://doi.org/10.1029/2021JF005694

contributing to the steepness of hillslopes and river channels (DiBiase et al., 2018; Montgomery & Brandon, 2002; Schmidt & Montgomery, 1995; Townsend et al., 2020a). The processes and rates by which landscapes evolve are sensitive to rock mass strength, which contributes to hillslope stability and failure mechanisms (Collins & Sitar, 2008; Gallen et al., 2015; Hoek & Brown, 1980; Selby, 1980), the architecture of the critical zone (CZ) and weathering processes (St. Clair et al., 2015; Medwedeff et al., 2019; Riebe et al., 2017), and the mechanisms of bedrock erosion in channels (Bursztyn et al., 2015; Forte et al., 2016; Gallen, 2018; Roy et al., 2015; Sklar & Dietrich, 2001). Rock strength is often quantified with laboratory tests on hand-sized samples, but we recognize that fractures and weathering dramatically reduce strength at the spatial scales relevant to geomorphic processes compared to their intact counterparts (Hoek & Brown, 1980; Schmidt & Montgomery, 1995; Townsend et al., 2020a). Laboratory approaches may overestimate near-surface rock strength at outcrop, hillslope, or regional spatial scales by an order of magnitude or more (Bunn et al., 2020; Gallen et al., 2015; Schmidt & Montgomery, 1995), yet adequately accounting for variability of rock mass strength in landscape evolution is challenged by the paucity of approaches for quantifying in-situ strength at the relevant spatial scales (Gallen et al., 2015; Schmidt & Montgomery, 1995; Townsend et al., 2020a).

Many efforts to model landscape evolution in mountainous terrain incorporate rock strength as an erodibility coefficient (e.g. 'K' in the stream power erosion model) that is typically estimated or assigned by lithologic type (Bursztyn et al., 2015; Stock & Montgomery, 1999). Although lithologic type is widely recognized to contribute to the strength of intact (i.e. unfractured) rock pieces (e.g. Sklar & Dietrich, 2001), recent studies have focused on quantifying the effect of fracture density and saprolite weathering on rock mass strength at geomorphically relevant spatial scales, which can be influenced by climatic and tectonic gradients (Gallen et al., 2015; Kirkpatrick et al., 2020; J. A. Marshall & Roering, 2014). Fracture generation and weathering are sensitive to a number of environmental factors, including climate (Gabet et al., 2010; Gallen et al., 2015; Goudie, 2016), tectonics (DiBiase et al., 2018; Kirkpatrick et al., 2020; Molnar et al., 2007; Neely et al., 2019), burial depth of sedimentary rocks (Townsend et al., 2020a), and geomorphic position on the landscape (Gabet et al., 2015; Leone et al., 2020; Medwedeff et al., 2019; Slim et al., 2015). Quantifying the relationships between these environmental variables and fracturing, weathering, and the resultant rock mass strength at appropriate spatial scales will further our ability to accurately model the evolution of active mountainous regions with respect to strength.

Active tectonic settings may present a paradox that challenges a simple view that weaker rocks erode faster than stronger rocks. On the one hand, active tectonism and bedrock uplift increase the density of fractures, thereby facilitating pathways for weathering in the subsurface and producing detachable blocks that are easily transported by surface processes (DiBiase et al., 2018; Dühnforth et al., 2010; Molnar et al., 2007; Scott & Wohl, 2018). This results in a reduction in rock mass strength and is associated with an increase in erodibility and in erosion rates (Roy et al., 2016). However, under steady-state conditions wherein the rate of climate-modulated erosion is balanced with the rate of rock uplift (Hack, 1975; Willett & Brandon, 2002), landscapes adjust to variability in rock strength through changes in slope, rather than erosion rate (Korup, 2008). In this case, active tectonism leading to increased erosion rates may lead to steeper slopes with reduced soil thickness and shorter residence times of rock masses in the CZ (Dixon et al., 2012; West et al., 2005). Reduced CZ residence leads to a decrease in the rate and extent of chemical weathering, thereby increasing the near-surface rock strength profile. These relationships are likely modulated by lithologic type, climate, and inheritance of fractures from earlier tectonic events, and variability in tectonic setting and history also likely influence bedrock fracture patterns. Untangling these competing influences on rock mass strength will require new approaches for quantifying scale-dependent strength while controlling for lithologic type, climate, and other factors that influence strength in the near-surface environment.

In this study, we present a novel approach to evaluating near surface strength profiles (up to 30 m depth) from surface and subsurface measurements. We assess strength at broad spatial scales (10s of meters) that extend ~15 to 40 m depth in the subsurface. Because soil thickness is thin (<50 cm) in our study area, our measurements largely represent the strength of fresh to weathered bedrock and saprolite. Using short geophysical arrays (< 80 m in length), we measure subsurface velocities of S-waves, which are a measure of the stiffness of rock masses (Barton, 2006). Stiffness is influenced by porosity, density, and elastic moduli, which vary with both weathering extent and degree of lithification of sedimentary rocks (Barton, 2006; Leung & Radhakrishnan, 1990; Vilder et al., 2019; Von Voigtlander et al., 2018), allowing us to use seismic velocities to explore these variables across environmental gradients. At outcrop sites, we use a Schmidt hammer to quantify hardness of intact rock blocks between fractures, and we assess the density, orientation, and surface conditions (i.e. weathering) of fractures with Geological Strength Index (GSI) observations (Hoek & Marinos, 2000). To aggregate the contributions of the intact (unfractured) strength, and the outcrop-scale fracture characteristics, we apply the Hoek & Brown criterion to quantify outcrop-scale shear strength as a function of depth (Hoek et al., 2002; Hoek & Brown, 1980, 1997). These approaches average subsurface rock strength over the relatively large spatial scales necessary to incorporate the strength-limiting behavior of fractures and discontinuities, which set the upper limit on strength at the outcrop- and hillslope-scales relevant for geomorphic processes (Gallen et al., 2015; Hoek & Brown, 1980, 1997; Townsend et al., 2020a).

3.3 Geologic Setting

3.3.1 Sampling Strategy

The unique geologic setting of the Western Transverse Ranges (WTR) of southern California, USA, enables us to isolate many variables that are recognized to affect rock mass strength, including tectonic history, erosion rate, lithologic type, and climate. The WTR contain multiple reverse-fault bounded mountain ranges where rock uplift rates are uniform within individual ranges, but vary from range to range (Niemi & Clark, 2018; Townsend et al., 2018) (Figure 3.1). Ranges are predominately composed of late-Cretaceous through Plio-Pleistocene age clastic sedimentary rocks that were deposited during multiple stages of regional extension and basin formation (Namson & Davis, 1988) (Figure 3.1 and Figure 3.2). Original burial depths in these Cenozoic basins range from < 1 km to up to 10 km, and corelative stratigraphic units are exposed in the individual ranges today. Because faults of the WTR are moving at different rates (S. T. Marshall et al., 2013), we interpret variable mean erosion rates across three studied ranges that are quantified by geochemical methods (Niemi & Clark, 2018; Portenga et al., 2017; Townsend et al., 2018). Lithologic types are similar throughout, and precipitation today is uniform across the region. Therefore, the WTR field area offers the ability to investigate the effect of burial and erosion histories on the mechanical properties and strength of rock masses while isolating for lithologic type and climate.

The ease at which our novel approach can be deployed in the field allows for broad spatial sampling across the study area. We quantify rock mass mechanical properties across regional gradients in subsidence and exhumation histories, as well as mean erosion rates measured over two different timescales. To explore the affect of variable basin history on rock

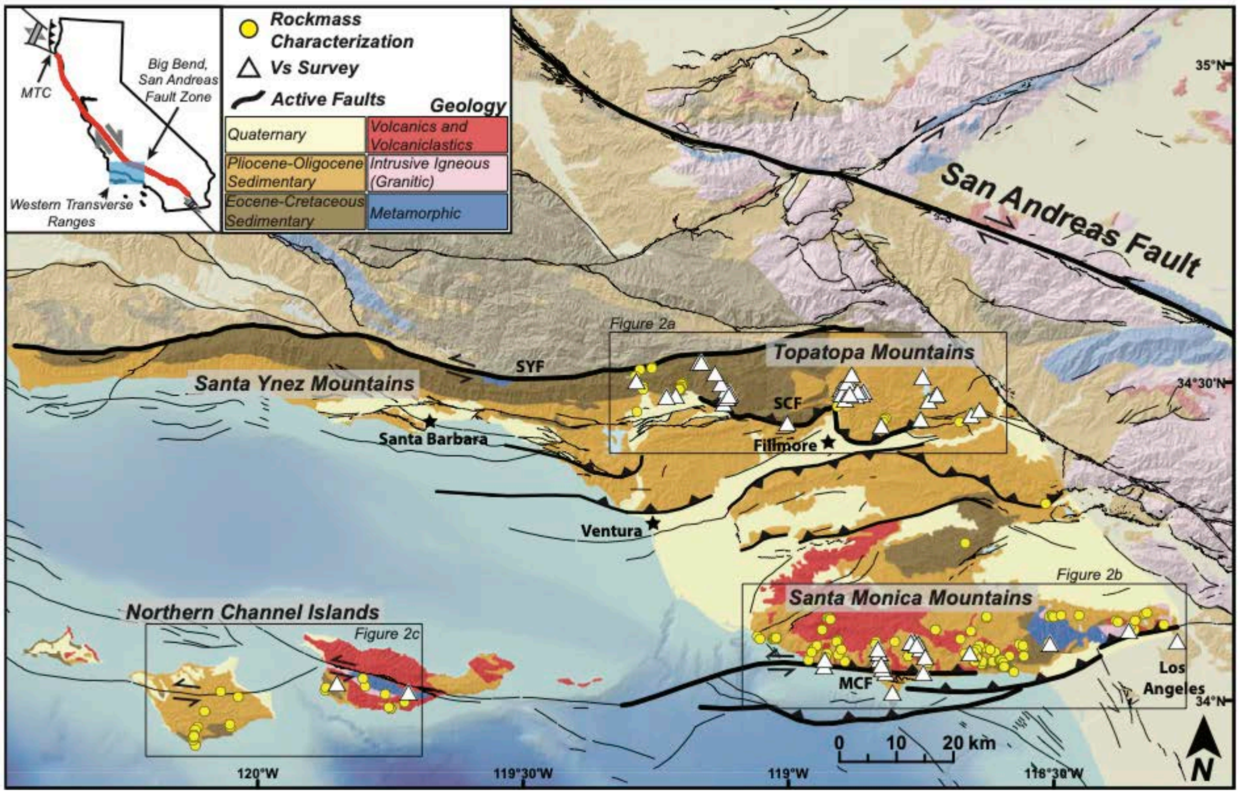

Figure 3.1: Simplified geology and structure of the Western Transverse Ranges (WTR). Sites from which Schmidt hammer rebound values and GSI observations were collected (Rockmass Characterization) are shown as yellow circles (n = 226), and locations surveyed for S-wave velocities are shown as white rectangles (n = 60). Black rectangles show extent of Figures 3.2a, 3.2b, and 3.2c. Inset map shows location of the WTR in southern California, USA. Shortening across the WTR is driven by convergence associated with the Big Bend in the SAFZ. MTC–Mendocino Triple Junction, SYF–Santa Ynez Fault, SCF–San Cayetano Fault, MCF–Malibu Coast Fault.

mass strength, we focus on the Topatopa Mountains on the northern boundary of the WTR (Figure 3.1). We then explore the affect of mean erosion rates by focusing on correlative stratigraphic units in the Topatopa Mountains, Santa Monica Mountains, and northern Channel Islands (Figure 3.1).

3.3.2 Burial and Exhumation Gradient in the Topatopa Mountains

Exposures of Late-Mesozoic to Cenozoic sedimentary rocks in the Topatopa Mountains allow us to investigate the affect of differential burial depths under constant rock uplift rates. The Topatopa Mountains expose more than 10 km of stratigraphic section of Plio-Pliestocene through Cretaceous age sedimentary rocks in a broad homocline that dips to the east with strike perpendicular to the range front (Dibblee, 1982) (Figures 3.2, B.1-B.4). Here, mapped geologic units are of a similar lithologic type (primarily clastic sedimentary rocks and predominately sandstones) but vary in maximum burial depth as a function of geologic age (i.e. stratigraphic interval). These rocks are being exhumed due to active reverse faulting along the San Cayetano

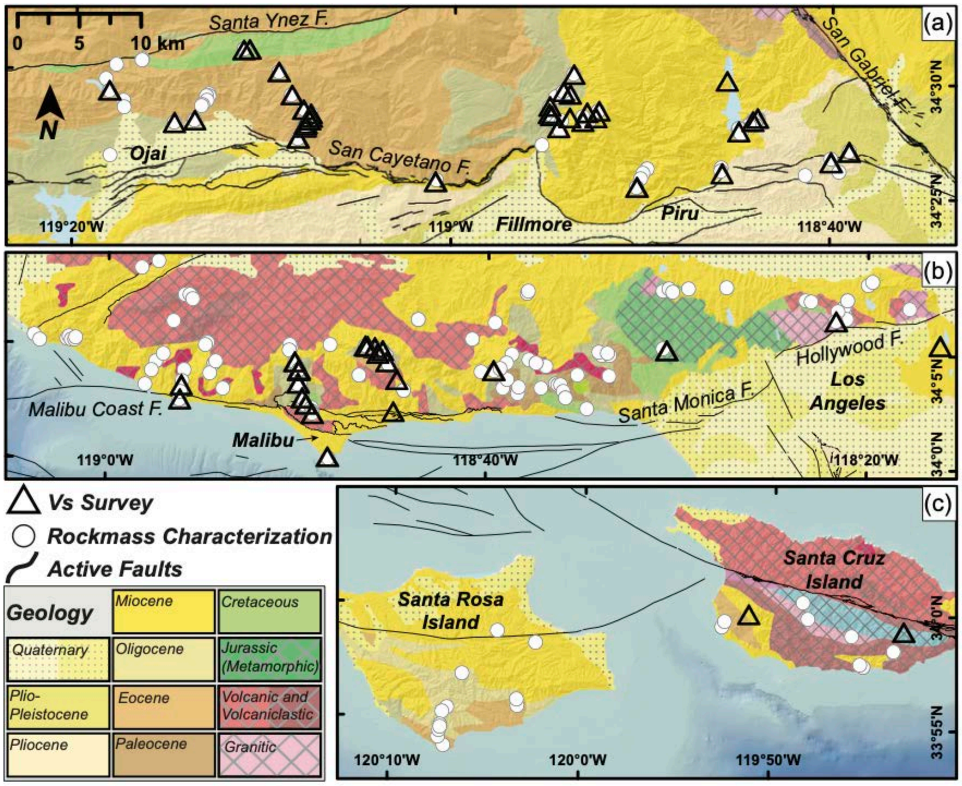

Figure 3.2: S-wave survey locations, rockmass characterization locations, and geologic units by age in the a) Topatopa Mountains, b) Santa Monica Mountains, and c) Santa Cruz and Santa Rosa Islands. Geologic map units with solid colors are sedimentary (predominately sandstones), cross-hatching indicates metamorphic or volcanic (intrusive and extrusive) lithologic types, and dots indicate Quaternary units. F–Fault.

Fault (Figure 3.1 and Figure 3.2), which initiated in the west during late-Miocene time and propagated eastward through Pliocene time, causing an increase in rock exhumation (i.e. structural relief) from west to east across the range while maintaining uniform uplift rates along strike of the fault (Rockwell, 1988; Townsend et al., 2018).

The Plio-Pleistocene Saugus Formation, exposed on the eastern end of the range (Figure 3.2), is the stratigraphically highest unit and has not been buried by additional sediments, providing a constraint on the maximum burial depth of underlying units in this continuous stratigraphic section (DeVecchio et al., 2012). Using this constraint, the Oligocene Sespe Formation was buried by up to 5-7 km of overlying sedimentary rocks prior to being exhumed, with stratigraphically higher units experiencing less burial prior to exhumation (Dibblee, 1991, 1993; Townsend et al., 2020a). The Cretaceous sediments at the bottom of the section were buried by as much as 7-10 km of overlying sediments during final basin formation prior to inversion by activity on the San Cayetano Fault. Because the range has a simple tectonic history of basin inversion, we can neglect the influence of deformation inherited from earlier tectonism.

3.3.3 Regional Differences in Erosion Rate

The Topatopa Mountains, Santa Monica Mountains, and northern Channel Islands share two mapped stratigraphic units, the Miocene Monterey Formation and the Oligocene Sespe Formation. The Oligocene Sespe Formation exhibits less regional variability in lithology compared to the Monterey Formation. Deposited in a broad coastal plain, the Sespe Formation is predominately a deltaic and fluvial unit composed of medium- to coarse-grained sandstones with occasional conglomerate and shale interbeds, and is often identified by distinctive red beds (Howard, 1988). The unit outcrops in the central Topatopa Mountains north of Fillmore, CA, the central Santa Monica Mountains north and east of Malibu, CA, and southern Santa Rosa Island (Figure 3.2). By targeting the Sespe Formation in each location, we can isolate and assess the contribution of erosion rate to rock strength while controlling for stratigraphic age, original burial depth, and lithologic type. Despite these efforts, we acknowledge that additional uncharacterized variables may systematically vary within the Sespe Formation across our study area, including but not limited to mineraology, composition of cements, degree of diagenesis, porosity, and hydrologic conductivity.While the Miocene Monterey Formation is ubiquitous across central and southern California, significant lateral facies variation within our study area precludes use of this unit for comparisons of erosion rates. The unit varies from medium-grained sandstones (locally known as the Modelo Formation) in the Topatopa Mountains to a fine-grained diatomaceous shale in the Santa Monica Mountains and northern Channel Islands (Dibblee, 1982; Gordon, 2014).

Erosion rates in the Topatopa Mountains, Santa Monica Mountains, and northern Channel Islands are quantified over two timescales from low-temperature thermochronology (Niemi & Clark, 2018; Townsend et al., 2018) and ^{10}Be cosmogenic radionuclides (Hughes, 2019; Portenga et al., 2017). Low-temperature (U-Th-Sm)/He thermochronometers are sensitive to tectonic and geomorphic processes affecting the upper crust, and the resultant time-temperature data provide constraints on the timing and rates of burial and subsequent erosion of inverted sedimentary basins over Myr to tens of Myr timescales (e.g. Ehlers, 2005). Apatite (U-Th-Sm)/He ages represent the time since a sample cooled below ~40-80°C, which occurs at depths of 2-4 km, assuming typical geothermal gradients (Farley, 2002; Flowers et al., 2009). Ages from the higher-temperature zircon (U-Th)/He thermochronometer represent the time since a sample cooled below ~180-200°C at depths of 5-8 km (Farley, 2002; Reiners et al., 2002).

Ages from paired thermochronometers, and/or multiple samples of one thermochronometer with vertical (stratigraphic or elevation) separation, can be inverted for million-year averages in erosion rate over several million years (Farley, 2002).

Apatite (U-Th-Sm)/He thermochronometry ages throughout the WTR generally range from late-Miocene to Pleistocene, implying recent and rapid rock exhumation (Niemi & Clark, 2018; Townsend et al., 2018). We observe variability in apatite (U-Th)/He ages, which are youngest in the Topatopa Mountains (1.3 to 4.5 Ma), older in the Santa Monica Mountains (2 to 7 Ma), and oldest from Santa Rosa Island (6 to 8 Ma) (Niemi & Clark, 2018; Townsend et al., 2018). Inverse thermal modelling of these data reveal gradients in cooling rates, and by assuming a geothermal gradient of 30 °C/km, exhumation rates of 1.2 to 1.6 mm/yr since 3 Ma are inferred for the central Topatopa Mountains, 0.7 to 1.0 mm/yr since 5 Ma are inferred in the central Santa Monica Mountains, and a slower rate of 0.3 mm/yr since ~10 Ma is inferred for Santa Rosa Island (Niemi & Clark, 2018; Townsend et al., 2018).

Basin-wide erosion rates that integrate over shorter time intervals of 10^2-10^3 years are calculated using ^{10}Be cosmogenic radionuclide concentrations in quartz. In-situ cosmogenic radionuclides are produced in minerals near the earth's surface by secondary cosmic radiation bombarding atomic nuclei (Granger et al., 1996). The cosmic ray flux decreases exponentially with depth below the surface, so the surface concentration of cosmogenic radionuclides is indirectly proportional to the erosion rate (von Blanckenburg, 2005). By measuring concentrations of cosmogenic radionuclides in stream sediments, a spatially-averaged erosion rate for the entire upstream catchment can be produced (von Blanckenburg, 2005; Granger et al., 1996). Two samples from the central Topatopa Mountains yield erosion rates of 1.92 mm/yr and 2.21 mm/yr, respectively (Hughes, 2019), whereas samples from five catchments in the central Santa Monica Mountains yield erosion rates ranging from 0.23 mm/yr to 0.36 mm/yr (Portenga et al., 2017). Published data for ^{10}Be cosmogenic radionuclide concentrations from the northern Channel Islands is not available.

Over both thermochronometric (10^5-10^6 years) and cosmogenic (10^2-10^3 years) integration time scales, erosion rates are higher in the Topatopa Mountains than in the Santa Monica Mountains. The differences in erosion rates are interpreted to reflect differences in the rate of fault slip on the San Cayetano Fault and the Malibu Coast Fault, respectively (Niemi & Clark, 2018; Portenga et al., 2017; Townsend et al., 2018). GPS velocities confirm the relative difference in fault slip rate between the two ranges, albeit at higher overall rates during this shorter timescale of 10^0-10^1 years (S. T. Marshall et al., 2013, 2017). Dip-slip motion on the San Cayetano Fault and the Malibu Coast Fault are estimated at 5.4 ± 1.7 mm/yr and 1.1 ± 0.8 mm/yr, respectively, which also imply relatively faster tectonically-driven erosion rates in the Topatopa Mountains than in the Santa Monica Mountains.

3.3.4 Climate

The climate is characterized as Mediterranean, with generally warm, dry summers, and cool, wet winters. Mean annual precipitation across the study area is similar, with weather stations at the base of the Topatopa Mountains reporting 45 to 54 cm/yr, and stations at the base of the Santa Monica Mountains reporting 40 to 62 cm/yr (WRCC, 2020), although rainfall is likely greater at higher elevations due to orographic effects. Mean annual precipitation reported from the one station on Santa Rosa Island is 29 cm/yr (WRCC, 2020).

3.4 Methods

3.4.1 Seismic Surveys

Shallow seismic surveys with short arrays and active sources are inexpensive, non-invasive, and portable, which make them adventageous for study of hillslope environments in mountainous topography (Befus et al., 2011; St. Clair et al., 2015; Flinchum et al., 2018; Von Voigtlander et al., 2018). Such surveys also aggregate material properties over larger spatial scales than other field testing methods, such as dynamic penetration tests, shear vane or point load testing, or laboratory approaches that measure uniaxial or triaxial compressive strength. S-wave velocity profiles are typically used in geotechnical engineering because shear wave velocities (Vs) are related to the low-strain shear modulus (G) such that $G = \rho Vs^2$, where ρ is the material density. Thus, subsurface propagation velocities of shear waves are a measure of stiffness of rock and soil and can be representative of the shear strength of the material. Shear wave velocities are also sensitive to the density of fractures and void spaces at multiple scales, such that a decrease in porosity and increase in density are expected with diagenetic changes associated with lithification of sedimentary rocks, resulting in an increase in stiffness and seismic velocities with increasing lithification. Conversely, an increase in porosity, decrease in density, and mineralogic changes associated with degree of weathering, contribute to a decrease of seismic velocities as weathering progresses (Barton, 2006). For example, typical S-wave speeds for fresh crystalline, unfractured bedrock are >1500 m/s, and a progressive reduction in seismic velocities to 300 m/s occurs from fresh bedrock to weathered or fractured bedrock, saprolite, and the near-surface disaggregated layer (mobile regolith, soils, and grus) (Martin & Diehl, 2004).

While it is possible to measure shear wave velocities directly, it requires three-component geophones that are expensive and time consuming to install (Park et al., 1999). Thus approaches using surface (Rayleigh) waves from multi-channel vertical-component arrays to interpret S-wave velocity profiles are commonly applied to geotechnical investigations because Rayleigh waves travel at 90% of the speed of shear waves (Anbazhagan & Sitharam, 2009; Park et al., 1999, 2000). These approaches rely on dispersion of Rayleigh waves, which occurs when the elastic properties of the near-surface changes with depth. Typically, lower frequency (or longer wavelength) waves travel at faster speeds because they sample higher velocity material at greater depths (Stokoe & Santamarina, 2000). Surface waves are also adventagous over P-wave profiles recently used in geomorphology studies (St. Clair et al., 2015; Clarke & Burbank, 2011; Holbrook et al., 2014) because of a low sensitivity to pore fluid content and the ability to interpret velocity inversions with depth.

Here we applied the multichannel analysis of surface waves (MASW) approach, in which an impulsive source and linear array of geophones are used to generate shot records, which are transformed to velocity-frequency relationships and then used in a forward modeling approach to produce Vs profiles as a function of depth (Park et al., 1998, 1999). Resolution is highest in the shallowest part of each profile, and the ability to resolve velocity decreases with depth because lower-frequency waves sample deeper material, which averages more of the subsurface (Stokoe & Santamarina, 2000). Both fundamental and higher-mode Rayleigh waves were considered in the analysis. Higher-mode Rayleigh waves can arise when low-velocity layers are interbedded with high-velocity layers (Stokoe et al., 1994), and utilizing higher modes is needed to better constrain and characterize these complex subsurface velocity structures (Xia et al., 2003).

3.4.1.1 Seismic Acquisition and Processing

Seismic data was recorded using a 16-channel Geometrics ES-3000 portable seismometer (12 profiles), and a 24-channel Geometrics Geode portable seismometer (48 profiles), using 4.5 Hz geophones spaced at 1.5 to 3 m intervals. Impulsive sources were produced by striking a 25-cm square, 5-cm thick plastic plate with a 7.2 kg sledge hammer, and shots were stacked 8-10 times to improve the signal-to-noise ratio. Shots were produced from the end of the array at an offset of 15-20% of the total array length to avoid near-field effects (Yoon & Rix, 2009). Total line lengths varied from 53 to 78 m, producing S-wave velocity profiles with typical depths of investigation of 15 to 45 m. At 10 sites, a second survey was recorded with a smaller geophone spacing of 0.7 to 1.0 m in order to increase the resolution of the S-wave velocity profile near the surface. These shorter surveys were centered over the midpoint of the longer array.

We generated S-wave velocity profiles using Geometrics SeisImager/SW software (Pickwin Version 5.2.1.3, WaveEq Version 4.0.1.0, 2016). Initial velocity structures with 30 layers were assumed for each site, and the maximum depth of each profile was set to half the longest measured wavelength. Dispersion curves were back-calculated from initial velocity profiles and compared against the measured dispersion curve. The difference between the observed and theoretical dispersion curves is described using the root mean square error (RMSE), which provides a means to assess the inverted velocity models. S-wave velocity profiles were iteratively adjusted by manually changing the velocity of each layer in order to minimize the RMSE between observed and theoretical dispersion curves. The best-fit dispersion curve matches were used to produce the final S-wave velocity profiles. It should also be noted that inversion of surface wave dispersion curves for S-wave velocity profiles is a non-unique solution, as multiple S-wave velocity profiles may produce similar theoretical dispersion curves (Foti et al., 2009). Geologic considerations, other site data, and judgment are commonly applied to derive a “best-estimate” S-wave velocity profile.

3.4.1.2 Calculation of Vs_{30}

Vs_{30} is a common parameter used in seismically active regions to characterize seismic site response and is defined as the time-averaged shear-wave velocity to 30 m depth (Borcherdt, 2012). Vs_{30} is calculated by dividing the total thickness of each profile by the total travel time, wherein travel time is the summation of the thickness divided by velocity of each layer. For the 38 (of 60) sites for which S-wave profiles do not reach 30 m, Vs_{30} was approximated following the approach of Wang & Wang (2015) using equation 1.

$$(1) \qquad \log V_s(30) = \log V_s(z_2) + \frac{\log 30 - \log z_2}{\log z_2 - \log z_1}[\log V_s(z_2) - \log V_s(z_1)]$$

Where $V_s(z_1)$ and $V_s(z_2)$ are the time-averaged shear-wave velocities to depths z_1 and z_2, respectively. Equation 1 interpolates Vs between z_1 and z_2, and then extrapolates to $z = 30$ m. With $z_1 = 10$ m and z_2 set to the maximum depth of each profile, we approximate Vs_{30}. We chose this approach because it is more likely to yield accurate Vs_{30} for individual sites than methods that rely on empirically-derived coefficients (e.g. Boore, 2004), which may be regionally dependent (Boore, 2004; Wang & Wang, 2015). Although dispersion curves are to some degree non-unique to a specific S-wave velocity profile, it has been shown that the final S-wave velocity profile and specific location of low-velocity layers has little effect on Vs_{30} of individual sites (Garofalo et al., 2016).

3.4.2 Shear Strength Depth Profiles using the Hoek and Brown Criterion

Shear strength ($\boldsymbol{\tau}$) is defined as the maximum shear stress that a material can sustain before failure, and is controlled by a number of variables, including porosity, mineralogy and the composition of interstitial cements and the structure and surface condition of fractures (Selby, 1993). Shear strength varies as a function of confining (normal) stresses, and the increase in shear strength with increasing confining stress defines the failure envelope in shear stress versus normal stress space (Hoek & Brown, 1997). We initially calculate shear strength at the surface from an outcrop, where the confining stress is zero. By then relating the confining stress to lithostatic earth pressure (Jaky, 1944; Mayne & Kulhawey, 1982), we calculate shear stress as a function of depth into the shallow subsurface, thereby enabling quantification of material strength over a depth interval that is relevant to geomorphic processes and facilitating direct comparison to measured subsurface S-wave velocities.

Rock mass strength (i.e. outcrop-scale) can be effectively estimated with ranked classification schemes that reduce the intact rock strength (i.e. the strength of the rock mass between fractures) by the structure and surface conditions (weathering) of discontinuities in the larger outcrop (Hoek & Brown, 1980, 1997; Selby, 1980). The Hoek and Brown criterion has an advantage over other rank classifications such as Selby (1980, 1993) because it was developed to quantify the strength and behavior of fractured rock masses for use in geotechnical engineering appliations using empirical calibrations. For a fractured rock mass, the ability of intact blocks to slide and rotate within a rock mass under varying stress conditions is controlled by the shape of the blocks, as well as the conditions of the surfaces separating the blocks (Hoek & Brown, 1997). A key input to the Hoek & Brown criterion is the Geological Strength Index, or GSI, of Hoek & Marinos (2000). GSI is a framework that ranks rock masses on a scale of 0 to 100 based on six classes of structure and five classes of discontinuity surface conditions, with low values reflecting highly fractured and weathered discontinuities, and high values reflecting unfractured, unweathered discontinuities. Where GSI = 100 (no or widely spaced discontinuities), the shear strength of the associated rock mass is entirely dependent on the parameters used for the intact strength of the rock blocks. GSI observations, typically over a range of ± 5, were recorded from each site in the field (Townsend et al., 2020b).

We specifically use the Hoek & Brown (2002) criterion, which empirically derives and predicts a non-linear increase in the maximum effective principal stress at failure with increasing minimum principal effective stress using equation 2.

$$(2) \qquad \boldsymbol{\sigma_1' = \sigma_3' + \sigma_{ci}\left(m_b \frac{\sigma_3'}{\sigma_{ci}} + s\right)^{a}}$$

Where σ_1’ is the maximum principal effective stress at failure, σ_3’ is the minimum principal effective stress at failure, and σ_{ci} is the uniaxial compressive strength of the intact rock blocks (Hoek et al., 2002). m_b is defined by equation 3,

$$(3) \qquad \boldsymbol{m_b = m_i \exp\left(\frac{GSI-100}{28-14D}\right)}$$

Where m_i is a material constant dependent on lithologic type, and D is the disturbance factor. m_b is effectively the material constant (m_i) reduced by GSI; where GSI = 100, $m_b = m_i$. We define m_i using values for each lithologic type in Table 2 of Hoek & Brown (1997). We set D = 0.7, the value used for excavations, as most outcrops studied are roadcuts (Hoek et al., 2002).

S and a are constants for each rock mass and are defined by equations 4 and 5 (Hoek et al., 2002).

$$(4) \qquad \boldsymbol{S = \exp\left(\frac{GSI-100}{9-3D}\right)}$$

$$(5) \qquad \boldsymbol{a = \frac{1}{2} + \frac{1}{6}\left(e^{-GSI/15} - e^{-20/3}\right)}$$

Shear strength is related to the principal stresses by equation 6

(6) $$\boldsymbol{\tau = (\sigma_1' - \sigma_3')\frac{\sqrt{d\sigma_1'/d\sigma_3'}}{d\sigma_1'/\sigma_3' + 1}}$$

Where $d\sigma_1'/\sigma_3'$ is given by equation 7

(7) $$\boldsymbol{d\sigma_1'/d\sigma_3' = 1 + am_b(m_b\sigma_3'/\sigma_{ci} + s)^{a-1}}$$

For the shear strength calculation, we assume σ_3' to be the horizontal confining stress at a given depth interval, defined by equation 8

(8) $$\boldsymbol{\sigma_3' = K_0\rho g z}$$

Where K_0 is the coefficient of lateral earth pressure at-rest, ρ is the rock mass density (set constant at $\rho = 2300$ kg/m^3), g is gravitational acceleration ($g = 9.8$ m/s^2), and z is depth below the surface. K_0 is related to the friction angle of the materials, and typically varies from ~0.5 for clayey materials with low friction angle at undrained conditions, to ~0.1 for intact rock masses with high friction angle (Jaky, 1944; Mayne & Kulhawy, 1982). Sandy soils and fractured rock masses typically yield intermediate values of ~0.25 to ~0.45 (Jaky, 1944; Mayne & Kulhawey, 1982), and here we set $K_0 = 0.35$ constant.

At each site where GSI observations were recorded, relative intact rock hardness of unfractured blocks was measured in-situ using a Schmidt hammer (Original Schmidt, type N, manufactured by Proceq; Townsend et al., 2020b). This is a spring-loaded device that measures rebound values that scale with laboratory measurements of uniaxial compressive strength (UCS) (Aydin & Basu, 2005; Selby, 1993). Due to rock heterogeneity and analytical variability of the Schmidt hammer, we calculated mean rebound-values (R) from 20 measurements taken from a horizontal position of the least fractured rock surface at each site. The rock surface was cleared of any debris prior to recording Schmidt hammer measurements, but was otherwise not altered. We removed any measurement that yielded a hollow sounding impact or fractured the rock, and all measurements of <10 were recorded as 0. We converted Schmidt hammer rebound values into uniaxial compressive strength using the regression from Deere & Miller (1966) (Equation 9).

$$\sigma_{ci} = \mathbf{UCS} = 6.9 \times 10^{[0.0087\,\gamma\,N+0.16]} \tag{9}$$

Where γ is density (set constant at γ = 2.3 g/cm^3) and N is the mean Schmidt hammer rebound value R. Although care was taken to ensure that measurements were recorded from relatively fresh, unweathered surfaces, it is important to recognize that near-surface conditions are likely weakened to varying degrees compared to subsurface conditions due to weathering within the near surface environment. As an alternative approach and a confirmation of our analysis, we also generated shear strength profiles using intact rock strength values from R Grade (Table 1 in Hoek et al., 1997) estimates recorded at 30 sites. The R Grade is a relative measure of intact rock strength based on blows to a rock mass from a geologic hammer in the field. R Grade scales from R0 to R6, and for each value, we defined UCS using the midpoint of the range reported in Table 1 of Hoek et al. (1997). For ranges of R Grade values (e.g. R1-R2), we used the UCS value on the Grade boundary. We find that mean values only differ by up to ~15% at the deepest part of the profiles, and that the patterns in shear strength profiles match to those produced using Schmidt R and Equation 9 for this same subset of data (Figure B.5). Given this consistency between Schmidt R and R Grade values, we calculate shear strength profiles for the entire field inventory with intact strength defined using Schmidt R field measurements and Equation 9.

We note that shear strength profiles presented here should be considered conservative estimates of the true strength of these materials at depth, due to the likelihood of near-surface weathering, rock mass relaxation, and the assumptions required to project strength curves into the subsurface.

3.4.3 S-wave Velocity Profiles vs. Shear Strength

We use the common depth axis of both shear wave and shear strength profiles to develop S-wave-shear strength relationships for each survey site where both outcrop observations and Vs surveys were measured. Mean S-wave velocities and shear strength were calculated from binned depth intervals of 3 m from individual S-wave and shear strength profiles. Although S-wave velocities are sensitive to rock mass characteristics, such as rock structure, porosity and type of rock, that also influence the strength of a rock mass, seismic velocities are a measure of stiffness and not a direct measurement of rock mass strength. Therefore, these relationships enable a direct quantification of strength from seismic velocities.

3.5 Results

3.5.1 Lithologic Type

S-wave velocity profiles were produced for 60 sites in the study region, and shear strength profiles were produced from Schmidt hammer R measurements and GSI observations recorded from 210 sites (Figure 3.2). Vs_{30} across the WTR ranges from 258 to 1441 m/s, mean Schmidt hammer R ranges from 0 to 60, GSI ranges from 10 to 95, and shear strength at 10 m depth ranges from < 0.1 to 10.3 MPa (Townsend et al., 2020b). Intact rock strength is known to vary by lithologic type, among other factors (Sklar & Dietrich, 2001), so we first separate our data into lithologic units (Figure 3.3 and Figure 3.4). We observe that mean Schmidt R and GSI is generally higher for clastic sedimentary rocks than igneous (mafic volcanic, volcaniclastic, and granitic) or metamorphic (slate, schist) rocks (Figure 3.3). The mean shear strength of sandstones specifically is higher than other lithologic types, as is mean Vs_{30} of both shale and sandstone sites, although S-wave velocities for other lithologic types were measured at just a single site (Figure 3.3). Looking at the S-wave velocity and shear strength profiles directly, we observe that sandstone and shale sites span a wide range, with subsurface S-wave velocities ranging from ~300 to ~1400 m/s, and shear strength ranging from near-zero to 13.6 MPa, whereas other lithologic types generally plot on the lower end of the range of sandstone and shale sites (Figure 3.4).

3.5.2 Stratigraphic Age in the Topatopa Mountains

Mean Schmidt R, GSI, shear strength at 10 m depth, and Vs_{30} by mapped geologic formation in the Topatopa Mountains are reported in Table 3.1. These data were collected from sandstones at different sites within each formation, and ± 1σ represent site-to-site variability in data. We observe that GSI, S-wave velocity profiles, and shear strength profiles increase with increasing stratigraphic age (Figure 3.5). When separated into individual stratigraphic units, mean Schmidt R values from the Plio-Pleistocene Saugus Formation at the top of the stratigraphic section are generally < 10, but reach 48 ± 11 at the base of the section in the unnamed Cretaceous unit (Table 3.1, Figure 3.6). Schmidt R is a measure of the hardness of intact rock blocks and not outcrop-scale strength, but we also observe that both GSI and Vs_{30} increase over this same interval. GSI values range from 23 in the Plio-Pleistocene section, to 83 ± 8 in the unnamed Cretaceous unit, and Vs_{30} ranges from 361 ± 18 m/s in the Pliocene Pico Formation, to 1092 ± 213 m/s in the Eocene Matilija Formation, indicating that rock mass

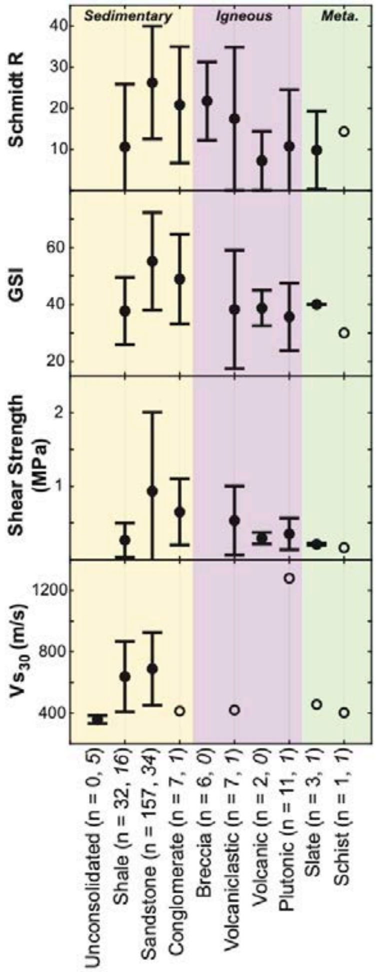

Figure 3.3: Mean (± 1σ) Schmidt R, GSI, shear strength at 10m depth, and Vs_{30} by lithologic type of all data in the Western Transverse Ranges. Shaded colors indicate sedimentary, igneous, and metamorphic (Meta.) rock types, and open circles indicate that a single measurement was made. For Schmidt R, GSI, and shear strength, 75% of the data is from sandstone units, 15% is from shale units, and 10% is from all other lithologic types. For Vs_{30}, 57% of the data is from sandstone units, 27% of the data is from shale units, and 16% of the data is from all other lithologic types. (n = number of geotechnical characterization sites, number of Vs profiles).

mechanical properties averaged over spatial scales larger than an intact block also increase over this interval. Collectively, we observe a consistent increase in all strength metrics and S-wave velocities with increasing stratigraphic age from the Plio-Pleistocene through Oligocene units (Figure 3.6).

Strength metrics and S-wave velocities from different sites within the Eocene and Cretaceous section are generally higher than the Plio-Pleistocene through Oligocene stratigraphic units, but data from different sites within these units also exhibit more variability within one standard deviation (Figure 3.5 and Figure 3.6). Notably, the mean Vs_{30} of the Eocene Coldwater and Juncal fms. is ~300 m/s slower than stratigraphically lower and higher units (Table 3.1 and Figure 3.6), which is mirrored by mean GSI values. However, mean Schmidt R values from

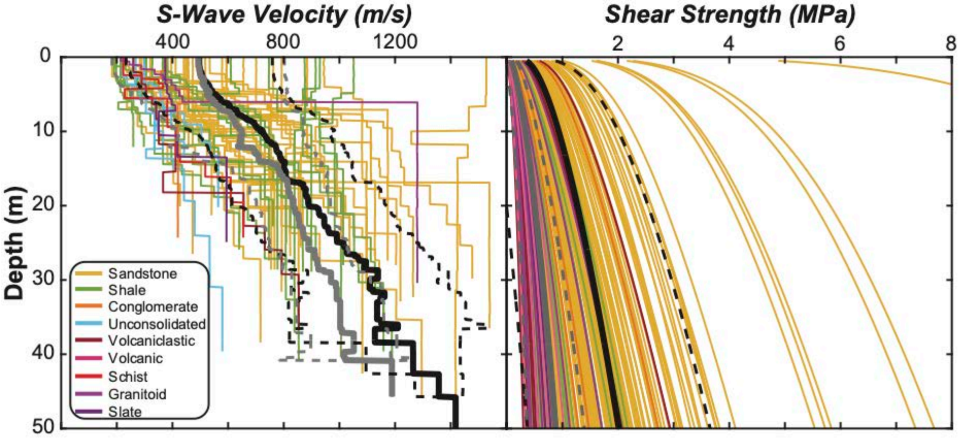

Figure 3.4: S-wave velocity and shear strength profiles from all sites in the Western Transverse Ranges, colored by lithologic type. Heavy black lines and dashed black lines are the mean and ± 1σ profile of sandstone profiles, and heavy grey lines and dashed grey lines are the mean and ± 1σ profile of shale profiles. Sandstone and shale sites demonstrate considerable variability in sub-surface S-wave velocities and shear strength, whereas sites overlying all other lithologic types measured, including unconsolidated fill, conglomerate, volcanic and volcaniclastic units, granitoids, schists, and slate generally yield S-wave velocities and shear strength on the low end of the ranges of sandstone and shale. Note that sandstone and shale shear strength profiles at < 1 MPa are obscured by other lithologic types at these low strength values.

different sites within the Eocene and Cretaceous units are nearly the same (Figure 3.5), which may suggest relatively consistent and high intact strength despite variability in strength at the larger spatial scales reflected by the GSI and S-wave velocity data.

3.5.3 Sespe Formation

Mean strength metrics and Vs_{30} of Sespe Formation sandstone sites in the Topatopa Mountains, Santa Monica Mountains, and Santa Rosa Island are reported in Table 3.2. Mean Schmidt R, GSI, shear strength at 10 m depth, and Vs_{30} of Sespe Formation sites are higher in the Topatopa Mountains than in the Santa Monica Mountains, although mean GSI, shear strength, and Vs_{30} overlap within one standard deviation (Table 3.2). Schmidt R and GSI were collected from just one Sespe Formation site on Santa Rosa Island, but each metric is lower than mean values of the Sespe Formation from either the Topatopa Mountains or Santa Monica Mountains (Table 3.1).

We observe variability of up to ~500 m/s in S-wave velocities in the uppermost 10 m of Sespe Formation sites from both the Topatopa Mountains and Santa Monica Mountains (Figure 3.7). However, from 10 m to 30 m depth, S-wave velocities of Sespe Formation sites more tightly diverge onto distinct trends of ~800 m/s for the Santa Monica Mountains, and ~1100 m/s in the Topatopa Mountains, and do not overlap within one standard deviation (Figure 3.7). Likewise, the mean shear strength profile of the Sespe Formation from the Topatopa Mountains is ~0.4 MPa stronger at 5 m depth, and ~0.7 MPa stronger at 30 m depth than the mean profile from the Santa Monica Mountains (Figure 3.7).

Mean GSI values from Sespe Formation sites are higher in the Topatopa Mountains than the Santa Monica Mountains, but individual values vary from 40 to 85 (Table 3.2). However, GSI values can be separated into their structural (out of 6) and surface quality (out of five) components to look at the relative contributions of fracturing and weathering, respectively. The mean structure component of Sepse Formation GSI from both ranges is identical (5.0 and 4.9),

Table 3.1: Mean strength metrics of sandstones by mapped formation in the Topatopa Mountains

Formation	Schmidt[†]	GSI[†]	GSI Structure[†]	GSI Surfaces[†]	τ at 10m Depth[†]	Vs_{30}[†]
Age	R	of 100	of 6	of 5	MPa	m/s
Saugus *Plio-Pleistocene*	0	23[‡]	2[‡]	2[‡]	0.15[‡]	-
Pico *Pliocene*	3 ± 4	30 ± 5	2.3 ± 0.4	2.2 ± 0.4	0.19 ± 0.03	361 ± 19
Towsley *Mio-Pliocene*	6 ± 4	30 ± 5	2.6 ± 0.5	2.4 ± 0.4	0.22 ± 0.03	480 ± 65
Sisquoc *Miocene*	14[‡]	33[‡]	4[‡]	4[‡]	0.28[‡]	-
Monterey *Miocene*	29 ± 10	53 ± 17	4.4 ± 1.3	3.4 ± 0.6	0.75 ± 0.26	727 ± 135
Vaqueros *Oligocene*	37 ± 2	45 ± 0	3.5 ± 0.5	3.3 ± 0.3	0.54 ± 0.02	-
Sespe *Oligocene*	32 ± 3	70 ± 8	5.0 ± 0.6	4.1 ± 0.6	1.35 ± 0.55	875 ± 164
Coldwater *Eocene*	31 ± 5	61 ± 11	4.6 ± 0.5	3.8 ± 0.4	0.92 ± 0.39	603 ± 62
Cozy Dell *Eocene*	42 ± 5	55 ± 0	5 ± 0	3.3 ± 0.3	0.84 ± 0.09	-
Matilija *Eocene*	42 ± 12	69 ± 7	5.4 ± 0.4	3.9 ± 0.5	1.78 ± 0.77	1092 ± 213
Juncal *Eocene*	39 ± 6	56 ± 8	4.2 ± 0.6	3.6 ± 0.5	0.86 ± 0.25	572 ± 41
Unnamed *Cretaceous*	48 ± 11	83 ± 8	5.8 ± 0.2	4.7 ± 0.5	5.49 ± 3.66	679[†]

[†] ± indicates 1σ
[‡] only one site measured

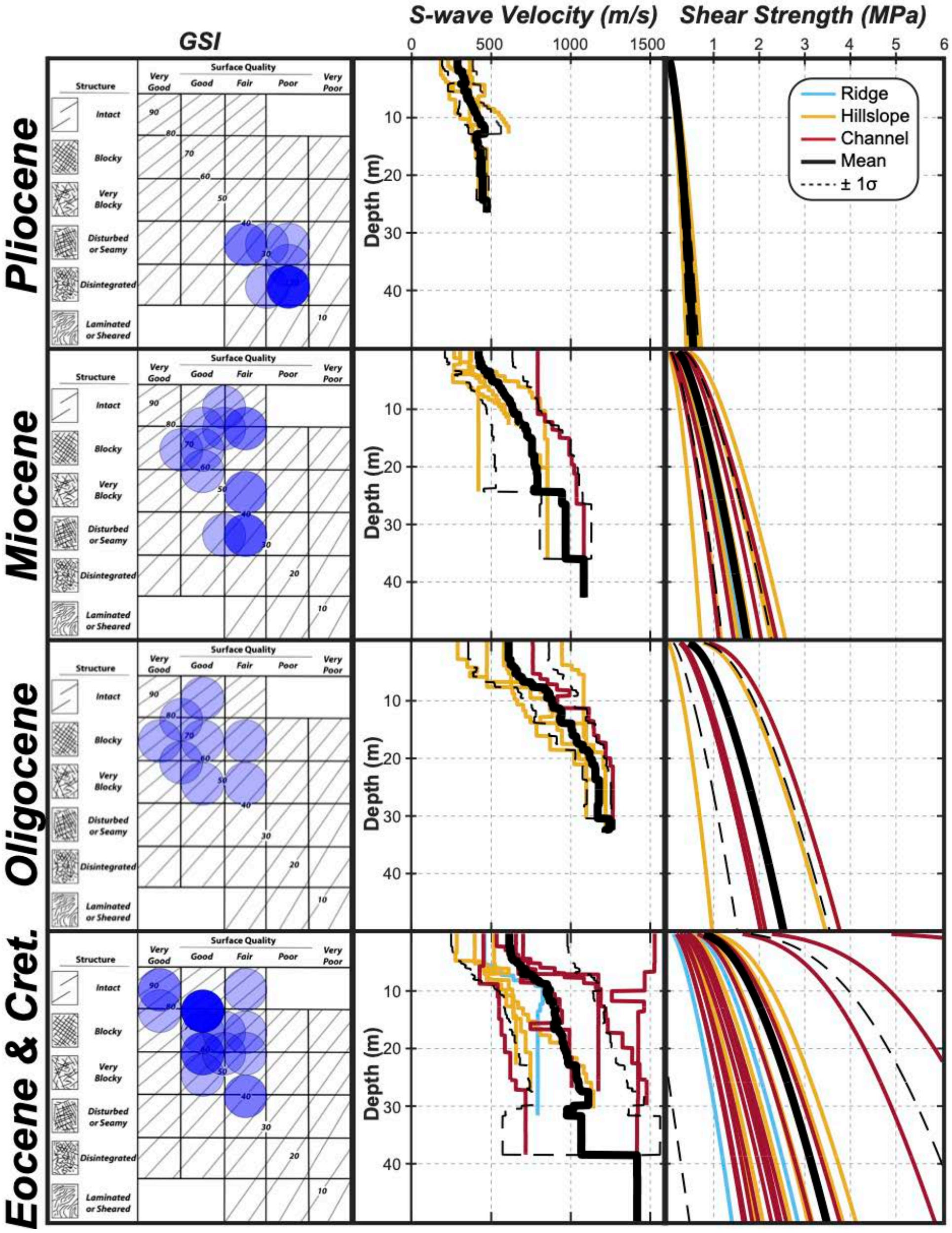

Figure 3.5: GSI, S-wave velocity profiles, and shear strength profiles of sandstone units in the Topatopa Mountains. Data are arranged by the stratigraphic age of the unit from which the data was collected. S-wave and shear strength profiles are colored by the geomorphic position of the site.

whereas the mean surface component of Sespe Formation GSI in the Santa Monica Mountains (3.6 ± 0.4) is lower than in the Topatopa Mountains (4.1 ± 0.6) (Table 3.2), reflecting greater degree of weathering on fracture surfaces.

3.5.4 S-wave Velocities and Shear Strength

Shear strength versus S-wave velocity are shown in Figure 3.8. These data include all lithologic types and are separated into four relationships based on geologic age. Data from

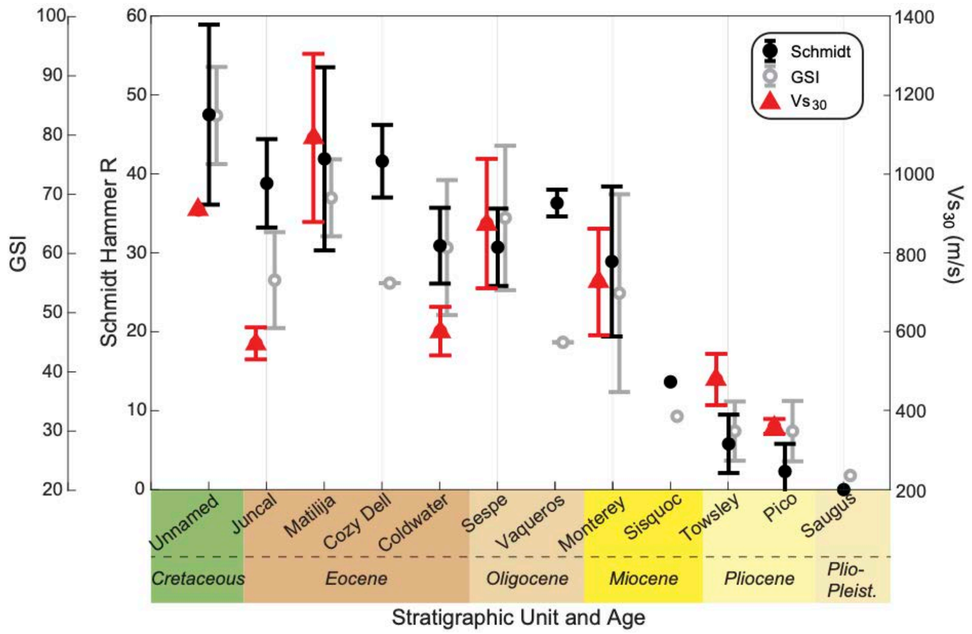

Figure 3.6: Mean Schmidt hammer rebound values, mean GSI, and mean Vs_{30} of sandstone sites by geologic unit in the Topatopa Mountains. Bars indicate ± 1σ variability about means, and data without error bars represent a single measurement. Geologic units are arranged from youngest (Plio-Pleistocene) to oldest (Cretaceous). Mean Schmidt hammer rebound values, GSI, and Vs_{30} on sandstone increase with increasing age from Plio-Pleistocene (Saugus) to Oligocene (Sespe). Mean Schmidt hammer rebound values are largely the same for Eocene and Cretaceous units, whereas mean Vs_{30} is variable for these units.

Pliocene, Miocene, Oligocene, and Eocene through Cretaceous sites define approximately linear trends, with Pliocene data plotting at lower shear strength and S-wave velocities, Miocene and Oligocene data plotting at intermediate values, and Eocene through Cretaceous data plotting at higher shear strength and S-wave velocities (Figure 3.8). We regressed through these data to produce relationships between shear strength and S-wave velocities (Table 3.3). These relationships may provide first-order estimates of S-wave velocities from GSI observations in the study area, if geophysical imaging or borehole data is unavailable (Medwedeff et al., 2019).

3.6 Discussion

3.6.1 Comparison to Typical Strength Values

Although all seismic surveys were conducted on rock units, S-wave velocities fall within ranges characteristic of 'stiff soil' (180 to 360 m/s), 'very dense soil and soft rock' (360 to 760 m/s), and 'rock' (760 to 1500 m/s) (Martin & Diehl, 2004). In particular, S-wave velocities from the Pliocene sandstones in the Topatopa Mountains range from ~200 to ~500 m/s despite being similar in composition to Oligocene and Eocene sandstones with S-wave velocities ranging from ~600 to ~1500 m/s, which further highlights the wide variability in rock mass properties within a single lithologic type. No sites from the WTR yield S-wave velocities characteristic of 'hard rock' (>1500 m/s), even at depth (Martin & Diehl, 2004). However, these high velocities are more characteristic of unweathered plutonic rocks than clastic sedimentary rocks (Barton, 2006). Our Vs_{30} values are consistent with bedrock (i.e. non-Quaternary) sites in the WTR from the USGS compilation of Vs_{30} (Yong et al., 2016).

Schmidt hammer rebound values generally fall within the range of very weak rock (10-35), weak rock (35-40), and moderately strong rocks (40-50) (Selby, 1993). Within this classification scheme, mean values from Plio-Pleistocene through Oligocene sandstones in the Topatopa Mountains are very weak, and Eocene and Cretaceous sandstones yield mean values characteristic of weak to moderately strong rocks (Selby, 1993).

3.6.2 Stratigraphic Age and Burial Depth

The physical and chemical changes associated with lithification and burial in deep sedimentary basins exert a strong control on the strength of sedimentary rockmassses (e.g. Collins & Sitar, 2008). In the Topatopa mountains, both strength and Vs show this expected relationship between increasing strength and seismic velocities with increasing formation age and stratigraphic depth interval. The stratigraphically highest unit (Plio-Pleistocene Saugus Formation) is only weakly cemented and the burial depth of the middle to upper-Miocene section is estimated at ~2-3 km (Townsend et al., 2018, 2020a). The Plio-Pleistocene through Oligocene units are a continuous section, and the Oligocene Sespe Formation at the base of this interval was buried by up to 5-7 km of overlying sedimentary rocks prior to being exhumed (Dibblee, 1991, 1993; Townsend et al., 2020a).

Table 3.2: Mean strength metrics of the Sespe Formation, by location

Location	Schmidt[†]	GSI[†]	GSI Structure[†]	GSI Surfaces[†]	τ at 10m Depth[†]	Vs_{30}[†]
	R	of 100	of 6	of 5	MPa	m/s
Topatopa Mountains	32.4 ± 2.8	69.6 ± 7.8	5.0 ± 0.6	4.1 ± 0.6	1.35 ± 0.55	875 ± 164
Santa Monica Mountains	22.1 ± 7.3	62.4 ± 13.2	4.9 ± 1.0	3.6 ± 0.4	0.84 ± 0.43	648 ± 113
Santa Rosa Island	15.3[‡]	50[‡]	4.5[‡]	3[‡]	0.43[‡]	-

[†] ± indicates 1σ
[‡] only one site measured

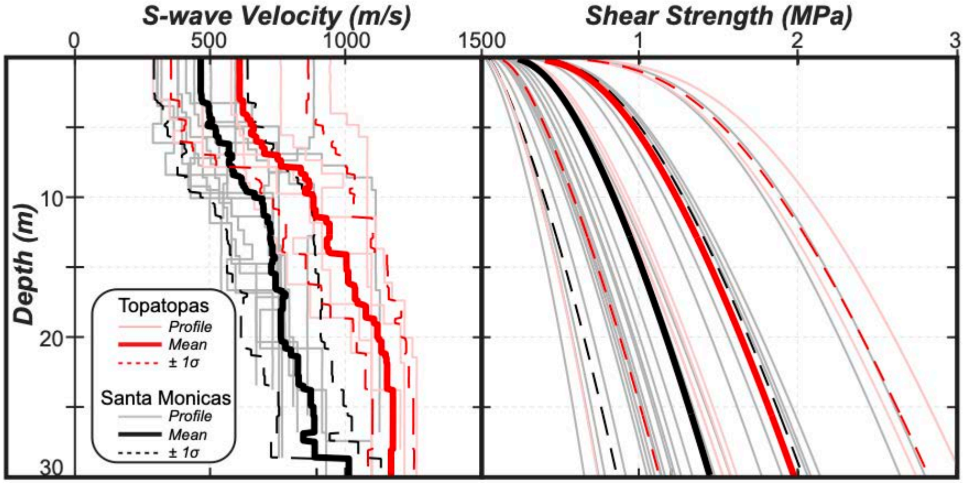

Figure 3.7: S-wave velocity profiles and shear strength profiles of the Oligocene Sespe Formation (sandstone units) in the Santa Monica Mountains and Topatopa Mountains.

Recently deposited sediments with no overburden are typically loosely packed, highly porous, and have not been cemented. Increases in temperature and pressure during subsequent burial increases grain packing and decreases porosity through both physical and chemical compaction. Chemical compaction enriches pore water with dissolved silica though partial dissolution of minerals, and precipitation of this silica in pore spaces further reduces porosity while adding cements, leading to lithification of the sediments (Boggs Jr., 2011). These physical and chemical changes occur with burial from the surface to at least 5 km depth (Worden & Burley, 2003), which is similar to the thickness of the stratigraphic interval over which we observe the highest increase in Schmidt R, GSI, shear strength, and S-wave velocities with burial depth (Figure 3.5 and Figure 3.6), also consistent with a compaction and lithification gradient. The positive correlation between strength and stratigraphic age is consistent with Townsend et al.'s (*2020*) finding that cohesive strength at spatial scales of both intact samples (direct-shear test) and hillslopes (landslide model estimates) increase as a function of original burial depth, both between and within formations, across the Plio-Pleistocene through Miocene section exposed in the eastern Topatopa Mountains. Geologic time likely also contributes to an increase in the degree of diagenesis and resultant rock strength, but we cannot separate this effect from maximum burial depth (i.e. both stratigraphic age and maximum burial depth covary with strength).

Burial to depths greater than 5 km is unlikely to drive further increased rock strength through lithification and diagenesis (Worden & Burley, 2003). The Oligocene through Cretaceous section in the Topatopa Mountains likely experienced burial to depths of 5-10 km,

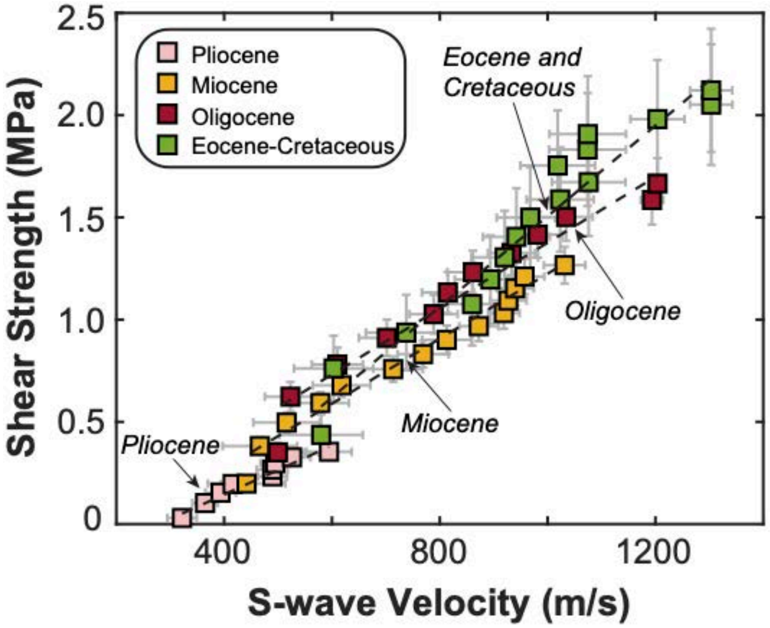

Figure 3.8: Mean shear strength against mean S-wave velocity profiles of all data from the Western Transverse Ranges, calculated in 3m intervals. Data are separated into four relationships by geologic age, which define linear trends. Dashed black lines indicate linear regressions through each of the four relationships, which are reported in Table 3. Error bars are standard error.

and although field proxies of rock strength from these units are generally higher than from the overlying Plio-Pleistocene through Oligocene section, they do not demonstrate much further increase in strength with increasing stratigraphic age (Figure 3.6). Mean values of Schmidt R and GSI are the same across Eocene and Cretaceous units (Figure 3.6), and mean S-wave velocity profile and mean shear strength profile of all Eocene and Cretaceous units are similar to the means of Oligocene data (Figure 3.2), although large ±1σ indicates significant variability about means of both formation-level data (Figure 3.6) and data binned by stratigraphic age (Figure 3.5), indicating significant variability in rockmass properties. Specifically, Mean Vs_{30} and GSI from the Juncal Formation are lower than values from overlying and underlying units (Figure 3.6). The reduced outcrop-scale strength of this unit may be explained by greater tectonic deformation, as Juncal Formation sites are within a complex structural zone where the generally north-south striking, gently east-dipping homocline of the Topatopa Mountains and the predominantly east-west striking, near-vertical homocline of the Santa Ynez Mountains intersect in a major syncline (Dibblee, 1982). At this same structural transition, strain accommodation transitions from the emergent portion of the San Cayetano Fault in the east to multiple blind structures in the west (Dibblee, 1982; Levy et al., 2019). Many hillslopes within this structural transition are mantled in landslides (Gutierrez et al., 2008), likely a consequence of tectonically-weakened bedrock, and we observe in the field that outcrops contain more open fractures than overlying or underlying stratigraphic units.

3.6.3 Rock Strength and Erosion Rate

Each metric of strength from the Sespe Formation shows a positive correlation with erosion rate, suggesting that rock strength decreases as a function of decreasing erosion rate (Figure 3.9). Erosion rate differences across these ranges are set by differences in the rate of fault slip and bedrock uplift. There is not a strong gradient in mean annual precipitation across the study area (WRCC, 2020) to explain the variation of weathering by climate differences, so we therefore posit that the decrease in rock mass strength reflects increased weathering due to longer residence times within the near surface environment (CZ) due to slower erosion rates driven by faulting. Although we have not directly quantified soil or bedrock weathering in the WTR, the surface quality axis of GSI observations provides a qualitative measure of the degree of weathering (Hoek & Brown, 1997). Surface quality values from Sespe Formation sites are higher (less weathered) in the Topatopa Mountains than the Santa Monica Mountains, which is in turn higher than the one site from Santa Rosa Island (Table 3.2). In the San Gabriel Mountains (east of our study area), increased erosion rates driven by increasing rates of tectonic uplift cause a decrease in the rates and extent of chemical weathering (Dixon et al., 2012). When erosion rates are sufficiently rapid, the extent and rate of weathering becomes limited by the kinetics of weathering reactions, and the decrease in chemical weathering leads to a decrease in soil residence time and soil thickness as weatherable minerals are eroded before they have sufficient time to weather completely (Dixon et al., 2012; West et al., 2005). The length of time that a

Table 3.3: Empirically derived relationships between shear strength and S-wave velocities

Geologic Age	Equation	R^2
Pliocene	$\tau = 0.0012V_s - 0.3325$	0.95
Miocene	$\tau = 0.0016V_s - 0.3869$	0.97
Oligocene	$\tau = 0.0017V_s - 0.2865$	0.96
Eocene to Cretaceous	$\tau = 0.0022V_s - 0.7123$	0.96

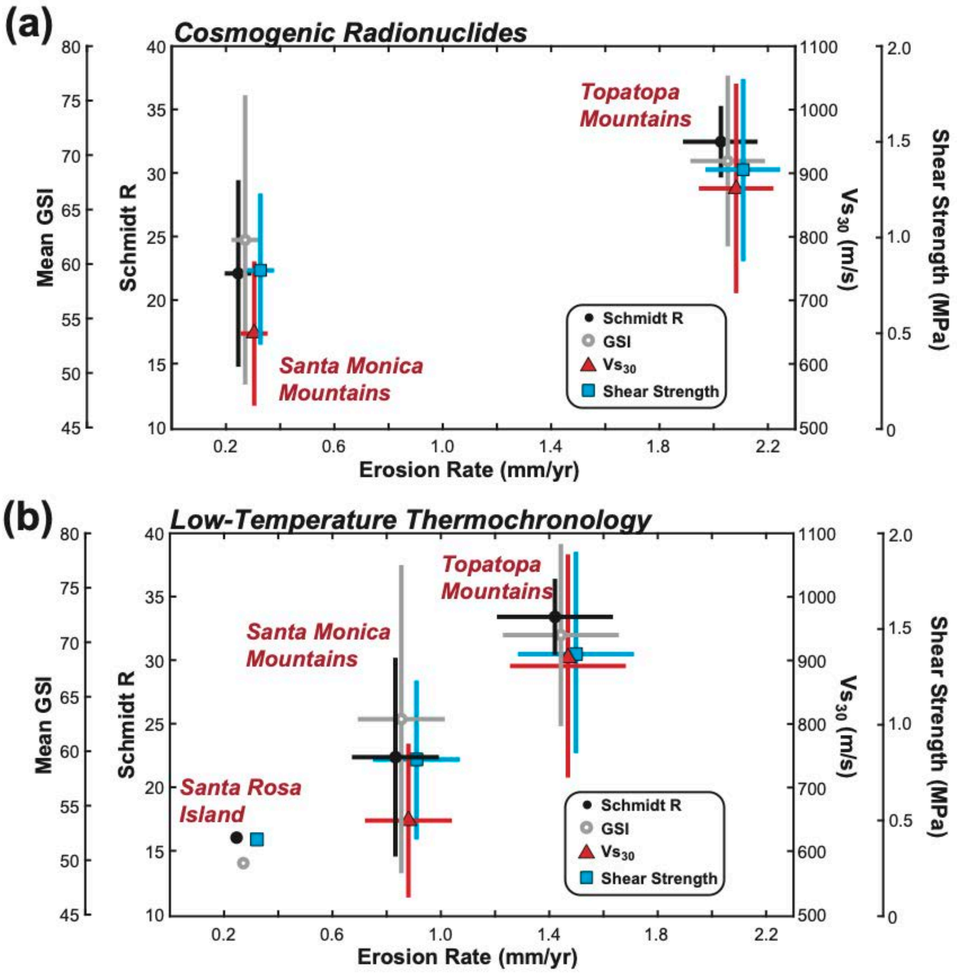

Figure 3.9: Mean strength metrics (± 1σ) of the Sespe Formation, including Schmidt hammer R, GSI, Vs30, and shear strength against erosion rates inferred from a) ^{10}Be catchment-averaged cosmogenic radionuclides, and b) apatite and zircon (U-Th)/He low-temperature thermochronometry. There are no ± 1σ bars about Santa Rosa Island values because only one data point was collected. Note that strength metrics are offset from true erosion rate by up to ~0.1 mm/yr for visibility.

particular parcel of rock resides in the CZ likely has a direct influence on the degree of weathering, and therefore, the strength of the rock mass once it reaches the surface (Moon & Jayawardane, 2004; de Vilder et al., 2019).

In locations with high weathering efficiency and relatively uniform bedrock lithologic types, S-wave velocities and shear strength may also vary with geomorphic position due to differences in erosion rate, weathering extent, and topographic stresses (St. Clair et al., 2015; Medwedeff et al., 2019). S-wave velocity and shear strength data from ridge and hillslope positions across the WTR are highly variable, but do not demonstrate systematic trends (Figure S7). Channel sites produce faster mean S-wave velocities and higher mean shear strengths than either hillslope or ridge sites (Figure 3.5), but this observation may be biased by the location of sites in the Eocene and Cretaceous section, which are predominately located near channels due to the inaccessibility of hillslope or ridge sites and the general lack of ridge sites in our study. However, we note that S-wave velocities from one channel site in the Miocene section and one site in the Oligocene section of the Topatopa Mountains plot at the higher end of the range of velocity profiles from hillslope sites (Figure 3.5), suggesting that the higher confining stress of this topographic position contributes to increased S-wave velocities.

Although we sought to control for stratigraphic age, inferred burial depth, and lithologic type, other factors that influence rock strength may vary systematically with our field sites, including but not limited to: original minerology, composition of interstitial cements, porosity, and hydrogeologic conditions. These datasets are currently unavailable across the study area, and given the correlations presented here, we suggest a weathering control as a plausible mechanism to explain the observed variability in strength. However, we acknowledge that other variables may contribute to the distribution of rock strength in the WTR.

3.6.4 Santa Ynez Mountains Comparison

Duvall et al. (2004) report Schmidt R values in the western Santa Ynez Mountains (Figure 3.1) for several stratigraphic units that also outcrop in the Topatopa Mountains. Mean Schmidt R values (± standard error) of the Monterey Formation (34.9 ± 1.0) and Matilija Sandstone (42.1 ± 1.3) from the Santa Ynez Mountains fall within the range of mean values (± 1σ) of sites in these same formations in the Topatopa Mountains (Table 3.1) (Duvall et al., 2004). However, mean Schmidt R values (± standard error) of the Vaqueros Sandstone (22.7 ± 0.34) and Sespe Formation (20.9 ± 0.35) from the Santa Ynez Mountains are lower than mean values from the same formations in the Topatopa Mountains (Table 3.1) (Duvall et al., 2004). The thickness of the paleo-basin in the Santa Ynez Mountains is thinner than in the western Topatopa Mountains (Helmold & van de Kamp, 1984), and these differing values may reflect variable basin histories. Alternatively, these lower Schmidt R values may reflect differing weathering extents, as long-term erosion rates inferred from low-temperature thermochronometry (Townsend et al., 2018), and geodetically-derived modern strain rates (S. T. Marshall et al., 2013) are lower in the Santa Ynez Mountains than the Topatopa Mountains.

3.6.5 Implications for Landscape Evolution

Landscape evolution models typically incorporate rock strength into a single erodibility parameter (e.g. *K,* Stock & Montgomery, 1999) that is often held fixed as an individual model simulation progresses through time. Data presented here demonstrates quantitatively that rock strength during the early stages of mountain building is instead a dynamic variable that evolves with time. Following initial inversion of a sedimentary basin, reverse faulting elevates poorly-consolidated, mechanically-weak sedimentary rocks, and with continued exhumation, progressively deeper sedimentary rocks with higher rock mass strength are exposed at the surface (Townsend et al., 2020a). This evolving distribution of rock mass strength will likely decrease the erodibility of the overlying landscape, which we expect will impart a signal on the relief structure of the landscape (Montgomery & Brandon, 2002; Schmidt & Montgomery, 1995; Whipple et al., 1999). With continued slip on the range-bounding San Cayetano Fault, we might expect that topographic relief in the eastern Topatopa Mountains, where the Oligocene through Plio-Pleistocene section is currently preserved (Figure 3.2), will increase through time as stronger stratigraphic units are incrementally exposed at the surface, without requiring an increase in the rate of rock uplift.

We also identify a positive correlation between rock mass mechanical properties and erosion rate, suggesting a decrease in erodibility as erosion rates increase. This observation may be indicative of a negative feedback, wherein an increase in rock mass strength due to increased erosion rates acts to resist further erosion, which in turn provides another mechanism to grow topographic relief. Our results apply to fresh and slightly weathered rock masses, but recent work on soil and saprolite strength demonstrates an increase in strength with increased weathering extent (Heimsath & Whipple, 2019). The relationship between erosion rate and soil/saprolite strength is opposite the relationship we document with rock masses, and suggests that as the strength of rock masses increases with decreased weathering, the strength of the overlying soil actually decreases. This may be one mechanism to explain the reduction in soil thickness with increased erosion rates, but further work will be required to identify and quantify the interdependencies of bedrock strength, erosion rates, weathering, and soil production. These relationships are likely to be influenced by other variables, including local climate, soil production efficiency, and fracture density (Neely et al., 2019), but data presented here provides insight into the behavior and interdependencies of rock mass strength in orogenic systems.

3.7 Conclusions

Here we apply field based methods for quantifying shear strength depth profiles of the near surface environment relevant for surface processes. We demonstrate that our approach can successfully produce expected patterns in mechanical properties that relate to burial and diagenesis of clastic sedimentary rocks. Or strength profiles also show a consistent relationship with changes in seismic velocity that lends further support to shear strength determinations over a range in values consistent with stiff soil to weak-moderately strong rock (0.1 to 13.6 MPa). We apply these same techniques to rock masses of the same geological age, lithologic type, and inferred burial depth, which outcrop in ranges bounded by faults with differing slip rates. Here we observe that each metric of rock mass strength is positively correlated with tectonically-driven erosion rates inferred from both catchment-averaged ^{10}Be cosmogenic radionuclides and low-temperature (U-Th)/He thermochronometry. We posit that the observed increase in strength with increasing erosion rate is a function of lesser weathering due to shorter residence time in the near-surface environment. Such an interpretation challeneges the simplistic notion that fast erosion rates associate with weaker rocks, and highlights to complex role that tectonics and relief may impart on the mechanical evolution of rock to transportable, erodible material.

3.8 References

Anbazhagan, P., & Sitharam, T. G. (2009). Spatial variability of the depth of weathered and engineering bedrock using multichannel analysis of surface wave method. *Pure and Applied Geophysics*, *166*(3), 409–428. https://doi.org/10.1007/s00024-009-0450-0

Aydin, A., & Basu, A. (2005). The Schmidt hammer in rock material characterization. *Engineering Geology*, *81*(1), 1–14. https://doi.org/10.1016/j.enggeo.2005.06.006

Barton, N. (2006). *Rock quality, seismic velocity, attenuation and anisotropy*. Boca Raton, FL: CRC press.

Befus, K. M., Sheehan, A. F., Leopold, M., Anderson, S. P., & Anderson, R. S. (2011). Seismic Constraints on Critical Zone Architecture, Boulder Creek Watershed, Front Range, Colorado. *Vadose Zone Journal*, *10*(3), 915. https://doi.org/10.2136/vzj2010.0108

von Blanckenburg, F. (2005). The control mechanisms of erosion and weathering at basin scale from cosmogenic nuclides in river sediment. *Earth and Planetary Science Letters*, *237*(3–4), 462–479. https://doi.org/10.1016/j.epsl.2005.06.030

Boggs Jr., S. (2011). *Principles of Sedimentology and Stratigraphy*. Pearson.

Boore, D. M. (2004). Estimating $\bar{V}$s(30) (or NEHRP site classes) from shallow velocity models (depths < 30 m). *Bulletin of the Seismological Society of America*, *94*(2), 591–597. https://doi.org/10.1785/0120030105

Borcherdt, R. D. (2012). VS30 – A Site-Characterization Parameter for Use in Paper Title Line Simplified Building Codes, Earthquake Resistant Design, GMPEs, and ShakeMaps. In *15th World Conference on Earthquake Engineering, Lisbon Portugal* (Vol. 10).

Bunn, M., Leshchinsky, B., & Olsen, M. J. (2020). Geologic Trends in Shear Strength Properties Inferred Through Three-Dimensional Back Analysis of Landslide Inventories. *Journal of Geophysical Research: Earth Surface*, *125*(9), 1–25. https://doi.org/10.1029/2019jf005461

Bursztyn, N., Pederson, J. L., Tressler, C., Mackley, R. D., & Mitchell, K. J. (2015). Rock strength along a fluvial transect of the Colorado Plateau - quantifying a fundamental control on geomorphology. *Earth and Planetary Science Letters*, *429*, 90–100. https://doi.org/10.1016/j.epsl.2015.07.042

St. Clair, J., Moon, S., Holbrook, W. S., Perron, J. T., Riebe, C. S., Martel, S. J., et al. (2015). Geophysical imaging reveals topographic stress control of bedrock weathering. *Science*, *350*(6260), 534–539. https://doi.org/10.1126/science.aab2210

Clarke, B. A., & Burbank, D. W. (2011). Quantifying bedrock-fracture patterns within the shallow subsurface: Implications for rock mass strength, bedrock landslides, and erodibility. *Journal of Geophysical Research: Earth Surface*, *116*(4). https://doi.org/10.1029/2011JF001987

Collins, B. D., & Sitar, N. (2008). Processes of coastal bluff erosion in weakly lithified sands, Pacifica, California, USA. *Geomorphology*, *97*(3–4), 483–501. https://doi.org/10.1016/j.geomorph.2007.09.004

Davis, W. M. (1899). The Geographical Cycle. *The Geographical Journal*, *14*(5), 481–504.

Deere, D., & Miller, R. (1966). *Engineering classification and index properties for intact rock.*

DeVecchio, D. E., Heermance, R. V., Fuchs, M., & Owen, L. A. (2012). Climate-controlled landscape evolution in the Western Transverse Ranges, California: Insights from Quaternary geochronology of the Saugus Formation and strath terrace flights. *Lithosphere*, *4*, 110–130. https://doi.org/10.1130/L176.1

Dibblee, T. W. (1982). Regional geology of the Transverse Ranges Province of southern California. In D. L. Fefe & J. A. Minch (Eds.), *Geology and Mineral Wealth of the Califrnia Transverse Ranges* (pp. 7–26). Santa Ana, California: South Coast Geological Society, Inc.

Dibblee, T. W. (1991). *Geologic Map of the Piru Quadrangle, Ventura County, California*. Santa Barbara, California: Dibblee Geological Foundation.

Dibblee, T. W. (1993). *Geologic Map of the Val Verde Quadrangle, Los Angeles and Ventura Counties, California*. Santa Barbara, California: Dibblee Geological Foundation.

DiBiase, R. A., Rossi, M. W., & Neely, A. B. (2018). Fracture density and grain size controls on the relief structure of bedrock landscapes. *Geology*, *46*(5), 399–402. https://doi.org/10.1130/G40006.1

Dixon, J. L., Hartshorn, A. S., Heimsath, A. M., DiBiase, R. A., & Whipple, K. X. (2012). Chemical weathering response to tectonic forcing: A soils perspective from the San Gabriel Mountains, California. *Earth and Planetary Science Letters*, *323–324*, 40–49. https://doi.org/10.1016/j.epsl.2012.01.010

Dühnforth, M., Anderson, R. S., Ward, D., & Stock, G. M. (2010). Bedrock fracture control of glacial erosion processes and rates. *Geology*, *38*(5), 423–426. https://doi.org/10.1130/G30576.1

Duvall, A. R., Kirby, E., & Burbank, D. W. (2004). Tectonic and lithologic controls on bedrock channel profiles and processes in coastal California. *Journal of Geophysical Research*, *109*(F3), 1–18. https://doi.org/10.1029/2003JF000086

Ehlers, T. A. (2005). Crustal Thermal Processes and the Interpretation of Thermochronometer Data. *Reviews in Mineralogy and Geochemistry*, *58*(1), 315–350. https://doi.org/10.2138/rmg.2005.58.12

Farley, K. A. (2002). (U-Th)/He Dating: Techniques, Calibrations, and Applications. *Reviews in Mineralogy and Geochemistry*, *47*(1), 819–844. https://doi.org/10.2138/rmg.2002.47.18

Flinchum, B. A., Steven Holbrook, W., Rempe, D., Moon, S., Riebe, C. S., Carr, B. J., et al. (2018). Critical zone structure under a granite ridge inferred from drilling and three-dimensional seismic refraction data. *Journal of Geophysical Research: Earth Surface*, *123*(6), 1317–1343. https://doi.org/10.1029/2017JF004280

Flowers, R. M., Ketcham, R. A., Shuster, D. L., & Farley, K. A. (2009). Apatite (U-Th)/He thermochronometry using a radiation damage accumulation and annealing model. *Geochimica et Cosmochimica Acta*, *73*(8), 2347–2365. https://doi.org/10.1016/j.gca.2009.01.015

Forte, A. M., Yanites, B. J., & Whipple, K. X. (2016). Complexities of landscape evolution during incision through layered stratigraphy with contrasts in rock strength. *Earth Surface Processes and Landforms*, *41*(12), 1736–1757. https://doi.org/10.1002/esp.3947

Foti, S., Comina, C., Boiero, D., & Socco, L. V. (2009). Non-uniqueness in surface-wave inversion and consequences on seismic site response analyses. *Soil Dynamics and Earthquake Engineering*, *29*(6), 982–993. https://doi.org/10.1016/j.soildyn.2008.11.004

Gabet, E. J., Wolff-Boenisch, D., Langner, H., Burbank, D. W., & Putkonen, J. (2010). Geomorphic and climatic controls on chemical weathering in the High Himalayas of Nepal. *Geomorphology*, *122*(1–2), 205–210. https://doi.org/10.1016/j.geomorph.2010.06.016

Gabet, E. J., Mudd, S. M., Milodowski, D. T., Yoo, K., Hurst, M. D., & Dosseto, A. (2015). Local topography and erosion rate control regolith thickness along a ridgeline in the Sierra Nevada, California. *Earth Surface Processes and Landforms*, *40*(13), 1779–1790. https://doi.org/10.1002/esp.3754

Gallen, S. F. (2018). Lithologic controls on landscape dynamics and aquatic species evolution in post-orogenic mountains. *Earth and Planetary Science Letters*, *493*, 150–160. https://doi.org/10.1016/j.epsl.2018.04.029

Gallen, S. F., Clark, M. K., & Godt, J. W. (2015). Coseismic landslides reveal near-surface rock strength in a highrelief, tectonically active setting. *Geology*, *43*(1), 11–14. https://doi.org/10.1130/G36080.1

Garofalo, F., Foti, S., Hollender, F., Bard, P. Y., Cornou, C., Cox, B. R., et al. (2016). InterPACIFIC project: Comparison of invasive and non-invasive methods for seismic site characterization. Part I: Intra-comparison of surface wave methods. *Soil Dynamics and Earthquake Engineering*, *82*, 222–240. https://doi.org/10.1016/j.soildyn.2015.12.010

Gilbert, G. K. (1877). *Report on the geology of the Henry Mountains: Geographical and geological survey of the Rocky Mountain region*. Washington. D.C.

Gordon, G. (2014). *Stratigraphic evolution and architectural analysis of structurally confined submarine fans: A tripartite outcrop-based study*. Colorado School of Mines.

Goudie, A. S. (2016). Quantification of rock control in geomorphology. *Earth-Science Reviews*, *159*, 374–387. https://doi.org/10.1016/j.earscirev.2016.06.012

Granger, D. E., Kirchner, J. W., & Finkel, R. (1996). Spatially-averaged long term erosion rates measured from in situ-produced cosmogenic nuclides in alluvial sediments. *The Journal of Geology*, *104*, 249–257. https://doi.org/10.2307/256788

Gutierrez, C. I., Tan, S. S., & Clahan, K. B. (2008). Preliminary geologic map of the east half Santa Barabara 30’ x 60’ quadrangle, California. *California Geological Survey Regional Geologic Map Series, 1:100,000 Scale*, 1.

Hack, J. T. (1975). Dynamic equilibrium and landscape evolution. *Theories of Landform Development: Publications in Geomorphology*. Retrieved from http://geomorphology.sese.asu.edu/Papers/Hack_1975.pdf

Heimsath, A. M., & Whipple, K. X. (2019). Strength Matters: Resisting Erosion Across Upland Landscapes. *Earth Surface Processes and Landforms*. https://doi.org/10.1002/esp.4609

Helmold, K. P., & van de Kamp, P. C. (1984). Diagenetic mineralogy and controls on albitization and laumontite formation in Paleogene Arkoses, Santa Ynez Mountains, California. *AAPG Memoir 37*, *0*(1), 239–276.

Hoek, E., & Brown, E. (1980). Empirical Strength Criterion for Rock Masses. *Journal of the Geotechnical Engineering Division*. https://doi.org/10.1016/0148-9062(81)90766-X

Hoek, E., & Brown, E. (1997). Practical estimates of rock mass strength. *International Journal of Rock Mechanics and Mining Sciences*, *34*(8), 1165–1186. https://doi.org/10.1016/S1365-1609(97)80069-X

Hoek, E., & Marinos, P. (2000). Predicting tunnel squeezing problems in weak heterogeneous rock masses. *Tunnels and Tunnelling International*, *Part 1-2*(November), 1–20. Retrieved from https://www.rocscience.com/documents/hoek/references/H2000d.pdf%0Ahttp://www.rockscience.com/hoek/references/H2000d.pdf

Hoek, E., Carranza, C., & Corkum, B. (2002). Hoek-brown failure criterion – 2002 edition. *Narms-Tac*, 267–273. https://doi.org/10.1016/0148-9062(74)91782-3

Holbrook, W. S., Riebe, C. S., Elwaseif, M., Hayes, J. L., Basler-Reeder, K., Harry, D. L., et al. (2014). Geophysical constraints on deep weathering and water storage potential in the Southern Sierra Critical Zone Observatory. *Earth Surface Processes and Landforms*, *39*(3), 366–380. https://doi.org/10.1002/esp.3502

Howard, J. L. (1988). Sedimentation of the Sespe Formation in southern California. *Santa Barbara and Ventura Basins: Tectonics, Structure, Sedimentation, Oil Fields along an East-West Transect.*, *64*(1988), 53–69.

Hughes, A. (2019). *Quaternary structural evolution and seismic hazards of the onshore Ventura basin, southern California, USA*. Imperial College London.

Jaky, J. (1944). The coefficient of earth pressure at rest. *Journal of the Society of Hungarian Architects and Engineers*, 355–358.

Kirkpatrick, H. M., Moon, S., Yin, A., & Harrison, T. M. (2020). Impact of fault damage on eastern Tibet topography. *Geology*, *48*. https://doi.org/10.1130/G48179.1/5137742/g48179.pdf

Korup, O. (2008). Rock type leaves topographic signature in landslide-dominated mountain ranges. *Geophysical Research Letters*, *35*(11), 1–5. https://doi.org/10.1029/2008GL034157

Leone, J. D., Holbrook, W. S., Riebe, C. S., Chorover, J., Ferré, T. P. A., Carr, B. J., & Callahan, R. P. (2020). Strong slope-aspect control of regolith thickness by bedrock foliation. *Earth Surface Processes and Landforms*, *3010*(July), 2998–3010. https://doi.org/10.1002/esp.4947

Leung, C. F., & Radhakrishnan, R. (1990). Geotechnical properties of weathered sedimentary rocks. *Geotechnical Engineering*, *21*(1), 29–48.

Levy, Y., Rockwell, T. K., Shaw, J. H., Plesch, A., Driscoll, N. W., & Perea, H. (2019). Structural Modeling of the Western Transverse Ranges: An Imbricated Thrust Ramp Architecture. *Lithosphere*, 1–38. https://doi.org/10.1130/L1124.1/4860092/l1124.pdf

Marshall, J. A., & Roering, J. J. (2014). Diagenetic variation in the Oregon Coast Range: Implications for rock strength, soil production, hillslope form, and landscape evolution. *Journal of Geophysical Research: Earth Surface*, *119*, 1395–1417. https://doi.org/10.1002/2013JF003004.

Marshall, S. T., Funning, G. J., & Owen, S. E. (2013). Fault slip rates and interseismic deformation in the western Transverse Ranges, California. *Journal of Geophysical Research: Solid Earth*, *118*(8), 4511–4534. https://doi.org/10.1002/jgrb.50312

Marshall, S. T., Funning, G. J., Krueger, H. E., Owen, S. E., & Loveless, J. P. (2017). Mechanical models favor a ramp geometry for the Ventura-pitas point fault, California. *Geophysical Research Letters*. https://doi.org/10.1002/2016GL072289

Martin, A. J., & Diehl, J. G. (2004). Practical Experience Using A Simplified Procedure To Measure Average Shear-Wave Velocity To A Depth Of 30 Meters (Vs30). *13th World Conference on Earthquake Engineering*, (952), 9. Retrieved from http://www.iitk.ac.in/nicee/wcee/article/13_952.pdf

Mayne, P. W., & Kulhawey, F. H. (1982). K0-OCR Relationship in Soil. *Journal of the Soil Mechanics and Foundations Division*, *108*(6), 851–872.

Medwedeff, W. G., Clark, M. K., Zekkos, D., West, A. J., Chamlagain, D., Atwood, A., et al. (2019). Seismic characterization of the Critical Zone in the Nepal Himalaya: a regional perspective. In *American Geophysical Union, Fall Meeting, Abstract #NS21C-0824*.

Molnar, P., Anderson, R. S., & Anderson, S. P. (2007). Tectonics, fracturing of rock, and erosion. *Journal of Geophysical Research: Earth Surface*, *112*(3), 1–12. https://doi.org/10.1029/2005JF000433

Montgomery, D. R., & Brandon, M. T. (2002). Topographic controls on erosion rates in tectonically active mountain ranges. *Earth and Planetary Science Letters*, *201*(3–4), 481–489. https://doi.org/10.1016/S0012-821X(02)00725-2

Moon, V., & Jayawardane, J. (2004). Geomechanical and geochemical changes during early stages of weathering of Karamu Basalt, New Zealand. *Engineering Geology*, *74*(1–2), 57–72. https://doi.org/10.1016/j.enggeo.2004.02.002

Namson, J. S., & Davis, T. L. (1988). Structural transect of the western Transverse Rances, California: Implications for lithospheric kinematics and seismic risk evaluation. *Geology*, *16*, 675–679.

Neely, A. B., DiBiase, R. A., Corbett, L. B., Bierman, P. R., & Caffee, M. W. (2019). Bedrock fracture density controls on hillslope erodibility in steep, rocky landscapes with patchy soil cover, southern California, USA. *Earth and Planetary Science Letters*, *522*, 186–197. https://doi.org/10.1016/j.epsl.2019.06.011

Niemi, N. A., & Clark, M. K. (2018). Long-term exhumation rates exceed paleoseismic slip rates in the central Santa Monica Mountains, Los Angeles County, California. *Geology*, *46*(1), 63–66. https://doi.org/10.1130/G39388.1

Park, C. B., Miller, R. D., & Xia, J. (1998). Imaging dispersion curves of surface waves on multi-channel record. In *Expanded Abstracts: 68th Annual International Meeting, Society of Exploration Geophysicists* (pp. 1377–1380). https://doi.org/10.1190/1.1820161

Park, C. B., Miller, R. D., & Xia, J. (1999). Multichannel analysis of surface waves. *Geophysics*, *64*(3), 800–808. https://doi.org/10.1190/1.1444590

Park, C. B., Miller, R. D., Xia, J., & Ivanov, J. (2000). Multichannel seismic surface-wave methods for geotechnical applications. *Proc. of the First Int. Conf. on the App …*. Retrieved from http://www.kgs.ku.edu/Geophysics2/Pubs/Pubs/PAR-00-03.pdf

Portenga, E. W., Clark, M. K., & Niemi, N. A. (2017). Spatial and Temporal Patterns of Motion Along the Malibu Coastal Fault Inferred from 10Be Erosion Rates. In *American Geophysical Union, Fall Meeting, Abstract #EP32C-02*. New Orleans, LA.

Reiners, P. W., Farley, K. A., & Hickes, H. J. (2002). He diffusion and (U-Th)/He thermochronometry of zircon: Initial results from Fish Canyon Tuff and Gold Butte. *Tectonophysics*, *349*(1–4), 297–308. https://doi.org/10.1016/S0040-1951(02)00058-6

Riebe, C. S., Hahm, W. J., & Brantley, S. L. (2017). Controls on deep critical zone architecture:

a historical review and four testable hypotheses. *Earth Surface Processes and Landforms*, *42*(1), 128–156. https://doi.org/10.1002/esp.4052

Rockwell, T. K. (1988). Neotectonics of the San Cayetano fault, Transverse Ranges, California. *Geological Society of America Bulletin*, *100*, 500–513.

Roy, S. G., Koons, P. O., Upton, P., & Tucker, G. E. (2015). The influence of crustal strength fields on the patterns and rates of fluvial incision. *Journal of Geophysical Research : Earth Surface*, *120*, 275–299. https://doi.org/10.1002/2015JF003602.Received

Roy, S. G., Tucker, G. E., Koons, P. O., Smith, S. M., & Upton, P. (2016). A fault runs through it: Modeling the influence of rock strength and grain-size distribution in a fault-damaged landscape. *Journal of Geophysical Research: Earth Surface*, *121*(10), 1911–1930. https://doi.org/10.1002/2015JF003662

Schmidt, K. M., & Montgomery, D. R. (1995). Limits to Relief. *Science*, *270*(5236), 617–620.

Scott, D. N., & Wohl, E. E. (2018). Bedrock fracture influences on geomorphic process and form across process domains and scales. *Earth Surface Processes and Landforms*. https://doi.org/10.1002/esp.4473

Selby, M. J. (1980). A rock mass strength classification for geomorphic purposes: With tests from Antarctica and New Zealand. *Z. Geomorphol*, *24*, 31–51.

Selby, M. J. (1993). *Hillslope materials and processes*. Oxford University Press.

Sklar, L. S., & Dietrich, W. E. (2001). Sediment and rock strength controls on river incision into bedrock. *Geology*, *29*(12), 1087–1090. https://doi.org/10.1130/0091-7613(2001)029<1087:SARSCO>2.0.CO

Slim, M., Perron, J. T., Martel, S. J., & Singha, K. (2015). Topographic stress and rock fracture: A two-dimensional numerical model for arbitrary topography and preliminary comparison with borehole observations. *Earth Surface Processes and Landforms*, *40*(4), 512–529. https://doi.org/10.1002/esp.3646

Stock, J. D., & Montgomery, D. R. (1999). Geologic constraints on bedrock river incision using the stream power law. *Journal of Geophysical Research: Solid Earth*, *104*(B3), 4983–4993. https://doi.org/10.1029/98JB02139

Stokoe, K. H., & Santamarina, J. C. (2000). Seismic-wave-based testing in geotechnical engineering. *Proceedings of the International Society for Rock Mechanics*.

Stokoe, K. H., Wright, S. G., Bay, J. A., & Roesset, J. M. (1994). Characterization of geotechical sites by SASW method. In R. D. Woods (Ed.), *Geophysical Characterization of Sites* (pp. 15–26). New York: International Science.

Townsend, K. F., Clark, M. K., & Niemi, N. A. (2018). Short-term variability versus long-term consistency of inferred fault slip rates in the Western Transverse Ranges, Southern California. In *American Geophysical Union, Fall Meeting, Abstract #T42B-02*. Washington. D.C.

Townsend, K. F., Gallen, S. F., & Clark, M. K. (2020a). Quantifying Near-Surface Rock Strength on a Regional Scale From Hillslope Stability Models. *Journal of Geophysical Research: Earth Surface*, *125*(7). https://doi.org/10.1029/2020JF005665

Townsend, K.F., Clark, M.K., & Zekkos, D. (2020b). Profiles of near-surface rock mass strength across gradients in erosion, burial, and time [Data set]. University of Michigan - Deep Blue. https://doi.org/10.7302/krah-yx31

Vilder, S. J., Brain, M. J., & Rosser, N. J. (2019). Controls on the geotechnical response of sedimentary rocks to weathering. *Earth Surface Processes and Landforms*. https://doi.org/10.1002/esp.4619 de Vilder, S. J., Brain, M. J., & Rosser, N. J. (2019). Controls on the geotechnical response of sedimentary rocks to weathering. *Earth Surface Processes and Landforms*, *1929*(May), 1910–1929. https://doi.org/10.1002/esp.4619

Von Voigtlander, J., Clark, M. K., Zekkos, D., Greenwood, W. W., Anderson, S. P., Anderson, R. S., & Godt, J. W. (2018). Strong variation in weathering of layered rock maintains hillslope-scale strength under high precipitation. *Earth Surface Processes and Landforms*, *1194*(March), 1183–1194. https://doi.org/10.1002/esp.4290

Wang, H. Y., & Wang, S. Y. (2015). A new method for estimating Vs (30) from a shallow shear-wave velocity profile (depth <30 m). *Bulletin of the Seismological Society of America*, *105*(3), 1359–1370. https://doi.org/10.1785/0120140103

West, A. J., Galy, A., & Bickle, M. (2005). Tectonic and climatic controls on silicate weathering. *Earth and Planetary Science Letters*, *235*(1–2), 211–228. https://doi.org/10.1016/j.epsl.2005.03.020

Western Regional Climate Center. https://wrcc.dri.edu. Accessed [17/04/2020].

Whipple, K. X., Kirby, E., & Brocklehurst, S. H. (1999). Geomorphic limits to climate-induced increases in topographic relief. *Nature*, *401*, 39–43. https://doi.org/10.1038/43375

Willett, S. D., & Brandon, M. T. (2002). On steady state in mountain belts. *Geology*, *30*(2), 175–178. https://doi.org/10.1130/0091-7613(2002)030<0175

Worden, R. H., & Burley, S. D. (2003). Sandstone Diagenesis: The Evolution of Sand to Stone. In *Sandstone Diagenesis: Recent and Ancient* (pp. 3–44). Malden, MA: Blackwell Publishing. https://doi.org/10.1002/9781444304459.ch

Xia, J., Miller, R. D., Park, C. B., & Tian, G. (2003). Inversion of high frequency surface waves with fundamental and higher modes. *Journal of Applied Geophysics*, *52*(1), 45–57. https://doi.org/10.1016/S0926-9851(02)00239-2

Yong, A., Thompson, E. M., Wald, D. J., Knudsen, K. L., Odum, J. K., William J Stephenson, & Haefner, S. (2016). Compilation of Vs30 Data for the United States, 8 p.

Yoon, S., & Rix, G. J. (2009). Near-Field Effects on Array-Based Surface Wave Methods with Active Sources. *Journal of Geotechnical and Geoenvironmental Engineering*.

Data Availability Statement

Raw seismic data (.dat files), dispersion curves, S-wave velocity profiles, and summary files with site information are available from the Deep Blue data repository at https://doi.org/10.7302/krah-yx31. Additional figures are included in Appendix B.

Acknowledgements

This work was supported by a National Science Foundation division of Earth Science, Geomorphology and Land Use Dynamics award (EAR-1528576) to M.K. Clark and research grants from the Evolving Earth Foundation, the Geological Society of America, the Department of Earth and Environ- mental Sciences at the University of Michigan, and the Rackham Graduate School at the University of Michigan to K.F. Townsend. The authors thank the U.S. National Park Service, U.S. Forest Service, and United Water Conservation District for field access and/or permits, Salvador Dominguez, Tim Cohen (Rancho Temescal), Gordon Kimball, and Jim Lynn for access to private properties, and Seneca Resources and Carbon Energy Corporation for access to oil fields. Logan Knoper, Abra Atwood, A. Joshua West, Nikolas Midttun, Bian Wang, Wing Yee Winnie Woo, and William Medwedeff assisted us in the field. The authors further thank William Medwedeff for discussions that helped refine the methodology and strengthen the arguments presented here. We acknowledge Heather Viles, Kelin Whipple, and one anonymous reviewer for constructive feedback that greatly improved this manuscript.

Chapter 4: Reverse Faulting Within a Continental Plate Boundary Transform System[3]

4.1 Abstract

Contractional deformation is common along transform plate margins where plate motion is oblique to the plate boundary. While faults that accommodate this deformation are often inferred to be subsidiary to the main plate boundary fault, we typically lack direct geometric or kinematic information. Here we investigate the timing of fault initiation and propagation in the Western Transverse Ranges (WTR) of southern California, USA, where active shortening is inferred to have initiated at ~5 Ma, coeval with development of the Big Bend of the San Andreas fault. Low-temperature thermochronometric ages from eleven vertical transects yield Miocene to Pleistocene apatite (U-Th-Sm)/He cooling ages and partially reset zircon (U-Th)/He ages. Inverse thermal modelling of thermochronometry data indicate that reverse faulting initiated as early as 10 Ma, several million years prior to development of the Big Bend. Reverse faults in the WTR propagate from west to east, towards the San Andreas Fault, rather than outwards from it. Together, these observations suggest that shortening in the WTR is driven by factors unrelated to the development of the Big Bend. This conclusion is supported by new and existing thermochronometry data that delineate the WTR as the locus of rapid post-Miocene exhumation, and which demonstrate that similar exhumation is not present in the broader region surrounding the Big Bend. We posit that reverse faulting is localized in the WTR because of a weak underlying lithosphere rather than the more recent geometric anomaly of the restraining bend in the transform margin.

4.2 Introduction

The mechanisms of fault initiation, propagation, and linkage are fundamental questions in structural geology and tectonics (Huntington & Klepeis, 2017). Continental transforms are characterized by complex fault systems in which the geometry and location of the active plate boundary fault evolves rapidly in geologic time (e.g. 3-10 Myr; Crowell, 1979; Şengör et al., 2005; Walcott, 1998). The evolution of such plate boundary faults is accompanied by development of subsidiary fault systems that may be related to compressional or extensional

---

[3] Submitted to *Tectonics* for peer-review as: Townsend, K.F., Clark, M.K., & Niemi, N., Reverse faulting within a continental plate boundary transform system

bends that evolve along the active plate boundary (Armijo et al., 2002; Dewey et al., 1998; Niemi et al., 2013; Spotila et al., 2001; Teyssier et al., 1995), or which may arise from the initiation and propagation of a new strand of the plate boundary fault (Armijo et al., 1999; Collett et al., 2019; Cowan et al., 1996; Little & Jones, 1998; Rohr, 2015; Wallace et al., 2012). Such subsidiary fault systems are often significant seismic hazards in their own right, thus amplifying regional seismic risk near plate boundaries (Davis & Namson, 1994; Dolan et al., 1995; Duffy et al., 2013; Quigley et al., 2012).

The relationship between oblique plate boundaries and subsidiary dip-slip fault systems have largely been explored with numerical models and physical experiments (Cooke et al., 2020; Hatem et al., 2015, 2017; Madden et al., 2017; McBeck et al., 2016, 2017). Restraining and releasing bends in continental transforms are associated with localized compression or extension (Dewey et al., 1998; Teyssier et al., 1995), and analog models demonstrate a geometric and kinematic link between primary plate boundary transforms and subsidiary reverse or normal faults (Cooke et al., 2013; Hatem et al., 2015). Therefore, it is often inferred that the initiation of reverse (normal) faults near restraining (releasing) bends in plate boundary transforms is driven by the geometry of the fault bend, with subsidiary faults initiating either during or subsequent to development of the bend itself (Crowell, 1979). However, the initiation of subsidiary fault systems with respect to establishment of a plate boundary fault, and linkages between the growth and propagation of the plate boundary fault and subsidiary fault systems is not well documented from field studies.

The timing of dip-slip fault initiation relative to the development of bends in continental transforms remains unresolved in most field settings. Spatiotemporal data constraining the timing of initiation of subsidiary faults is generally unavailable, but such data is required to assess the mechanistic relationship between these structures and the primary plate boundary transform faults. In the absence of precise age constraints, two mutually exclusive hypotheses have been proposed from previous studies. The commonly-accepted hypothesis is that dip-slip faults are mechanically linked to the adjacent plate boundary transforms, with the initiation of dip-slip faults driven by the geometry and kinematics of the principal faults (e.g. Crowell, 1979; Hatem et al., 2015). However, a second hypothesis proposes that dip-slip structures initiate independently within diffuse plate boundary zones as a manifestation of inherited structural heterogeneities, rheologic contrasts, or other forcings (e.g. Woodcock, 1986). High resolution thermochronometry data can potentially discriminate between these two hypotheses.

The Western Transverse Ranges (WTR) of southern California, USA are a ~200 km by 70 km series of mountain ranges bounded by east-west oriented oblique-reverse faults (Figure 4.1). These structures are in close proximity to the ~160-km long restraining bend (i.e. the Big Bend) in the dextral San Andreas Fault Zone, the main continental transform fault between the Pacific and North American plates (Atwater, 1998; Crowell, 1979; Huftile & Yeats, 1996; Jackson & Molnar, 1990; Luyendyk, 1991; Namson & Davis, 1988; Nicholson et al., 1994; Yeats, 1981). Development of the Big Bend is reasonably well constrained by fossil assemblages to ~5 Ma (Crowell, 1982; Link, 1982). Due to the close proximity of the WTR, as well as the structural implications of an adjacent transpressive bend, the timing of reverse fault initiation within the WTR is generally inferred to be at around the same time (Crowell, 1979). Independent timing of the initiation of reverse faulting in the WTR is currently poorly constrained by stratigraphic data, and consequently, the kinematic relationship between the San Andreas Fault and the WTR has not been explicitly tested.

The San Andreas fault is the archetypal continental transform system, and understanding the temporal and geometric relationships between the evolution of the Big Bend and the WTR is likely to lead to kinematic models that can be exported beyond western North America (e.g., the Marlborough Fault System of New Zealand, the North Anatolian Fault system of Turkey, and the Queen Charlotte Fault system offshore western Canada and Alaska). Spatially dense thermochronometric data provide insight into the relationship between the reverse faults within the WTR and the evolution of California’s transform plate boundary. Here we present new apatite and zircon (U-Th-[Sm])/He thermochronometry data from the northern and southern boundaries of the WTR, where structural relief is greatest and reverse faulting is inferred to have initiated earliest. Samples from nine new transects and two published transects (Niemi & Clark, 2018) reveal predominantly Pliocene to Pleistocene apatite cooling ages in the Santa Ynez and Topatopa Mountains on the northern boundary, and latest-Miocene to Pliocene cooling ages in the Santa Monica Mountains and northern Channel Islands on the southern boundary (Figure 4.1). These data suggest recent and rapid rock exhumation, and inverse thermal modelling for time-temperature histories yield constraints on the timing of cooling and inferred reverse faulting. We also evaluate our thermochronometric results from samples collected both on and

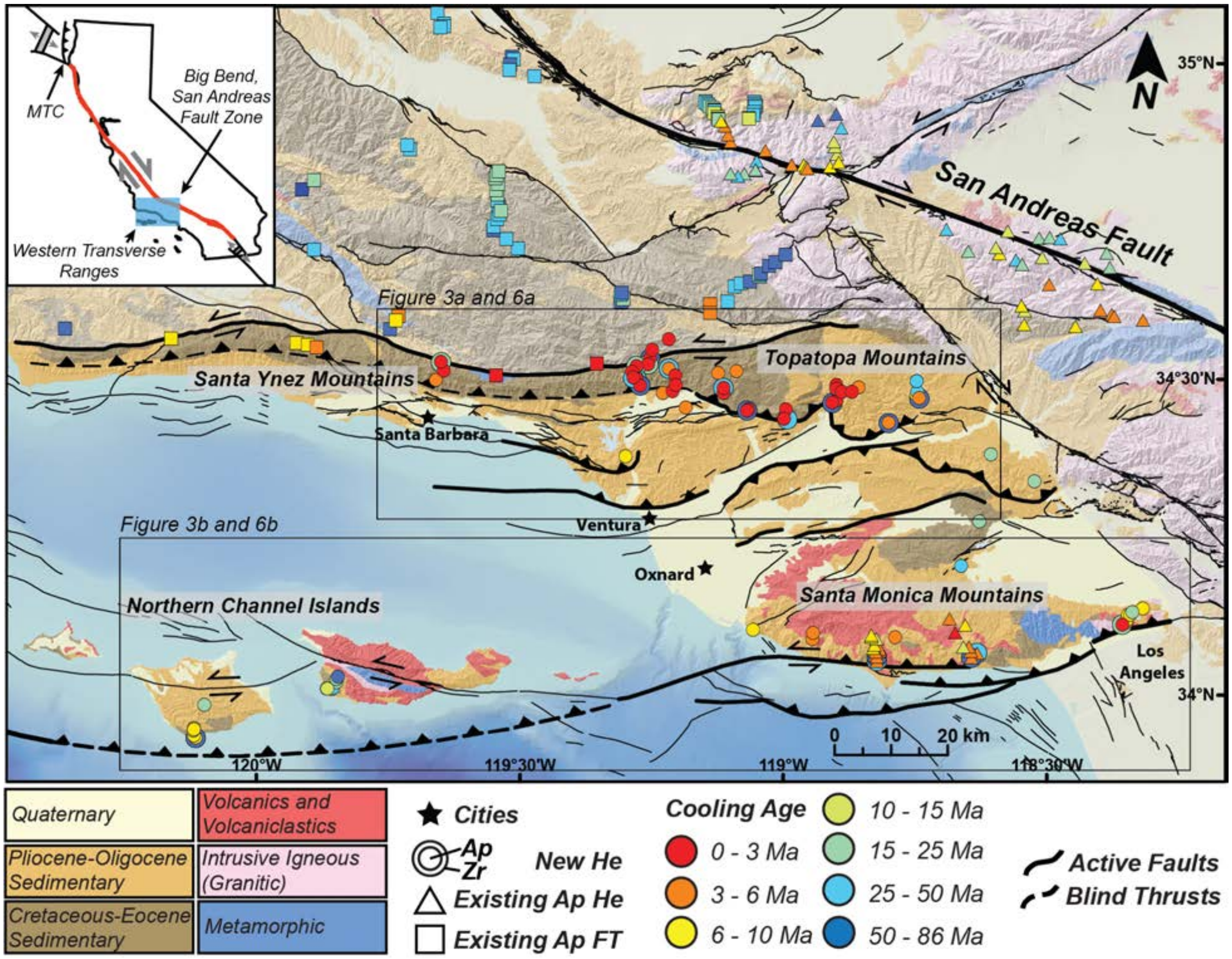

Figure 4.1: Simplified geology and structure of the Western Transverse Ranges (WTR) with sample locations. New apatite (U-Th-Sm)/He samples are shown by small circles with a concentric larger circle where paired with zircon (U-Th)/He ages. Previously published AHe are shown by small rectangles (Buscher et al., 2007; Niemi et al., 2013; Niemi & Clark, 2018), and previously published apatite fission track (AFT) are shown by small squares (White, 1992; Niemi et al., 2013).

off of our main transects with respect to published thermochronometric ages (Buscher & Spotila, 2007; Niemi et al., 2013; White, 1992) from the broader region around the Big Bend in the San Andreas Fault to identify spatial trends in the localization of post-Miocene rapid exhumation.

4.3 Geologic Background

The Western Transverse Ranges (WTR) have experienced a complex history of extension, vertical-axis rotation, and shortening (Atwater, 1998). Forearc strata within the WTR were deposited on the margin of the North American plate above the subducting Farallon Plate in Cretaceous through Oligocene time, and the WTR were subsequently torn from the continent following complete subduction of the Farallon Plate (Atwater, 1998; Crowell, 1979). The WTR underwent over 90° of clockwise vertical-axis rotation within the new diffuse transform margin between the Pacific and North American plates in Miocene time, and syn-rotation extension created deep, localized normal fault-bounded basins that filled with siliciclastic and volcaniclastic sedimentary strata (Atwater, 1998; Hornafius et al., 1986). The WTR are typically thought to have transitioned from extension to shortening following development of the Big Bend restraining bend in the San Andreas Fault at ~5 Ma (Crowell, 1979), but the timing of initiation of the principal reverse structures with the greatest structural relief remains unconstrained. Without dense, high-resolution data from the principal structures, the mechanistic relationship between the WTR and the San Andreas Fault zone from Miocene-time to present remains unresolved.

4.3.1 Southern San Andreas Fault and the Big Bend

The San Andreas Fault system is the continental transform boundary between the Pacific and North American plates throughout much of California (Figures 4.1 and 4.2). Although the central San Andreas fault has largely remained in its current configuration since middle-Miocene time (Crowell, 1979; Graham et al., 1989), the southern section of the San Andreas Fault developed more recently at ~5 Ma (Crowell, 1982) (Figure 4.2). From about 12 to 5 Ma, the San Gabriel Fault linked directly with the San Andreas Fault to form the main plate boundary structure (Crowell, 1979; Ehlig et al., 1975). As slip progressed, an 11,000 m thick section of breccia, conglomerates, sandstone, and mudstone, collectively the ‘Violin Breccia,’ was deposited in a narrow basin directly above the fault zone (Crowell, 1982; Link & Osborne, 1978). The deposition of the Hungry Valley formation overtop both the Violin Breccia and the fault zone at ~5 Ma is interpreted to reflect the cessation of slip on the San Gabriel Fault and the abandonment of this structure as the principal trace of the North American-Pacific Plate boundary (Crowell, 1982; Link, 1982; Link & Osborne, 1978). The new southern San Andreas Fault formed to the east of the San Gabriel Fault, and connected with the central section of the San Andreas Fault to the north, creating the ~160 km restraining bend (i.e. the Big Bend) in the fault (Crowell, 1979) (Figure 4.2). Development of this structure is typically thought to have initiated regional shortening across the WTR, causing normal faults that were active within a transtensional stress field during Miocene time to re-activate as high-angle reverse faults in

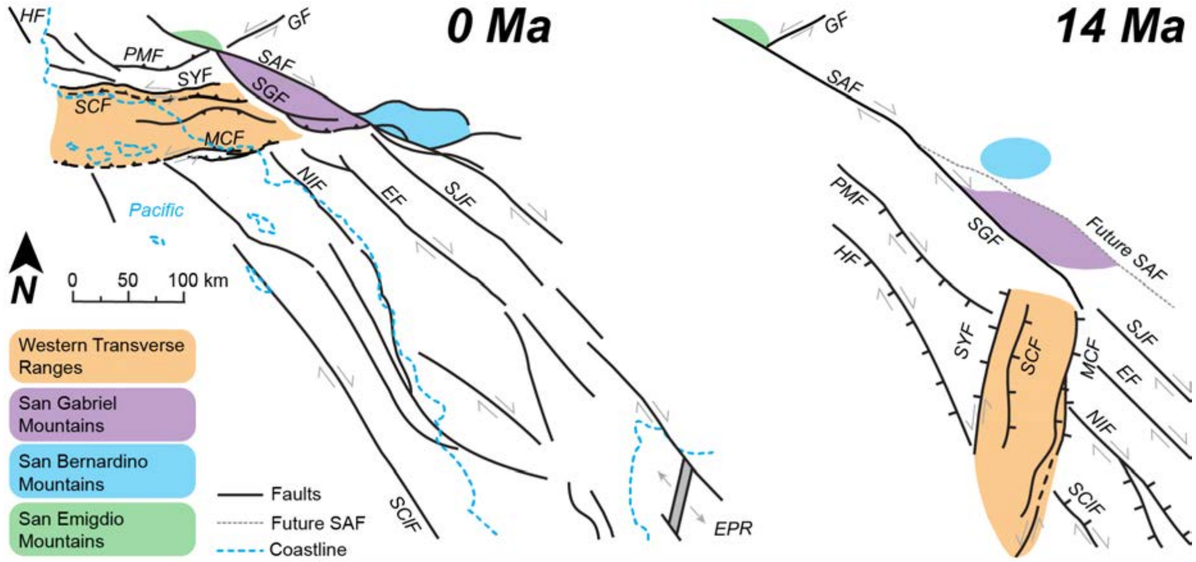

Figure 4.2: Present active faults in coastal southern California, USA, and Baja, Mexico (left) showing the locations of principal mountain ranges within the broader Transverse Ranges, including the San Gabriel Mountains, San Bernardino Mountains, San Emigdio Mountains, and the collective Western Transverse Ranges. The Western Transverse Ranges has undergone over 90° of clockwise rotation and translated northwest with the Pacific Plate since Middle-Miocene time (right) (Luyendyk, 1991; Nicholson et al., 1994). Prior to 5 Ma, the San Gabriel Fault was the principal plate boundary structure. Abandonment of this structure and development of the new southern San Andreas Fault to the east of the San Gabriel Mountains gave rise to the Big Bend restraining bend in the San Andreas Fault. EF–Elsinore Fault; EPR–East Pacific Rise; GF–Garlock Fault; HF–Hosgri Fault; MCF–Malibu Coast Fault; NIF–Newport Inglewood Fault; PMF–Pine Mountain Fault; SAF–San Andreas Fault; SCF–San Cayetano Fault; SClF–San Clemente Fault; SGF–San Gabriel Fault; SJF–San Jacinto Fault; SYF–Santa Ynez Fault.

Pliocene time (Dolan et al., 1995; Hornafius et al., 1986; Huftile & Yeats, 1996; Wright, 1991). This transpressional stress state persists to the present time (Marshall et al., 2013, 2017).

4.3.2 Sedimentology and Rotation of the Western Transverse Ranges

The Western Transverse Ranges are predominantly composed of a ~13 km thick section of late-Mesozoic through Cenozoic clastic sedimentary rocks and Miocene volcanic and volcaniclastic rocks that overlie continental plutonic and metamorphic basement in the east (locally exposed in the eastern Santa Monica Mountains), and oceanic ophiolitic-Franciscan basement complex in the west (exposed on Santa Cruz Island and the central Santa Ynez Mountains) (Dibblee, 1982; Namson & Davis, 1988). During Cretaceous and early Cenozoic time, the WTR accumulated sediments derived from the continent in the forearc above the subducting Farallon Plate (Atwater, 1998). Shallow-marine to terrestrial sandstones and conglomerates were deposited in Oligocene time as the Pacific Plate first made contact with the North American Plate and the boundary transitioned from subduction to predominantly transform (Crowell, 1979). During Miocene time, thick sections of marine siliceous mudstones, marine sandstones, and volcaniclastic rocks locally accumulated in extensional basins as the region underwent rotation and left-lateral shearing in a predominantly transtensional tectonic regime (Atwater, 1998; Namson & Davis, 1988; Nicholson et al., 1994; Wright, 1991).

Sedimentation across the WTR in Middle-Miocene time was associated with vertical-axis rotation of the region (Luyendyk, 1991; Sorensen, 1985). The WTR has undergone over 90° of clockwise rotation since ~15 Ma, as indicated by both geologic evidence (Crouch, 1979; Sorensen, 1985) and paleomagnetic data (Hornafius et al., 1986; Kamerling & Luyendyk, 1979, 1985; Luyendyk, 1991) (Figure 4.2). The WTR are thought to have rotated as a coherent block within a diffuse transform margin between the Pacific and North American plates, and are juxtaposed against non-rotated crust to the north and south (Hornafius et al., 1986; Luyendyk, 1991; Nicholson et al., 1994). A number of kinematic models have been proposed for this rotation. The most common mechanism posited invokes rotation along left-lateral strike-strike faults bounding the eastern and western margins of the WTR, with non-rotating blocks to the north and south (Luyendyk et al., 1980) (Figure 4.2). To address space problems in these kinematic models, the width of both the rotating block and the bounding shear zone are thought to have changed through time, with an initial period of extension followed by contraction (Dickinson, 1996; Luyendyk, 1991). Sedimentation in deep, localized basins in Miocene time record this initial phase of extension (Atwater, 1998; Namson & Davis, 1988; Nicholson et al., 1994), but geologic evidence for a subsequent phase of transpressional deformation prior to development of the Big Bend has yet to be documented.

4.3.3 Principal Fault Systems

The Western Transverse Ranges can be broadly divided into two principal fault systems, which parallel one another and accommodate north-south contraction on east-west trending fault systems in the current geometry. Herein, we refer to these two principal fault systems as San Cayetano and Santa Monica-Channel Islands fault systems, respectively.

4.3.3.1 San Cayetano Fault System

The San Cayetano fault system includes the Santa Ynez Fault and San Cayetano Fault, which bound the Santa Ynez and Topatopa Mountains on the northern boundary of the WTR (Figures 4.1 and 4.3a). The main structural feature of the Santa Ynez Mountains is the ~160-km long, east-west striking Santa Ynez anticlinorium, which has a predominantly overturned south limb and is composed of a 5-km thick section of Cretaceous, Eocene, and Oligocene strata

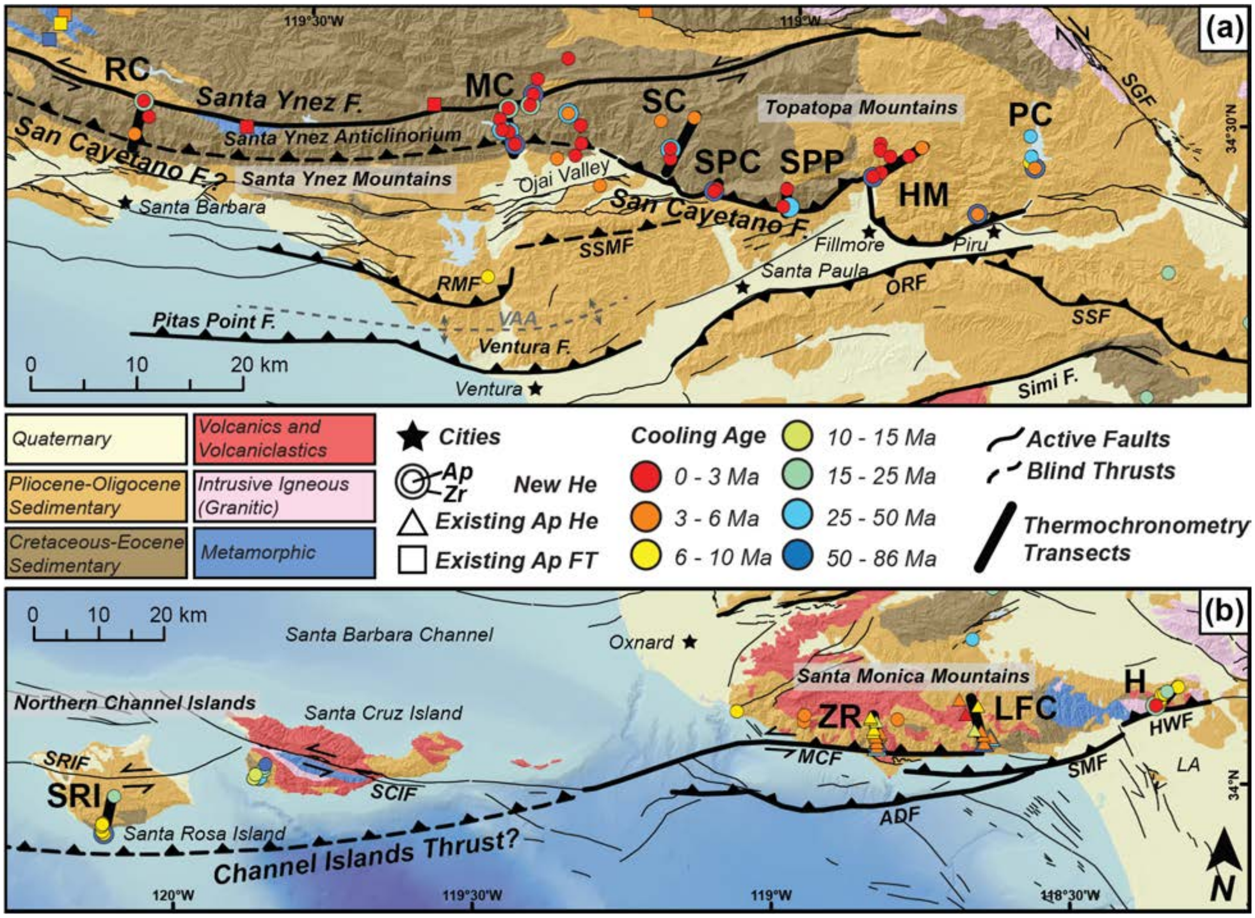

Figure 4.3: Bedrock geology and thermochronometry sample locations along (a) the San Cayetano fault system and (b) the Channel Islands-Santa Monica fault system in the Western Transverse Ranges. Transect labels: RC–Rattlesnake Canyon; MC–Matilija Canyon; SC–Sisar Canyon; SPC–Santa Paula Canyon; SPP–Santa Paula Peak; HM–Hopper Mountain; PC–Piru Canyon; SRI–Santa Rosa Island; ZR–Zuma Ridge (Niemi and Clark, 2018); LFC–Las Flores Canyon (Niemi and Clark, 2018); H–Hollywood. Fault abbreviations: ADF–Anacapa-Dume Fault; HWF–Hollywood Fault; MCF–Malibu Coast Fault; ORF–Oak Ridge Fault; RMF–Red Mountain Fault; SGF–San Gabriel Fault; SMF–Santa Monica Fault; SCIF–Santa Cruz Island Fault; SRIF–Santa Rosa Island Fault; SSF–Santa Susana Fault; SSMF–South Sulphur Mountain Fault; VAA–Ventura Avenue Anticline. F–Fault.

(Dibblee, 1982). Although the Santa Ynez Fault bounds the range to the north, late-Quaternary motion on this structure is predominantly left-lateral strike-slip (Darrow & Sylvester, 1984), and the fault is considered too far north of the anticlinorium to have produced this structure (Levy et al., 2019). It is instead argued that a blind extension of the San Cayetano Fault west of where surface displacement terminates in the Ojai Valley may lie beneath the Santa Ynez Mountains and be responsible for most of the surface uplift and folding of the anticlinorium (Figure 4.3a) (Levy et al., 2019; Namson & Davis, 1988). The south-verging San Cayetano Fault becomes emergent in the easternmost Santa Ynez Mountains, where it cuts the south limb of the anticlinorium in a structurally complex series of plunging folds that form the boundary between the Santa Ynez and Topatopa Mountains (Rockwell, 1988). To the east, the Topatopa Mountains are largely composed of the same Eocene through Miocene strata as the Santa Ynez Mountains, but here these units generally strike north-south and dip gently off to the east (Figure 4.3a) (Dibblee, 1990b, 1990a, 1991c). The emergent portion of the San Cayetano Fault juxtaposes Eocene strata in the hanging wall against Quaternary sediments in the footwall with as much as 9 km of stratigraphic separation (Rockwell, 1988).

Recent work on the San Cayetano fault system suggests that these structures and associated folds have evolved as a classic forward-propagating fold and thrust belt (Hubbard et al., 2014; Levy et al., 2019). The blind portion of the San Cayetano Fault beneath the Santa Ynez Mountains is likely no longer active as deformation stepped southward beginning around ~1 Ma (Yerkes & Lee, 1987), first to the Red Mountain and South Sulphur Mountain faults, and most recently to the Ventura-Pitas Point fault system (Figure 4.3a) (Hubbard et al., 2014; Levy et al., 2019; Perea et al., 2017). These structures likely converge onto a mid-crustal decollement at depth, which has been interpreted to be a south-verging structure (Levy et al., 2019; Rockwell, 1983). Rupture of this thrust ramp may be responsible for the large (up to ~10 m) co-seismic surface uplift and fault displacements documented along the Ventura-Pitas Point fault system (Hubbard et al., 2014; Hughes et al., 2018; Levy et al., 2019; McAuliffe et al., 2015; Rockwell et al., 2016).

4.3.3.2 Santa Monica-Channel Islands Fault System

On the southern boundary of the WTR, the Santa Monica-Channel Islands fault system includes a series of south-verging reverse to left-lateral strike-slip faults (Figure 4.3b) (Davis & Namson, 1994; Dolan et al., 1997, 2000; Dolan & Pratt, 1997; Seeber & Sorlien, 2000; Shaw & Suppe, 1994). The Santa Monica Mountains and northern Channel Islands have been exhumed in the hanging wall of these structures and are generally composed of Cretaceous through Miocene marine sedimentary rocks and Miocene volcaniclastic units. The oldest rocks are exposed at the eastern end of the Santa Monica Mountains, where granitic basement and Jurassic metamorphic rocks (the Santa Monica Slate) are exposed in the hanging wall of the Santa Monica and Hollywood faults (Dibblee, 1991b, 1991a), and on Santa Cruz Island, where Jurassic-age schist is exposed south of the Santa Cruz Island Fault (Hill, 1976). The Paleocene through late-Miocene strata generally dip gently to the north and are continuous along-strike for ~220 km from San Miguel Island in the west through the central Santa Monica Mountains in the east. The northward dip of the Paleocene through late-Miocene strata is likely a consequence of rotation in the hanging walls of the underlying north-dipping thrusts (Davis & Namson, 1994; Seeber & Sorlien, 2000; Shaw & Suppe, 1994; Sorlien et al., 2006). Progressive northward-tilting of the hanging walls of the north-dipping thrusts during Pliocene time suggests that these structures are listric (Pinter et al., 2001; Seeber & Sorlien, 2000).

4.4 Low-Temperature Thermochronometry Methods

Fault initiation and fault slip rates are commonly interpreted from low-temperature thermochronometry data. Ages from low-temperature thermochronometers are sensitive to tectonic and geomorphic processes affecting the upper few kilometers of the crust, and as such, are ideal for constraining the history of relatively young, brittle structures (Ehlers, 2005). Apatite (U-Th-Sm)/He ages (AHe) represent the time since a sample cooled below ~40-80°C, depending on radiation damage, grain size, and cooling rate, which equates to 2-4 km depth for typical geothermal gradients (Farley, 2002; Flowers, et al. 2009). Zircon (U-Th)/He (ZHe) ages record cooling below ~180-200°C, or depths of 5-8 km (Farley, 2002; Reiners et al., 2002). Here, samples were collected on vertical transects with respect to elevation and depth beneath a stratigraphic horizon, and resultant gradients in age versus depth represent exhumation rates averaged over several million years (Farley, 2002). We targeted multiple vertical and stratigraphic transects for sampling along-strike of the principal fault zones (Figure 4.3). Collection of thermochronometry data from sedimentary rocks requires particular attention to the thermal history of individual mineral grains within the rock. Detrital grains commonly record an older thermal history related to the sedimentary source terrain, unless burial during sedimentation reaches a high enough temperature to reset the thermochronometer. Cooling ages that are younger than the depositional age of the sampled rock are assumed to be reset, and thus to record a thermal event related to the exhumation of the sedimentary rock. Conversely, cooling ages older than the depositional age of a sedimentary rock are inferred to be inherited from the source terrane from which the sedimentary rock was derived (Lock & Willett, 2008).

4.4.1 Apatite and Zircon (U-Th-[Sm])/He Methods

Samples were processed using standard methods to isolate apatite and zircon (Appendix C). Individual mineral grains were hand-selected under a high-powered binocular microscope to screen for clarity, crystal morphology, and minimal inclusions of other potentially radiogenic minerals. All grains analyzed are >80 μm in both length and width. Helium outgassing was conducted on an Alphachron Helium Instrument at the University of Michigan following the procedures in Niemi & Clark (2018), and concentrations of U, Th, and Sm (apatite only) were measured using a Thermo Scientific Element 2 ICP-MS at the University of Arizona following the procedures in Reiners & Nicolescu (2006). Mean ages reported here are based on 3-10 individual replicate analyses for each sample. Individual grains were excluded from calculation of mean ages and thermal models following the criteria of Niemi & Clark (2018) (Appendix C).

4.4.2 Inverse Thermal Modelling Approach

We develop thermal histories using QTQt (Gallagher, 2012; Macintosh version 64R5.7.0), which inverts thermochronometry age data from multiple samples on vertical profiles simultaneously. Uncorrected grain ages, grain sizes, and concentrations of He, U, Th, and Sm (AHe only) were entered into QTQt for each apatite and zircon grain (Appendix C). Models were run with a burn-in of 30,000 iterations and then sampled over 80,000 iterations with a thinning of 1. Grain age error resampling using MCMC (Markov Chain Monte Carlo) was enabled to account for observed differences between analytical uncertainties in individual grain ages and reproducibility of ages (e.g. McDowell et al., 2005). Due to predominantly young cooling ages, no radiation damage model was used for apatite samples, however, the Guenthner et al. (2013) radiation model was implemented for all zircon grains.

Thermal models were constrained by stratigraphic data and higher temperature thermochronometry. Typically, models were constrained to a time and temperature range of 0 to 110 Ma and 0 to 300°C, respectively. Depositional age constraints of samples from sedimentary rocks were inferred from stratigraphic ages on published geologic maps and used as depositional age constraints in the thermal models (Table 4.1; Dibblee, 1985, 1987b, 1987a, 1990b, 1990a, 1991b, 1991a; Dibblee et al., 1998; Dibblee & Ehrenspeck, 1986, 1997). A crystallization age for the two samples collected from the pluton at the base of the Hollywood transect is constrained by a hornblende K/Ar age of 105 ± 3.2 Ma (Miller & Morton, 1980). Fission track length and count data from a single apatite sample (WG2-90) from White (1992) was included in the Matilija Canyon transect thermal model. WG2-90 track length and count data were included in the QTQt input file for sample 17-OJ-07, which was collected from the same outcrop.

For each thermal model, the geothermal gradient was set to the range 30 ± 5 °C. This range is consistent with modern geothermal gradients measured in boreholes within the WTR (Bostick et al., 1978; Nathenson Marianne, 1987), as well as maximum paleo-geothermal gradients inferred from vitrinite reflectance data from Miocene through Pliocene sedimentary rocks in the Ventura Basin (Bostick et al., 1978) and the Cretaceous through Eocene section in the Santa Ynez Mountains (Helmold & van de Kamp, 1984). The agreement between modern and paleo-geothermal data suggests that the Cenozoic section in the WTR has not been subject to a higher geothermal gradient than is measured today, so we assume that the modern geothermal gradient is representative of the geothermal gradient during the last few million years. We define a present-day surface temperature of 12 ± 5 °C in each thermal model, and we assume that all samples were at the surface (5 ± 5 °C) at the time of deposition (Niemi & Clark, 2018). The present-day temperature difference between the highest and lowest samples on each transect was set to a typical atmospheric lapse rate of 6 ± 2 °C/km (Stone & Carlson, 1979).

The spatial relationship of individual samples within in the thermal field through which they cooled can be used in a model to derive exhumation rates from cooling rates. Typically, elevation or stratigraphic depth are used. Here, we defined vertical separation of individual samples in thermal models using stratigraphic separation between samples as derived from cross sections constructed from published geologic maps (Figures C.1-C.4; Dibblee, 1985, 1987, 1991a; Dibblee et al., 1998; Dibblee & Ehrenspeck, 1986). Where the stratigraphic separation was unclear or minimal, samples were modeled with vertical separation defined by present-day elevations above sea level (Figure 4.4).

4.5 Apatite and Zircon Age Data

New helium thermochronometry data are presented for seven transects in the Santa Ynez Mountains and Topatopa Mountains on the San Cayetano fault system, and two transects on the Santa Monica-Channel Islands fault system (Figures 4.1 and 4.3, Tables 4.1 and 4.2). Sixty-seven apatite ages were produced, for which 16 samples also have ZHe data. Age and thermal modelling results from two transects in the central Santa Monica Mountains (Niemi & Clark, 2018) are also interpreted in a regional context here. All samples were collected from the hanging walls of reverse faults that bound the principal ranges. Additional samples were collected off the main transects to identify the spatial distribution of young cooling ages (Figures 4.1 and 4.3, Table 4.2).

Pliocene to early Quaternary AHe ages from samples collected from Oligocene – Cretaceous sedimentary strata indicate that most samples are thermally reset and record recent exhumation on fault bounded ranges (Table 4.1). Reset AHe ages from the San Cayetano fault system transects range from 1.3 – 5.9 Ma, and AHe ages from the Santa Monica-Channel Islands fault system transects range from 2.6 – 8.6 Ma. Notably however, AHe samples are reset only in Oligocene and older samples (Tables 4.1 and 4.2). Samples from Miocene strata yield variable

Table 4.1: Thermochronometry data used in inverse thermal modelling. We exclude grains with uranium concentrations under 5 ppm from thermal models and calculation of mean ages. Outliers were identified using the Q-test at the 90% confidence interval. We consider samples with a standard error greater than 1.0 Ma that is also greater than 20 percent of the mean age to have low reproducibility, and report ranges of individual grain ages instead of mean ages. We also report ranges of individual grain ages instead of mean ages for samples with grain ages that are older than the depositional age of the sedimentary rock from which they were collected as these ages are likely inherited and do not reflect recent cooling of the sample.

Sample Name	Longitude	Latitude	Elevation	Modelled Stratigraphic Position	Geologic Formation	Age of Formation	Mean Apatite He Age	Mean Zircon He Age
	(degrees)	(degrees)	(m)	(m)			(Ma)	(Ma)
Rattlesnake Canyon Transect (RC)								
18-SBRC-03	-119.6805	34.4745	763	1222	Cozy Dell Shale	Late-Eocene	3.8 ± 0.3	
18-SBRC-05	-119.6660	34.4892	1113	641	Juncal	Early- to Middle-Eocene	3.0 ± 0.1	
18-SBRC-07	-119.6715	34.5025	693	35	Unnamed Marine	Cretaceous	2.0 ± 0.1	15.3 ± 0.6
Matilija Canyon Transect (MC)								
16-OJ-01	-119.2897	34.4737	280	2428	Coldwater Sandstone	Late-Eocene	2.9 ± 0.3	52.0 - 71.4 #
16-OJ-02	-119.3033	34.4855	315	1493	Matilija Sandstone	Middle- to Late-Eocene	2.0 ± 0.03	34.3 ± 3.8
17-OJ-06	-119.2753	34.5072	540	428	Unnamed Marine	Cretaceous	1.6 ± 0.2	10.3 - 36.3 **
17-OJ-07	-119.2974	34.5040	418	901	Juncal	Early- to Middle-Eocene	1.95 ± 0.53	17.7 ± 3.1
17-OJ-08	-119.3058	34.4946	368	1072	Juncal	Early- to Middle-Eocene	1.5 - 2.1 ***	
17-OJ-09	-119.2964	34.4839	282	1892	Cozy Dell Shale	Late-Eocene	2.0 ± 0.1	35.3 ± 0.7
Sisar Canyon Transect (SC)								
18-OSC-03	-119.1298	34.4641	723		Matilija Sandstone	Middle- to Late-Eocene	2.1 ± 0.1	
18-OSC-05	-119.1302	34.4725	1085		Juncal	Early- to Middle-Eocene	2.7 ± 0.2	11.8 - 40.5 *
18-OSC-07	-119.1059	34.4993	1928		Juncal	Early- to Middle-Eocene	3.3 ± 0.2	
18-OSC-10	-119.1405	34.4959	1606		Matilija Sandstone	Middle- to Late-Eocene	3.4 ± 0.02	
Santa Paula Canyon (SPC)								
16-SP-03	-119.0843	34.4375	342		Coldwater Sandstone	Late-Eocene	2.1 ± 0.1	56.3 ± 8.8
Santa Paula Peak (SPP)								
18-SPP-02	-119.0134	34.4254	760		Matilija Sandstone	Middle- to Late-Eocene	1.3 ± 0.2	
18-SPP-03	-119.0097	34.4403	1512		Matilija Sandstone	Middle- to Late-Eocene	2.7 ± 0.3	
18-SPP-06	-119.0068	34.4248	936		Matilija Sandstone	Middle- to Late-Eocene		50.0 ± 7.8
Hopper Mountain Transect (HM)								
16-FM-01	-118.9218	34.4522	264		Sespe	Oligocene	1.7 ± 0.1	53.2 - 72.0 #
17-FC-01	-118.9133	34.4560	353		Vaqueros Sandstone	Oligocene to Early-Miocene	1.6 ± 0.2	
17-FC-02	-118.9148	34.4804	756		Sespe	Oligocene	1.9 ± 0.4	
17-FC-03	-118.9149	34.4750	671		Sespe	Oligocene	1.7 ± 0.1	
17-FC-04	-118.9042	34.4695	552		Vaqueros Sandstone	Oligocene to Early-Miocene	1.8 ± 0.2	
18-FC-01	-118.8722	34.4778	1263		Monterey	Middle- to Late-Miocene	3.3 ± 0.3	
18-FC-02	-118.8849	34.4702	1142		Monterey	Middle- to Late-Miocene	1.9 ± 0.2	
Santa Rosa Island Transect (SRI)								
18-SRI-05	-120.1220	33.9123	249	874	Glendora Volcanics	Early-Miocene	8.6 ± 1.3	
18-SRI-06	-120.1188	33.8975	160	283	South Point Sandstone	Middle-Eocene	6.4 ± 0.1	51.3 - 85.0 #
18-SRI-07	-120.1214	33.9005	163	397	Sespe	Oligocene	8.4 ± 0.9	
18-SRI-10	-120.1217	33.9103	247	647	Sespe	Oligocene	7.6 ± 0.5	
Hollywood Transect (H)								
16-NC-01	-118.3612	34.1083	176	1	Granitic Rocks	Cretaceous	3.0 ± 0.1	22.1 ± 1.5
17-HW-01	-118.3510	34.1236	292	1755	Middle Topanga	Middle-Miocene	7.1 ± 0.8 [a]	
17-HW-02	-118.3471	34.1246	289	1980	Upper Topanga	Middle-Miocene	8.5 - 8.7 *** [a]	
17-HW-03	-118.3533	34.1127	357	855	Granitic Rocks	Cretaceous	4.6 ± 0.2	
17-HW-04	-118.3537	34.1157	378	1020	Unnamed Strata	Cretaceous	8.6 ± 1.3	
17-HW-06	-118.3232	34.1346	511	2476	Upper Topanga	Middle-Miocene	8.7 ± 1.6 [a]	

Mean cooling age is older than the depositional age of the sedimentary rock. Range of grain ages reported instead of mean age. Grains not used in thermal modelling.

* Standard error is >20% of mean age, and two of four grain ages are the same as the depositional age of the sedimentary rock. Range of grain ages reported instead of mean age. Grains not used in thermal modelling.

** Standard error is >20% of mean age. Range of grain ages reported instead of mean age.

*** Less than three grains analyzed or remaining after rejecting outliers and low-U grains. Range of grain ages reported instead of mean age.

[a] Mean cooling age is within the depositional age of the sampled strata. Not used in inverse modeling, but predicted cooling histories and ages are included.

AHe cooling ages, with individual grain ages ranging from 1.4 – 79 Ma. Five Miocene samples yield replicate ages with poor grain reproducibility, and eight Miocene samples yield cooling ages that are older than the depositional age of the sampled strata, suggesting that Miocene and younger strata were not buried deeply enough to fully reset the apatite helium thermochronometer. However, these non-reset ages provide an upper limit on the magnitude of

Table 4.2: Thermochronometry data not used in inverse thermal modelling. Thermochronometry data assessment and rejection criteria is identical to Table 4.1.

Sample Name	Longitude	Latitude	Elevation	Geologic Formation	Age of Formation	Mean Apatite He Age	Mean Zircon He Age
	(degrees)	(degrees)	(m)			(Ma)	(Ma)
Matilija Canyon							
17-OJ-05	-119.2722	34.5166	586	Coldwater Sandstone	Late-Eocene	2.7 ± 0.3	49.4 - 62.9 # **
Gridley Canyon							
17-GC-02	-119.2357	34.5008	1253	Juncal	Early- to Middle-Eocene	3.3 ± 0.1	26.3 ± 3.5
17-GC-05	-119.2227	34.4908	763	Juncal	Early- to Middle-Eocene	2.8 ± 0.2	
17-GC-07	-119.2215	34.4757	482	Cozy Dell Shale	Late-Eocene	2.4 ± 0.3	
17-GC-08	-119.2276	34.4652	309	Coldwater Sandstone	Late-Eocene	2.6 ± 0.2	
17-GC-09	-119.2459	34.4621	295	Sespe	Oligocene	3.6 ± 0.6	
Ojai Valley							
17-OJ-01	-119.2017	34.4398	368	Sespe	Oligocene	5.0 ± 0.8	
17-OJ-03	-119.2681	34.5293	801	Cozy Dell Shale	Late-Eocene	2.3 ± 0.2	
17-OJ-04	-119.2370	34.5473	1094	Matilija Sandstone	Middle- to Late-Eocene	2.7 ± 0.5	
17-VC-01	-119.3145	34.3604	79	Sespe	Oligocene	2.4 - 9.2 **	
Santa Paula Canyon							
16-SP-01	-119.0821	34.4393	356	Cozy Dell Shale	Late-Eocene	2.3 ± 0.2	
Piru Canyon							
16-PC-01	-118.7612	34.4670	344	Monterey	Middle- to Late-Miocene	4.8 - 24.3 **	
16-PC-02	-118.8137	34.4223	333	Monterey	Middle- to Late-Miocene	5.9 ± 1.0	75.2 - 89.4 #
16-PC-03	-118.7597	34.4715	346	Monterey	Middle- to Late-Miocene	20.5 - 48.7 # **	
16-PC-04	-118.7557	34.4622	365	Monterey	Middle- to Late-Miocene	2.8 - 27.0 **	63.7 - 86.3 #
16-PC-06	-118.7607	34.4889	341	Monterey	Middle- to Late-Miocene	- ****	
Santa Susana Mountains							
14-Sy-01	-118.5328	34.3334	760	Towsley	Late-Miocene	14.4 - 35.3 # ***	
14-Sy-02	-118.6173	34.3746	525	Towsley	Late-Miocene	14.0 - 24.8 # ***	
Simi Hills							
17-ESC-01b	-118.6701	34.1972	354	Detrital Sediments of Lindero Canyon	Middle Miocene	22.3 - 43.7 #	
17-RP-01	-118.6372	34.2686	501	Chatsworth	Late-Cretaceous	17.4 ± 1.0	
Santa Rosa Island							
18-SRI-02	-120.1036	33.9500	467	Rincon Formation	Early-Miocene	12.0 - 34.3 #	
18-SRI-09	-120.1229	33.9081	297	South Point Sandstone	Middle-Eocene	7.6 ± 0.4	
Santa Cruz Island							
18-PS-01	-119.8720	33.9804	7	Beachers Bay	Middle-Miocene	21.9 - 31.9 #	
18-PS-03	-119.8626	33.9802	15	Vaqueros	Early-Miocene	7.0 ± 0.6	
18-PS-04	-119.8604	33.9822	23	Jolla Viejo	Middle-Eocene	29.5 ± 2.7	
18-PS-05	-119.8539	33.9917	65	Canada	Middle- to Late-Eocene	18.2 ± 2.3	
18-PS-06	-119.8542	33.9966	195	Pozo	Paleocene	22.5 ± 0.4	
18-PS-07	-119.8519	34.0005	288	Rincon	Early-Miocene	10.4 - 79.2 #	
18-PS-08	-119.8710	33.9807	15	San Onofre Breccia	Early-Miocene	14.3 ± 0.9	
Central and Western Santa Monica Mountains							
16-SM-02	-118.7939	34.0830	547	Lower Topanga	Early- to Middle-Miocene	2.2 - 6.3 **	
16-YB-01	-118.9510	34.0777	219	Lower Topanga	Early- to Middle-Miocene	5.2 ± 0.2	
16-YB-02	-118.9501	34.0868	304	Lower Topanga	Early- to Middle-Miocene	4.2 ± 0.8	
17-PMB-01	-119.0642	34.0903	5	Lower Topanga	Early- to Middle-Miocene	6.5 ± 0.4	
Hollywood							
17-HW-09	-118.3425	34.1283	294	Upper Topanga	Middle-Miocene	6.8 - 44.1 # **	
# Mean cooling age is older than the depositional age of the sedimentary rock. Range of grain ages reported instead of mean age.							
** Standard error is >20% of mean age. Range of grain ages reported instead of mean age.							
*** Less than three grains analyzed or remaining after rejecting outliers and low-U grains. Range of grain ages reported instead of mean age.							
**** All but one grain rejected due to <5 ppm U concentration. Mean age not reported							

recent exhumation at the sampled locations, which cannot have exceeded ~2 km, assuming typical geothermal gradients (e.g. Townsend et al., 2020). Non-reset AHe ages were not included in thermal models.

Samples both on and off transects yield mean ZHe cooling ages that range from 15 – 56 Ma. Samples collected from stratigraphic units that are middle-Eocene or older yield reset ZHe cooling ages. However, ZHe cooling ages that are considerably older than AHe cooling ages from the same sample suggests that these samples were variably thermally reset within the ZHe partial retention zone. Samples from stratigraphic units that are late-Eocene and younger yield ZHe cooling ages that are the same as, or older than, the depositional ages of the sedimentary rocks from which they were collected. We infer that these samples were not thermally reset during burial and therefore do not record cooling related to post-depositional exhumation.

4.5.1 Santa Ynez Mountains

We collected samples for AHe and ZHe thermochronometry along Rattlesnake Canyon, north of Santa Barbara, CA, and along Matilija Canyon north of Ojai, CA (Figure 4.3a). These transects are above the blind section of the San Cayetano Fault and within the inferred hanging wall of the near-vertical Santa Ynez Fault. The Rattlesnake Canyon transect includes three samples that span 2,100 meters of stratigraphic separation in Cretaceous through Oligocene sandstones (Dibblee & Ehrenspeck, 1986). AHe ages range from 2.0 to 3.8 Ma, and ZHe analyses from the stratigraphically lowest sample (18-SBRC-07) yield a mean age of 15.3 ± 0.6 Ma (Table 4.1). The Matilija Canyon transect includes six samples that span 3,500 meters of stratigraphic separation in Cretaceous through Oligocene sandstones (Dibblee, 1985, 1987a). AHe ages range from 1.6 to 2.9 Ma, and ZHe analyses on five samples yield mean ages of 17.7 to 35.3 Ma (Table 4.1). A ZHe cooling age from one additional sample (17-OJ-01) exceeds the depositional age of the sampled Oligocene strata. Additionally, White (1992) reported a mean apatite fission track age of 2.0 ± 1.2 Ma (WG2-90) from a sample collected from the same outcrop as 17-OJ-07 (AHe age of 2.0 Ma). The mean age and track lengths of sample WG2-90 were incorporated into the thermal models. AHe and ZHe analyses on both transects demonstrate clear age-stratigraphic relationships, but no age-elevation trend (Table 4.1).

4.5.2 Topatopa Mountains

We collected samples for AHe and ZHe thermochronology along five transects in the Topatopa Mountains, including, from west to east, Sisar Canyon northeast of Ojai, CA, Santa

Paula Canyon and Santa Paula Peak north of Santa Paula, CA, Hopper Mountain north of Fillmore, CA, and Piru Canyon north of Piru, CA (Figure 4.3a). All transects are in the hanging wall of the emergent section of the San Cayetano Fault, and AHe cooling ages from Eocene through lower-Miocene strata range from 2.1 – 3.4 Ma in the western transects, to 1.3 – 3.3 Ma in the eastern transects. ZHe cooling ages from Eocene strata are 27 to 56 Ma, but ZHe cooling ages from Oligocene and Miocene strata are older than depositional ages of the sampled strata. Stratigraphic separation across the San Cayetano Fault decreases from west to east, as does the stratigraphic age of units exposed in the hanging wall (Rockwell, 1988). AHe cooling ages from samples collected from middle-upper Miocene strata along the easternmost transect at Piru are variably reset. For AHe samples that were fully reset on the Piru transect, we were unable to solve for unique time-temperature histories with thermal history modeling due to the lack of stratigraphic or elevation separation between samples. AHe and ZHe data from one sample were used to produce the Santa Paula Canyon thermal model, so no elevation or stratigraphic separation information was incorporated. Cooling ages from the Sisar Canyon, Santa Paula Peak, and Hopper Mountain transects show systematic age-elevation relationships.

4.5.3 Santa Monica Mountains and Northern Channel Islands

Samples were collected along one transect in the easternmost Santa Monica Mountains (Hollywood) (Figure 4.3b). AHe cooling ages from a Cretaceous quartz diorite and nonconformably overlying Cretaceous sandstone at the base of the Hollywood transect range from 2.6 to 8.6 Ma (Table 4.1). ZHe analyses from the lowest sample on the transect yield a mean cooling age of 20.6 Ma (Table 4.1). The Cretaceous sandstone is disconformably overlain by Miocene strata, and AHe cooling ages of 7.1 to 8.7 Ma from three samples collected from Middle-Miocene units are within the depositional age range of the sampled strata. These samples were included in the thermal model for predicted time-temperature histories but were not included in the inverse modeling for the best-fit thermal histories (Figure 4.4). One sample on the Hollywood transect yielded a cooling age older than the depositional age of the sampled strata (Table 4.2).

Samples were collected along two transects in the northern Channel Islands (Figure 4.3b). On Santa Rosa Island, five samples spanning 1000 meters of stratigraphic separation across Eocene through Miocene strata yield AHe ages of 6.4 to 9.6 Ma. A sixth sample from overlying Miocene strata yielded grain ages that exceed the depositional age of the formation. ZHe analyses from the stratigraphically lowest sample yield grain ages ranging from 51 to 85 Ma, which are older than the Middle-Eocene depositional age of the formation. On Santa Cruz Island, AHe cooling ages of seven samples from Paleocene through Miocene sedimentary rocks do not exhibit a systematic age-stratigraphic depth or age-elevation relationships. AHe analyses from one sample (18-PS-03) yield a relatively young cooling age of 7.0 ± 0.6 Ma, which is consistent with cooling ages from Santa Rosa Island (Figure 4.3b, Tables 4.1 and 4.2). However, AHe cooling ages from three other samples are within or older than the depositional ages of the sampled Miocene strata, and AHe ages of three samples from Eocene and Paleocene strata yield variable cooling ages ranging from 18.2 – 29.5 Ma.

Previously published ages from the central Santa Monica mountains were reported by Niemi & Clark (2018) (Figure 4.3b). AHe and ZHe data were collected along Las Flores Canyon and Zuma Ridge spanning 1,600 meters (Las Flores Canyon) and 900 meters (Zuma Ridge) of stratigraphic separation. AHe ages from eight samples on the Las Flores Canyon transect range from 2.3 to 11.5 Ma, and AHe ages of thirteen samples from Zuma Ridge range from 4.5 to 12.6 Ma. AHe ages exhibit both age-stratigraphic depth and age-elevation trends. ZHe ages from three samples on these transects range from 36 to 61 Ma.

4.6 Exhumation Histories from Thermal Models

Thermal history models were produced in QTQt and yield constraints on the timing and rates of cooling of rocks above individual faults. We infer that the thermal histories record burial histories of the sedimentary rocks from which samples were collected, followed by the initiation of exhumation and rates of exhumation averaged over the last several million years. Models generally reveal cooling initiating in late Miocene through Pliocene time and continuing to the present (Figures 4.4, C.4-C.14). We assume that cooling is associated with rock exhumation (erosion) driven by reverse faulting. Full thermal histories are included in Appendix C (Figures C.4 – C.14). Here we focus on the post-depositional exhumation history.

An implicit assumption of the thermal modeling approach is that the current vertical sample separation reflects the paleo-vertical separation as samples passed through the AHe and ZHe partial retention zones (Farley, 2002). In a rapidly evolving structural system like the WTR, or where fault geometry is listric (Seeber & Sorlien, 2000), rotation of structural blocks in the uppermost crust may change the vertical separation of samples between the time the block passed through the helium partial retention zones and its exhumation to the surface (Figure 4.5).

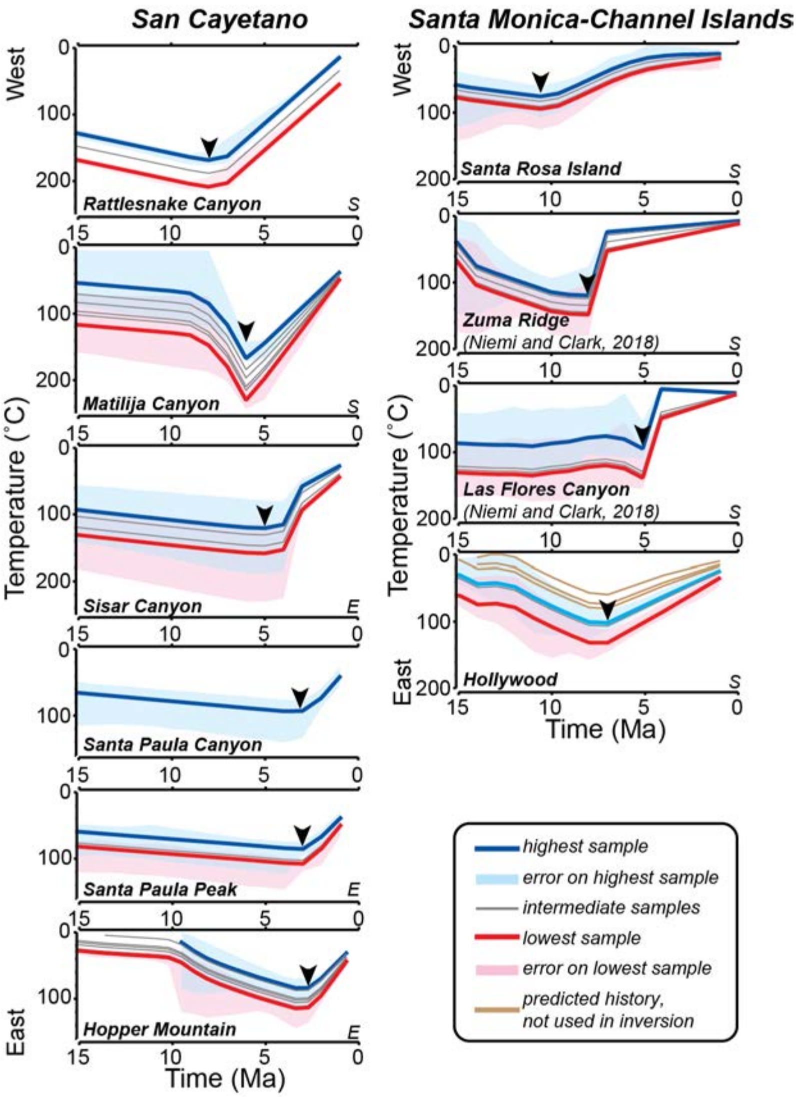

Figure 4.4: Inverse models of best-fit thermal histories for the last 15 Ma. Thermal history models from transects on both the San Cayetano and Santa Monica-Channel Islands fault systems are arranged from west (top) to east (bottom) (see Appendix C for full thermal histories). Black arrows show timing of cooling initiation. Samples were buried between Cretaceous and late Miocene time, and have been exhumed since early Pliocene time from temperatures of 100°C to 220°C. Predicted thermal histories for three samples collected from Miocene strata on the Hollywood are shown, but these samples were not used in the inversion. See Table 4.1 for samples included in each model. S – vertical sample separation defined by stratigraphic separation; E – vertical sample separation defined by elevation.

We observe an inverse relationship between stratigraphic depth and cooling ages on the Rattlesnake Canyon and Matilija Canyon transects despite the near-vertical attitude of the strata today, suggesting that a component of the rotation occurred after the samples passed through the helium partial retention zone. For these transects, we modeled samples using vertical separation defined by both elevation and stratigraphic separation, but we found that for both cases, predicted AHe and ZHe ages poorly fit the observed data (Figures 4.5, C.4-C.8). Samples on

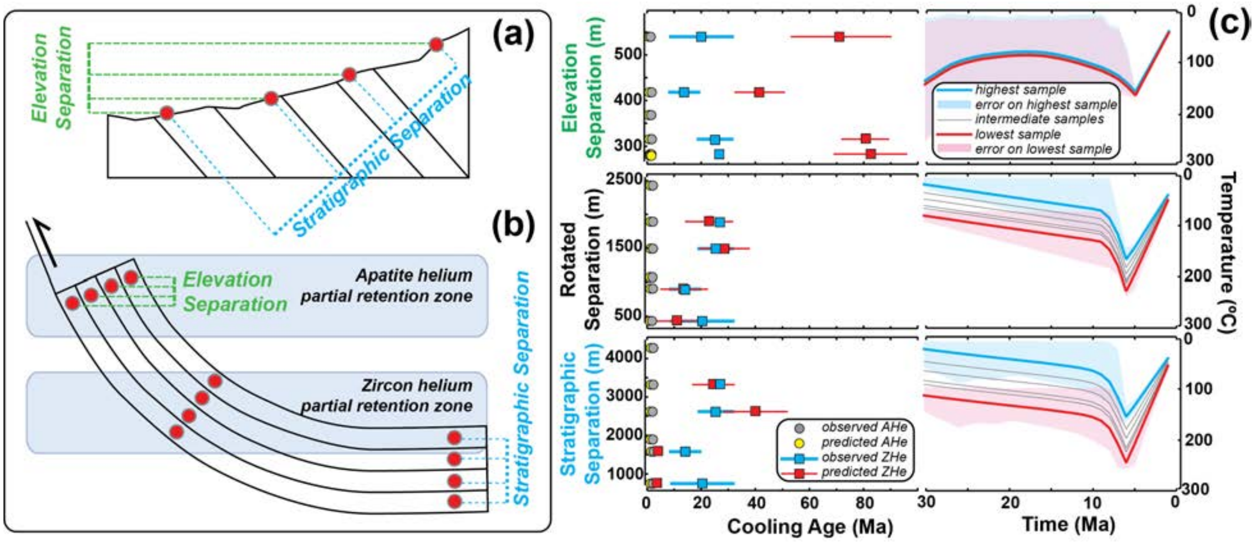

Figure 4.5: Schematic figures and cooling histories demonstrating the effect of changing vertical sample separation on transects. (a) Schematic cross section demonstrating the relative difference in vertical spacing between samples (red dots) on an individual transect depending on whether elevation or stratigraphic separation are used to define the distance between samples. b) Rotation of strata in the hanging wall of a thrust ramp as sampled units pass through the apatite helium and zircon helium partial retention zones. c) Inverse thermal modelling results for the Matilija Canyon transect, with observed and predicted apatite He and zircon He cooling ages (left) and best-fit thermal histories (right). Vertical sample separation was defined using elevation in the upper model, using a 35-degree paleo-dip in the center model, and using stratigraphic separation in the lower model. Note that the highest-elevation sample is the stratigraphically lowest. Error bars are ranges of sampled zircon Helium ages. Ranges of sampled apatite He ages are < 2 Ma.

both transects were collected from a narrow elevation range, so defining the vertical sample separation using stratigraphic separation increases the spacing between samples as compared to elevation separation (Figure 4.5). We find that thermal models from these transects with vertical separation defined by stratigraphic separation underpredict ZHe ages from the lowest samples (Figures 4.5, C.5 and C.7). However, thermal models from these transects produced with vertical separation defined by elevation overpredict ZHe ages (Figure 4.5, C.8). Based on the results of end-member models with vertical sample separation defined using elevation or stratigraphic separation, and the near-vertical attitude of the strata that we sampled, we infer that the strata rotated from horizontal to vertical as they passed through the AHe and ZHe partial retention zones. We assess the orientation of the samples at the time of cooling through the partial retention zones by calculating sample separation for several possible paleo-orientation configurations. We find that reducing vertical sample separation by rotating the stratigraphic sections back 55° from the current near-vertical dip to a paleo-dip of ~35° results in thermal models with predicted AHe and ZHe ages that closely match observed ages (Figure 4.5). Rates of exhumation inferred from thermal models with vertical sample separation defined using the full stratigraphic separation and reduced vertical sample separation defined using the rotated sections differ by less than 10 percent, and the timing of cooling initiation is unchanged. We also note that the modeled ~35° paleo-dip is consistent with typical thrust ramp geometries.

Cooling on the San Cayetano fault system begins at ~8 Ma, as recorded by the Rattlesnake Canyon Transect (Table 4.3, Figure 4.4). At 6 Ma, cooling initiates at Matilija Canyon in the eastern Santa Ynez Mountains, at 5 Ma cooling initiates at Sisar Canyon at the boundary between the Santa Ynez Mountains and Topatopa Mountains, cooling initiates at 4 Ma at Santa Paula Canyon, and cooling initiates at 3 Ma at Santa Paula Peak and Hopper Mountain in the central to eastern Topatopa Mountains (Figure 4.4). Collectively, these data record cooling initiating first on the west end of the San Cayetano fault system and progressing eastward until at least ~3 Ma. Samples collected from the Miocene Modelo Formation at Piru Canyon at the eastern end of the Topatopa Mountains are variably reset for apatite, and therefore do not record a cooling age. However, the 3 Ma timing of exhumation inferred from the thermal models to the west at Hopper Mountain and Santa Paula Peak is consistent with an inferred ~3.2 Ma timing of initiation of the San Cayetano Fault in the easternmost Topatopa Mountains (Levy et al., 2019; Rockwell, 1983). The timing of fault initiation is not constrained directly, but is inferred from microfauna analysis of the Lower Pliocene Pico Formation (Rockwell, 1983).

On the Santa Monica-Channel Islands fault system, the earliest cooling begins at ~10 Ma on Santa Rosa Island (Table 4.3, Figures 4.4 and 4.6). The timing of cooling is consistent with the end of deposition of the Beechers Bay Formation, the youngest sedimentary unit exposed on Santa Rosa Island today, in Middle Miocene time (Dibblee et al., 1998). Cooling initiates at 8 Ma at Zuma Ridge in the central Santa Monica Mountains, and at 5 Ma at Las Flores Canyon, which lies further to the east (Figures 4.4 and 4.6). Collectively, these data suggest cooling and inferred exhumation along the Santa Monica-Channel Islands fault system initiating first in the west and propagated east over ~5 million years (Figure 4.6). However, we acknowledge that the data density here is lower than in the north; sampling was limited by both the Pacific Ocean and the exposure of apatite-bearing sedimentary rocks that experienced sufficient burial to reset the apatite thermochronometer. Thermal history models from the Hollywood transect at the easternmost end of the Santa Monica Mountains imply cooling initiating between 7 and 8 Ma, earlier than cooling observed in the central portion of the range (Figures 4.4 and 4.6). The Santa Rosa Island, Zuma Ridge, and Las Flores Canyon cooling histories each experienced an initial

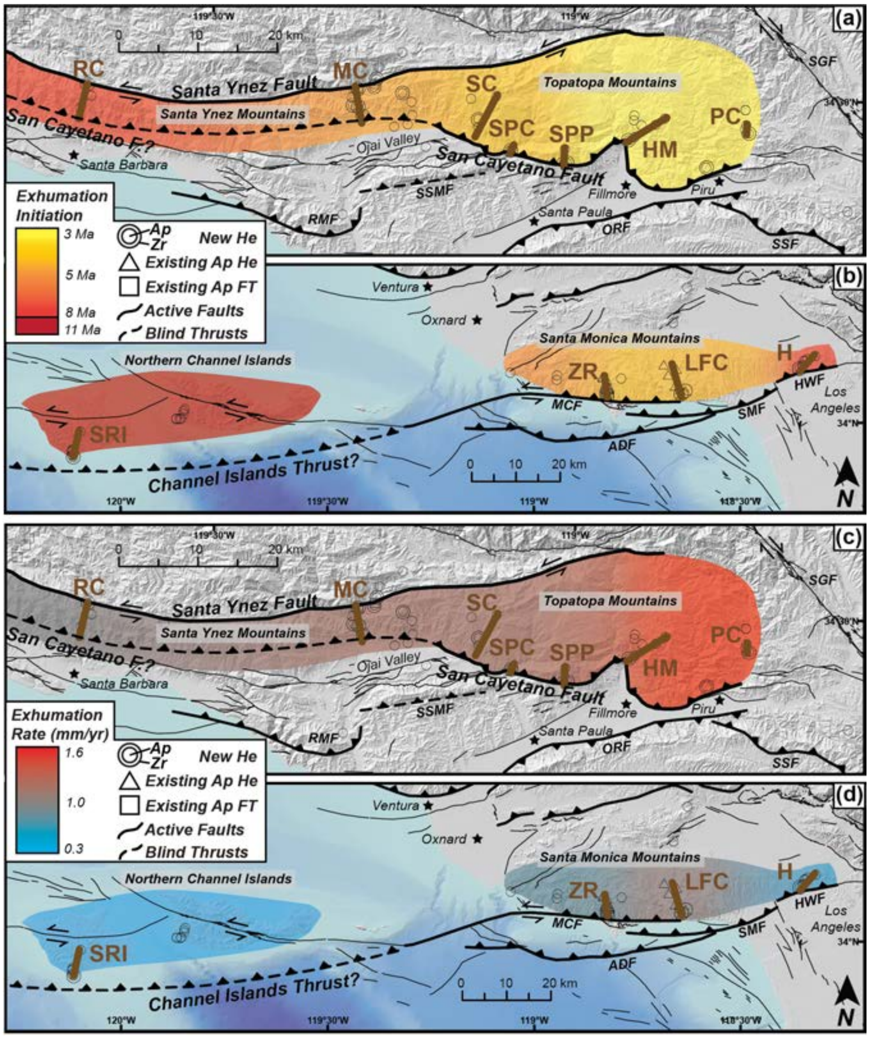

Figure 4.6: Timing of exhumation initiation along the (a) San Cayetano fault system, and (b) Santa Monica-Channel Islands fault system. (c) and (d) show apparent exhumation rates as inferred from the thermal models, assuming a geothermal gradient of 30°C/km. Panels (c) and (d) are the same extent as (a) and (b), respectively. Transect labels: RC–Rattlesnake Canyon; MC–Matilija Canyon; SC–Sisar Canyon; SPC–Santa Paula Canyon; SPP–Santa Paula Peak; HM–Hopper Mountain; PC–Piru Canyon; SRI–Santa Rosa Island; ZR–Zuma Ridge (Niemi & Clark, 2018); LFC–Las Flores Canyon (Niemi & Clark, 2018); H–Hollywood. Fault abbreviations: ADF–Anacapa-Dume Fault; HWF–Hollywood Fault; MCF–Malibu Coast Fault; ORF–Oak Ridge Fault; RMF–Red Mountain Fault; SGF–San Gabriel Fault; SMF–Santa Monica Fault; SSM –South Sulphur Mountain Fault; SSF–Santa Susana Fault.

phase of rapid cooling, followed by an apparent slower rate of cooling that continued until the present (Figure 4.4). However, the apparent decrease in cooling rate occurs at temperatures below the closure temperature of the AHe thermochronometer. The thermal histories are unconstrained at these low temperatures, and it is equally likely that no further cooling occurred after the initial pulse of rapid cooling (Figure 4.4), although marine terraces (Colson, 1996; Shaller & Heron, 2004) and geodetic data (Marshall et al., 2013) indicate Pleistocene to recent fault motion.

Time averaged rates of apparent exhumation (assuming a geothermal gradient of 30 °C/km) are generally higher on the San Cayetano fault system than the Santa Monica-Channel Islands system (Figure 4.6 and Table 4.3). Exhumation rates along the six transects from Rattlesnake Canyon in the west, through Santa Paula Peak to the east range from 0.9 mm/yr to 1.2 mm/yr. The Hopper Mountain transect to the east of Santa Paula Peak records a more rapid exhumation rate of 1.6 mm/yr. On the Santa Monica-Channel Islands fault system, Las Flores Canyon in the center of the range records the highest exhumation rate, at 1.0 mm/yr. Zuma Ridge records a slower exhumation rate of 0.7 mm/yr, and the Hollywood and Santa Rosa Island transects on the margins of the range record slower exhumation rates of 0.5 mm/yr and 0.3 mm/yr, respectively (Table 4.3).

4.7 Discussion

The regional pattern of thermochronometry ages around the Big Bend indicates that shortening strain is localized within the WTR (Figure 4.1; Blythe et al., 2002; Buscher & Spotila, 2007; Spotila et al., 2001; White, 1992). Latest Miocene through Quaternary low-temperature thermochronometric cooling ages throughout the region are generally confined to the WTR; apatite fission track cooling ages to the north of the WTR are early Miocene, Oligocene, and Eocene in age (White, 1992), and are early-Miocene and Oligocene immediately south of the SAF fault near the San Emigdio Mountains (Niemi et al., 2013) (Figure 4.1). AHe cooling ages

Table 4.3: Timing of exhumation initiation and average exhumation rates as inferred from thermal models

Transect	**Deepest Strata Exhumed**	**Timing of Exhumation Initiation**	**Rate of Exhumation**
		(Ma)	**(mm/yr)**
San Cayetano Fault System			
Rattlesnake Canyon	Cretaceous	8.0	0.9
Matilija Canyon	Cretaceous	6.0	1.2
Sisar Canyon	Early- to Middle-Eocene	5.0	1.2
Santa Paula Canyon	Late-Eocene	4.0	1.0
Santa Paula Peak	Middle- to Late-Eocene	3.0	1.2
Hopper Mountain	Oligocene	2.7	1.6
Santa Monica-Channel Islands Fault System			
Santa Rosa Island	Middle-Eocene	10.0	0.3
Zuma Ridge	Paleocene	8.0	0.7
Las Flores Canyon	Upper Cretaceous	5.0	1.0
Hollywood	Cretaceous (pluton)	7.0	0.5

from the northern San Gabriel Mountains generally exceed 10 Ma (Buscher & Spotila, 2007), and widely-distributed middle Miocene through Cretaceous AHe cooling ages in the San Gabriel and San Bernardino Mountains also suggest relatively little recent exhumation (Blythe et al., 2002). Collectively, these datasets demonstrate that cooling ages from ranges bounded by the San Andreas Fault are older than cooling ages from the WTR, despite their proximity to the San Andreas Fault (Figure 4.1).

4.7.1 Initiation and Propagation of Reverse Faulting within the Western Transverse Ranges

It has been previously assumed that the formation of the Big Bend geometry of the San Andreas fault caused regional shortening within the surrounding area (Crowell, 1979, 1982; Link, 1982; Link & Osborne, 1978). From that perspective, we could anticipate that (1) reverse faults would initiate synchronously with the initiation of the Big Bend at ~5 Ma, and (2) that reverse faults would propagate away from the SAF (i.e., east to west). However, our inferred fault histories challenge this assumed relationship, based on both the timing of fault initiation and the propagation directions of the major fault systems.

For both the northern and southern WTR, we observe initial faulting in the west and prior to the formation of the Big Bend at ~5 Ma, with propagation of major fault systems toward the east over several million years. The initiation of rock exhumation beneath the Santa Ynez and Topatopa Mountains starts at ~8 Ma and continues through 3 Ma (Figure 4.6). We suggest that this ~5 million year progression reflects the initiation and linkage of faults within the San Cayetano fault system (e.g. Abbey & Niemi, 2018), likely driven by eastward tip propagation of the San Cayetano Fault that underlies the Santa Ynez Mountains and becomes emergent in the Topatopa Mountains (Levy et al., 2019). This pattern of fault initiation mirrors the gradient in stratigraphic age of the sedimentary rocks exposed in the hanging wall of the fault, where Cretaceous strata are exposed in the west and Plio-Pleistocene sediments are exposed in the east (Dibblee, 1982). Similarly, exhumation initiates in the Santa Monica-Channel Islands fault system in the northern Channel Islands at ~10 Ma, followed by Zuma Ridge in the central Santa Monica Mountains at ~7 Ma, and Las Flores Canyon further to the east at 5 Ma (Niemi & Clark, 2018) (Figure 4.6). The Santa Monica-Channel Islands system is composed of a series of vertical sinistral and north-dipping thrusts that are argued to be part of regional, although segmented, thrust fault system, rather than a single through going fault (Davis & Namson, 1994; Seeber & Sorlien, 2000; Shaw & Suppe, 1994; Sorlien et al., 2006). Our data imply a ~5 million year eastward progression in the initiation of these individual structures, starting with the Channel Islands Thrust (Pinter et al., 2003; Shaw & Suppe, 1994) in the west, to the Malibu Coast Fault and Santa Monica Fault in the central and eastern Santa Monica Mountains (Niemi & Clark, 2018). However, we also acknowledge that the thermal history model of the Hollywood transect data implies that reverse faulting here initiated at ~7 Ma, prior to reverse faulting in the central portion of the Santa Monica Mountains.

Restraining bend tectonism driven by the Big Bend is likely not the dominant cause of fault initiation or shortening within the WTR. The west-to-east propagation of reverse faulting is documented on multiple generations of faults within the WTR; in addition to the San Cayetano and Santa Monica-Channel Islands fault systems, the North-Channel-Pitas Point and Ventura Fault trend similarly demonstrates a west-to-east propagation of reverse faulting and folding (Figure 4.3a; Hughes et al., 2018; Levy et al., 2019; Rockwell et al., 1984; Sorlien & Nicholson, 2015). This structure is considerably younger than the principal fault systems on the boundaries of the WTR block, having likely initiated at ~1 Ma as a forward step in the San Cayetano fold-and-thrust belt system (Levy et al., 2019). The west-to-east propagation direction of multiple fault systems, as well as the early initiation of reverse faulting on the San Cayetano and Santa Monica-Channel Islands fault systems, imply that the initiation and propagation of reverse faulting may be a manifestation of stresses unrelated to the restraining bend (e.g. Woodcock, 1986). Therefore, the current proximity of the WTR to the Big Bend is likely a coincidence, and restoration of slip across the San Andreas Fault places the WTR 300 km further south at 10 Ma, assuming a long-term slip rate of ~30 mm/yr (e.g. Figure 4.2; Crowell, 1979; Sieh & Jahns, 1984). At the time the Big Bend developed at 5 Ma, the WTR were located 150 km south of their current location, likely well beyond the compressive stress field generated by the Big Bend. Although kinematic models of block rotation suggest contraction across the WTR block during the latter stages of rotation from ~10 to ~5 Ma (Dickinson, 1996; Luyendyk, 1991), a geodynamic mechanism to explain strain localization within the WTR has not been proposed previously.

4.7.2 Regional Heterogeneities in Deformation and Rheology

A question raised by the distribution of young thermochronometric ages is why recent (post-Miocene) deformation appears to be localized within the rotated WTR range block, and largely absent outside that block (Figure 4.1; Blythe et al., 2002; Buscher & Spotila, 2007;

Spotila et al., 2001; White, 1992; this study). We hypothesize that large-scale lithologic heterogeneities within the Pacific Plate likely play a role in localizing deformation within the WTR. Although the WTR contain a similar sequence of forearc sedimentary rocks as found in non-rotated lithospheric blocks to the north and south, the complicated history of extension, vertical-axis rotation, and subsequent shortening of the block potentially weakened the underlying deep lithosphere (Figure 4.7 and 4.8; Atwater, 1998; Eymold & Jordan, 2019; Hornafius et al., 1986; Luyendyk, 1991). Deformed forearc rocks of the WTR are also underlain by pervasively sheared, mechanically weak Franciscan Complex rocks (Dibblee, 1982; Namson & Davis, 1988), although there remains uncertainty over whether or not the WTR may also be underlain by oceanic lithosphere (ten Brink et al., 2000; Crouch, 1979; Lekic et al., 2011; Reeves et al., 2015).

The basement rocks of the WTR are juxtaposed against terranes on the Pacific Plate with comparatively greater lithospheric strength (Figure 4.7). The southern California Borderlands region to the south of the WTR consists of a series of generally northwest- to southeast-striking terranes of variable composition (Bohannon & Geist, 1998; ten Brink et al., 2000; Crouch, 1979; Crouch & Suppe, 1993; M. Grove et al., 2008; Reeves et al., 2015) (Figure 4.7). Two of these terranes have relatively high lithosphere-scale strength, including the Nicolas Terrane south of Santa Cruz and Santa Rosa Islands, which consists of more than three km of relatively undeformed Cretaceous through Oligocene forearc strata overlying oceanic crust (Crouch, 1979), and the Peninsular terrane southeast of the Santa Monica Mountains, which consists of relatively undeformed Mesozoic arc rocks overlain by forearc sedimentary strata (ten Brink et al., 2000; Crouch, 1979; Reeves et al., 2015) (Figure 4.7). To the north, the WTR are bounded by relatively strong forearc strata overlying Mesozoic arc rocks (Salinian block) of similar rheology to the Peninsular Terrane in the south (K. Grove, 1993; Vedder et al., 1983). These lithospheric blocks are translating to the northwest along the main plate boundary (Zeng & Shen, 2016), with the weak, extended, and rotated WTR caught in between. We suggest that the contrast in lithospheric strength of the relatively strong terranes to the south and north with the weak WTR, as well as differential motions between the blocks, result in shortening within the WTR. This mechanism

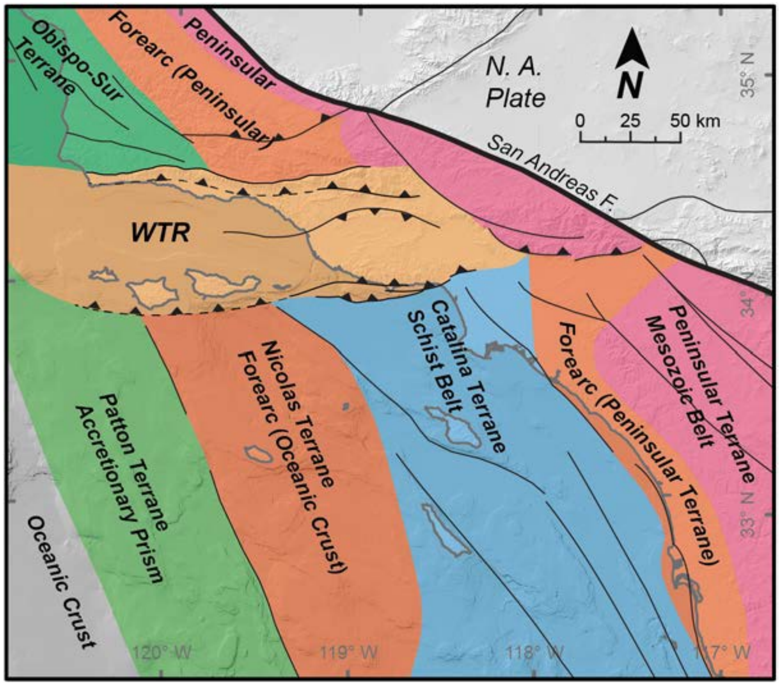

Figure 4.7: Generalized map of terranes and faults west of the Pacific-North American plate boundary in southern California. The east-west trending Western Transverse Ranges (WTR) are bounded to the north and south by northwest-southeast trending terranes of variable composition and lithospheric strength. The Patton Terrane is predominantly composed of unmetamorphosed to low-grade metamorphosed graywacke and argillite, similar in composition to the Franciscan Complex (Bohannon & Geist, 1998). The Nicolas Terrane Forarc belt consists of 3+ km of Cretaceous through Oligocene forarc strata overlying oceanic crust. The Catalina terrane consists of highly deformed blueschist to amphibolite-grade accretionary rocks overlain by Neogene volcanic and sedimentary rocks (Grove et al., 2008). The Peninsular Terrance Mesozoic Terrane is overlain by a forearc sedimentary section both north and south of the WTR. The Obispo-Sur terrain consists of Franciscan complex rocks and is compositionally similar to the Patton Terrane (Vedder et al., 1983). Although the forarc strata of the WTR are likely part of the same Great Valley sequence that includes the Peninsular Terrane and Nicolas Terrane strata, the lithosphere-scale mechanical strength of the WTR is likely weaker due to its multi-stage history of rotation and extension. F–Fault; N. A.–North American; Adapted from Bohannon & Geist (1998), Fisher et al. (2009), and Grove et al. (2008).

may explain the localization of deformation so far from the restraining bend in the main transform margin between the Pacific and North American plates.

Similarly, lithosphere-scale contrasts in rheology have been suggested to control the localization of deformation elsewhere along the Pacific-North American plate boundary (ten Brink et al., 2018; Niemi et al., 2013; Spotila et al., 2007; Zoback et al., 1987). Within the San Andreas Fault system, thermochronometry data from opposing sides of the transform margin reveal that Miocene to present deformation is localized within the weakened basement rocks of the San Emigdio Mountains (Niemi et al., 2013). This weak, deformed lithosphere is caught between comparatively strong Mesozoic Peninsular Ranges batholith and Proterozoic gneiss in the Mt. Pinos block to the south, and strong, dense oceanic lithosphere beneath the San Joaquin Valley to the north (Chapman et al., 2010; Holbrook & Mooney, 1987; Namson & Davis, 1988;

Niemi et al., 2013). Niemi et al. (2013) hypothesize that these strong contrasts in the mechanical strength of the lithosphere played a role in localizing deformation within the weak lithosphere of the San Emigdio Mountains. A similar pattern is observed on the Queen Charlotte transform margin further north along the Pacific-North American plate boundary, where deformation localized on the boundary between continental and oceanic lithosphere (ten Brink et al., 2018). The formation of the Big Bend itself is likely a consequence of lithosphere-scale contrasts in rheology; the location of the main strand of the Pacific-North American transform margin has stepped east through time, and the restraining bend developed with the opening of the Gulf of California and an eastward step of the southern San Andreas Fault into the deformed, weak basement of the Mojave Block (Atwater & Stock, 1998; Crowell, 1979; Oskin & Stock, 2003). The central segment of the San Andreas Fault is currently fixed on the western margin of the Sierran Microplate, where strong oceanic lithosphere and Sierran arc basement rocks likely explain a lack of observed internal deformation and prevent eastward stepping of the margin (Argus & Gordon, 1991; Plattner et al., 2010). The Big Bend is therefore required to transfer plate boundary motion from the eastward-stepping southern Santa Andreas Fault, around the mechanically strong Sierran Microplate to the central segment of the San Andreas, and ultimately north to the Mendocino Triple Junction (Argus & Gordon, 1991; Crowell, 1979; Fuis et al., 2012; Nicholson et al., 1994; Le Pourhie & Saleeby, 2013).

Although the hypothesis that rheological contrasts may explain strain localization is not new (ten Brink et al., 2018; Niemi et al., 2013; Spotila et al., 2007; Zoback et al., 1987), our results from the WTR suggest that rheological contrasts may be more important to strain localization than proximity to restraining or releasing bends. The San Andreas Fault is the archetypal transform margin system from which new hypotheses are exported to other field settings, and detailed studies on dip-slip fault systems near other continental transform margins may reveal similarly complex fault initiation timing and propagation that challenge simple models of restraining- and releasing-bend tectonism.

4.8 Conclusions

Thermochronometric data from the Western Transverse Ranges provide insight into the evolution of reverse faulting adjacent to the Big Bend restraining bend in the North American-Pacific Plate transform margin. High-density sampling for thermochronometric data from nine new transects and two published transects (Niemi & Clark, 2018) reveal predominantly Pliocene

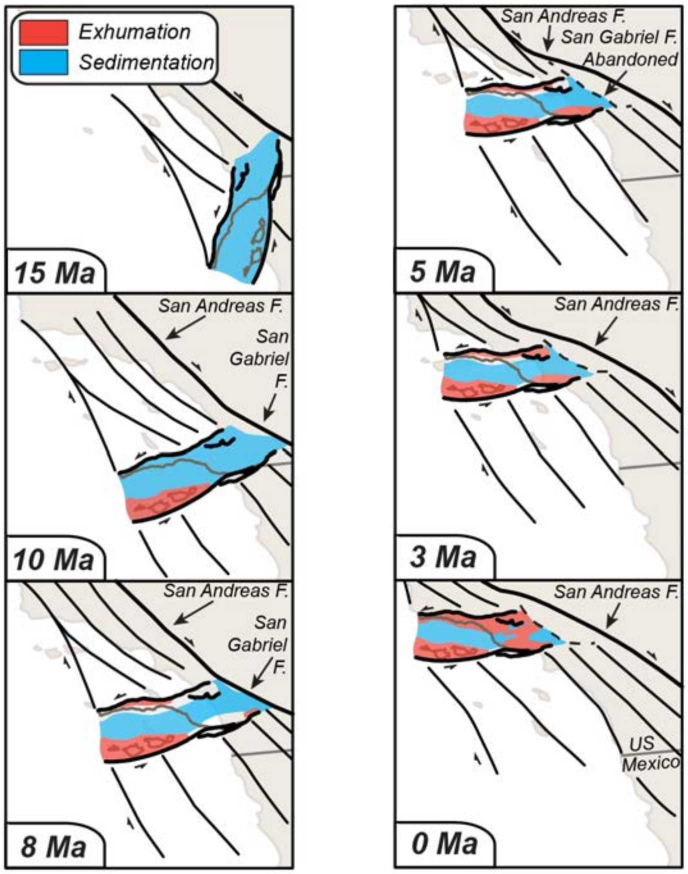

Figure 4.8: Time steps showing the rotation, sedimentation, and exhumation of the Western Transverse Ranges since 15 Ma. The modern coastline of southern California, USA and Baja California, Mexico, are shown for geographic context. Solid black lines are faults. Clockwise rotation of the WTR initiates between 16-14 Ma, and sedimentation occurs throughout the region under a predominantly transtensional tectonic regime. The first pulse of rock exhumation initiates at ~10 Ma on Santa Rosa Island as rotation, regional extension, and basin formation slows. At 8 Ma, cooling initiates in the Santa Ynez Mountains on the western end of the San Cayetano fault system as the WTR transitions from predominantly transtensional to transpressional. By 5-6 Ma, the San Gabriel Fault is abandoned as the main plate boundary structure as the southern San Andreas Fault forms to the east, creating the Big Bend restraining bend. By this time, reverse faulting on the southern margin has propagated east to the central Santa Monica Mountains, and reverse faulting on the northern margin has propagated east into the Topatopa Mountains. By 3 Ma, exhumation across the southern margin has slowed, whereas exhumation on the northern margin has continued propagating east. From 3 Ma to the present, forward propagation of the San Cayetano fold and thrust belt system results in rock exhumation in the center of the WTR block between the Santa Monica Mountains and Topatopa Mountains.

to Pleistocene apatite (U-Th-Sm)/He cooling ages along the San Cayetano fault system on the northern boundary of the WTR, and latest-Miocene to Pliocene cooling ages along the Santa Monica-Channel Islands fault system on the southern boundary. Cooling histories from inverse modelling of thermochronometry data imply a westward propagation of reverse faulting over ~5 Myr on both fault systems. In the north, exhumation initiates in the Santa Ynez Mountains on the west end of the San Cayetano fault system at 8 Ma and progresses east until 3 Ma. In the south, exhumation first initiates in the northern Channel Islands at 10 Ma and propagates east to the central Santa Monica Mountains by 5 Ma. Along both boundaries, reverse faulting initiates prior to development of the Big Bend and propagates towards the San Andreas Fault, suggesting that restraining bend tectonism is not the primary source of shortening in the WTR, as previously assumed. Post-Miocene deformation in the broader region around the Big Bend is localized within the WTR, which has mechanically weaker basement rocks. We posit that contrasts in lithosphere-scale mechanical strength may explain the distribution of young cooling ages and active reserve faulting in the WTR. The hypothesis that rheological contrasts may be a more important control on strain localization than proximity to bends in continental transform margins, developed here from the San Andreas transform margin, has the potential to be exported broadly to other transform margin systems.

4.9 References

Abbey, A. L., & Niemi, N. A. (2018). Low-temperature thermochronometric constraints on fault initiation and growth in the northern Rio Grande rift, upper Arkansas River valley, Colorado, USA. *Geology*, *46*(7), 627–630. https://doi.org/10.1130/G40232.1

Argus, D. F., & Gordon, R. G. (1991). Current Sierra Nevada-North America motion from very long baseline interferometry: implications for the kinematics of the western United States. *Geology*, *19*(11), 1085–1088. https://doi.org/10.1130/0091-7613(1991)019<1085:CSNNAM>2.3.CO;2

Armijo, R., Meyer, B., Hubert, A., & Barka, A. (1999). Westward propagation of the North Anatolian fault into the northern Aegean: Timing and kinematics. *Geology*, *27*(3), 267–270. https://doi.org/10.1130/0091-7613(1999)027<0267:WPOTNA>2.3.CO;2

Armijo, R., Meyer, B., Navarro, S., King, G., & Barka, A. (2002). Asymmetric slip partitioning in the sea of Marmara pull-apart: A clue to propagation processes of the North Anatolian Fault? *Terra Nova*, *14*(2), 80–86. https://doi.org/10.1046/j.1365-3121.2002.00397.x

Atwater, T. (1998). Plate tectonic history of southern California with emphasis on the Western Transverse Ranges and northern Channel Islands. In P. W. Weigand (Ed.), *Contributions to the geology of the Northern Channel Islands, Southern California* (pp. 1–8). American Association of Petroleum Geologists, Pacific Section.

Atwater, T., & Stock, J. (1998). Pacific-North America plate tectonics of the Neogene Southwestern United States: An update. *International Geology Review*, *40*(5), 375–402. https://doi.org/10.1080/00206819809465216

Blythe, A. E., House, M. A., & Spotila, J. A. (2002). Low-temperature thermochronology of the San Gabriel and San Bernardino Mountains, Southern California; constraining structural evolution. *Special Paper - Geological Society of America*, *365*, 231–250. https://doi.org/10.1130/0-8137-2365-5.231

Bohannon, R. G., & Geist, E. (1998). Upper crustal structure and Neogene tectonic development of the California continental borderland. *Geological Society of America Bulletin*, *110*(6), 779–800.

Bostick, N. H., Cashman, S. M., McCulloh, T. H., & Waddell, C. T. (1978). Gradients of vitrinite reflectance and present temperature in the Los Angeles and Ventura Basins, California, 65–96.

ten Brink, U. S., Zhang, J., Brocher, T. M., Okaya, D. A., Klitgord, K. D., & Fuis, G. S. (2000). Geophysical evidence for the evolution of the California Inner Continental Borderland as a metamorphic core complex. *Journal of Geophysical Research*, *105*, 5835–5857.

ten Brink, U. S., Miller, N. C., Andrews, B. D., Brothers, D. S., & Haeussler, P. J. (2018). Deformation of the Pacific/North America Plate Boundary at Queen Charlotte Fault: The Possible Role of Rheology. *Journal of Geophysical Research: Solid Earth*, *123*(5), 4223–4242. https://doi.org/10.1002/2017JB014770

Buscher, J. T., & Spotila, J. A. (2007). Near-field response to transpression along the southern San Andreas fault, based on exhumation of the northern San Gabriel Mountains, southern California. *Tectonics*, *26*(5), 1–15. https://doi.org/10.1029/2006TC002017

Chapman, A. D., Kidder, S., Saleeby, J. B., & Ducea, M. N. (2010). Role of extrusion of the Rand and Sierra de Salinas schists in Late Cretaceous extension and rotation of the southern Sierra Nevada and vicinity. *Tectonics*, *29*(5), 1–21. https://doi.org/10.1029/2009TC002597

Collett, C. M., Duvall, A. R., Flowers, R. M., Tucker, G. E., & Upton, P. (2019). The timing and style of oblique deformation within New Zealand's Kaikōura Ranges and Marlborough Fault System based on low-temperature thermochronology. *Tectonics*, 1–23. https://doi.org/10.1029/2018TC005268

Colson, K. B. (1996). *Neotectonics of the Left-Lateral Santa Rosa Island Fault, Western Transverse Ranges, Southern California*. San Diego State University.

Cooke, M. L., Schottenfeld, M. T., & Buchanan, S. W. (2013). Evolution of fault efficiency at restraining bends within wet kaolin analog experiments. *Journal of Structural Geology*, *51*, 180–192. https://doi.org/10.1016/j.jsg.2013.01.010

Cooke, M. L., Toeneboehn, K., & Hatch, J. L. (2020). Onset of slip partitioning under oblique convergence within scaled physical experiments. *Geosphere*, *16*(3), 875–889. https://doi.org/10.1130/ges02179.1

Cowan, H., Nicol, A., & Tonkin, P. (1996). A comparison of historical and paleoseismicity in a newly formed fault zone and a mature fault zone, North Canterbury, New Zealand. *Journal of Geophysical Research B: Solid Earth*, *101*(3), 6021–6036. https://doi.org/10.1029/95jb01588

Crouch, J. K. (1979). Neogene tectonic evolution of the California Continental Borderland and western Transverse Ranges. *Bulletin of the Geological Society of America*, *90*(4), 338–345. https://doi.org/10.1130/0016-7606(1979)90<338:NTEOTC>2.0.CO;2

Crouch, J. K., & Suppe, J. (1993). Late Cenozoic tectonic evolution of the Los Angeles Basin and inner California borderland: a model for core complex-like crustal extension. *Geological Society of America Bulletin*, *105*(11), 1415–1434. https://doi.org/10.1130/0016-7606(1993)105<1415:LCTEOT>2.3.CO;2

Crowell, J. C. (1979). The San Andreas fault system through time. *Journal of the Geological Society*, *136*, 293–302. https://doi.org/10.1144/gsjgs.136.3.0293

Crowell, J. C. (1982). The tectonics of Ridge Basin, southern California. In J. C. Crowell & M. H. Link (Eds.), *Geologic History of Ridge Basin, Southern California* (pp. 25–42). Society of Economic Paleontologists and Mineralogists.

Darrow, A. C., & Sylvester, A. G. (1984). *Activity of the Central Reach of the Santa Ynez Fault: Continuation of Investigations: U.S. Geological Survey Technical Report, Contract 21367.*

Davis, T. L., & Namson, J. S. (1994). A balanced cross-section of the 1994 Northridge earthquake, southern California. *Nature*, *372*, 167–169. https://doi.org/10.1038/372167a0

Dewey, J. ., Holdsworth, R. ., & Strachan, R. A. (1998). Transpression and transtension zones. In

R. . Holdsworth, R. A. Strachan, & J. F. Dewey (Eds.), *Continental Transpressional and Transtensional Tectonics* (Vol. 135, pp. 1–14). Geological Society, London, Special Publications.

Dibblee, T. W. (1982). Regional geology of the Transverse Ranges Province of southern California. In D. L. Fefe & J. A. Minch (Eds.), *Geology and Mineral Wealth of the Califrnia Transverse Ranges* (pp. 7–26). Santa Ana, California: South Coast Geological Society, Inc.

Dibblee, T. W. (1985). *Geologic Map of the Wheeler Springs Quadrangle, Ventura County, California*. Santa Barbara, California: Dibblee Geological Foundation.

Dibblee, T. W. (1987a). *Geologic Map of the Matilija Quadrangle, Ventura County, California*. Santa Barbara, California: Dibblee Geological Foundation.

Dibblee, T. W. (1987b). *Geologic Map of the Ojai Quadrangle, Ventura County, California*. Santa Barbara, California: Dibblee Geological Foundation.

Dibblee, T. W. (1990a). Geologic Map of the Fillmore Quadrangle. *Santa Barbara Museum of Natural History*.

Dibblee, T. W. (1990b). Geologic Map of the Santa Paula Peak Quadrangle. *Santa Barbara Museum of Natural History*.

Dibblee, T. W. (1991a). *Geologic Map of the Beverly Hills and South 1/2 Van Nuys Quadrangles, Los Angeles County, California*. Santa Barbara, California: Dibblee Geological Foundation.

Dibblee, T. W. (1991b). *Geologic Map of the Hollywood and South 1/2 Burbank Quadrangles*. Santa Barbara, California: Dibblee Geological Foundation.

Dibblee, T. W. (1991c). *Geologic Map of the Piru Quadrangle, Ventura County, California*. Santa Barbara, California: Dibblee Geological Foundation.

Dibblee, T. W., & Ehrenspeck, H. E. (1986). *Geologic map of the Santa Barbara quadrangle, Santa Barbara County, California*. Santa Barbara, California: Dibblee Geological Foundation.

Dibblee, T. W., & Ehrenspeck, H. E. (1997). *Geologic map of the Whitaker Peak quadrangle, Los Angeles and Ventura Counties, California*. Dibblee Geological Foundation.

Dibblee, T. W., Woodley, J. J., & Ehrenspeck, H. E. (1998). *Geologic Map of the Santa Rosa Island Quadrangle, Santa Barbara County, California*. Santa Barbara, California: Dibblee Geological Foundation.

Dickinson, W. R. (1996). *Kinematics of transrotational tectonism in the california transverse ranges and its contribution to cumulative slip along the san andreas transform fault system*. *Special Paper of the Geological Society of America* (Vol. 305). https://doi.org/10.1130/0-8137-2305-1.1

Dolan, J. F., & Pratt, T. L. (1997). High-resolution seismic reflection profiling of the Santa Monica Fault Zone, West Los Angeles, California. *Geophysical Research Letters*, *24*(16), 2051–2054.

Dolan, J. F., Sieh, K., Rockwell, T. K., Yeats, R. S., Shaw, J. H., Suppe, J., et al. (1995). Prospects for Larger or More Frequent Earthquakes in the Los Angeles Metropolitan Region. *Science*, *267*(5195), 199–205. https://doi.org/10.1126/science.267.5195.199

Dolan, J. F., Sieh, K., Rockwell, T. K., Guptill, P., & Miller, G. (1997). Active tectonics, paleoseismology, and seismic hazards of the Hollywood fault, northern Los Angeles basin, California. *Bulletin of the Geological Society of America*, *109*(12), 1595–1616. https://doi.org/10.1130/0016-7606(1997)109<1595:ATPASH>2.3.CO;2

Dolan, J. F., Sieh, K., & Rockwell, T. K. (2000). Late quaternary activity and seismic potential of the Santa Monica fault system, Los Angeles, California. *Bulletin of the Geological Society of America*, *112*(10), 1559–1581. https://doi.org/10.1130/0016-7606(2000)112<1559:LQAASP>2.0.CO;2

Duffy, B., Quigley, M., Barrell, D. J. A., Van Dissen, R., Stahl, T., Leprince, S., et al. (2013). Fault kinematics and surface deformation across a releasing bend during the 2010 MW 7.1 Darfield, New Zealand, earthquake revealed by differential LiDAR and cadastral surveying. *Bulletin of the Geological Society of America*, *125*(3–4), 420–431. https://doi.org/10.1130/B30753.1

Ehlers, T. A. (2005). Crustal Thermal Processes and the Interpretation of Thermochronometer Data. *Reviews in Mineralogy and Geochemistry*, *58*(1), 315–350. https://doi.org/10.2138/rmg.2005.58.12

Ehlig, P. L., Ehlert, K. W., & Crowem, B. M. (1975). Offset of the upper Miocene Caliente and Mint Canyon formations along the San Gabriel and San Andreas faults. *California Division of Mines and Geology Special Report 118*, 83–92.

Eymold, W. K., & Jordan, T. H. (2019). Tectonic Regionalization of the Southern California Crust From Tomographic Cluster Analysis. *Journal of Geophysical Research: Solid Earth*, *124*(11), 11840–11865. https://doi.org/10.1029/2019JB018423

Farley, K. A. (2002). (U-Th)/He Dating: Techniques, Calibrations, and Applications. *Reviews in Mineralogy and Geochemistry*, *47*(1), 819–844. https://doi.org/10.2138/rmg.2002.47.18

Fisher, M. A., Langenheim, V. E., Nicholson, C., Ryan, H. F., & Sliter, R. W. (2009). Recent developments in understanding the tectonic evolution of the Southern California offshore area: Implications for earthquake-hazard analysis. *Special Paper of the Geological Society of America*, *2454*(454), 229–250. https://doi.org/10.1130/2009.2454(4.2)

Fuis, G. S., Scheirer, D. S., Langenheim, V. E., & Kohler, M. D. (2012). A new perspective on the Geometry of the San Andreas fault in southern California and its relationship to Lithospheric structure. *Bulletin of the Seismological Society of America*, *102*(1), 236–251. https://doi.org/10.1785/0120110041

Gallagher, K. (2012). Transdimensional inverse thermal history modeling for quantitative thermochronology. *Journal of Geophysical Research: Solid Earth*, *117*(2), 1–16. https://doi.org/10.1029/2011JB008825

Graham, S. A., Stanley, R. G., Bent, J. V., & Carter, J. B. (1989). Oligocene and Miocene paleogeography of central California and displacement along the San Andreas fault. *Geological Society of America Bulletin*, *101*(5), 711–730. https://doi.org/10.1130/0016-7606(1989)101<0711:OAMPOC>2.3.CO;2

Grove, K. (1993). Latest Cretaceous basin formation within the Salinian terrane of west-central California. *Geological Society of America Bulletin*, *105*(4), 447–463. https://doi.org/10.1130/0016-7606(1993)105<0447:LCBFWT>2.3.CO;2

Grove, M., Bebout, G. E., Jacobson, C. E., Barth, A. P., Kimbrough, D. L., King, R. L., et al. (2008). The Catalina Schist: Evidence for middle Cretaceous subduction erosion of southwestern North America. In A. E. Draut, P. D. Clift, & D. W. Scholl (Eds.), *Formation and Applications of the Sedimentary Record in Arc Collision Zones*. The Geological Society of America Special Paper 436, p. 335-361. https://doi.org/10.1130/2008.2436(15)

Guenthner, W. R., Reiners, P. W., Ketcham, R. A., Nasdala, L., & Giester, G. (2013). Helium diffusion in natural zircon: radiation damage, anisotropy, and the interpretation of zircon (U-TH)/He thermochronology. *American Journal of Science*, *313*(3), 145–198.

https://doi.org/10.2475/03.2013.01

Hatem, A. E., Cooke, M. L., & Madden, E. H. (2015). Evolving efficiency of restraining bends within wet kaolin analog experiments. *Journal of Geophysical Research: Solid Earth*, *120*, 1975–1992. https://doi.org/10.1002/2014JB011735

Hatem, A. E., Cooke, M. L., & Toeneboehn, K. (2017). Strain localization and evolving kinematic efficiency of initiating strike-slip faults within wet kaolin experiments. *Journal of Structural Geology*, *101*, 96–108. https://doi.org/10.1016/j.jsg.2017.06.011

Helmold, K. P., & van de Kamp, P. C. (1984). Diagenetic mineralogy and controls on albitization and laumontite formation in Paleogene Arkoses, Santa Ynez Mountains, California. *AAPG Memoir 37*, *0*(1), 239–276.

Hill, D. J. (1976). Geology of the Jurassic Basement Rocks, Santa Cruz Island, California, and Correlation with Other Mesozoic Basement Terranes in California. *American Association of Petroleum Geologists Pacific Section*, 16–46.

Holbrook, W. S., & Mooney, W. D. (1987). The crustal structure of the axis of the Great Valley, California, from seismic refraction measurements. *Tectonophysics*, *140*(1), 49–63. https://doi.org/10.1016/0040-1951(87)90139-9

Hornafius, J. S., Luyendyk, B. P., Terres, R. R., & Kamerling, M. J. (1986). Timing and extent of Neogene tectonic rotation in the western Transverse Ranges, California (USA). *Geological Society of America Bulletin*, *97*(12), 1476–1487. https://doi.org/10.1130/0016-7606(1986)97<1476:TAEONT>2.0.CO;2

Hubbard, J., Shaw, J. H., Dolan, J. F., Pratt, T. L., McAuliffe, L., & Rockwell, T. K. (2014). Structure and seismic hazard of the Ventura Avenue anticline and ventura fault, California: Prospect for large, multisegment ruptures in the western transverse ranges. *Bulletin of the Seismological Society of America*, *104*(3), 1070–1087. https://doi.org/10.1785/0120130125

Huftile, G. J., & Yeats, R. S. (1996). Deformation rates across the Placerita (Northridge Mw = 6.7 Aftershock Zone) and Hopper Canyon segments of the western transverse ranges deformation belt. *Bulletin of the Seismological Society of America*, *86*, 3–18.

Hughes, A., Rood, D. H., Whittaker, A. C., Bell, R. E., Rockwell, T. K., Levy, Y., et al. (2018). Geomorphic evidence for the geometry and slip rate of a young, low-angle thrust fault: Implications for hazard assessment and fault interaction in complex tectonic environments. *Earth and Planetary Science Letters*, *504*, 198–210. https://doi.org/10.1016/j.epsl.2018.10.003

Huntington, K. W., & Klepeis, K. A. (2017). Challenges & Opportunities for Research in Tectonics: Understanding deformation & the processes that link Earth systems, from geologic time to human time. A community vision document submitted to the U.S. National Science Foundation.

Jackson, J., & Molnar, P. (1990). Active faulting and block rotations in the western Transverse Ranges, California. *Journal of Geophysical Research*, *95*(B13). https://doi.org/10.1029/jb095ib13p22073

Kamerling, M. J., & Luyendyk, B. P. (1979). Tectonic rotations of the Santa Monica Mountains region, western Transverse Ranges, California, suggested by paleomagnetic vectors. *Bulletin of the Geological Society of America*, *90*(4), 331–337. https://doi.org/10.1130/0016-7606(1979)90<331:TROTSM>2.0.CO;2

Kamerling, M. J., & Luyendyk, B. P. (1985). Paleomagnetism and Neogene tectonics of the northern Channel Islands, California (USA). *Journal of Geophysical Research*, *90*(B14), 12,485-12,502. https://doi.org/10.1029/jb090ib14p12485

Lekic, V., French, S. W., & Fischer, K. M. (2011). Lithospheric Thinning Beneath Rifted Regions of Southern California. *Science*, *334*, 783–787. https://doi.org/10.7551/mitpress/8876.003.0036

Levy, Y., Rockwell, T. K., Shaw, J. H., Plesch, A., Driscoll, N. W., & Perea, H. (2019). Structural Modeling of the Western Transverse Ranges: An Imbricated Thrust Ramp Architecture. *Lithosphere*, 1–38. https://doi.org/10.1130/L1124.1/4860092/l1124.pdf

Link, M. H. (1982). Stratigraphic Nomenclature and Age of Miocene Strata, Ridge Basin, Southern California. In J. C. Crowell & M. H. Link (Eds.), *Geologic History of Ridge Basin, Southern California* (pp. 5–12). Pacific Section, Society of Economic Paleontologists and Mineralogists.

Link, M. H., & Osborne, R. H. (1978). Lacustrine facies in the Pliocene Ridge Basin Group: Ridge Basin, California. *Modern and Ancient Lake Sediments*, *Special Pu*, 169–187.

Little, T. A., & Jones, A. (1998). Seven million years of strike-slip and related off-fault deformation, northeastern Marlborough fault system, South Island, New Zealand. *Tectonics*, *17*(2), 285–302.

Lock, J., & Willett, S. (2008). Low-temperature thermochronometric ages in fold-and-thrust belts. *Tectonophysics*, *456*, 147–162. https://doi.org/10.1016/j.tecto.2008.03.007

Luyendyk, B. P. (1991). A model for Neogene crustal rotations, transtension, and transpression in southern California. *Geological Society of America Bulletin*, *103*(11), 1528–1536. https://doi.org/10.1130/0016-7606(1991)103<1528:AMFNCR>2.3.CO;2

Luyendyk, B. P., Kamerling, M. J., & Terres, R. (1980). Geometric model for Neogene crustal rotations in southern California, (4), 211–217. https://doi.org/10.1130/0016-7606(1980)91<211

Madden, E. H., Cooke, M. L., & McBeck, J. A. (2017). Energy budget and propagation of faults via shearing and opening using work optimization. *Journal of Geophysical Research: Solid Earth*, *122*(8), 6757–6772. https://doi.org/10.1002/2017JB014237

Marshall, S. T., Funning, G. J., & Owen, S. E. (2013). Fault slip rates and interseismic deformation in the western Transverse Ranges, California. *Journal of Geophysical Research: Solid Earth*, *118*(8), 4511–4534. https://doi.org/10.1002/jgrb.50312

Marshall, S. T., Funning, G. J., Krueger, H. E., Owen, S. E., & Loveless, J. P. (2017). Mechanical models favor a ramp geometry for the Ventura-pitas point fault, California. *Geophysical Research Letters*. https://doi.org/10.1002/2016GL072289

McAuliffe, L. J., Dolan, J. F., Rhodes, E. J., Hubbard, J., Shaw, J. H., & Pratt, T. L. (2015). Paleoseismologic evidence for large-magnitude (MW 7.5-8.0) earthquakes on the Ventura blind thrust fault: Implications for multifault ruptures in the Transverse Ranges of southern California. *Geosphere*, *11*(5), 1629–1650. https://doi.org/10.1130/GES01123.1

McBeck, J. A., Madden, E. H., & Cooke, M. L. (2016). Growth by Optimization of Work (GROW): A new modeling tool that predicts fault growth through work minimization. *Computers and Geosciences*, *88*, 142–151. https://doi.org/10.1016/j.cageo.2015.12.019

McBeck, J. A., Cooke, M., & Madden, E. (2017). Work Optimization Predicts the Evolution of Extensional Step Overs Within Anisotropic Host Rock: Implications for the San Pablo Bay, CA. *Tectonics*, *36*(11), 2630–2646. https://doi.org/10.1002/2017TC004782

McDowell, F. W., McIntosh, W. C., & Farley, K. A. (2005). A precise 40Ar-39Ar reference age for the Durango apatite (U-Th)/He and fission-track dating standard. *Chemical Geology*, *214*(3–4), 249–263. https://doi.org/10.1016/j.chemgeo.2004.10.002

Miller, F., & Morton, D. (1980). Potassium-argon geochronology of the eastern Transverse

Ranges and southern Mojave Desert, southern California. *United States Geological Survey Professional Paper*, *1152*, 1–30. Retrieved from http://www.getcited.org/pub/102118719

Namson, J. S., & Davis, T. L. (1988). Structural transect of the western Transverse Rances, California: Implications for lithospheric kinematics and seismic risk evaluation. *Geology*, *16*, 675–679.

Nathenson Marianne, M. G. (1987). Compilation of geothermal-gradient data in the conterminous United States. *USGS Open-File Report*, *87–592*, 33. Retrieved from http://pubs.usgs.gov/of/1987/0592/report.pdf%5Cnhttp://pubs.usgs.gov/of/1987/0592/plate-1.pdf%5Cnhttp://pubs.er.usgs.gov/thumbnails/usgs_thumb.jpg%5Cnhttp://pubs.usgs.gov/of/1987/0592/plate-2.pdf

Nicholson, C., Sorlien, C. C., Atwater, T., Crowell, J. C., & Luyendyk, B. P. (1994). Microplate capture, rotation of the western Transverse Ranges, and initiation of the San Andreas transform as a low-angle fault system. *Geology*, *22*(6), 491–495.

Niemi, N. A., & Clark, M. K. (2018). Long-term exhumation rates exceed paleoseismic slip rates in the central Santa Monica Mountains, Los Angeles County, California. *Geology*, *46*(1), 63–66. https://doi.org/10.1130/G39388.1

Niemi, N. A., Buscher, J. T., Spotila, J. A., House, M. A., & Kelley, S. A. (2013). Insights from low-temperature thermochronometry into transpressional deformation and crustal exhumation along the San Andreas fault in the western Transverse Ranges, California. *Tectonics*, *32*(6), 1602–1622. https://doi.org/10.1002/2013TC003377

Oskin, M., & Stock, J. (2003). Marine incursion synchronous with plate-boundary localization in the Gulf of California. *Geology*, *31*(1), 23–26. https://doi.org/10.1130/0091-7613(2003)031<0023:MISWPB>2.0.CO;2

Perea, H., Ucarkus, G., Driscoll, N. W., Kent, G. M., Levy, Y., & Rockwell, T. K. (2017). Holocene deformation events in the offshore Transverse Ranges (California, USA) constrained by new high-resolution geophysical data. In *Expanded abstract for the 8th International Union for Quaternary Research (INQUA) Meeting on Paleoseis- mology, Active Tectonics and Archeoseismology (PATA), New Zealand, 13–16 November 2017* (p. 4).

Pinter, N., Johns, B., Little, B., & Vestal, W. D. (2001). Fault-related folding in California's Northern Channel Islands documented by rapid-static GPS positioning. *GSA Today*, *11*(5), 4–9. https://doi.org/10.1130/1052-5173(2001)011<0004:FRFICN>2.0.CO;2

Pinter, N., Sorlien, C. C., & Scott, A. T. (2003). Fault-related fold growth and isostatic subsidence, California Channel Islands. *American Journal of Science*, *303*(4), 300–318. https://doi.org/10.2475/ajs.303.4.300

Plattner, C., Malservisi, R., Furlong, K. P., & Govers, R. (2010). Development of the Eastern California Shear Zone - Walker Lane belt: The effects of microplate motion and pre-existing weakness in the Basin and Range. *Tectonophysics*, *485*(1–4), 78–84. https://doi.org/10.1016/j.tecto.2009.11.021

Le Pourhie, L., & Saleeby, J. (2013). Lithospheric convective instability could induce creep along part of the San Andreas fault. *Geology*, *41*(9), 999–1002. https://doi.org/10.1130/G34244.1

Quigley, M., Van Dissen, R., Litchfield, N., Villamor, P., Duffy, B., Barrell, D., et al. (2012). Surface rupture during the 2010 Mw 7.1 darfield(canterbury) earthquake: Implications for fault rupture dynamics and seismic-hazard analysis. *Geology*, *40*(1), 55–58. https://doi.org/10.1130/G32528.1

Reeves, Z., Lekic, V., Schmerr, N., Kohler, M., & Weeraratne, D. (2015). Lithospheric structure across the California Continental Borderland from receiver functions. *Geochemistry, Geophysics, Geosystems*, *16*, 246–266. https://doi.org/10.1002/2014GC005617

Reiners, P. W., & Nicolescu, S. (2006). Measurement of parent nuclides for (U-Th)/He chronometry by solution sector ICP-Ms. *ARDHL Report 1*, (December 2006), 1–33. Retrieved from http://www.geo.arizona.edu/~reiners/arhdl/arhdl.html

Reiners, P. W., Farley, K. A., & Hickes, H. J. (2002). He diffusion and (U-Th)/He thermochronometry of zircon: Initial results from Fish Canyon Tuff and Gold Butte. *Tectonophysics*, *349*(1–4), 297–308. https://doi.org/10.1016/S0040-1951(02)00058-6

Rockwell, T. K. (1983). *Soil Chronology, Geology, and Neo- tectonics of the North Central Ventura Basin, California*. University of California, Santa Barbara.

Rockwell, T. K. (1988). Neotectonics of the San Cayetano fault, Transverse Ranges, California. *Geological Society of America Bulletin*, *100*, 500–513.

Rockwell, T. K., Keller, E. A., Clark, M. N., & Johnson, D. L. (1984). Chronology and rates of faulting of Ventura River terraces, California. *Geological Society of America Bulletin*, *95*(12), 1466–1474. https://doi.org/10.1130/0016-7606(1984)95<1466:CAROFO>2.0.CO;2

Rockwell, T. K., Clark, K., Gamble, L., Oskin, M. E., Haaker, E. C., & Kennedy, G. L. (2016). Large Transverse Range Earthquakes Cause Coastal Upheaval near Ventura, Southern California. *Bulletin of the Seismological Society of America*, *106*(6), 2706–2720. https://doi.org/10.1785/0120150378

Rohr, K. M. M. (2015). Plate boundary adjustments of the southernmost queen charlotte fault. *Bulletin of the Seismological Society of America*, *105*(2B), 1076–1089. https://doi.org/10.1785/0120140162

Seeber, L., & Sorlien, C. C. (2000). Listric thrusts in the western Transverse Ranges, California. *Bulletin of the Geological Society of America*, *112*(7), 1067–1079. https://doi.org/10.1130/0016-7606(2000)112<1067:LTITWT>2.0.CO;2

Şengör, A. M. C., Tüysüz, O., Imren, C., Sakinç, M., Eyidoğan, H., Görür, N., et al. (2005). The North Anatolian Fault: A new look. *Annual Review of Earth and Planetary Sciences*, *33*, 37–112. https://doi.org/10.1146/annurev.earth.32.101802.120415

Shaller, P. J., & Heron, C. W. (2004). Proposed revision of marine terrace extent, geometry, and rates of uplift, Pacific Palisades, California. *Environmental and Engineering Geoscience*, *10*(3), 253–275. https://doi.org/10.2113/10.3.253

Shaw, J. H., & Suppe, J. (1994). Active faulting and growth folding in the eastern Santa Barbara Channel, California. *Geological Society of America Bulletin*, *106*(5), 607–626. https://doi.org/10.1130/0016-7606(1994)106<0607:AFAGFI>2.3.CO;2

Sieh, K. E., & Jahns, R. H. (1984). Holocene activity of the San Andreas fault at Wallace Creek, California Holocene activity of the San Andreas fault at Wallace Creek, California. *Geological Society of America Bulletin*, (8), 883–896. https://doi.org/10.1130/0016-7606(1984)95<883

Sorensen, S. (1985). Petrologic evidence for Jurassic, island-arc-like basement rocks in the southwestern Transverse Ranges and California continental borderland. *Geological Society of America, Bulletin*, *96*(8), 997–1006. https://doi.org/10.1130/0016-7606(1985)96<997:PEFJIB>2.0.CO;2

Sorlien, C. C., & Nicholson, C. (2015). Post-1 Ma Deformation History of the Pitas Point-North Channel-Red Mountain Fault System and Associated Folds in Santa Barbara Channel, California. *U.S. Geological Survey National Earthquake Hazards Reduction Program Final*

Report, Award G14AP00012, 1–24.

Sorlien, C. C., Kamerling, M. J., Seeber, L., & Broderick, K. G. (2006). Restraining segments and reactivation of the Santa Monica-Dume-Malibu Coast fault system, offshore Los Angeles, California. *Journal of Geophysical Research: Solid Earth*, *111*(11), 1–22. https://doi.org/10.1029/2005JB003632

Spotila, J. A., Farley, K. A., Yule, J. D., & Reiners, P. W. (2001). Near-field transpressive deformation along the San Andreas fault zone in southern California, based on exhumation constrained by (U-Th)/He dating. *Journal of Geophysical Research*, *106*, 30909. https://doi.org/10.1029/2001JB000348

Spotila, J. A., Niemi, N., Brady, R., House, M., Buscher, J., & Oskin, M. (2007). Long-term continental deformation associated with transpressive plate motion: The San Andreas fault. *Geology*, *35*(11), 967–970. https://doi.org/10.1130/G23816A.1

Stone, P. H., & Carlson, J. H. (1979). Atmospheric Lapse Rate Regimes and Their Parameterization. *Journal of the Atmospheric Sciences*, *36*(3), 415–423.

Teyssier, C., Tikoff, B., & Markley, M. (1995). Oblique plate motion and continental tectonics. *Geology*, *23*(5), 447–450. https://doi.org/10.1130/0091-7613(1995)023<0447:OPMACT>2.3.CO;2

Townsend, K. F., Gallen, S. F., & Clark, M. K. (2020). Quantifying Near-Surface Rock Strength on a Regional Scale From Hillslope Stability Models. *Journal of Geophysical Research: Earth Surface*, *125*(7). https://doi.org/10.1029/2020JF005665

Vedder, J. G., Howell, D. G., & McLean, H. (1983). Stratigraphy, sedimentation, and tectonic ccretion of exotic terranes, southern California Coast Ranges, California. *American Association of Petroleum Geologists Memoir*, *34*, 471–496.

Walcott, R. I. (1998). Modes of oblique compression: Late cenozoic tectonics of the South Island of New Zealand. *Reviews of Geophysics*, *36*(1), 1–26. https://doi.org/10.1029/97RG03084

Wallace, L. M., Barnes, P., Beavan, J., Van Dissen, R., Litchfield, N., Mountjoy, J., et al. (2012). The kinematics of a transition from subduction to strike-slip: An example from the central New Zealand plate boundary. *Journal of Geophysical Research: Solid Earth*, *117*(2). https://doi.org/10.1029/2011JB008640

White, L. (1992). *Thermal and unroofing history of the Western Transverse Ranges, California: Results from apatite fission track thermochronology*. The University of Texas at Austin.

Woodcock, N. H. (1986). The role of strike-slip fault systems at plate boundaries. *Philosophical Transactions of the Royal Society*, *317*, 13–29.

Wright, T. L. (1991). Structural Geology and Tectonic Evolution of the Los Angeles Basin, California. In K. T. Biddle (Ed.), *Active Margins Basins* (pp. 35–135). American Association of Petroleum Geologists Memoir 52. https://doi.org/10.1306/9488784D-1704-11D7-8645000102C1865D

Yeats, R. S. (1981). Quaternary flake tectonics of the California Transverse Ranges. *Geology*, *9*(1), 16–20. https://doi.org/10.1130/0091-7613(1981)9<16:QFTOTC>2.0.CO;2

Yerkes, R. F., & Lee, W. H. K. (1987). *Late Quaternary deformation in the Western Transverse Ranges*. *Recent Reverse Faulting in the Transverse Ranges, California: U.S. Geological Survey Professional Paper 1339*.

Zeng, Y., & Shen, Z. K. (2016). A fault-based model for crustal deformation, fault slip rates, and off-fault strain rate in California. *Bulletin of the Seismological Society of America*, *106*(2), 766–784. https://doi.org/10.1785/0120140250

Zoback, M. D., Zoback, M. Lou, Van Mount, S., Suppe, J., Eaton, J. P., Healy, J. H., et al.

(1987). New evidence on the state of stress of the san andreas fault system. *Science*, *238*(4830), 1105–1111. https://doi.org/10.1126/science.238.4830.1105

Data Availability Statement

Thermochronometry sample and analytical data is available at the University of Michigan Deep Blue data repository (https://deepblue.lib.umich.edu/data).

Acknowledgements

This work was supported by a National Science Foundation division of Earth Science, Geomorphology and Land Use Dynamics award (EAR-1528576) to M.K. Clark and research grants from the Evolving Earth Foundation, the Geological Society of America, and the Department of Earth and Environmental Sciences at the University of Michigan to K.F. Townsend. We thank the U.S. National Park Service and Forest Service for access and sample collection permits, and further thank Salvador Dominguez, Tim Cohen (Rancho Temescal), Jim Lynn, Gordon Kimball, The Nature Conservancy, Seneca Resources, Carbon Energy Corporation, and Aera Energy for access to private or restricted properties. We further thank Amanda Maslyn for laboratory support, Alyssa Abbey, Alexander Tye, and Nikolas Midttun for discussions and feedback on the thermal modelling methodology, and A. Joshua West, Nikolas Midttun, Bian Wang, Logan Knoper, William Medwedeff, Abra Atwood, Maxwell Dahlquist, and Eric Portenga for assistance in the field.

Chapter 5: The Scale-Dependent and Non-Linear Relationship Between Topographic Metrics and Rock Strength[4]

5.1 Abstract

It is often assumed that rock mass strength contributes to topographic form in mountain belts. While strength can be quantified in the field or laboratory for small rock pieces, the integration of larger scale discontinuities remains challenging, and as such we currently lack observational and quantitative data to elucidate scale-dependent variability in rock strength. Consequently, we lack quantitative understanding of how topography is related to changes in strength at the appropriate scale. Here we use a new rock strength dataset to evaluate the contribution of strength to topographic form in the Topatopa Mountains, southern California, USA, which exhibit a strong gradient in the maximum burial depth of Cretaceous through Plio-Pleistocene clastic sedimentary rocks exposed at the surface and for which long-term erosion rates and climate conditions are spatially uniform. Field metrics demonstrate a three- to ten-fold increase in strength with increasing stratigraphic age, and we find that for rocks of a given stratigraphic age, outcrop-scale shear strength is an order of magnitude lower than the shear strength of intact rock pieces. Topographic metrics including channel steepness, local relief, hillslope relief, and slope demonstrate a non-linear relationship with shear strength at both spatial scales. This relationship suggests that channel and hillslope gradients, as well as relief, initially increase rapidly with increasing strength, but become progressively less sensitive to rock strength variations with the exposure of stronger rocks. This may explain the observed limiting values of topographic form or threshold conditions and cautions against interpretation of steady-state landscapes based on topography alone.

5.2 Introduction

Topographic form in active mountain belts is recognized to reflect a steady-state condition, wherein the rate of climate-modulated erosion is balanced with the rate of rock uplift to produce topography that is broadly unchanging in time (Hack, 1975; Montgomery and Brandon, 2002; Willett and Brandon, 2002). Hillslopes in these landscapes often hold gradients

---

[4] Prepared for submission to *Geology* for peer-review as: Townsend, K.F., Clark, M.K., & West, A.J., The scale-dependent and non-linear relationship between topographic metrics and rock strength

near the angle-of-repose, which has been hypothesized to reflect threshold conditions set by the frictional strength of cohesionless hillslope materials (Burbank et al., 1996; Montgomery, 2001). As rock strength is often perceived as a minor contribution to topography in threshold landscapes, topographic metrics including the steepness of the channel network, and relief across both the fluvial system and hillslopes, are often used to infer variability in climate or tectonic forcings (Snyder et al., 2000; Kirby and Whipple, 2012; Clubb et al., 2020). In contrast to the conventional view of topographic steady state, Korup (2008) shows that mountain ranges composed of materials with uniform rock mass properties hold common morphologies across gradients in precipitation, rock uplift rates, landslide density, and glaciation, which is argued to reflect an adjustment of hillslope morphologies to rock-mass strength regardless of climate or tectonic forcing. Further, recent work demonstrates significant variability in landscape-scale rock-mass strength, suggesting that hillslope materials require a component of cohesive strength to remain stable (Gallen et al., 2015; Townsend et al., 2021). Following from these observations, we might expect landscape-scale variability in rock-mass strength to be expressed in the morphology of the overlying landscape (Schmidt and Montgomery, 1995). However, strength-dependent variability has not been explicitly explored, and quantitatively testing this corollary hypothesis is challenged by the difficulty in isolating for tectonic and climatic variables, a lack of direct data on rock mass properties, and the scale-dependent nature of rock strength.

Rock mass strength is strongly scale-dependent (Schmidt and Montgomery, 1995; Hoek and Brown, 1997). While strength can be quantitatively measured in the field or laboratory for small rock pieces, the integration of larger scale discontinuities at the outcrop- and landscape-scales remains challenging. Because discontinuities (fractures, bedding planes) disrupt and lower the bulk strength of rock masses compared to their intact components (Hoek and Brown, 1980, 1997), the difference between small-scale measurements of intact strength, and landscape-scale rockmass properties is likely significant (Gallen et al., 2015; Townsend et al., 2021). While accepted on principle, demonstration of this effect from observational and quantitative data has not been shown previously. Consequently, recognition of the dependency topography on scale-dependent strength has remained elusive.

Here we evaluate relationships between rock mass strength and topographic metrics in the Topatopa Mountains (TM) of southern California, USA (Figure 5.1). Stratigraphic units in this recently inverted sedimentary basin are similar in lithologic type and have a simple tectonic history. Inverse thermal modelling of low-temperature apatite (ApHe) and zircon (ZrHe) (U-Th)/He thermochronometry data yield similar long-term erosion rates along-strike (Townsend et al.), suggesting that variability in topographic metrics are unlikely driven by differences in the rate of rock uplift. Rock mass strength is quantified over the spatial scales of small (hand-sized) intact pieces and larger outcrops (several meters), which includes the effect of strength-limiting discontinuities (Hoek and Brown, 1997; Townsend et al., 2021). Strength at both scales show a strong dependency on stratigraphic age, reflecting variability in lithification associated with maximum burial depth (Townsend et al., 2020, 2021). The along-strike similarity of long-term erosion rates, consistency of climate, and strong gradients in rock mass mechanical properties thus make the TM an ideal natural laboratory to assess the relationships between scale-dependent rock strength and topographic form.

5.3 Geology and Climate of the Topatopa Mountains

The TM are composed of Cretaceous through Plio-Pleistocene marine and non-marine clastic sedimentary rocks deposited during multiple stages of regional extension and basin formation (Figure 5.1). Cretaceous turbidites are conformably overlain by Eocene marine sediments, Oligocene shallow-marine to terrestrial sandstones, and post-Oligocene sandstones and shales deposited in transtensional basins (Dibblee, 1982; Atwater, 1998). This ~11 km section is exposed in a broad homocline that dips to the east with strike perpendicular to the range front, with differential magnitude of exhumation along-strike (Dibblee, 1982) (Figure 5.1). The TM today are being uplifted due to active reverse faulting on the San Cayetano Fault (Figure 5.1) (Rockwell, 1988). The range thus has a simple history of sedimentation followed by recent exhumation, with no deformation inherited from earlier tectonic events.

ApHe and ZrHe cooling ages provide constrains on the timing and rates of tectonically-driven erosion in the TM. ApHe ages represent the time since a sample cooled below ~40-80°C at depths of 2-4 km (Flowers et al., 2009), whereas ZrHe ages represent the time since a sample cooled below ~180-200°C at depths of 5-8 km (Farley, 2002; Reiners et al., 2002). ApHe ages in the TM range from 1.3 to 4.5 Ma, and ZrHe ages range from 15 to 56 Ma. Inverse thermal modelling of these data on transects with vertical sample separation reveals that cooling began in the west at ~6 Ma and propagated to the east through ~3 Ma (Chapter 4). As cooling is likely driven by fault-driven erosion, these models imply that the San Cayetano Fault initiated in the west and grew eastward by tip-propagation, leading to the differential magnitude of rock

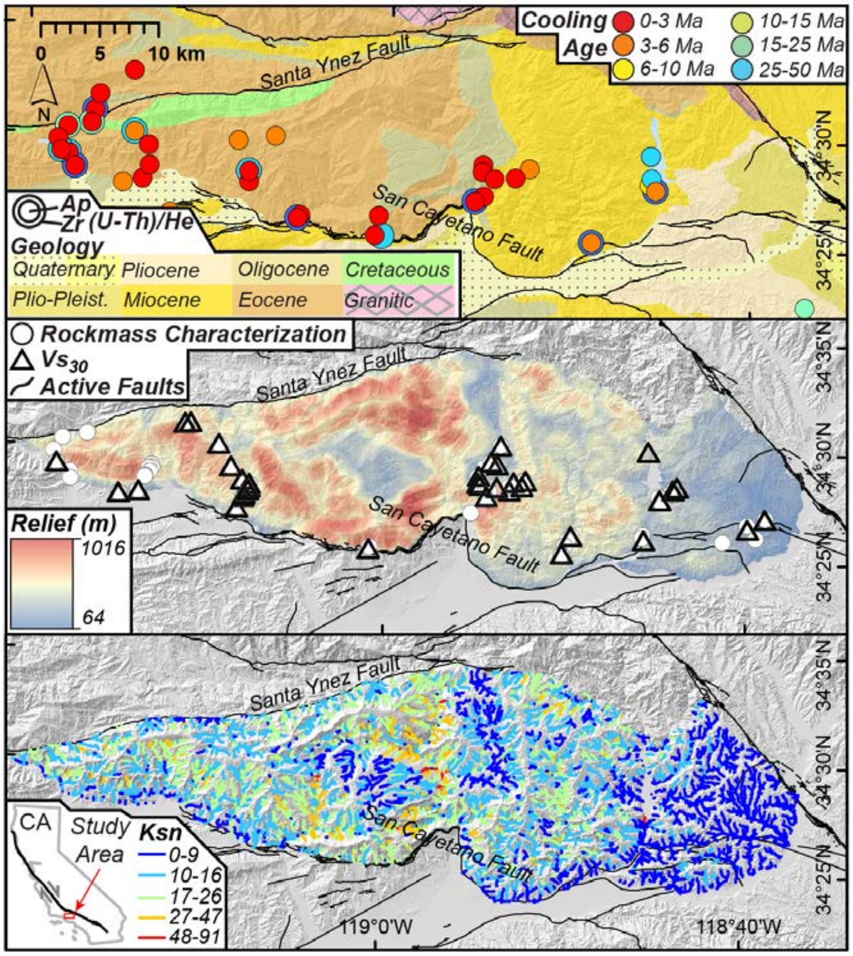

Figure 5.1: Generalized maps of the Topatopa Mountains with A) geology, active faults, and (U-Th)/He ages; B) relief within a 1 km moving window, Vs30, and geotechnical data sample locations; C) Ksn. CA-California

exhumation (Figure 5.1). Inferred erosion rates are ~1.0 to 1.2 mm/yr, with the easternmost transect at ~1.6 mm/yr (Chapter 4).

The climate of the Topatopa Mountains is characterized as Mediterranean, with generally warm, dry summers, and cool, wet winters. Mean annual precipitation along-strike of the range is similar, with weather stations in the Ojai and Santa Clara River valleys along the base of the range reporting 45 to 54 cm/yr (WRCC, 2020), although rainfall is likely greater at higher elevations due to orographic effects. We infer from similar mean annual precipitation values that climate conditions are relatively uniform along-strike of the range, and that variability in local climate likely does not explain differences in the height and steepness of the landscape.

5.4 Gradient in Rock Strength

Strong gradients in rock mass strength across the TM are inferred from multiple metrics (Townsend et al., 2020, 2021). Apparent cohesion inferred from remote sensing approaches using hillslope stability models (Townsend et al., 2020), as well as field datasets including Schmidt hammer measures of intact rock hardness, fracture structure and surface conditions assessed with Geological Strength Index (GSI) observations (Hoek and Marinos, 2000), and subsurface S-wave velocities measured from short geophysical arrays (< 80 m long) (Townsend et al., 2021), demonstrate a systematic increase in strength with increasing stratigraphic age across the Plio-Pleistocene through Cretaceous section in the TM. This variability in strength is likely driven by increasing degree of lithification associated with maximum burial depth of these units (Worden and Burley, 2003; Townsend et al., 2020). These approaches average material properties over a variety of spatial scales, but the specific component of strength (i.e. cohesion, stiffness, etc.) measured differs, thereby making a direct comparison of scale-effects challenging.

Here we focus on the shear strength of both intact (unfractured) rocks, and outcrop-scale rock masses. Schmidt R were converted to Unconfined Compressive Strength (UCS) using the Deere and Miller (1966) relationship, from which intact shear strength is inferred as 0.5(UCS). To aggregate the contributions of the intact strength and the outcrop-scale fracture characteristics, the Hoek & Brown criterion was used to quantify outcrop-scale shear strength (Hoek et al., 2002; Townsend et al., 2021). Both intact- and outcrop-scale shear strength increase with increasing stratigraphic age (from 10 to 100 MPa and 0.1 to 13.6 MPa, respectively), but for each stratigraphic age interval, we find that outcrop-scale shear strength is an order of magnitude lower than the intact, unfractured strength (e.g. Schmidt and Montgomery, 1995).

5.5 Topographic Metrics

Gradients in channel steepness normalized for contributing area (Ksn) are typically used to infer patterns of deformation in active mountain belts (Kirby and Whipple, 2012). Given the consistency in long-term erosion rates and inferred bedrock uplift rates, we expect a gradient in Ksn to instead match the strong gradients in rock strength, as strength controls the efficiency at which streams incise into their channels (Sklar and Dietrich, 2001). Ksn was produced using standard flow routing procedures on a 3-meter DEM (Kirby and Whipple, 2012). For a reference concavity of 0.37, resulting Ksn values range from 0.01 to 91 (Figure 5.1). Mean Ksn by stratigraphic age ranges from 3.7 in the Plio-Pleistocene units to 18.4 in the Eocene and Cretaceous units (Figure 5.2).

Local relief was calculated on a per-pixel basis as the range in elevation within a circular moving window with 1 km radius. Hillslope relief was calculated as the difference between

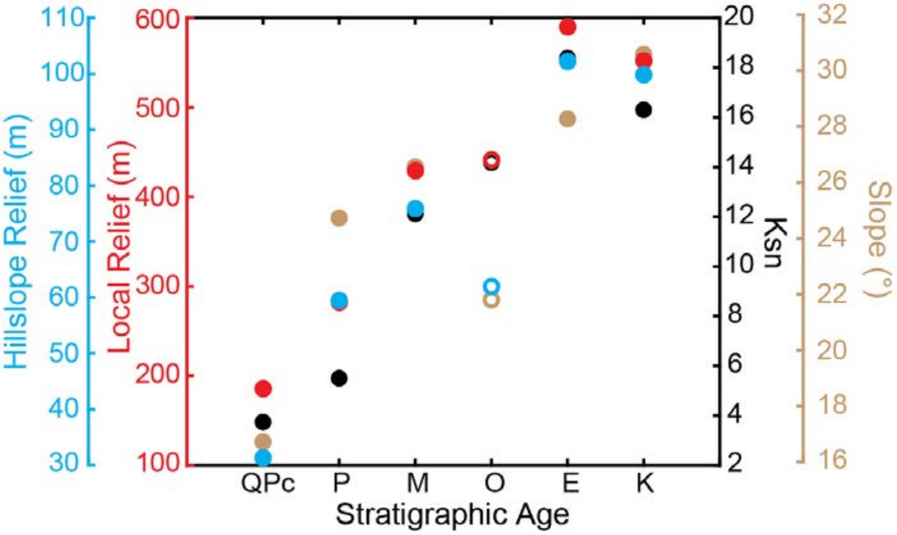

Figure 5.2: Mean Ksn, local relief (within a 1 km moving window), hillslope relief, and slope by stratigraphic age of underlying sedimentary rocks. QPc–Plio-Pleistocene, P–Pliocene, M–Miocene, O–Oligocene, E–Eocene, K–Cretaceous. Hollow points are Oligocene.

maximum and minimum elevations on hillslope flow paths, which were created from hillslope pixels with contributing areas less than 0.1 km^2 (e.g. Townsend et al., 2020). Mean values of local and hillslope relief range from 186 to 590 m and 31 to 102 m, respectively, and generally increase from the Plio-Pleistocene through Eocene and Cretaceous units (Figure 5.2). Mean pixel slope also increases from 17 to 31° across this same stratigraphic gradient, although mean slope from the Oligocene section plots below the trend (Figure 5.2).

5.6 Discussion

5.6.1 Correlation of Rock Strength and Topographic Metrics

Ksn increases with increasing stratigraphic age of Cenozoic rocks (Figure 5.2), and for each stratigraphic age, we find a positive non-linear correlation between Ksn and shear strength at spatial scales of both intact rock pieces and fractured outcrops (Figure 5.3). This correlation suggests that variability in channel steepness across the TM is likely driven by the increasing resistance to stream incision with increasing rock strength (Moglen and Bras, 1995). Local relief, hillslope relief, and slope are also positively correlated with stratigraphic age (Figure 5.2), and non-linearly correlated with rock mass strength (Figure 5.3). If landscape form represents a strength-limited condition, this implies that topographic metrics reflect the critically-stable morphology between gravity acting to destabilize the slope and the resistance provided by rock strength (Schmidt and Montgomery, 1995; Korup, 2008).

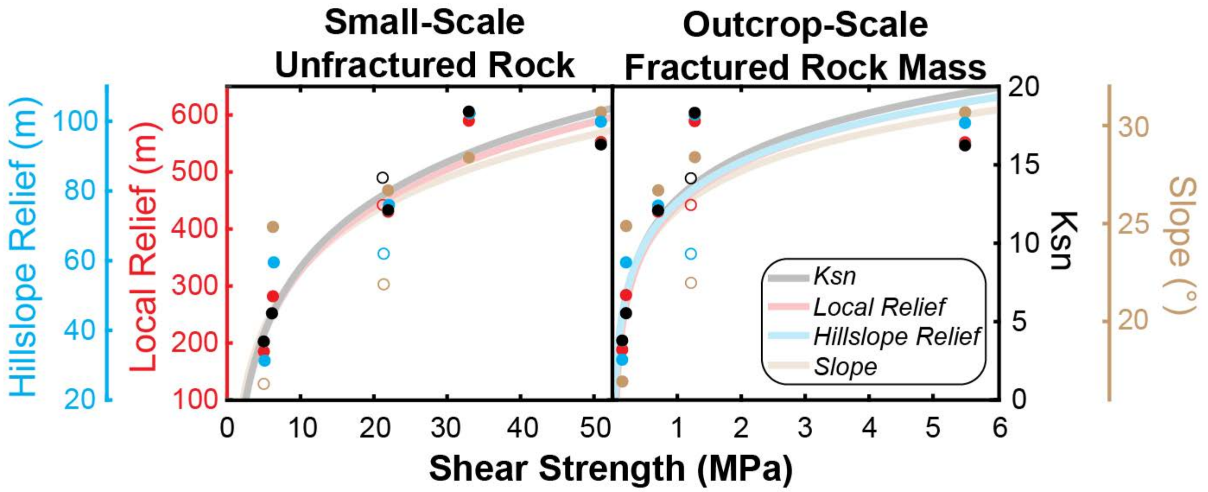

Figure 5.3: Mean Ksn, local relief (within a 1 km moving window), hillslope relief, and slope against shear strength of intact (unfractured) rock and outcrop-scale rock masses. Hollow points are Oligocene units, which were not included in regressions. Lines show best-fit logarithmic regressions between each topographic metric and shear strength.

Intact- and outcrop-scale shear strength demonstrate similar non-linear relationships with topographic metrics, despite order-of-magnitude differences in absolute strength values (Figure 5.3). Variability in burial depth and lithification is the dominant control on strength in this setting, which predominately contributes to intact rock strength but which also likely influences the susceptibility of these rock masses to fracturing (Townsend et al., 2021). In settings with crystalline or metamorphosed rock, tectonic deformation and weathering are likely the dominant controls on outcrop-scale strength (Medwedeff et al.; DiBiase et al., 2018). In these settings, measurements on intact rock pieces are likely to miss outcrop-scale gradients in strength, which are important for predicting hillslope stability, landscape response to extreme events, and long-term landscape evolution.

Slope and hillslope relief of the Oligocene strata plot below the trends defined by adjacent units (Figures 5.2 and 5.3). Outcrops of the Oligocene section are structurally controlled, with the surface exposure dominated by dip-slopes (Dibblee, 1990). The overlying topography is therefore not strength-limited, and topographic measurements on a local (per meter) scale are likely lower than what the strength of the material could support. Relief within a 1 km moving window and Ksn plot on the trends defined by other units (Figure 5.2), which is likely due to the larger spatial scales over which these metrics average.

5.6.2 Non-Linearity and Implications for Landscape Evolution

Chi-transformed longitudinal profiles (e.g. Perron and Royden, 2013) of tributary channels generally align with mainstem channels for small watersheds in the TM (Figures D.5-

D.17), and knickpoints are located on the most resistant stratigraphic units in the range (Townsend et al., 2021). These features are likely non-transient, and from these observations we suggest that landscape form in the TM reflects a steady-state condition (Willett and Brandon, 2002). As neither long-term uplift rates as inferred from low-temperature thermochronometry nor climate vary significantly along-strike, we hypothesize that differences in topographic metrics in the TM reflect gradients in rock strength.

The non-linear relationships between topographic metrics and shear strength implies that hillslope steepness, channel steepness, and relief initially increase rapidly with the strength of relatively weak rocks (< 20 MPA and < 1 MPa for intact and outcrop, respectively), but as rock shear strength increases, the corresponding rate of increase in topographic metrics incrementally decreases. Schmidt and Montgomery (1995) argue that bedrock landsliding, driven by rock mass strength, may limit mountain relief, particularly for ranges underlain by weak rocks. Our results at low rock strength are consistent with this interpretation but demonstrate that increases in shear strength beyond ~1 MPa (outcrop-scale) are not associated with additional gains in topographic metrics. This relationship suggests an upper limit to the contribution of rock strength to the relief structure of mountainous landscapes.

The relationships between shear strength (which aggregates the contributions of frictional and cohesive strength) and topographic metrics implies that even in steady-state landscapes, hillslope morphology reflects the strength of the underlying materials, particularly for weak rocks. From this observation, we caution against interpretation of steady-state from hillslope gradient alone. Although mature orogens may show common gradients due to the minimal contribution of relatively strong mid-crustal rocks to topography (Figure 5.3), nascent mountain ranges composed of young, poorly-lithified sediments will attain threshold morphologies that strongly reflect that strength of the underlying materials at gradients and relief lower than is typically associated with steady-state. Gradients in channel steepness and hillslope morphologies that would typically be interpreted as tectonic signals may instead reflect contrasts in rock strength (e.g. Duvall et al., 2004).

5.7 Conclusions

Topographic metrics in the TM are non-linearly correlated with the shear strength of both intact rock pieces and outcrop-scale fractured rock masses, despite an order-of-magnitude difference in strength at the two spatial scales. The non-linear relationship implies a strong dependency of topography on the strength of weak rock masses, but additional topographic gains diminish with increasing strength. These observations imply strength-dependent variability in the morphology of threshold hillslopes and cautions against interpretation of steady-state conditions from topography alone.

5.8 References

Atwater, T., 1998, Plate tectonic history of southern California with emphasis on the Western Transverse Ranges and northern Channel Islands, *in* Weigand, P.W. ed., Contributions to the geology of the Northern Channel Islands, Southern California, American Association of Petroleum Geologists, Pacific Section, p. 1–8.

Burbank, D.W., Leland, J., Fielding, E., Anderson, R.S., Brozovic, N., Reid, M.R., and Duncan, C., 1996, Bedrock incision, rock uplift and threshold hillslopes in the northwestern Himalayas: Nature, v. 379, p. 505–510, doi:10.1038/379505a0.

Clubb, F.J., Mudd, S.M., Hurst, M.D., and Grieve, S.W.D., 2020, Differences in channel and hillslope geometry record a migrating uplift wave at the Mendocino triple junction, California, USA: Geology, v. 48, p. 184–188, doi:10.1130/G46939.1.

Deere, D., and Miller, R., 1966, Engineering classification and index properties for intact rock.:

Dibblee, T.W., 1990, Geologic Map of the Fillmore Quadrangle: Santa Barbara Museum of Natural History,.

Dibblee, T.W., 1982, Regional geology of the Transverse Ranges Province of southern California, *in* Fefe, D.L. and Minch, J.A. eds., Geology and Mineral Wealth of the Califrnia Transverse Ranges, Santa Ana, California, South Coast Geological Society, Inc., p. 7–26.

DiBiase, R.A., Rossi, M.W., and Neely, A.B., 2018, Fracture density and grain size controls on the relief structure of bedrock landscapes: Geology, v. 46, p. 399–402, doi:10.1130/G40006.1.

Duvall, A.R., Kirby, E., and Burbank, D.W., 2004, Tectonic and lithologic controls on bedrock channel profiles and processes in coastal California: Journal of Geophysical Research, v. 109, p. 1–18, doi:10.1029/2003JF000086.

Farley, K.A., 2002, (U-Th)/He Dating: Techniques, Calibrations, and Applications: Reviews in Mineralogy and Geochemistry, v. 47, p. 819–844, doi:10.2138/rmg.2002.47.18.

Flowers, R.M., Ketcham, R.A., Shuster, D.L., and Farley, K.A., 2009, Apatite (U-Th)/He thermochronometry using a radiation damage accumulation and annealing model: Geochimica et Cosmochimica Acta, v. 73, p. 2347–2365, doi:10.1016/j.gca.2009.01.015.

Gallen, S.F., Clark, M.K., and Godt, J.W., 2015, Coseismic landslides reveal near-surface rock strength in a highrelief, tectonically active setting: Geology, v. 43, p. 11–14, doi:10.1130/G36080.1.

Hack, J.T., 1975, Dynamic equilibrium and landscape evolution: Theories of Landform Development: Publications in Geomorphology, p. 91–102, http://geomorphology.sese.asu.edu/Papers/Hack_1975.pdf.

Hoek, E., and Brown, E., 1980, Empirical Strength Criterion for Rock Masses: Journal of the Geotechnical Engineering Division, v. 106, p. 1013–1035, doi:10.1016/0148-9062(81)90766-X.

Hoek, E., and Brown, E., 1997, Practical estimates of rock mass strength: International Journal of Rock Mechanics and Mining Sciences, v. 34, p. 1165–1186, doi:10.1016/S1365-1609(97)80069-X.

Hoek, E., Carranza, C., and Corkum, B., 2002, Hoek-brown failure criterion – 2002 edition: Narms-Tac, p. 267–273, doi:10.1016/0148-9062(74)91782-3.

Hoek, E., and Marinos, P., 2000, Predicting tunnel squeezing problems in weak heterogeneous rock masses: Tunnels and Tunnelling International, v. Part 1-2, p. 1–20, https://www.rocscience.com/documents/hoek/references/H2000d.pdf%0Ahttp://www.rockscience.com/hoek/references/H2000d.pdf.

Kirby, E., and Whipple, K.X., 2012, Expression of active tectonics in erosional landscapes: Journal of Structural Geology, v. 44, p. 54–75, doi:10.1016/j.jsg.2012.07.009.

Korup, O., 2008, Rock type leaves topographic signature in landslide-dominated mountain ranges: Geophysical Research Letters, v. 35, p. 1–5, doi:10.1029/2008GL034157.

Medwedeff, W.G., Clark, M.K., Zekkos, D., West, A.J., and Chamlagain, D. What does the critical zone look like across an active orogen? Lessons from geotechnical observations in central Nepal: Journal of Geophysical Research: Earth Surface,.

Moglen, G.E., and Bras, R.L., 1995, The effect of spatial heterogeneities on geomorphic expression in a model of basin evolution: Water Resources Research, v. 31, p. 2613–2623.

Montgomery, D.R., 2001, Slope distributions, threshold hillslopes, and steady-state topography: American Journal of Science, v. 301, p. 432–454, doi:10.2475/ajs.301.4-5.432.

Montgomery, D.R., and Brandon, M.T., 2002, Topographic controls on erosion rates in tectonically active mountain ranges: Earth and Planetary Science Letters, v. 201, p. 481–489, doi:10.1016/S0012-821X(02)00725-2.

Perron, J.T., and Royden, L., 2013, An integral approach to bedrock river profile analysis: Earth Surface Processes and Landforms, v. 38, p. 570–576, doi:10.1002/esp.3302.

Reiners, P.W., Farley, K.A., and Hickes, H.J., 2002, He diffusion and (U-Th)/He thermochronometry of zircon: Initial results from Fish Canyon Tuff and Gold Butte: Tectonophysics, v. 349, p. 297–308, doi:10.1016/S0040-1951(02)00058-6.

Rockwell, T.K., 1988, Neotectonics of the San Cayetano fault, Transverse Ranges, California: Geological Society of America Bulletin, v. 100, p. 500–513.

Schmidt, K.M., and Montgomery, D.R., 1995, Limits to Relief: Science, v. 270, p. 617–620.

Sklar, L.S., and Dietrich, W.E., 2001, Sediment and rock strength controls on river incision into bedrock: Geology, v. 29, p. 1087–1090, doi:10.1130/0091-7613(2001)029<1087:SARSCO>2.0.CO.

Snyder, N.P., Whipple, K.X., Tucker, G.E., and Merritts, D.J., 2000, Stream profiles in the Mendocino triple junction region, northern California: GSA Bulletin, v. 112, p. 1250–1263, doi:10.1130/0016-7606(2000)112<1250:lrttfd>2.3.co;2.

Townsend, K.F., Clark, M.K., and Niemi, N.A. Low-temperature thermochronometric constraints on the timing of reverse fault initiation in the Western Transverse Ranges, southern California, USA: Tectonics,.

Townsend, K.F., Clark, M.K., and Zekkos, D., 2021, The control of depositional and erosional histories on the near-surface strength of clastic sedimentary rocks: Journal of Geophysical Research: Earth Surface,.

Townsend, K.F., Gallen, S.F., and Clark, M.K., 2020, Quantifying Near-Surface Rock Strength on a Regional Scale From Hillslope Stability Models: Journal of Geophysical Research: Earth Surface, v. 125, doi:10.1029/2020JF005665.

Western Regional Climate Center. https://wrcc.dri.edu. Accessed [17/04/2020].

Willett, S.D., and Brandon, M.T., 2002, On steady state in mountain belts: Geology, v. 30, p. 175–178, doi:10.1130/0091-7613(2002)030<0175.

Worden, R.H., and Burley, S.D., 2003, Sandstone Diagenesis: The Evolution of Sand to Stone, *in* Sandstone Diagenesis: Recent and Ancient, Malden, MA, Blackwell Publishing, p. 3–44, doi:10.1002/9781444304459.ch.

Acknowledgements

This work was supported by National Science Foundation award EAR-1528576, the Evolving Earth Foundation, the Geological Society of America, and the University of Michigan. We acknowledge the U.S. Forest Service, S. Dominguez, T. Cohen, J. Lynn, Seneca Resources, and Carbon Energy for field access and/or permits. We thank L. Knoper, A. Atwood, A. J. West, N. Midttun, B. Wang, and W. Medwedeff for assistance in the field.

Chapter 6: The Contribution of Rock-Mass Strength to Post-Wildfire Erosion, Santa Monica Mountains, Southern California, USA [5]

6.1 Abstract

Scale-dependent rock-mass strength is typically assumed to influence geomorphic processes by setting the erodibility of landscapes. However, the contribution of rock-mass strength to topographic form is often overlooked, rendering the interdependencies of rock strength, erosion, and topography largely unresolved. Here we leverage the erosional response of an extreme event to assess the contribution of rock strength to event-driven erosion and topography in the Santa Monica Mountains, southern California, USA, where a new dataset of rock-mass mechanical properties demonstrates strong landscape-scale gradients in strength. We map and quantify erosion following the 2018 Woolsey Fire with repeat airborne-LiDAR surveys, and we document positive relationships between area-normalized erosion, rock strength, and channel slope. We posit that strength is expressed as differences in slope that help set the erosional capacity of channels to transport sediment. Although near-surface materials have some intrinsic erodibility, in natural landscapes rock strength and slope become inexorably coupled, with slope dominating the erosional response following wildfire.

6.2 Plain Language Summary

In geomorphology, the primary contribution of rock and regolith strength to the evolution of topography is usually assumed to be in setting how easy it is to erode those materials. It is often suggested that weaker rocks should experience greater erosion rates than stronger rocks, but geomorphologists also recognize that where erosion rates are uniform, rock strength should contribute to the steepness of river channels and the height of hillslopes. These competing hypotheses have not been explicitly tested because rock strength is difficult to quantify broadly across landscapes. In this study, we assess the role of rock strength in controlling topography and erosion within the Santa Monica Mountains, southern California, USA, where we can leverage a a new dataset that quantitatively demonstrates strong variability in bedrock strength across the mountain range. We quantify volumes of erosion by measuring change between airborne-LiDAR

---

[5] Prepared for submission to *Geophysical Research Letters* for peer-review as: Townsend, K.F., Rengers, F.K., Clark, M.K., & DeLong, S.B., The contribution of rock-mass strength to post-wildfire erosion, Santa Monica Mountains, southern California, USA.

surveys flown before and after the 2018 Woolsey Fire. We find that the amount of erosion within the channel network increases with increasing mean strength of the underlying geologic formation, but that the slope of channels also increases with increasing mean strength. As erosion is most immediately sensitive to slope, we suggest that rock strength influences post-wildfire erosion primarily by setting the steepness of the overlying landscape, which controls the ability of channels to erode and transport sediment.

6.3 Introduction

The mechanical properties of rock masses are an important control in landscape evolution (Bursztyn et al., 2015; Gallen, 2018; Kirkpatrick et al., 2020). Variability in rock strength contributes to the erosional processes acting on hillslopes (Larsen et al., 2010; Schmidt & Montgomery, 1995) and channels (Bursztyn et al., 2015; Sklar & Dietrich, 2001), as well as overall rates of landscape change (Darling et al., 2019; Forte et al., 2016; Gallen, 2018; Sklar & Dietrich, 2001; Stock & Montgomery, 1999; Whipple & Tucker, 1999). All other variables being equal, landscapes underlain by weaker rocks are expected to erode more quickly than landscapes underlain by stronger rocks, as rock-mass strength sets the erodibility of bedrock channels and the ability of hillslopes to resist gravity (Schmidt & Montgomery, 1995; Sklar & Dietrich, 2001; Stock & Montgomery, 1999). However, in landscapes where long-term erosion rates are set by fault slip or bedrock uplift rates, the strength of bedrock and regolith is also expected to contribute to the steepness and relief of hillslopes and river channels (Bursztyn et al., 2015; DiBiase et al., 2018; Moglen & Bras, 1995; Montgomery & Brandon, 2002; Schmidt & Montgomery, 1995; Townsend et al., 2020, 2021). If long-term erosion rates are spatially uniform across steep topography, landscape form must adjust to gradients in rock-mass strength for shear stresses acting on channel beds and gravity acting on hillslopes to overcome strength-dependent resistance to erosion (Montgomery & Brandon, 2002).

Quantitatively untangling the interdependencies and feedbacks between rock strength, erosion rates, and topography has long been challenged by a paucity of data that quantifies the mechanical properties of rock masses over the broad spatial scales relevant to geomorphic systems (Gallen et al., 2015; Schmidt & Montgomery, 1995; Townsend et al., 2020, 2021). However, recent methodological advances have enabled us to resolve geologic and environmental controls on the scale-dependent spatial distribution of strength across landscapes (Gallen et al., 2015; Townsend et al., 2020, 2021). As we begin to recognize these gradients in rock mass properties, we should expect to observe strength-dependent variability in either the morphology or erosion of topography.

Wildfires are extreme geomorphic events that often drive rapid landscape change (Santi & Rengers, 2020), creating an opportunity to quantify erosional response as a function of rock strength. Recently burned landscapes are more susceptible to erosion due to reductions in vegetative cover and soil cohesion, thereby rendering hillslopes soils and unconsolidated materials easier to remove (Dibiase & Lamb, 2013; Gabet, 2003). Wildfires also drive an increase in overland flow due to a reduction of water infiltration into the subsurface and decreased surface roughness, resulting in increased downslope transport capacity (Doerr et al., 2000; Ebel & Moody, 2017; Schmidt et al., 2011; Shakesby & Doerr, 2006). These increases in erodibility and transport capacity often lead to erosion rates that are an order-of-magnitude or higher in the two to three years following wildfire than long-term background erosion rates (Moody & Martin, 2009; Orem & Pelletier, 2016; Warrick et al., 2012). These short-term, extreme erosion rates drive measurable topographic change within short time frames that can be mapped across landscapes, thereby enabling us to resolve potential controls on the magnitude and rates of erosion with finer spatial and temporal resolution than afforded by geochemical proxies for long-term erosion rates.

In this study, we resolve the contribution of rock strength to the morphology and erosion of a mountainous landscape. We focus on the San Monica Mountains (SMM), southern California, USA (Figure 6.1), where rock-mass strength data quantified over multiple spatial scales demonstrate a strong gradient in strength with the stratigraphic age and original burial depth of the underlying clastic sedimentary and volcaniclastic rocks (Townsend et al., 2021). The central SMM burned in the Woolsey Fire in November 2018, and subsequent winter storms caused hillslope rilling, erosion within low-order channels, and aggradation in mainstem channels. Here we map and quantify erosion caused by the Woolsey Fire with repeat airborne-LiDAR surveys of a 60 km^2 study area flown prior to the fire and following the subsequent rainy season (Figure 6.1). We assess the contribution of rock mass properties to erosion and topographic form by comparing area-normalized post-fire erosion fluxes with rock mass strength metrics mapped by across the landscape by stratigraphic age (Dibblee & Ehrenspeck, 1993). By focusing on this landscape, we can control for other variables known to influence post-wildfire erosion, including rainfall intensity, burn severity, soil compositional and hydrologic properties, vegetative types, and hydroclimatic regimes (Cannon, 2001; Cannon et al., 2008, 2010; Staley et al., 2017). The resulting dataset demonstrates an important relationship between rock-mass properties and the morphology and erosion of the overlying landscape, and has implications for our understanding of the evolution of steep topography with respect to rock-mass strength beyond the studied landscape.

6.4 Field Setting

The SMM are characterized by a Mediterranean climate, with generally cool winters and warm, dry summers. Mean annual precipitation reported by stations within the mountains range from 40 to 62 mm/yr, with most precipitation falling as rain during the winter months (WRCC, 2021). The 15-minute duration rainfall intensities are 39, 50, 60, 84, and 94 mm/hr for the 2-, 5-, 10-, 50-, and 100-year recurrence intervals (Perica et al., 2014). The SMM are in the Venturan-Angelno Coastal Hills ecoregion, and ground cover is predominantly annual grassland, California sagebrush, California buckwheat, mixed sage, chamise chaparral, mixed chaparral, and coast live oak (Griffith et al., 2016). Elevations range from sea level to 948 meters, with the Pacific Ocean bounding the southern margin of the range (Figure 6.1).

The central SMM are composed of Cretaceous through Miocene marine to terrestrial clastic sedimentary rocks and Miocene volcaniclastic rocks (Dibblee & Ehrenspeck, 1993). Mapped clastic sedimentary rocks are of a similar lithologic type (predominately sandstones, with interbedded shales) but vary in maximum burial depth as a function of geologic age (i.e., stratigraphic interval). Late-Cretaceous marine turbidites are overlain by ~6 km of broadly conformable shallow marine to non-marine strata of Paleocene to late Miocene age, which are in turn overlain by more spatially variable late-Miocene strata (Dibblee & Ehrenspeck, 1993). A thick sequence of Miocene volcanic and volcaniclastic rocks (Conejo Volcanics) outcrop extensively in the central and western SMM (Dibblee & Ehrenspeck, 1993). The clastic sedimentary and volcaniclastic rocks are being exhumed in the hanging walls of the Malibu Coast Fault and Anacapa-Dume Fault, which has been active since ~5-7 Ma (Niemi & Clark, 2018). Long-term erosion rates inferred from thermochronometry data reach ~ 1 mm/yr, but basin-averaged cosmogenic radionuclide concentrations suggest much lower erosion rates of ~0.1 to 0.4 mm/yr over the shorter integration time scale (Niemi & Clark, 2018; Portenga et al., 2017). These slower erosion rates match uplift rates inferred from marine terraces along the southern margin of the SMM (Shaller & Heron, 2004).

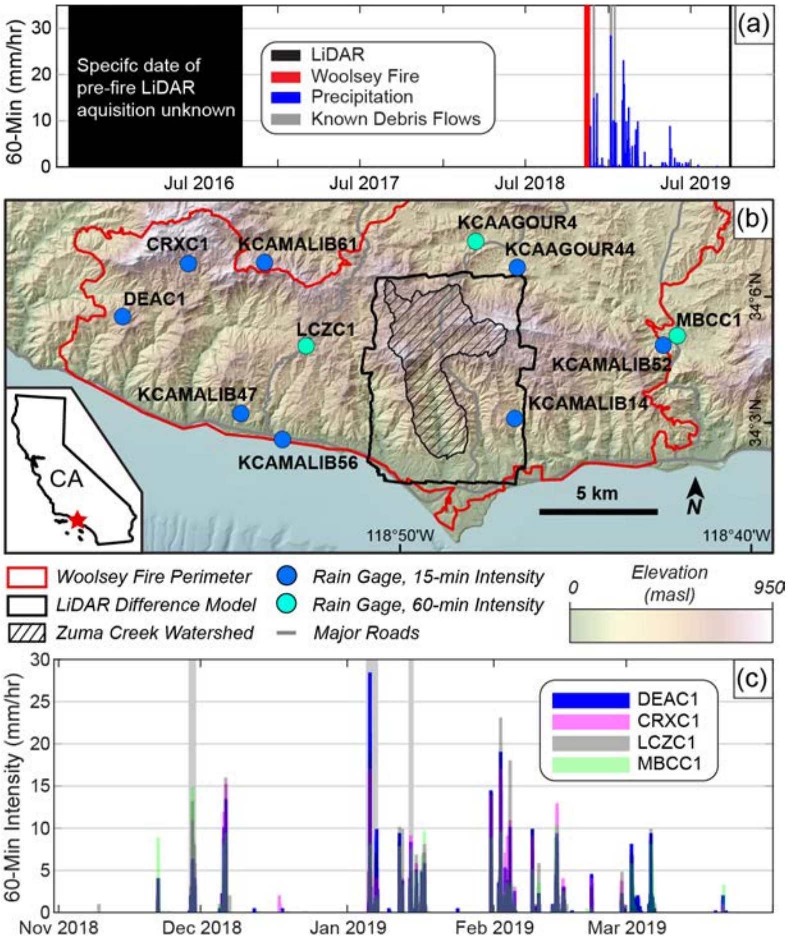

Figure 6.1: (a) Timeline of airborne-LiDAR surveys, Woolsey Fire, post-fire 60-minute rainfall intensities recorded by rain gages DEAC1, CRXC1, LCZC1, and MBCC1, and dates with known debris flows. (b) Map of field locations in the Santa Monica Mountains, with Zuma Creek watershed, LiDAR-derived topographic change model, Woolsey Fire perimeter, and rain gage locations. Inset: location of study site (red star) within southern California, USA. (c) 60-minute rainfall intensities from November 2018 to April 2019. For simplicity in visualizing the data, we are only highlighting four rain gages that span burn area, but their distributions are consistent with the other gages. Gray bars indicate dates with known debris flows.

The Woolsey fire burned 97,000 acres in the SMM and Simi Hills between November 8-21, 2018. Forty-one percent of the burn area is characterized as moderate- to high-severity burn (MTBS, 2018). The fire burned ~36% of the total area of the SMM, destroying 1,643 structures and resulting in three fatalities. Widespread landscape change was observed following heavy rainfall events on November 29, 2018, January 5, 2019, and January 14, 2019, causing full- to partial-closure of California Highway 1. Extensive rill formation, sediment-laden and debris flows, and sedimentation in high-order channels was observed following these rainfall events (Figures E.1-E.9).

We focus on the central SMM within Los Angeles County, where pre-fire airborne-LiDAR data was collected between July 2015 and October 2016. The 60.3 km^2 study area fully contains the watershed of Zuma Creek, which drains the relatively low-relief center of the range and the high-relief range front. 67% of this study area experienced moderate- to high-burn severity. Within this study area, we document coarsening-upwards levees on side channels to Zuma Creek that are indicative of debris flows (Figures E.1-E.2). We do not find definitive field evidence of debris flows on the Zuma Creek mainstem, although widespread recent sedimentation indicates heavily sediment-laden flows (Figure E.9).

6.5 Methods

We mapped erosion and deposition in the central SMM with repeat airborne-LiDAR surveys, and quantified the area and volumes of channel erosion with respect to mapped geologic formations. Using these data, we compared the sediment yield, normalized by area, of the material eroded against field metrics of rock mass mechanical properties quantified over multiple spatial scales (Townsend et al., 2021).

6.5.1 Rock Mass Strength

Rock strength data used in this study were taken from published results in Townsend et al., 2021. In-situ strength was measured using three field geotechnical approaches that average mechanical properties of rock masses over differing spatial scales. At the smallest spatial scale, we use a Schmidt hammer to measure the hardness of intact rock blocks between fractures (Original Schmidt, type N). This spring-loaded device measures rebound values that scale with laboratory measurements of uniaxial compressive strength of unfractured rock masses (Aydin & Basu, 2005; Deere & Miller, 1966; Selby, 1993). At progressively larger spatial scales, the strength of rock masses is limited by the presence of discontinuities (fractures, bedding planes), which produce detached rock blocks and provide pathways for fluid flow and weathering (Gallen et al., 2015; Hoek & Brown, 1980, 1997). At each field site, we characterize outcrop-scale fracture characteristics using the Geologic Strength Index (GSI) of Hoek & Marinos (2000). To aggregate the contributions of both the intact strength of the unfractured rock blocks, as well as the outcrop-scale fracture characteristics, we used the Hoek et al. (2002) criterion to calculate outcrop-scale rock mass shear strength from paired GSI and Schmidt hammer measurements (Townsend et al., 2021).

6.5.2 LiDAR Acquisition and Processing

Airborne LiDAR was collected prior to the Woolsey Fire by the Los Angeles Region Imagery Acquisition Consortium (LARIAC) between July 27, 2015 and October 18, 2016.

Following the wildfire and storms, the National Center for Airborne Laser Mapping (NCALM) flew a repeat airborne-LIDAR survey on September 25, 2019.

The pre-fire LiDAR point cloud produced by LARIAC was obtained from Open Topography in the NAD83 UTM Zone 11n coordinate system, and the post-fire LiDAR point cloud was provided by NCLAM in the WGS84 UTM Zone 11n coordinate system. We used the National Oceanic and Atmospheric Administration's vertical datum transformation tool, (VDatum) to convert the vertical coordinate system of the post-fire point cloud from NCALM from WGS84 to NAVD88 with GEOID 12b, and we closely aligned the datasets using Iterative Closest Point (ICP) registration in CloudCompare (Appendix E). After achieving a final RMS of 0.34, we extracted points along six transects perpendicular to paved roads to estimate the level of detection (LoD) at 20 cm (Figure E.10). We reclassified LiDAR returns in both point clouds to improve ground classifications and ensure consistency between point clouds (Appendix E).

We quantified volumes of material eroded and deposited from the summation of vertical elevation change between the pre- and post-fire airborne LiDAR point clouds (Figure 6.2; Bernard et al., 2020; DiBiase & Lamb, 2020; Lague et al., 2013). The change in ground return points between the two point clouds was estimated using the vertical option with the Multiscale Model to Model Cloud Comparison (M3C2) program, which quantifies point-to-point distances (Lague et al., 2013). The M3C2 program requires a user-specified projection scale (*d*) to define the diameter of a moving cylinder (Lague et al., 2013). We chose $d = 2.5$ m, because a cylinder of this diameter captures at least five points for 95% of the point cloud area in both point clouds (e.g. Lague et al., 2013). The M3C2 program also requires a user-defined normal scale (*D*) that defines the size of a spherical neighborhood around each core point. From Lague et al. (2013), *D* can be estimated using:

$$(1) \qquad \frac{D}{\sigma(d)} > 25$$

where $\sigma(d)$ is the slope-normalized standard deviation of elevation, which serves as a proxy for roughness. We found that $D = 5$ m satisfies this ratio for both points clouds over 95% of the point cloud areas. We specified a maximum depth of 10 m, and we used the pre-fire LARIAC point cloud for core points. We subsequently gridded the vertical change point data to a raster with pixel size 1.0 m^2, and we estimated volumes by multiplying the pixel area by the vertical change in each pixel. We infer that patterns of vertical elevation loss and gain reflect erosion and deposition due to the Woolsey Fire and subsequent rainfall events, although it is important to

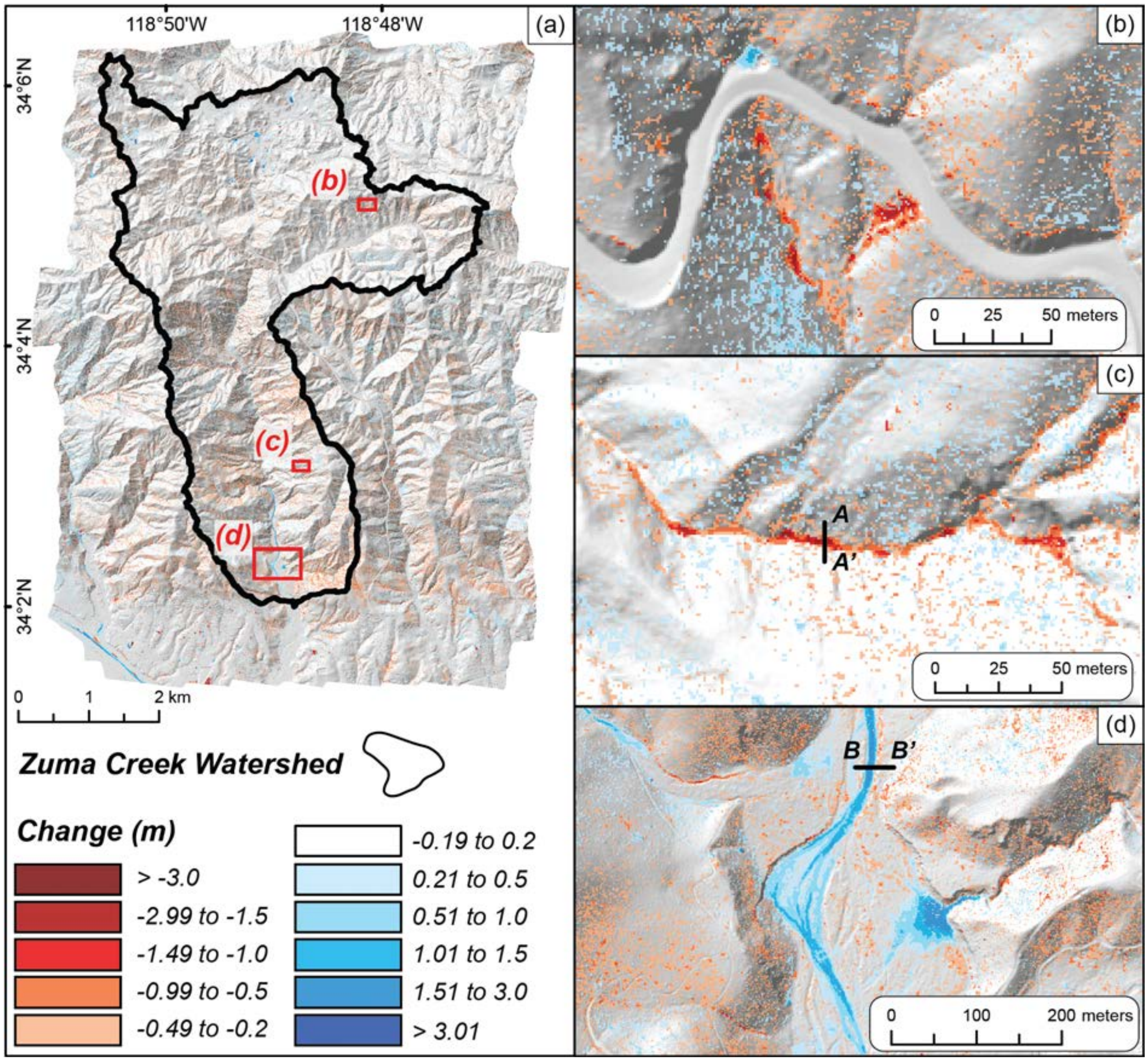

Figure 6.2: Surface change map derived from repeat airborne-LiDAR surveys in the central Santa Monica Mountains (location shown in Figure 1b). Blue shades represent deposition (positive values) and red shades represent erosion (negative values). (a) full 60.3 km^2 study area with rectangles indicating location of panels b, c, d. (b) inset map showing channel erosion below a paved road, which remained stable between LiDAR surveys. (c) erosion in low-order tributary channel to Zuma Creek. Location of cross-section A-A' (Figure 6.3d). (d) deposition on an alluvial fan and within lower Zuma Creek near the catchment outlet at the mountain front. Location of cross-section B-B' (Figure 6.3d)

note that three to four years elapsed between the LiDAR surveys, and nine months elapsed between the Woolsey fire and post-wildfire LiDAR acquisition. Field evidence including rilling, debris flows levees, and channel aggradation in Zuma Creek confirm that measurable topographic change occurred during storms in the post-fire period (Figures E.1-E.9).

We focused our analysis on vertical changes in the channel network, as the vertical change on hillslopes is lower and likely within the LOD. Further, vegetation regrowth on hillslopes in the nine months between the Woolsey Fire and post-wildfire LiDAR survey obscures change resulting from the fire. We defined the channel network as pixels with upstream contributing areas exceeding 500 m^2 using the D8 flow routing algorithm. We excluded all slopes >45°, as imperfect horizontal point cloud registration leads to increasing vertical errors that may exceed our LOD on steep slopes (Pelletier & Orem, 2014). However, the results of this study are relatively insensitive to specific values for the LOD, or a slope-dependent LOD (Figure E.11). For each geologic unit, we summed the negative per-pixel vertical change to quantify volumes of material removed (m^3). We then normalized eroded volumes by the aerial extent of each geologic formation within the channel network as a measure of erosional flux from each formation in units of m^3/m^2 (Figure 6.3). We also quantified sediment flux by aspect and slope using the same approach. For each slope or aspect bin, we sum the per-pixel negative vertical change and divided it by the sum of the pixel areas (Figure 6.3).

6.5.3 Precipitation

We assessed variability in rainfall intensity as a potential control on differences in post-wildfire erosion across our study area. Rainfall intensities were measured at 11 rain gages within and surrounding the study region, 6 of which recorded intensities over durations of 15 minutes or less (Figure 6.1) (MesoWest, 2021; Wunderground, 2021). As these stations cover a large geographic area mostly outside the study area, we use weather radar base reflectivity to infer potential patterns of precipitation intensity between rain gages (Figure E.12). Base reflectivity (dBZ) at the 0.50° elevation angle were acquired through the National Oceanic and Atmospheric Administration's radar toolkit (NOAA, 2020).

6.6 Results

6.6.1 Rock Strength

Mean Schmidt R, GSI, and shear strength collected from different sites within the SMM demonstrate an increase in strength with increasing stratigraphic age of clastic sedimentary units (Townsend et al., 2021). Mean Schmidt R values, which reflect the strength of intact rock blocks, range from 14.3 ± 14.2 from sites in the Middle- to late-Miocene formations at the top of the stratigraphic section, to 26.5 ± 15.6 in the Cretaceous units at the bottom of the stratigraphic section (Figure 6.4). GSI and Vs_{30}, which are measures of outcrop-scale rock mass properties, also increase over this interval. GSI values are generally < 50 in the Miocene units but increase to 62 ± 13 in the Oligocene units (Figure 6.4). Mean outcrop-scale shear strength, which incorporates both Schmidt R and GSI, demonstrate a progressive increase from 0.5 ± 0.36 MPa

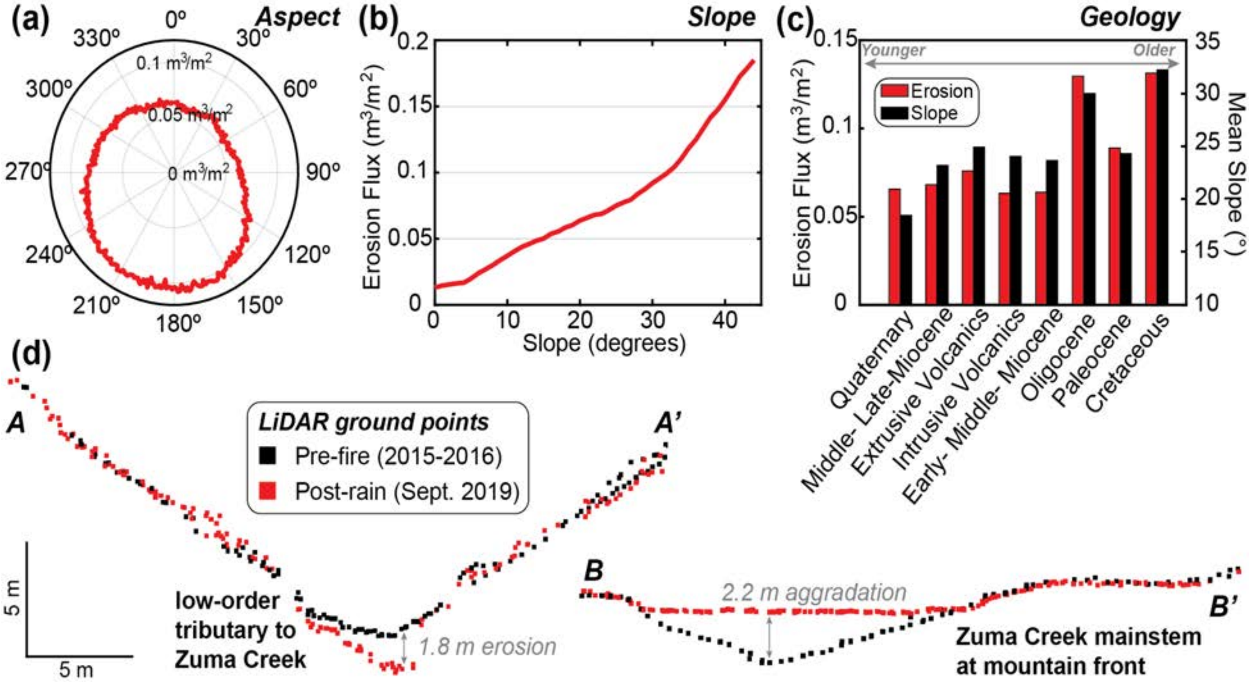

Figure 6.3: Flux of erosion (m^3/m^2) in convergent topographic positions by (a) aspect, (b) slope, and (c) geology. Mean topographic slope by geologic unit shown in (c). (D) cross sections of LiDAR ground return points. A-A' shows 1.8 m of erosion in a low-order channel. B'B' shows 2.2 m of aggradation in lower Zuma Creek at the mountain front. See Figure 6.2 for locations.

in the Middle- to Late-Miocene units to 1.21 ± 1.39 MPa in the Cretaceous units. These gradients in rock strength with stratigraphic age enabled us to map mean strength values across the study area using a published geologic map (Dibblee & Ehrenspeck, 1993).

6.6.2 Erosional Flux

The total volume of material eroded from the channel network within the LiDAR difference model area is 3.4x10^5 m^3. Miocene extrusive volcanic units, Middle- to Late-Miocene sedimentary units, and Oligocene sedimentary units yielded the most sediment, but these units are the most spatially extensive within the study area. When normalized by the spatial extent of each geologic formation, the erosional flux highest in the Oligocene (0.13 m^3/m^2), Paleocene (0.09 m^3/m^2), and Cretaceous (0.13 m^3/m^2) units, and lower in Quaternary through Middle-Miocene units (0.06 to 0.07 m^3/m^2) (Figure 6.3 and E.13). These erosional flux values are lower than the per-pixel LOD due to averaging across areas with undetected vertical change. We used a Kruskal-Wallis ANOVA to confirm that the per-pixel channel erosion within each geologic unit does not come from the same distribution. The distribution of channel erosion pixels from each geologic unit are statistically significant at $p < 0.05$, suggesting that erosion by geologic unit is uniquely different.

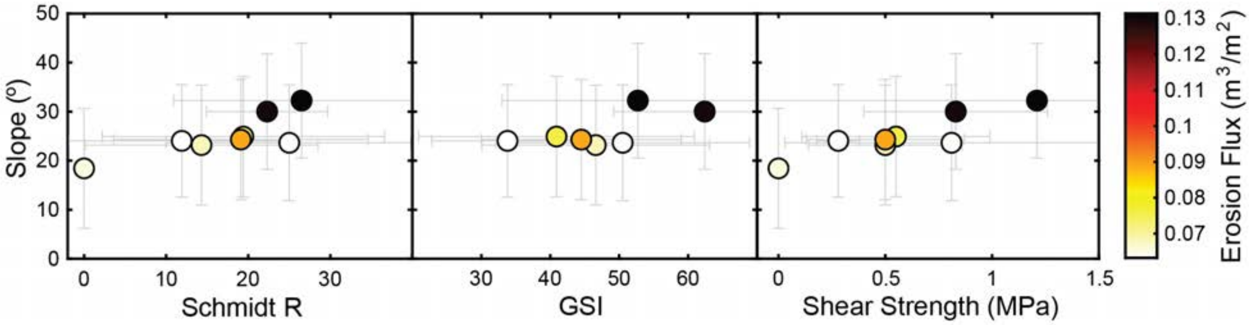

Figure 6.4: Mean slope against mean values of strength metrics including Schmidt hammer rebound (R) values, Geological Strength Index (GSI) observations, and outcrop-scale shear strength for each geologic unit. Points are colored by erosional flux. Erosion flux increases with mean slope, and mean slope increases with increasing strength of the underlying geologic unit.

The modal pixel slope of the study area is 29°, but the modal slope of material eroded from the channel network is steeper at 37°. However, when normalized for the spatial extent of each slope value, the erosional flux increases with increasing slope up to our 45° measurement threshold (Figure 6.3). We observe a strong association of erosional flux and aspect, and south-facing slopes eroded nearly double the volume of material of north-facing slopes (Figure 6.3). The tendency for south-facing slopes (north-facing slope in southern hemisphere) to experience greater erosion than north-facing slopes has been observed following other wildfires and is likely related to aspect-controlled soil moisture, pre-fire vegetation densities, and burn intensities (Abrahams et al., 2018; Inbar et al., 2018).

Fifteen-minute rainfall intensities recorded from rain gages in the SMM outside the study area peak at 26 mm/hr during the November 29, 2018 storm, 64 mm/hr during the January 6, 2019 storm, and 21 mm/yr during the January 14, 2021 storm (Figure E.12). Despite geographic separation of up to 20 km, rain gages throughout the SMM generally recorded similar peak rainfall intensities accept for station DEAC1 during the January 6, 2019 storm, which recorded 64 mm/hr while all other stations recorded peak intensities of 20-30 mm/hr. Weather radar data record bands of similar reflectivity that sweep across the SMM during each storm, suggesting similar rainfall intensities throughout each storm (Figure E.12). From these observations, we do not expect strong differences in rainfall intensity across the study area that could have contributed to the observed differences in erosional flux.

6.7 Discussion

The LiDAR-derived change map represents the net elevation change caused by the fire, including post-wildfire sediment loading, sediment evacuation, and potentially bedrock incision.

However, we are unable to resolve the relative contributions of sediment evacuation and bedrock incision. Soil survey data indicate that hillslope soils in the central SMM are generally thin (~30cm, Natural Resources Conservation Service, 2021), but data constraining the depth of unconsolidated material overlying bedrock channels prior to the fire is unavailable. Field reconnaissance and satellite imagery suggest that prior to the fire, most low-order channels had variable bedrock exposure and alluvial reaches, and that post-wildfire debris and sediment-laden flows excavated many channels formerly mantled in fill down to bedrock (e.g. Figure S3). These observations raise the possibility that some degree of bedrock channel scour may have also occurred but given the difference in erodibility between unconsolidated materials and bedrock, we infer that our results predominantly reflect evacuation of sediment. This inference is consistent with observations from other wildfires that suggest that post-wildfire erosion occurs predominantly by re-working sediment that was already detached from underlying bedrock (DeLong et al., 2018; Rengers et al., 2016; Staley et al., 2014).

We document a positive correlation between erosional flux from the channel network and Schmidt R, GSI, and shear strength (Figure 6.4). Although we might expect that weaker rocks should erode more quickly (e.g. Sklar & Dietrich, 2001), our results instead demonstrate that post-wildfire erosion increases with increasing rock mass strength, suggesting that the gradient in rock strength within the SMM does not manifest as a gradient in erodibility. Instead, it appears that differences in rock strength are expressed in the relief structure of the overlying landscape (e.g. DiBiase et al., 2018; Moglen & Bras, 1995; Montgomery & Brandon, 2002; Schmidt & Montgomery, 1995; Townsend et al., 2020). We find that the mean slope of channels and hillslopes overlying each geologic unit increases with the mean strength of each geologic category (Figures 6.3 and 6.4), suggesting that landscape form has adjusted to the underlying bedrock and regolith strength (Figure 6.4). As erosion increases with increasing slope (Figures 6.3 and 6.4), we suggest that the increasing strength of bedrock units leads to increasing mean slope of the overlying landscape, thereby increasing the susceptibility of the overlying sediment to erosion following wildfire.

Metrics of rock mass strength presented here characterize the properties of the weathered to unweathered bedrock, rather than the mechanical properties of the overlying unconsolidated material, but erosion inferred from our LiDAR-derived topographic change model most likely reflects the evacuation of this overlying fill. We therefore infer that the observed relationship between bedrock strength, slope, and evacuation of unconsolidated sediment from channels reflects slope-dependent variability in shear stress. As channel slope increases with increasing rock strength, shear stress and sediment transport capacity should also increase (Bursztyn et al., 2015; Pederson & Tressler, 2012). Prior to wildfire, the ability of channels to evacuate unconsolidated material is limited by both the available discharge, as well as vegetative cover that shield. Wildfires simultaneously increases overland flow while reducing vegetation cover and soil cohesion (Dibiase & Lamb, 2013; Gabet, 2003; Schmidt et al., 2011; Shakesby & Doerr, 2006), thereby generating enhanced discharge of dense sediment-laden flows and the shear stress necessary to evacuate unconsolidated material from the channels. Within this framework, we posit that strength-dependent channel gradients exert a control on the post-wildfire shear stresses acting on the channel bed, which then sets the erosional capacity of channels to transport unconsolidated soil, sediment, and regolith. Through this process, rock mass strength influences the event-driven erosional response through coupling with slope.

Incorporating rock strength or lithology as an input to the U.S. Geological Survey emergency assessments of post-wildfire debris flows has been suggested as a future step to improving model predictions (Staley et al., 2016, 2017). Results from this study suggest that rock strength is expressed in landscape morphology and sets the local topographic slope, rather than influencing landscape erodibility following wildfire. As slope is already an input to these models, incorporating rock strength as an additional input variable is unlikely to significantly improve model results. However, these results do not preclude lithologic type as a possible control on post-wildfire erosion. The lithologic type of bedrock underlying burned catchments has been hypothesized to influence the detachment and transport of sediment and soil particles following wildfire, potentially by setting the size and shape of disaggregated material (DiBiase & Lamb, 2020; Moody et al., 2008). Differences in the erosional response on either side of the San Gabriel Fault Zone following the 2009 Station Fire in the San Gabriel Mountains may have been associated with contrasting lithologic types on either side of the fault (DiBiase & Lamb, 2020). Conversely, Moody et al. (2008) find that lithologic type does not appear to influence erosional efficiencies following wildfire, although significant differences in rainfall intensities between their study areas challenge the comparison. Further work is needed to resolve potential lithology-dependent differences in post-wildfire erosion and debris flow hazards.

6.8 Conclusions

Rock mass mechanical properties likely play an important role in the evolution of mountainous landscapes, but quantifying the contribution of rock strength to landscape form and geomorphic processes has previously been challenged by a lack of data. Here we leverage a new dataset of scale-dependent rock-mass strength to assess the interdependencies of strength, topography, and extreme event-driven erosion rates. In the central Santa Monica Mountains, we document positive relationships between rock mass mechanical properties, post-wildfire channel erosion as quantified from repeat airborne-LiDAR surveys, and channel gradients. We suggest that rock-mass strength indirectly controls erosion by setting channel gradients, which controls shear stress acting on the channel bed and thus the ability of channels to erode and evacuate material following wildfire. While most earth materials likely have some inherent erodibility, slope and rock strength are coupled in real landscapes, and variability in slope dominates the erosional response to an extreme event.

6.9 References

Abrahams, E. R., Kaste, J. M., Ouimet, W., & Dethier, D. P. (2018). Asymmetric hillslope erosion following wildfire in Fourmile Canyon, Colorado. *Earth Surface Processes and Landforms*, *43*(9), 2009–2021. https://doi.org/10.1002/esp.4348

Aydin, A., & Basu, A. (2005). The Schmidt hammer in rock material characterization. *Engineering Geology*, *81*(1), 1–14. https://doi.org/10.1016/j.enggeo.2005.06.006

Bernard, T., Lague, D., & Steer, P. (2020). Beyond 2D inventories: synoptic 3D landslide volume calculation from repeat LiDAR data. *Earth Surface Dynamics Discussions*, *[preprint]*. https://doi.org/10.5194/esurf-2020-73

Bursztyn, N., Pederson, J. L., Tressler, C., Mackley, R. D., & Mitchell, K. J. (2015). Rock strength along a fluvial transect of the Colorado Plateau - quantifying a fundamental control on geomorphology. *Earth and Planetary Science Letters*, *429*, 90–100. https://doi.org/10.1016/j.epsl.2015.07.042

Cannon, S. H. (2001). Debris-flow generation from recently burned watersheds. *Environmental & Engineering Geoscience*, *7*, 321–341.

Cannon, S. H., Gartner, J. E., Wilson, R. C., Bowers, J. C., & Laber, J. L. (2008). Storm rainfall conditions for floods and debris flows from recently burned areas in southwestern Colorado and southern California. *Geomorphology*, *96*(3–4), 250–269. https://doi.org/10.1016/j.geomorph.2007.03.019

Cannon, S. H., Gartner, J. E., Rupert, M. G., Michael, J. A., Rea, A. H., & Parrett, C. (2010). Predicting the probability and volume of postwildfire debris flows in the intermountain western United States. *Bulletin of the Geological Society of America*, *122*(1–2), 127–144. https://doi.org/10.1130/B26459.1

Darling, A., Whipple, K., Bierman, P., Clarke, B., & Heimsath, A. M. (2019). Resistant Rock Layers Amplify Cosmogenicaly-Determined Erosion Rates. *Earth Surface Processes and Landforms*. https://doi.org/10.1002/esp.4730

Deere, D., & Miller, R. (1966). *Engineering classification and index properties for intact rock*.

DeLong, S. B., Youberg, A. M., DeLong, W. M., & Murphy, B. P. (2018). Post-wildfire landscape change and erosional processes from repeat terrestrial lidar in a steep headwater catchment, Chiricahua Mountains, Arizona, USA. *Geomorphology*, *300*, 13–30. https://doi.org/10.1016/j.geomorph.2017.09.028

Dibblee, T. W., & Ehrenspeck, H. E. (1993). *Geologic Map of the Point Dume Quadrangle, Los Angeles and Ventura Counties, California*. Santa Barbara, California: Dibblee Geological Foundation.

Dibiase, R. A., & Lamb, M. P. (2013). Vegetation and wildfire controls on sediment yield in bedrock landscapes. *Geophysical Research Letters*, *40*(6), 1093–1097. https://doi.org/10.1002/grl.50277

DiBiase, R. A., & Lamb, M. P. (2020). Dry sediment loading of headwater channels fuels post-wildfire debris flows in bedrock landscapes. *Geology*, *48*(2), 189–193. https://doi.org/10.1130/G46847.1

DiBiase, R. A., Rossi, M. W., & Neely, A. B. (2018). Fracture density and grain size controls on the relief structure of bedrock landscapes. *Geology*, *46*(5), 399–402. https://doi.org/10.1130/G40006.1

Doerr, S. H., Shakesby, R. A., & Walsh, R. P. D. (2000). Soil water repellency: Its causes, characteristics and hydro-geomorphological significance. *Earth Science Reviews*, *51*(1–4), 33–65. https://doi.org/10.1016/S0012-8252(00)00011-8

Ebel, B. A., & Moody, J. A. (2017). Synthesis of soil-hydraulic properties and infiltration timescales in wildfire-affected soils. *Hydrological Processes*, *31*, 324–340. https://doi.org/10.1002/hyp.10998

Forte, A. M., Yanites, B. J., & Whipple, K. X. (2016). Complexities of landscape evolution during incision through layered stratigraphy with contrasts in rock strength. *Earth Surface Processes and Landforms*, *41*(12), 1736–1757. https://doi.org/10.1002/esp.3947

Gabet, E. J. (2003). Post-fire thin debris flows: Sediment transport and numerical modelling. *Earth Surface Processes and Landforms*, *28*, 1341–1348. https://doi.org/10.1002/esp.590

Gallen, S. F. (2018). Lithologic controls on landscape dynamics and aquatic species evolution in post-orogenic mountains. *Earth and Planetary Science Letters*, *493*, 150–160. https://doi.org/10.1016/j.epsl.2018.04.029

Gallen, S. F., Clark, M. K., & Godt, J. W. (2015). Coseismic landslides reveal near-surface rock strength in a highrelief, tectonically active setting. *Geology*, *43*(1), 11–14. https://doi.org/10.1130/G36080.1

Griffith, G. E., Omernik, J. M., Smith, D. W., Cook, T. D., Tallyn, E., Moseley, K., & Johnson, C. B. (2016). *Ecoregions of California (poster). U.S. Geological Survey Open-File Report 2016–1021, with map, scale 1:1,100,000,*.

Hoek, E., & Brown, E. (1980). Empirical Strength Criterion for Rock Masses. *Journal of the Geotechnical Engineering Division*. https://doi.org/10.1016/0148-9062(81)90766-X

Hoek, E., & Brown, E. (1997). Practical estimates of rock mass strength. *International Journal of Rock Mechanics and Mining Sciences*, *34*(8), 1165–1186. https://doi.org/10.1016/S1365-1609(97)80069-X

Hoek, E., & Marinos, P. (2000). Predicting tunnel squeezing problems in weak heterogeneous rock masses. *Tunnels and Tunnelling International*, *Part 1-2*(November), 1–20. Retrieved from https://www.rocscience.com/documents/hoek/references/H2000d.pdf%0Ahttp://www.rocks cience.com/hoek/references/H2000d.pdf

Hoek, E., Carranza, C., & Corkum, B. (2002). Hoek-brown failure criterion – 2002 edition. *Narms-Tac*, 267–273. https://doi.org/10.1016/0148-9062(74)91782-3

Inbar, A., Nyman, P., Rengers, F. K., Lane, P. N. J., & Sheridan, G. J. (2018). Climate Dictates Magnitude of Asymmetry in Soil Depth and Hillslope Gradient. *Geophysical Research Letters*, *45*, 6514–6522. https://doi.org/10.1029/2018GL077629

Kirkpatrick, H. M., Moon, S., Yin, A., & Harrison, T. M. (2020). Impact of fault damage on eastern Tibet topography. *Geology*, *48*. https://doi.org/10.1130/G48179.1/5137742/g48179.pdf

Lague, D., Brodu, N., & Leroux, J. (2013). Accurate 3D comparison of complex topography with terrestrial laser scanner: Application to the Rangitikei canyon (N-Z). *ISPRS Journal of Photogrammetry and Remote Sensing*, *82*(February 2013), 10–26. https://doi.org/10.1016/j.isprsjprs.2013.04.009

Larsen, I. J., Montgomery, D. R., & Korup, O. (2010). Landslide erosion controlled by hillslope material. *Nature Geoscience*, *3*(4), 247–251. https://doi.org/10.1038/ngeo776

MesoWest. (2021). Surface Weather Maps-California.

Moglen, G. E., & Bras, R. L. (1995). The effect of spatial heterogeneities on geomorphic expression in a model of basin evolution. *Water Resources Research*, *31*(10), 2613–2623.

Montgomery, D. R., & Brandon, M. T. (2002). Topographic controls on erosion rates in tectonically active mountain ranges. *Earth and Planetary Science Letters*, *201*(3–4), 481–489. https://doi.org/10.1016/S0012-821X(02)00725-2

Moody, J. A., & Martin, D. A. (2009). Synthesis of sediment yields after wildland fire in different rainfall regimes in the western United States. *International Journal of Wildland Fire*, *18*, 96–115. https://doi.org/10.1071/WF07162

Moody, J. A., Martin, D. A., & Cannon, S. H. (2008). Post-wildfire erosion response in two geologic terrains in the western USA. *Geomorphology*, *95*(3–4), 103–118. https://doi.org/10.1016/j.geomorph.2007.05.011

MTBS. (2018). Normalized Burn Ratio Map - Woolsey Fire. Retrieved May 17, 2021, from https://www.mtbs.gov/viewer/index.html

Natural Resources Conservation Service, U. S. D. of A. (2021). Web Soil Survey.

Niemi, N. A., & Clark, M. K. (2018). Long-term exhumation rates exceed paleoseismic slip rates in the central Santa Monica Mountains, Los Angeles County, California. *Geology*, *46*(1), 63–66. https://doi.org/10.1130/G39388.1

NOAA. (2020). Weather and Climate Toolkit. Retrieved March 15, 2021, from https://www.ncdc.noaa.gov/wct/

Orem, C. A., & Pelletier, J. D. (2016). The predominance of post-wildfire erosion in the long-term denudation of the Valles Caldera, New Mexico. *Journal of Geophysical Research F: Earth Surface*, *121*(5), 843–864. https://doi.org/10.1002/2015JF003663

Pederson, J. L., & Tressler, C. (2012). Colorado River long-profile metrics, knickzones and their meaning. *Earth and Planetary Science Letters*, *345–348*, 171–179. https://doi.org/10.1016/j.epsl.2012.06.047

Pelletier, J. D., & Orem, C. A. (2014). How do sediment yields from post-wildfire debris-laden flows depend on terrain slope, soil burn severity class, and drainage basin area? Insights from airborne-LiDAR change detection. *Earth Surface Processes and Landforms*, *39*(13), 1822–1832. https://doi.org/10.1002/esp.3570

Perica, S., Dietz, S., Heim, S., Hiner, L., Maitaria, K., Martin, D., et al. (2014). *Precipitation-*

Frequency Atlas of the United States, California. *NOAA Atlas 14* (Vol. 6). Washington. D.C.

Portenga, E. W., Clark, M. K., & Niemi, N. A. (2017). Spatial and Temporal Patterns of Motion Along the Malibu Coastal Fault Inferred from 10Be Erosion Rates. In *American Geophysical Union, Fall Meeting, Abstract #EP32C-02*. New Orleans, LA.

Rengers, F. K., Tucker, G. E., Moody, J. A., & Ebel, B. A. (2016). Illuminating wildfire erosion and deposition patterns with repeat terrestrial lidar. *Journal of Geophysical Research: Earth Surface*, *121*(3), 588–608. https://doi.org/10.1002/2015JF003600

Santi, P. M., & Rengers, F. K. (2020). *Wildfire and Landscape Change*. *Reference Module in Earth Systems and Environmental Sciences* (2nd ed.). Elsevier Inc. https://doi.org/10.1016/b978-0-12-818234-5.00017-1

Schmidt, K. M., & Montgomery, D. R. (1995). Limits to Relief. *Science*, *270*(5236), 617–620.

Schmidt, K. M., Hanshaw, M. N., Howle, J. F., Kean, J. W., Staley, D. M., Stock, J. D., & Bawdeng, W. (2011). Hydrologic conditions and terrestrial laser scanning of post-fire debris flows in the San Gabriel Mountains, CA, U.S.A. *International Conference on Debris-Flow Hazards Mitigation: Mechanics, Prediction, and Assessment, Proceedings*, 583–593. https://doi.org/10.4408/IJEGE.2011-03.B-064

Selby, M. J. (1993). *Hillslope materials and processes*. Oxford University Press.

Shakesby, R. A., & Doerr, S. H. (2006). Wildfire as a hydrological and geomorphological agent. *Earth-Science Reviews*, *74*, 269–307. https://doi.org/10.1016/j.earscirev.2005.10.006

Shaller, P. J., & Heron, C. W. (2004). Proposed revision of marine terrace extent, geometry, and rates of uplift, Pacific Palisades, California. *Environmental and Engineering Geoscience*, *10*(3), 253–275. https://doi.org/10.2113/10.3.253

Sklar, L. S., & Dietrich, W. E. (2001). Sediment and rock strength controls on river incision into bedrock. *Geology*, *29*(12), 1087–1090. https://doi.org/10.1130/0091-7613(2001)029<1087:SARSCO>2.0.CO

Staley, D. M., Wasklewicz, T. A., & Kean, J. W. (2014). Characterizing the primary material sources and dominant erosional processes for post-fire debris-flow initiation in a headwater basin using multi-temporal terrestrial laser scanning data. *Geomorphology*, *214*, 324–338. https://doi.org/10.1016/j.geomorph.2014.02.015

Staley, D. M., Negri, J. A., Kean, J. W., Laber, J. L., Tillery, A. C., & Youberg, A. M. (2016). Updated logistic regression equations for the calculation of post-fire debris-flow likelihood in the western United States. U.S. Geological Survey Open-File Report 2016–1106. https://doi.org/10.3133/ofr20161106

Staley, D. M., Negri, J. A., Kean, J. W., Laber, J. L., Tillery, A. C., & Youberg, A. M. (2017). Prediction of spatially explicit rainfall intensity–duration thresholds for post-fire debris-flow generation in the western United States. *Geomorphology*, *278*, 149–162. https://doi.org/10.1016/j.geomorph.2016.10.019

Stock, J. D., & Montgomery, D. R. (1999). Geologic constraints on bedrock river incision using the stream power law. *Journal of Geophysical Research: Solid Earth*, *104*(B3), 4983–4993. https://doi.org/10.1029/98JB02139

Townsend, K. F., Gallen, S. F., & Clark, M. K. (2020). Quantifying Near-Surface Rock Strength on a Regional Scale From Hillslope Stability Models. *Journal of Geophysical Research: Earth Surface*, *125*(7). https://doi.org/10.1029/2020JF005665

Townsend, K. F., Clark, M. K., & Zekkos, D. (2021). Profiles of near-surface rock mass strength across gradients in burial, erosion, and time. *Journal of Geophysical Research: Earth*

Surface, *126*(e2020JF005694). Retrieved from https://doi.org/10.1029/2020JF005694

Warrick, J. A., Hatten, J. A., Pasternack, G. B., Gray, A. B., Goni, M. A., & Wheatcroft, R. A. (2012). The effects of wildfire on the sediment yield of a coastal California watershed. *Bulletin of the Geological Society of America*, *124*(7–8), 1130–1146. https://doi.org/10.1130/B30451.1

Whipple, K. X., & Tucker, G. E. (1999). Dynamics of the stream-power river incision model: Implications for height limits of mountain ranges, landscape response timescales, and research needs. *Journal of Geophysical Research*, *104*(B8), 17661. https://doi.org/10.1029/1999JB900120

Wunderground. (2021). WunderMap Precipitation Summaries.

Data Availability Statement

Rock mass strength data are available from the Deep Blue data repository at https://doi.org/10.7302/krah-yx31. The airborne-LiDAR datasets are available from Open Topography at https://opentopography.org. Rainfall intensity data were obtained from MesoWest at https://mesowest.utah.edu and Weather Underground at https://www.wunderground.com.

Acknowledgements

This work was supported by an INTERNSHIP supplement to NSF award EAR-1640797, NSF award EAR-1528576, the Evolving Earth Foundation, the Geological Society of America, and the University of Michigan. We thank the National Center for Airborne Laser Mapping for the post-wildfire LiDAR survey, and we acknowledge the U.S. National Park Service for field access and permits. L. Knoper, N. Midttun, and B. Wang assisted us in the field.

Chapter 7: Conclusions

7.1 Summary of primary dissertation results

This dissertation focusses on understanding the role of mass mechanical properties in landscape evolution and active tectonism. Although rock strength has long been hypothesized as a major control on landscape morphology and evolution, many of the factors controlling strength have been unquantified due to a lack of techniques that quantify strength at the appropriate spatial scale (Gallen et al., 2015; Schmidt & Montgomery, 1995). Chapter 2 of this dissertation focusses on developing and testing two techniques for quantifying cohesive and frictional strength at the hillslope-scale using digital topography, earthquake ground acceleration, and a mapped co-seismic landslide inventory in the eastern Topatopa Mountains, within the Western Transverse Ranges (WTR) of southern California, USA. Chapter 3 builds on this work to quantify rock mass properties over multiple spatial scales using field-based approaches within the Topatopa Mountains study site of Chapter 2, as well as older sedimentary rocks in the western Topatopa Mountains and correlative units in adjacent mountain ranges within the broader WTR. By adapting the Hoek & Brown criterion (Hoek et al., 2002) to produce shallow depth profiles of rock mass shear strength, I demonstrate order-of-magnitude differences in strength that appear to be related to maximum burial depth of clastic sedimentary rocks. I also resolve smaller differences in strength (~25%) that appear to be related to erosion rates as quantified from ^{10}Be cosmogenic radionuclides and my low-temperature thermochronometry dataset. With Chapter 4, I expand the low-temperature thermochronometry dataset from Chapter 3 to resolve the timing of reverse fault initiation and patterns of fault propagation within the broader WTR. Results suggest that the Big Bend restraining bend is not the primary source of shortening within the WTR, and lithosphere-scale contrasts in rheology and strength likely play a larger role in localizing regional deformation within the WTR.

The final two chapters of this dissertation focus on understanding the contributions of rock strength to topography and erosion. In Chapter 5, I compare topographic metrics including normalized channel steepness, slope, and relief to the rock strength dataset from Chapter 3 and thermochronometry dataset from Chapter 4 to demonstrate a positive but non-linear relationship between topography and rock mass shear strength. This relationship implies that the height and steepness of topography are sensitive to the strength of relatively weak rocks, but that additional topographic gains progressively diminish with the exposure of stronger rock masses. In Chapter 6, I focus on resolving the contribution of rock strength to the volume and distribution of channel erosion following wildfire. Results demonstrate that rock mass shear strength is positively correlated with erosional flux following wildfire, but that mean channel gradients also increase with increasing strength. Therefore, variability in rock strength controls post-wildfire erosion by setting the steepness of the overlying landscape, which influences the capacity of channels to evacuate material following wildfire.

7.1.1 Chapter 2 summary

This chapter focusses on developing and refining two approaches methods for extracting rock mass strength information from digital datasets at geomorphically-relevant spatial scales. The first approach uses hillslope morphology extracted from digital elevation models to estimate strength under static conditions using the Culmann finite-slope stability model, which may be generally exportable to other landscapes as a way to quantify rock strength from topography. The second approach leverages earthquake-driven landslide inventories and peak ground accelerations as a means to invert for rock strength properties using the simplified Newmark infinite-slope stability model for co-seismic landsliding. The spatial distribution afforded by these methods enabled me to quantify rock strength across a tectonic gradient in the eastern Topatopa Mountains, where differences in fault motion exposed young (Miocene through Plio-Quaternary) sedimentary rocks with variable burial and exhumation histories. Results from each model approach show similar trends in strength with respect to stratigraphic position and have comparable strength estimates to the lowest values of published direct-shear test data. Cohesion estimates are low, with Culmann model results ranging from 3 to 60 kPa and Newmark model results from 6 to 30 kPa, while friction angle estimates range from 24 to 44 degrees from the Culmann model. I find that maximum burial depth exerts the strongest apparent control on the strength of these young sedimentary rocks, likely through diagenetic changes in porosity, cementation, and ultimately, lithification.

7.1.2 Chapter 3 summary

This chapter builds on the remote sensing approaches developed and applied in Chapter 2 to quantify rock mass mechanical properties across environmental gradients using field-based techniques. At 210 field sites, I assessed outcrop-scale structure and weathering conditions on fracture surfaces using the Geological Strength Index (GSI), and I quantified the intact (unfractured) strength of rock blocks using Schmidt hammer hardness values. I developed an approach to produce shallow depth profiles of rock mass shear strength from these measures of outcrop-scale fracture characteristics and intact strength by adapting the Hoek & Brown criterion (Hoek et al., 2002). At 60 sites, I complemented these projected subsurface shear strength profiles with subsurface S-wave velocities on depth profiles measured from short geophysical arrays. I applied these techniques to the broader WTR of southern California, which includes the study site of Chapter 2 as well as older sedimentary rocks in the western Topatopa Mountains and correlative geologic units in the Santa Monica Mountains and northern Channel Islands. Across these mountain ranges, gradients in the stratigraphic age of clastic sedimentary rocks exposed at the surface, and in erosion rates quantified from geochemical proxies, enabled me to evaluate this methodology and identify potential controls on landscape-scale rock strength. I resolved strength differences of 200 kPa to ~5 MPa that appear to be related to diagenetic changes associated with the maximum burial depth of young clastic sedimentary rocks. For rocks of the same lithologic type, stratigraphic age, and inferred burial histories that outcrop in ranges bounded by faults with differing slip rates, I resolve smaller differences in strength (300 kPa – 1.5 MPa) that appear to be positively correlated with mean erosion rates inferred from both catchment-averaged ^{10}Be cosmogenic radionuclides and low-temperature (U-Th)/He thermochronometry. I suggest that the observed increase in strength with increasing erosion rate is a function of lesser weathering due to shorter residence time in the near-surface environment. Such an interpretation challenges the simplistic notion that fast erosion rates associate with weaker rocks, and highlights to complex role that tectonics and relief may impart on the mechanical evolution of rock to transportable, erodible material.

7.1.3 Chapter 4 summary

With this chapter, I sought to resolve controls on the initiation and propagation of reverse faulting within the WTR using low-temperature thermochronometry. Active shortening within the WTR has been inferred to have initiated at ~5 Ma, coeval with development of the Big Bend restraining bend in the North American-Pacific Plate transform margin, but direct geochronologic data constraining the initiation of reverse faulting had previously been unavailable. High-density sampling for thermochronometric data from nine new transects and two published transects (Niemi & Clark, 2018) reveal predominantly Pliocene to Pleistocene apatite (U-Th-Sm)/He cooling ages along the San Cayetano fault system on the northern boundary of the WTR, and latest-Miocene to Pliocene cooling ages along the Santa Monica-Channel Islands fault system on the southern boundary. Cooling histories from inverse modelling of the thermochronometry data imply a westward propagation of reverse faulting over ~5 Myr on both fault systems. In the north, exhumation initiates in the Santa Ynez Mountains on the west end of the San Cayetano fault system at 8 Ma and progresses east until 3 Ma. In the south, exhumation first initiates in the northern Channel Islands at 10 Ma and propagates east to the central Santa Monica Mountains by 5 Ma. Along both boundaries, reverse faulting initiates prior to development of the Big Bend and propagates towards the transform plate margin, rather than outwards from it, suggesting that restraining bend tectonism is not the primary source of shortening within the WTR. New and previously-published thermochronometry data reveal that post-Miocene deformation in the broader region around the Big Bend is localized within the WTR, which has mechanically weak basement rocks compared to terranes to the north and south. I posit that contrasts in lithosphere-scale mechanical strength may explain the distribution of young cooling ages and active reserve faulting in the WTR. The hypothesis that rheological contrasts may be a more important control on strain localization than proximity to bends in continental transform margins has the potential to be exported broadly to other transform margin systems.

7.1.4 Chapter 5 summary

With this chapter, I built on the datasets that I generated in Chapters 1-3 in order to explore the contribution of rock strength to the topographic structure of a tectonically-active mountain range. Topographic metrics are often used as proxies for the forcing of landscape change, typically inferred to be driven by bedrock uplift due to fault activity. However, it is also recognized that rock strength should impart a signal on the relief structure of tectonically-active mountain ranges (Korup, 2008; Montgomery & Brandon, 2002; Schmidt & Montgomery, 1995). Here I evaluate the contribution of rock strength to topographic form in the Topatopa Mountains, within which long-term erosion rates and climate conditions are spatially uniform. Topographic metrics including channel steepness, local relief, hillslope relief, and slope demonstrate a non-linear relationship with shear strength at both intact (unfractured) and outcrop (fractured) spatial scales. This relationship suggests that channel and hillslope gradients, as well as relief, initially increase rapidly with increasing strength, but become progressively less sensitive to rock strength variations with the exposure of stronger rocks. This observation cautions interpretation of steady-state landscapes based on topography alone.

7.1.5 Chapter 6 summary

In Chapter 6, I sought to explore how the controls on rock strength identified in Chapter 3 might be expressed in the erosional response to an extreme event. I used repeat airborne-LiDAR surveys to map and quantify the volume of material removed from the channel network following the 2018 Woolsey Fire in the Santa Monica Mountains. I documented expected relationships of post-wildfire erosion with aspect and local slope, but I also recognized a positive relationship between erosional flux and mean rock mass strength of the underlying bedrock. I show that the mean slope of channels overlying each geologic unit increases with increasing rock strength, which suggest that variability in rock strength is expressed as differences in the steepness of the overlying landscape. The capacity of the channel network to erode and transport material following wildfire is most immediately sensitive to local slope, and I posit that variability in rock strength influences the erosional response of burned landscapes by contributing to the topographic structure of the landscape.

7.2 Implications for landscape evolution and directions for future work

Overall, this dissertation demonstrates the utility of several new approaches for quantifying rock mass mechanical properties at multiple spatial scales, identifies and quantifies several important controls on regional distributions of strength, and evaluates the contribution of variability in rock strength to landscape evolution and active tectonics. Geomorphologists have typically used lithology as a stand-in for variability in rock mass properties due to the challenges in quantifying strength and the widespread availability of detailed geologic maps (Sklar & Dietrich, 2001; Stock & Montgomery, 1999), but results from Chapters 2 and 3 demonstrate significant variability in strength within a single lithologic type. In chapters 5 and 6, I demonstrate that the order-of-magnitude variability in the strength of sandstones documented in Chapters 2 and 3 imparts a strong signal in both the relief structure of the studied landscapes and in the erosional response of these landscapes following disturbance by wildfire. These results strongly imply that controlling for lithologic type alone is insufficient to capture the role of rock mass properties in landscape evolution studies. However, Chapters 2 and 3 also provide new approaches for quantifying strength over a variety of spatial scales that future researchers may use to address this gap.

This dissertation lends itself as a starting point for future research. Although I recognize original burial depth as a strong control on the strength of late-Mesozoic and Cenozoic sandstones, significant site-to-site variability in strength within each geologic formation indicates that other potential factors may contribute to near-surface rock strength. Inter-unit variability in rock strength may be driven by differing stresses with topographic position, variability in composition of either the matrix or cements, or differences in local groundwater flow and weathering, and resolving these potential controls will require well-designed studies with additional field data collection and geochemical or thin-section analyses (St. Clair et al., 2015; Gabet et al., 2015; Leone et al., 2020; Slim et al., 2015). Future work should also focus on using the rock strength datasets produced in this dissertation to model the co-seismic landslide response to earthquakes, as numerous faults in the WTR and throughout southern California have rapid slip rates and are capable of generating earthquakes in excess of M_w 6.0 (e.g. Dolan & Rockwell, 2001; Hughes et al., 2018; Marshall et al., 2013; McAuliffe et al., 2015; Rockwell et al., 2016). This effort will be useful from both hazards reduction and scientific perspectives, as constraining the location and volumes of potential co-seismic landslides may both inform local communities of areas with greatest risk (Marano et al., 2010; Petley, 2010), as well as enable assessments of the contribution of large earthquakes to the long-term evolution of these landscapes (Li et al., 2014).

Additional work on the methodology presented in Chapter 2 is also warranted. Specifically, automating the approach to quantifying static rock strength from topography using the Culmann finite-slope stability model could lead to rapid, robust estimates of rock strength across entire mountain ranges with just a digital elevation model as input. Although developing the criteria to separate measurement basins and automatically extract hillslope geometry information may be relatively straightforward, the primary limitation in automating this process is developing an objective, reproducible approach to fitting the Culmann equation to the outer threshold of data in hillslope height versus gradient space. This limitation is discussed extensively in Chapter 2 and in Appendix A, and pursuing this problem further would likely require new collaborations with statisticians and data scientists. However, such an effort could lead to important, high-profile advances in our understanding of the contribution of rock strength to landscape evolution and geomorphic processes.

Chapter 4 demonstrates that significant gaps remain in our understanding of the tectonic history and geodynamic mechanisms operating in southern California, despite over a century of focused study and a wealth of geologic data in the region. Although many models have been proposed to describe the kinematic evolution of the WTR as it underwent clockwise rotation in Miocene time (Dickinson, 1996; Hornafius et al., 1986; Luyendyk, 1991; Nicholson et al., 1994), a geodynamic explanation for this rotation has yet to be identified. Timing of fault initiation on structures bounding the WTR is also still uncertain, and expanding the thermochronometry analyses to reverse fault-bounded islands and ranges in the California borderlands region south of the WTR, and the San Rafael Mountains to the north and northwest of the WTR, may further refine the boundaries of the actively-deforming zone and resolve the kinematic relationship between the WTR and bounding structures.

Chapter 4 of this dissertation also challenges assumptions of the mechanistic relationship between dip-slip structures and adjacent continental transform margins. It is typically assumed that reverse or normal faults adjacent to bends in continental transforms accommodate local extension or shortening where plate motion is oblique to plate boundary (Dewey et al., 1998; Teyssier et al., 1995). The San Andreas Fault and Transverse Ranges are the archetypal example system from which early ideas of restraining bend tectonism were developed (Crowell, 1979), but results from this dissertation suggest that the Big Bend in the San Andreas Fault is not responsible for the initiation of reverse faulting or the localization of deformation within the WTR. The relationship between bends in other continental transform margins and adjacent dip-slip structures should be revisited, especially where direct geochronologic data constraining the relative timing and kinematic relationship between structures has not been produced.

The contribution of lithologic type to post-fire sediment yield and debris-flow hazards is still unclear. As discussed elsewhere in this dissertation, ‘lithology’ is often used as shorthand by geomorphologists to refer to variability in rock strength. Although Chapter 6 of this dissertation suggests that the strength of rock masses composed of similar lithologic type does not directly influence post-wildfire erosion, lithology-dependent differences in the disaggregation of rock are hypothesized to influence sediment mobility in burned catchments by controlling the size and shape of sediment particles (DiBiase & Lamb, 2020). Testing this hypothesis will require a study design that includes a field area with multiple bedrock lithologic types underlying topography with similar slope distributions, vegetative cover, and burn severities.

7.3 References

St. Clair, J., Moon, S., Holbrook, W. S., Perron, J. T., Riebe, C. S., Martel, S. J., et al. (2015). Geophysical imaging reveals topographic stress control of bedrock weathering. *Science*, *350*(6260), 534–539. https://doi.org/10.1126/science.aab2210

Crowell, J. C. (1979). The San Andreas fault system through time. *Journal of the Geological Society*, *136*, 293–302. https://doi.org/10.1144/gsjgs.136.3.0293

Dewey, J. ., Holdsworth, R. ., & Strachan, R. A. (1998). Transpression and transtension zones. In R. . Holdsworth, R. A. Strachan, & J. F. Dewey (Eds.), *Continental Transpressional and Transtensional Tectonics* (Vol. 135, pp. 1–14). Geological Society, London, Special Publications.

DiBiase, R. A., & Lamb, M. P. (2020). Dry sediment loading of headwater channels fuels post-wildfire debris flows in bedrock landscapes. *Geology*, *48*(2), 189–193. https://doi.org/10.1130/G46847.1

Dickinson, W. R. (1996). *Kinematics of transrotational tectonism in the california transverse ranges and its contribution to cumulative slip along the san andreas transform fault system*. *Special Paper of the Geological Society of America* (Vol. 305). https://doi.org/10.1130/0-8137-2305-1.1

Dolan, J. F., & Rockwell, T. K. (2001). Paleoseismologic evidence for a very large (Mw >7), Post-A.D. 1660 surface rupture on the Eastern San Cayetano fault, Ventura county, California: Was this the elusive source of the damaging 21 December 1812 earthquake? *Bulletin of the Seismological Society of America*, *91*(6), 1417–1432. https://doi.org/10.1785/0120000602

Gabet, E. J., Mudd, S. M., Milodowski, D. T., Yoo, K., Hurst, M. D., & Dosseto, A. (2015). Local topography and erosion rate control regolith thickness along a ridgeline in the Sierra Nevada, California. *Earth Surface Processes and Landforms*, *40*(13), 1779–1790. https://doi.org/10.1002/esp.3754

Gallen, S. F., Clark, M. K., & Godt, J. W. (2015). Coseismic landslides reveal near-surface rock strength in a highrelief, tectonically active setting. *Geology*, *43*(1), 11–14. https://doi.org/10.1130/G36080.1

Hoek, E., Carranza, C., & Corkum, B. (2002). Hoek-brown failure criterion – 2002 edition. *Narms-Tac*, 267–273. https://doi.org/10.1016/0148-9062(74)91782-3

Hornafius, J. S., Luyendyk, B. P., Terres, R. R., & Kamerling, M. J. (1986). Timing and extent of Neogene tectonic rotation in the western Transverse Ranges, California (USA). *Geological Society of America Bulletin*, *97*(12), 1476–1487. https://doi.org/10.1130/0016-7606(1986)97<1476:TAEONT>2.0.CO;2

Hughes, A., Rood, D. H., Whittaker, A. C., Bell, R. E., Rockwell, T. K., Levy, Y., et al. (2018). Geomorphic evidence for the geometry and slip rate of a young, low-angle thrust fault: Implications for hazard assessment and fault interaction in complex tectonic environments. *Earth and Planetary Science Letters*, *504*, 198–210. https://doi.org/10.1016/j.epsl.2018.10.003

Korup, O. (2008). Rock type leaves topographic signature in landslide-dominated mountain ranges. *Geophysical Research Letters*, *35*(11), 1–5. https://doi.org/10.1029/2008GL034157

Leone, J. D., Holbrook, W. S., Riebe, C. S., Chorover, J., Ferré, T. P. A., Carr, B. J., & Callahan, R. P. (2020). Strong slope-aspect control of regolith thickness by bedrock foliation. *Earth Surface Processes and Landforms*, *3010*(July), 2998–3010. https://doi.org/10.1002/esp.4947

Li, G., West, A. J., Densmore, A. L., Jin, Z., Parker, R. N., & Hilton, R. G. (2014). Seismic mountain building: Landslides associated with the 2008 Wenchuan earthquake in the context of a generalized model for earthquake volume balance. *Geochemistry, Geophysics, Geosystems*, *15*(4), 833–844. https://doi.org/10.1002/2013GC005067

Luyendyk, B. P. (1991). A model for Neogene crustal rotations, transtension, and transpression in southern California. *Geological Society of America Bulletin*, *103*(11), 1528–1536. https://doi.org/10.1130/0016-7606(1991)103<1528:AMFNCR>2.3.CO;2

Marano, K. D., Wald, D. J., & Allen, T. I. (2010). Global earthquake casualties due to secondary effects: A quantitative analysis for improving rapid loss analyses. *Natural Hazards*, *52*(2), 319–328. https://doi.org/10.1007/s11069-009-9372-5

Marshall, S. T., Funning, G. J., & Owen, S. E. (2013). Fault slip rates and interseismic deformation in the western Transverse Ranges, California. *Journal of Geophysical Research: Solid Earth*, *118*(8), 4511–4534. https://doi.org/10.1002/jgrb.50312

McAuliffe, L. J., Dolan, J. F., Rhodes, E. J., Hubbard, J., Shaw, J. H., & Pratt, T. L. (2015). Paleoseismologic evidence for large-magnitude (MW 7.5-8.0) earthquakes on the Ventura blind thrust fault: Implications for multifault ruptures in the Transverse Ranges of southern California. *Geosphere*, *11*(5), 1629–1650. https://doi.org/10.1130/GES01123.1

Montgomery, D. R., & Brandon, M. T. (2002). Topographic controls on erosion rates in tectonically active mountain ranges. *Earth and Planetary Science Letters*, *201*(3–4), 481–489. https://doi.org/10.1016/S0012-821X(02)00725-2

Nicholson, C., Sorlien, C. C., Atwater, T., Crowell, J. C., & Luyendyk, B. P. (1994). Microplate capture, rotation of the western Transverse Ranges, and initiation of the San Andreas transform as a low-angle fault system. *Geology*, *22*(6), 491–495.

Niemi, N. A., & Clark, M. K. (2018). Long-term exhumation rates exceed paleoseismic slip rates in the central Santa Monica Mountains, Los Angeles County, California. *Geology*, *46*(1), 63–66. https://doi.org/10.1130/G39388.1

Petley, D. N. (2010). Landslide Hazards. In *Geomorphological hazards and disaster prevention* (pp. 63–74). Cambridge, U.K.: Cambridge University Press.

Rockwell, T. K., Clark, K., Gamble, L., Oskin, M. E., Haaker, E. C., & Kennedy, G. L. (2016). Large Transverse Range Earthquakes Cause Coastal Upheaval near Ventura, Southern California. *Bulletin of the Seismological Society of America*, *106*(6), 2706–2720. https://doi.org/10.1785/0120150378

Schmidt, K. M., & Montgomery, D. R. (1995). Limits to Relief. *Science*, *270*(5236), 617–620.

Sklar, L. S., & Dietrich, W. E. (2001). Sediment and rock strength controls on river incision into bedrock. *Geology*, *29*(12), 1087–1090. https://doi.org/10.1130/0091-7613(2001)029<1087:SARSCO>2.0.CO

Slim, M., Perron, J. T., Martel, S. J., & Singha, K. (2015). Topographic stress and rock fracture: A two-dimensional numerical model for arbitrary topography and preliminary comparison with borehole observations. *Earth Surface Processes and Landforms*, *40*(4), 512–529. https://doi.org/10.1002/esp.3646

Stock, J. D., & Montgomery, D. R. (1999). Geologic constraints on bedrock river incision using the stream power law. *Journal of Geophysical Research: Solid Earth*, *104*(B3), 4983–4993.

https://doi.org/10.1029/98JB02139

Teyssier, C., Tikoff, B., & Markley, M. (1995). Oblique plate motion and continental tectonics. *Geology*, *23*(5), 447–450. https://doi.org/10.1130/0091-7613(1995)023<0447:OPMACT>2.3.CO;2

Appendices

Appendix A: Supporting Information for Chapter 2. Quantifying Near-Surface Rock Strength on a Regional Scale from Hillslope Stability Models

A.1 Introduction

This appendix contains a summary of laboratory and analytical protocols for analysis of apatite (U-Th)/He thermochronometry, landslide mapping methods, Culmann model landslide thickness calculations, and a discussion of model misfit. Thirty-one supplemental figures and four supplemental tables are included.

A.2 Apatite (U-Th)/He Methods

Bedrock samples for (U-Th)/He low-temperature thermochronometry were collected in April 2016 to infer magnitudes of exhumation. Samples were crushed, sieved, and separated using standard methods to isolate apatite by exploiting differences in density and magnetic susceptibility. Individual mineral grains were hand-selected under a high-powered binocular microscope to screen for clarity, crystal morphology, and minimal inclusions of other potentially radiogenic minerals. Grains selected for analysis were measured along major and minor axes, photographed, packaged into individual Pt tubes, and analyzed for ^{4}He content using an Australian Scientific Instruments Helium Instrument (Alphachron) at the University of Michigan Thermochronology Laboratory. Grains were heated for 5 minutes at 900°C, released ^{4}He was spiked with ^{3}He, and the ^{4}He /^{3}He ratio was measured on a Pfeiffer quadrupole mass spectrometer to determine the quantity of ^{4}He. Following this initial ^{4}He measurement, these analytical procedures were repeated to check for any additional extraction of ^{4}He that might be indicative of micro-inclusions of high-temperature radiogenic minerals that were not observed optically during grain selection. The Durango apatite age standard was also analyzed with our samples to ensure accuracy of measurements of unknown age. After measurement of ^{4}He, grains were dissolved and analyzed for U, Th and Sm concentrations following standard procedures (Reiners and Nicolescu, 2006) using a Thermo Scientific Elements 2 ICP-MS at the University of Arizona Radiogenic Helium Dating Laboratory.

Individual grain dates were solved for numerically in Matlab using parent and daughter nuclide concentrations and the age equation. Analytical uncertainties were propagated through the age equation using Monte Carlo methods. Grains with low uranium concentrations are particularly susceptible to age biases that result from uranium-implantation from surrounding U-rich phases (Spiegel et al., 2009). Grains with uranium concentrations under 5 ppm are reported but excluded from calculation of mean values. Outliers were identified following the Dean-Dixon method (Dean and Dixon, 1951) based on the 90 percent confidence interval at two significant digits. We applied this outlier test only to bedrock samples with a 2-sigma standard error greater than 15 percent of the mean age. Using the remaining grain ages, we calculated a mean apatite (U-Th)/He age for each sample (Table A.1). Because the observed variability in our (U-Th)/He ages for individual bedrock samples is larger than the analytical error for single grains, we report mean ages for bedrock samples with uncertainty as the standard error of the mean for the multiple grains analyzed (reported as two-sigma uncertainty in Table A.1). We consider bedrock samples that have a one-sigma standard deviation greater than 45 percent of the mean age to have low reproducibility, and we do not report a mean age for 16-PC-1 for this reason. Each replicate age of 16-PC-3 is as older or older than the middle- to late-Miocene depositional age of the Monterey Formation, indicating that the ages are inherited and do not reflect cooling of the sample. We therefore do not report a mean age here.

We examined our data to identify any existing grainsize-age or eU-age trends for individual bedrock samples. Grainsize-age trends may indicate the effect of crystal size on closure temperature (Reiners and Farley, 2001), whereas trends between effective uranium (eU) and age may reflect the effects of radiation damage on helium diffusion (Flowers et al., 2009; Guenthner et al., 2013). We do not observe significant grainsize-age trends in our data, but we do observe a positive eU-age trend in 16-PC-04. Excluding the outlier, this trend falls within the typical age variability expected from bedrock samples. However, the eU-age trend may also indicate radiation damage. Regardless, helium ages from this sample indicate that it was buried deeply enough to be thermally reset, which is sufficient for the argument presented in this manuscript.

A.3 Landslide Inventory Remapping Methods

Landslides were identified in Google Earth using aerial imagery from May 1994. Where 1994 Google Earth imagery was unavailable, we referenced the original ~1:60,000 scale IRIS II photo strips used by Harp and Jibson (1995, 1996), which were acquired by the United States Air Force on January 17, 1994. We used a stereoscope, 10X magnification, and 20X magnification loupes to identify landslides on the physical image strips, and matched these areas to equivalent topography in Google Earth to map a 3D polygon. The IRIS photo strips were also used to spot-check regions of particularly concentrated landsliding where remapping in Google Earth proved challenging.

In photographic or satellite images, landslides are typically recognized by changes in appearance due to surface disturbance (increased albedo and surface roughness) and loss of vegetative cover. However, in areas of dense landsliding where adjacent slopes simultaneously fail, it can be challenging to determine unique polygon areas that define individual landslides. In these cases, we define the lateral margins using intact vegetation. Linear downslope sections of vegetation likely separated flow paths and were mapped as stable margins to adjacent landslides. Disturbed regions typically project to ridgetops, which we interpreted to be landslide source areas. Occasionally, individual source areas were recognized by scarps on ridge tops. Morphologic features were commonly difficult to identify in the 1994 imagery, so landslide toes were mapped as the furthest downslope extent of disturbance. We chose to remove landslide polygons in our remapping where the apparent density of disturbed area was less than the area of vegetative cover. We shifted landslide polygon locations if they were offset from the area of disturbance as inferred from the imagery. We also recognized additional disturbed areas in the imagery that were not originally outlined as landslides. As the USGS conducted field surveys in tandem with their original mapping effort, we chose to only outline landslides that the USGS had originally included within a landslide polygon.

Digital topography was also used to separate individual landslides by identifying minor ridges. Branching landslide polygons indicating multiple source areas and overlapping deposits were remapped by separating each source area and assigning the deposit to the largest. Where similarly sized landslides originated from distinct slopes and coalesced in a valley bottom, the deposits were divided equally and mapped with the respective sources (Figure 2.4B). Less frequently, USGS polygons with a single source contained multiple branched runout areas. If individual source areas could not be identified for each runout, only the largest runout area was outlined with the source. Within landslide polygons covering cliff bands, individual source areas could either be identified with the 1994 imagery or recognized based on the position of subtle ridges. Margins of the sources were outlined and projected downslope into the overlapping deposits to assign the portion of the deposit immediately below each source to the corresponding source area.

A.4 Culmann Model Landslide Thickness Calculations

Landslides produced by the M_w 6.7 Northridge Earthquake predominately occurred as planar failures with thicknesses of 1 to 5 m (Harp and Jibson, 1996). Here we describe how landslide thickness predictions from the Culmann model are calculated. Newmark model landslide thickness calculation methods are in the main manuscript text and Gallen et al., (2015).

The derivation of the Culmann equation yields the following expression:

$$\theta = \frac{\beta + \phi}{2} \tag{1}$$

wherein the angle of the landslide failure plane (θ) is equal to the geometric mean of the average hillslope gradient (β) and the angle of internal friction (ϕ) (Figure A.1). Equation 1 yields landslide failure surfaces that are steeper than the hillslope gradient for hillslope segments with β less than ϕ, suggesting that the Culmann model is not capable of modeling landslides for shallow slopes. This is consistent with previous findings (Lu and Godt, 2013), so we restrict our calculation to hillslope segments with $\beta \geq \phi$. Using the basin-averaged ϕ, we calculate θ of theoretical landslide failures for hillslope segments within each basin. The Culmann model predicts landslides with a wedge-shaped geometry (Figure A.1), so we use θ, β, and the critically-stable hillslope height (H_c) to calculate the change in length across the top of the landslide wedge (ΔL) with the following expression:

$$\Delta L = \frac{H_c}{\tan(\theta)} - \frac{H_c}{\tan(\beta)} \tag{2}$$

The maximum thickness of the landslide, t_{max} is then:

$$t_{max} = \sin(\theta) * \Delta L \tag{3}$$

Dividing t_{max} by two yields the average thickness of each landslide. The mean model thickness of all landslides estimated from measured hillslope segments in all 24 measurement regions is 1.4 m, and mean model landslide thickness of hillslopes segments within each measurement region are listed in Table A.3. Despite the Culmann model's wedge-shaped approximation of landslide geometry, this mean value falls within the range of actual landslide thicknesses.

In applying the Culmann model to digital topography, we assume that hillslope segments that define the threshold in H vs. β represent the strength-limited portions of the landscape. Therefore, we expect that these hillslopes would be the most likely to fail in a landslide. We explore the theoretical distribution of landslide thicknesses sourced from only threshold hillslope segments. For constant material strength, we calculate H_c in increments of 0.1° of β between ϕ and 90° to produce a distribution of threshold hillslope segments. We then calculate theoretical landslide thicknesses in the same manner as described above for actual hillslope segments. The mean model thickness of all landslides estimated from theoretical critically-stable hillslope segments is 3.7 m, and mean model landslide thickness of critical hillslope segments within each measurement region are listed in Table A.3. Mean landslide thicknesses of threshold hillslope segments are thicker than landslide thicknesses estimated by the measured hillslope geometries in each basin. This is expected given the wedge-shaped geometry of landslides modeled by the Culmann equation; threshold segments represent the tallest and steepest components of the landscape, and the greater mean difference between β and θ in threshold data results in higher ΔL and t_{max}. Importantly, the mean values of landslide thickness from threshold hillslope segments is within the range of actual landslide thickness produced during the M_w 6.7 Northridge Earthquake.

A.5 Synthetic Landslide Geometries for the Newmark Approach

Following Gallen et al. (2015), we use a set of geometric rules to calculate the location and 3D volume of each landslide. From each cell identified as a landslide failure point by the simplified Newmark model (Jibson, 2007), Equation 4 projects a failure plane upslope from a point at depth assuming the slope of the failure plane to be equal to the topographic gradient of the failure grid cell (Figure A.30):

$$z_{fp} = z_f + d_{fp} \tan[S_{fp}] \tag{4}$$

Where z_{fp} is the elevation of each grid cell on the failure plane, z_f is the elevation of the Newmark failure cell, d_{fp} is the distance of each cell on the failure plane from the Newmark failure cell, and S_{fp} is the topographic slope of the Newmark failure cell. Next, the model calculates the maximum slope, S_m, of the topography above the failure plane using the maximum relief of the potential failure mass and distance between this point and the failure cell (Figure A.30). If S_m is greater than S_{fp}, which only occurs for ~0.5 – 3% of modeled landslides, the model will progressively curve the failure plane to reduce the landslide thickness while preserving its plan view area using Equation 5:

$$z_{fp} = z_f + d_{fp} \tan\left[S_{fp} + d_{fp}\left(\frac{S_m - S_{fp}}{max(d_{fp})}\right)\right] \tag{5}$$

Equation 5 acts to progressively curve the failure plane from the gradient of the Newmark failure cell to a maximum angle set by the maximum slope (S_m) of failure mass above the plane defined by Equation 4 (Figure A.30). The plan-view area of each landslide is defined with a searching algorithm that sequentially finds the three steepest neighboring grid cells upslope of the landslide failure cell until the failure plan daylights. For any given pixel, if the elevation of the topography exceeds the elevation of the projected failure plane, it is included as part of the landslide area. If the elevation of the projected landslide failure plane exceeds the elevation of the topography, the cell is removed from the landslide area.

This simple geometric approximation applied to digital topography produces synthetic landslide distributions that closely match observed power-law scaling of landslide frequency-area statistical distributions (Gallen et al., 2015). We note that this approach produces power law landslide frequency-area distributions for intermediate to large landslides, but cannot reproduce the rollover at small landslide areas seen in most mapped distributions, as a 1D approximation to slope stability does not censor short slopes where the driving stress is diminished compared to longer slopes.

A.6 Quality of Model Fits to Data

We note variability in the quality of both Newmark synthetic landslide frequency-area fits to observed distributions, and the ‘threshold’ of hillslopes in height vs. gradient space (Figures A.5 to A.29). In this section we discuss reasons for the misfit and variability in agreement of the two models.

The variable quality of fits in the Newmark approach is mostly driven by a mismatch between the portions of the landscape that are predicted to fail by the simplified Newmark analysis of Jibson (2007), and the portions of the landscape that actually failed during the Northridge earthquake. The approach as adapted here is most sensitive to the number of landslides in each basin, but the distribution of landslide areas within that number of landslides is determined by the topography where the Newmark model predicts landslide failures. In log-transformed frequency-area space, our model approach only changes the y-intercept of the power-law distribution, but not the slope of that relationship, which is a function of the topography within which the simplified Newmark model predicts failure cells. The poor fit to data in some catchments (e.g. catchments 1 and 21) suggests that the simplified Newmark model is predicting failures on topography that is dissimilar to what actually failed. We note that applying a scar correction to reduce landslide polygon areas does not improve the quality of fits. The size of landslides we can model is controlled by the resolution of the DEM, and despite the relatively high resolution (3m) of the DEM used here, reducing landslide polygon sizes severely reduces the number of landslides modeled. As we are fitting the total number of landslides in each basin, and the slope of the log-transformed line in frequency-area space is controlled by the topography where the landslides fail, reducing the number of landslides does not change the quality of the fits, but instead bias the results towards higher strength.

For the Culmann analysis, the threshold of hillslope data in height versus gradient space is variably well defined, with some regions yielding data with a larger number of tall moderately steep hillslopes than anticipated by a Culmann model. The approach taken here assumes that the strength of shallow bedrock underlying every hillslope in each basin is the same, but we recognize that in real landscapes, rock strength can be a function of many local variables, including topographic position, groundwater and hydrology, aspect, etc., that will produce local variability in strength that influence the local morphology of any individual hillslope. Further, the approach assumes topographic steady-state, but in reality, most landscapes will contain transient features (e.g. landslide head scarps) that may push a hillslope towards a steeper or shallower gradient than is average for the landscape. Results presented here represent an approximation of the average strength of shallow bedrock underlying hillslopes within each basin. Hillslope segments that fall along the threshold are distributed broadly across each catchment, which lends confidence to the interpretation of average strength.

The basins with poor Newmark fits are not systematically the basins that yield poorly-defined thresholds in hillslope height vs. gradient for the Culmann strength interpretations, and basins with large disagreement in cohesion do not necessarily exhibit poor model fits. For example, Basin 1 yields a poor fit between Newmark predicted and observed landslide frequency-area statistics, but the threshold in height vs. gradient space for the Culmann analysis is moderately well-defined. In contrast, basin 15 yields a close fit between Newmark predicted and observed frequency-area statistics, but the threshold in height vs. gradient space for the Culmann is diffuse and poorly-defined. The mismatch between model cohesion is noticeable in Basin 9 (Culmann C = 50 kPa, Newmark C = 6 kPa), which appears as an outlier in Figure 2.7B and 2.8. However, the synthetic Newmark landslide distribution closely fits the mapped distribution, and the threshold in height vs. gradient space is well defined for the Newmark model (Figure A.13). A possible source of this disagreement is the assumption of strength-limited hillslopes for the Culmann analysis. We note the distribution of the tallest hillslopes is at a lower gradient (~30°) in basin 9 than for most basins underlain by the Pico Formation (~35-45°), but the width of this region is constrained by the San Cayetano fault to the south and the Piru Creek valley to the north. There may not be enough space for hillslopes over the entire distribution of gradients to reach lengths at which they become unstable. Approximating the threshold including these relatively low-gradient, tall hillslopes in height vs. gradient space with the Culmann model requires an anomalously low friction angle, yielding the high cohesion estimate. If hillslopes at ~35-45° are not strength-limited, and additional height is required before these hillslopes become unstable, then the distribution of hillslope data would yield a Culmann threshold with lower cohesion and higher friction, which would be more consistent with other basins overlying the Pico fm.

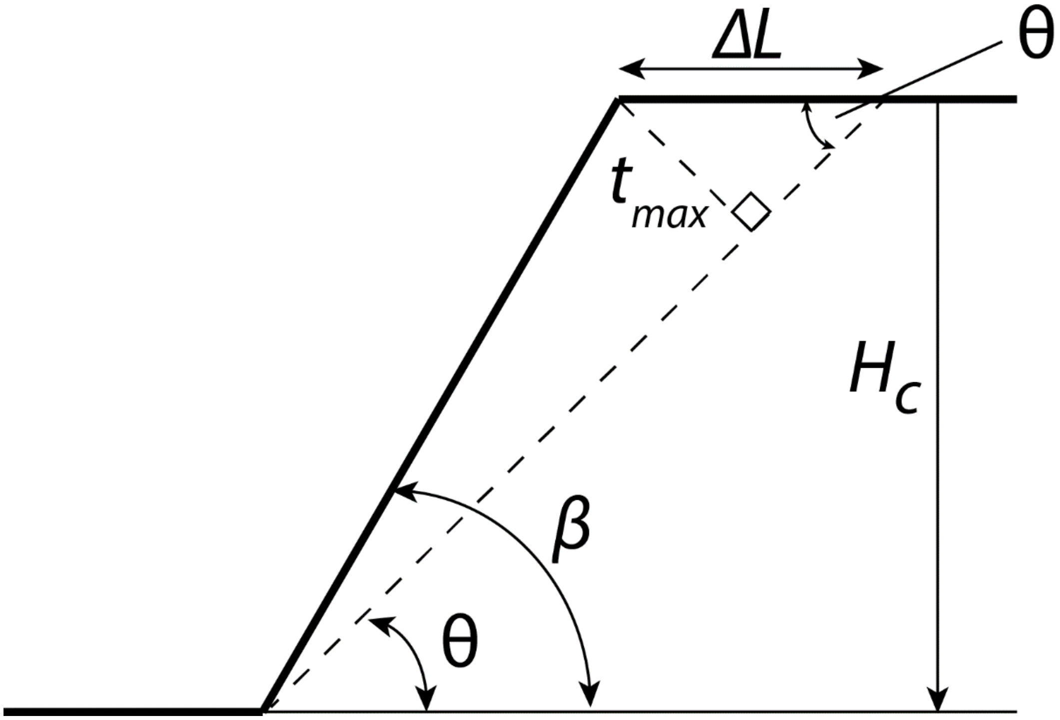

Appendix Figure A.1: Illustration of the Culmann approximation of hillslope geometry and landslide thickness.

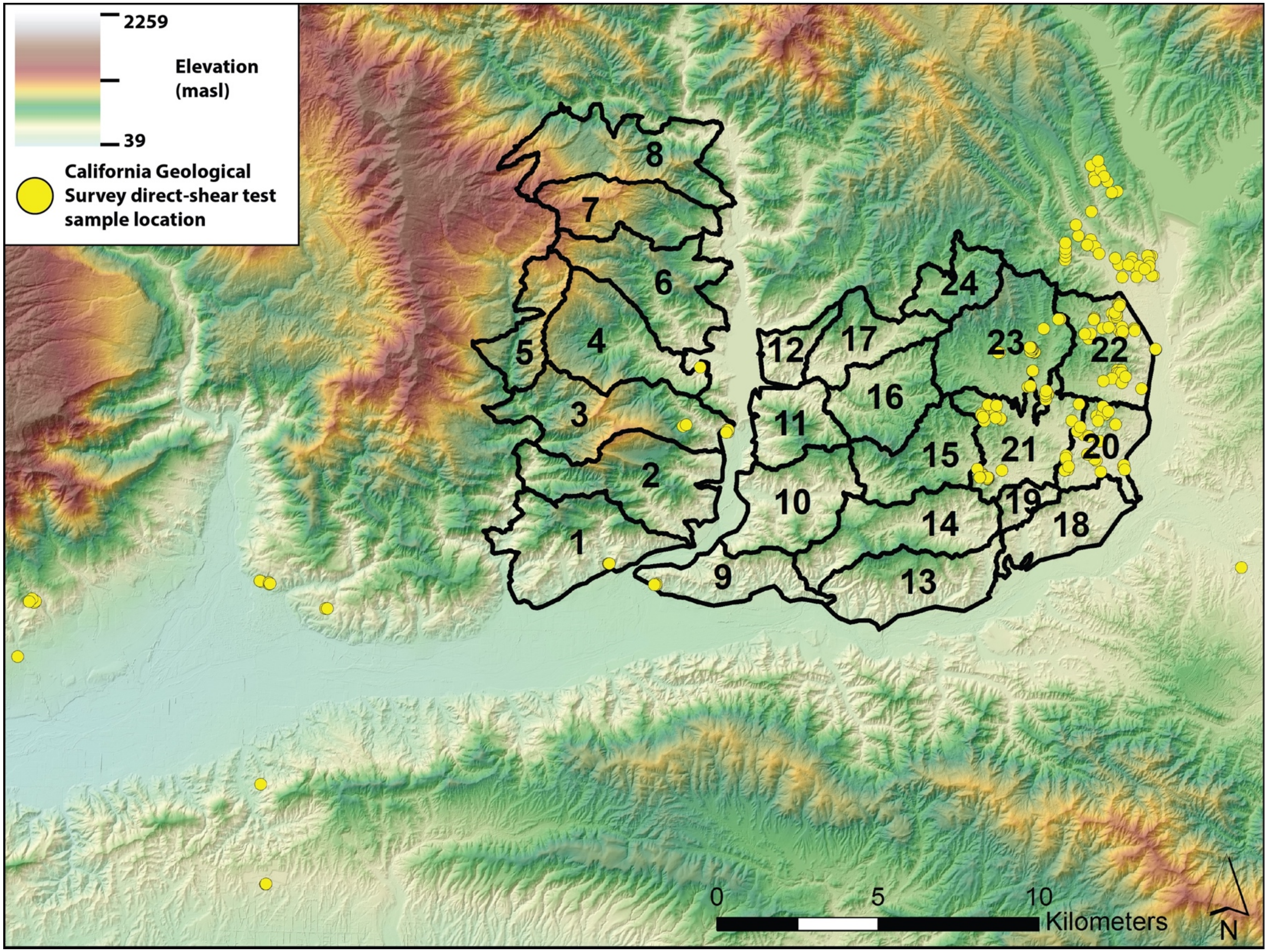

Appendix Figure A.2: California Geological Survey sample locations for direct-shear testing used to produce mean estimates reported in Table 2.1.

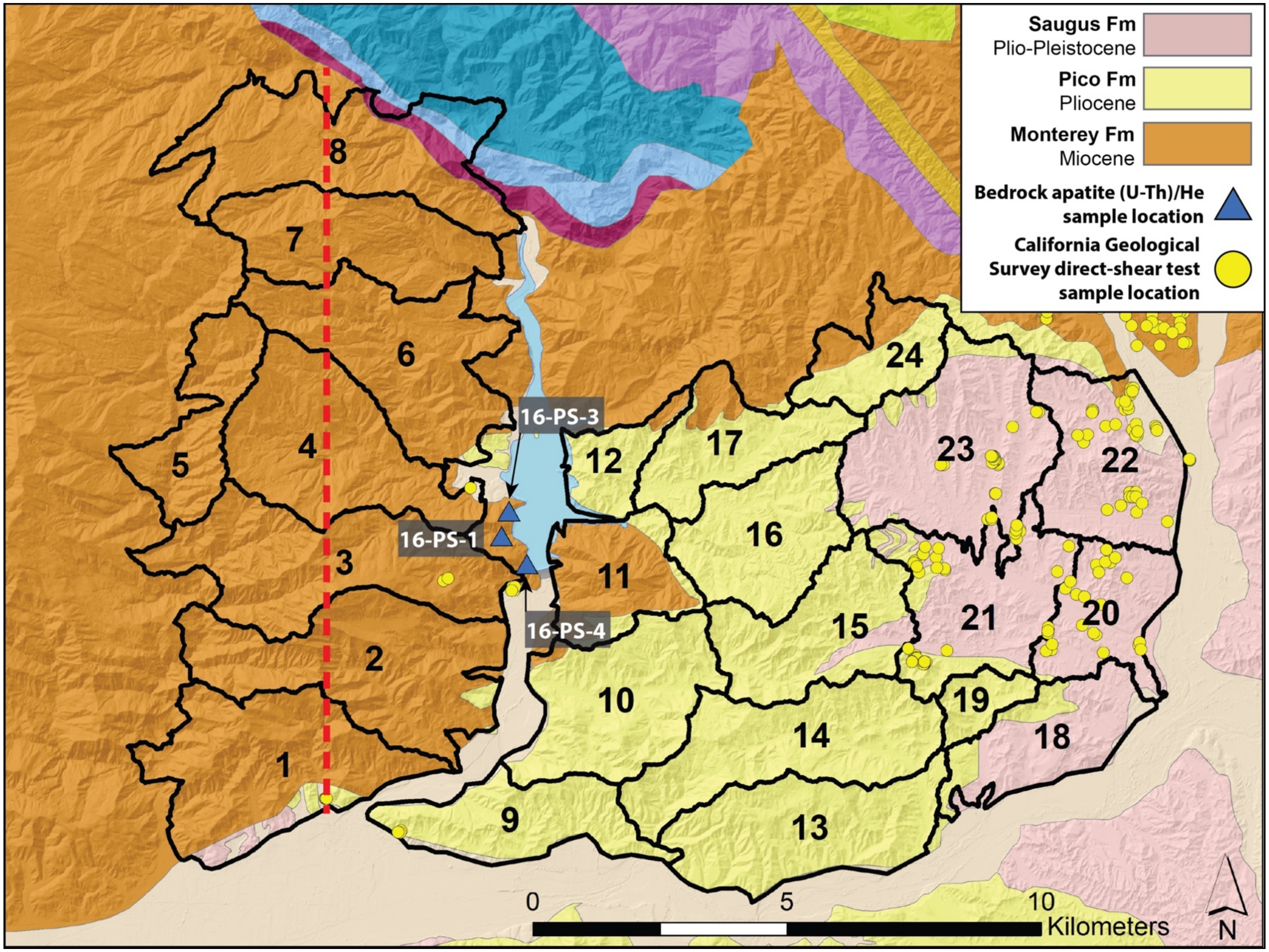

Appendix Figure A.3: Topatopa basin numbers overlying mapped bedrock geology. Adapted from Dibblee (1991, 1993) and Dibblee and Ehrenspeck, (1996, 1997). Bedrock apatite (U-Th)/He thermochronology sample locations and California Geological Survey sample locations for direct-shear testing are shown. Red dashed line is the location of the geologic cross section and strength transects shown in Figure 2.8.

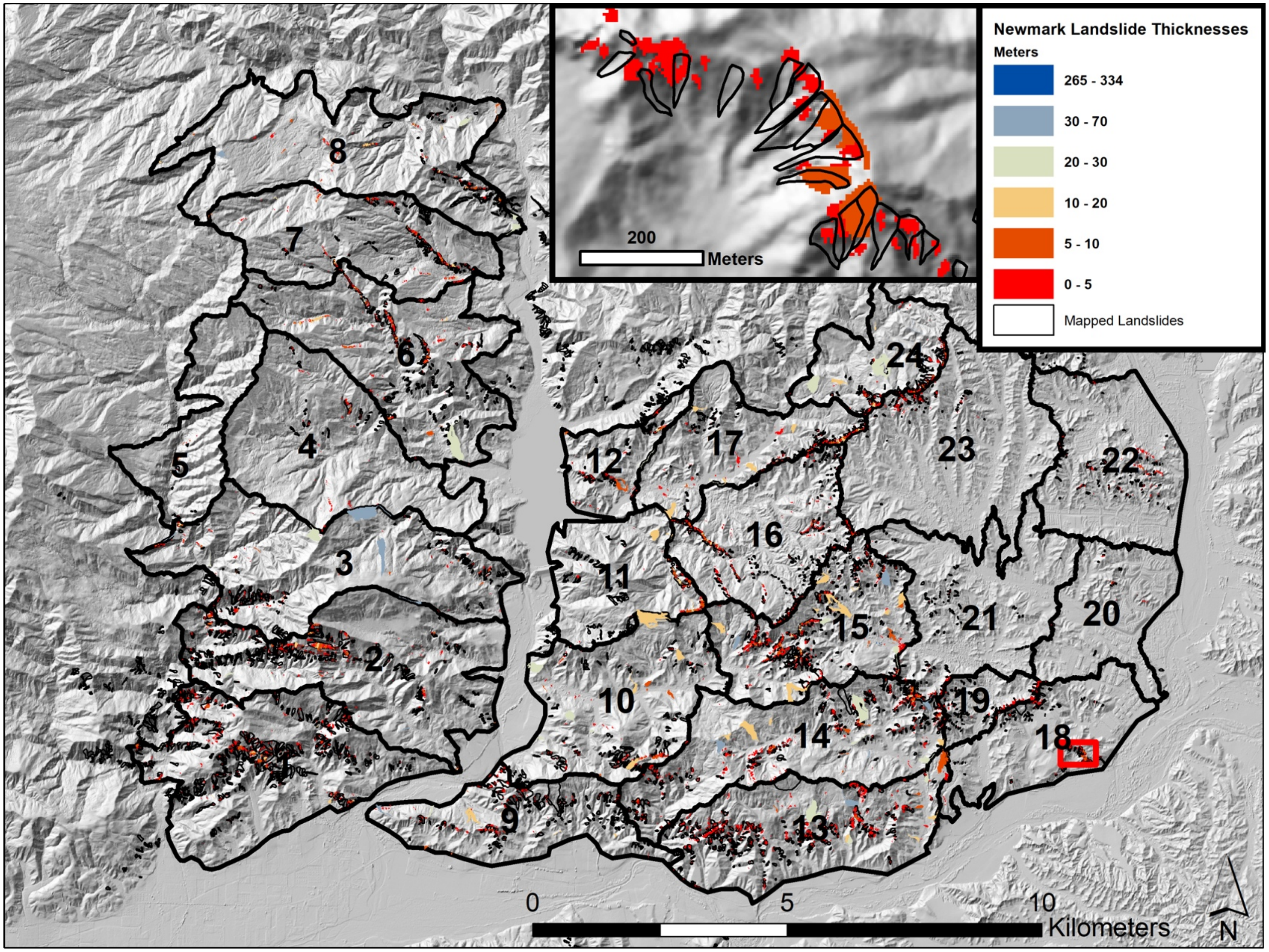

Appendix Figure A.4: Distribution of synthetic landslides (n = 6185) produced using the Newmark approach, and landslides from the remapped inventory presented in this manuscript. Landslides are colored by modeled thickness. 92% of landslides are < 10 meters thick. Eight outlier landslides have thicknesses of 265-333 meters, but these are limited in spatial extent (maximum area of 325 square meters). Inset map shows close-up example of agreement between synthetic and mapped landslides from Basin 18 (red outline).

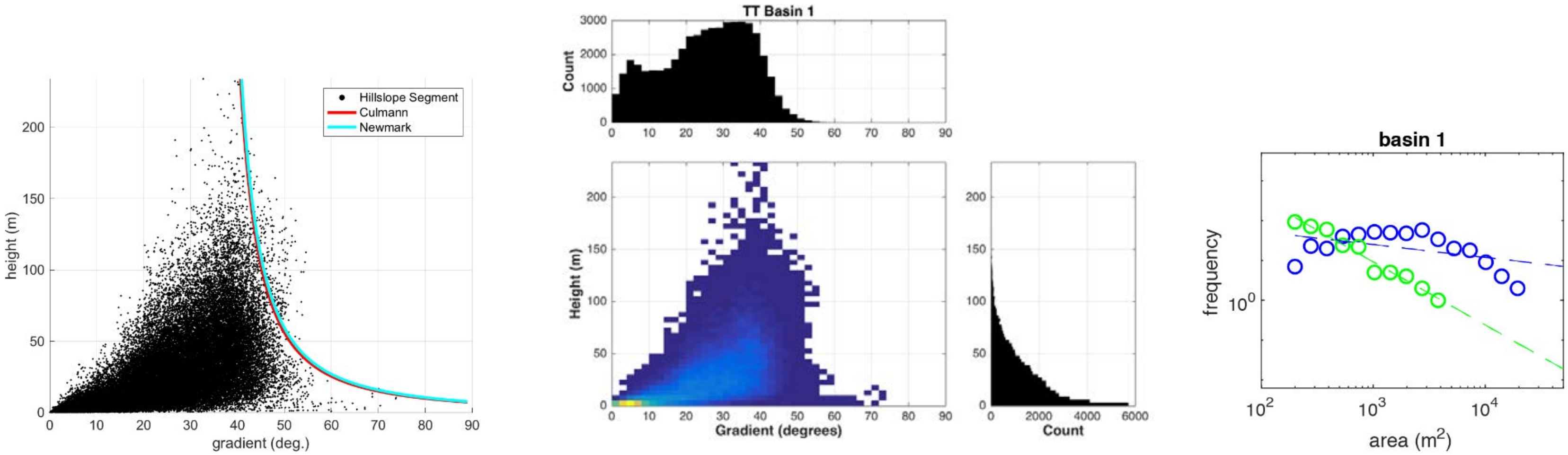

Appendix Figure A.5: (left) Basin 1 hillslope gradient-height scatter plot with Culmann and Newmark curves, (center) hillslope gradient-height density plot and histograms, (right) frequency-area plots of mapped (blue) and synthetic (green) landslide distributions.

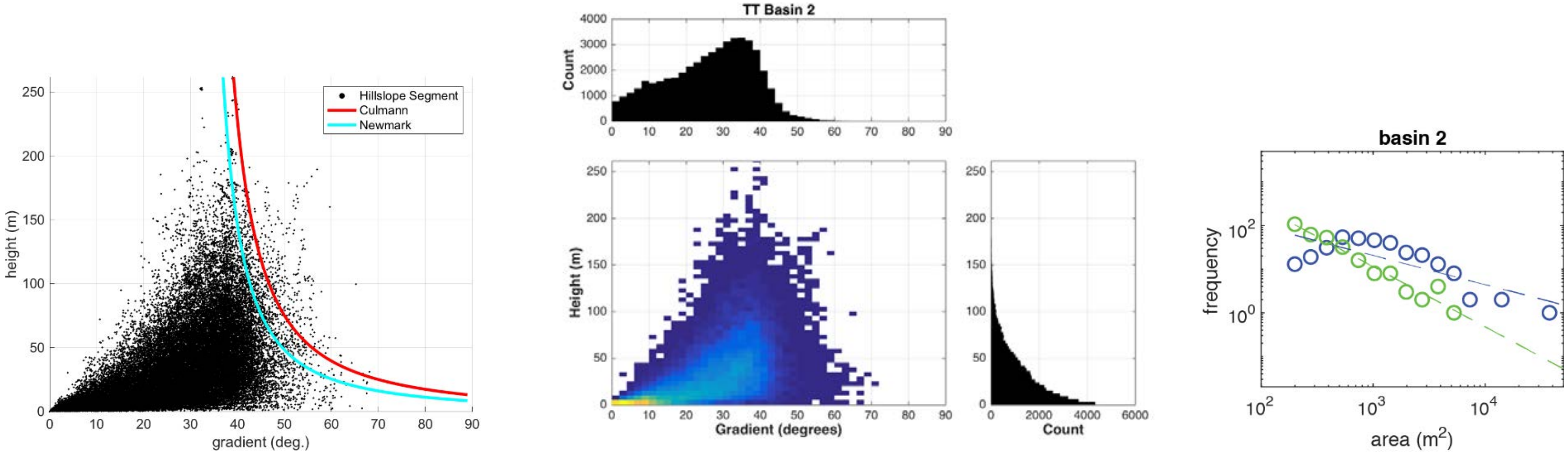

Appendix Figure A.6: (left) Basin 2 hillslope gradient-height scatter plot with Culmann and Newmark curves, (center) hillslope gradient-height density plot and histograms, (right) frequency-area plots of mapped (blue) and synthetic (green) landslide distributions.

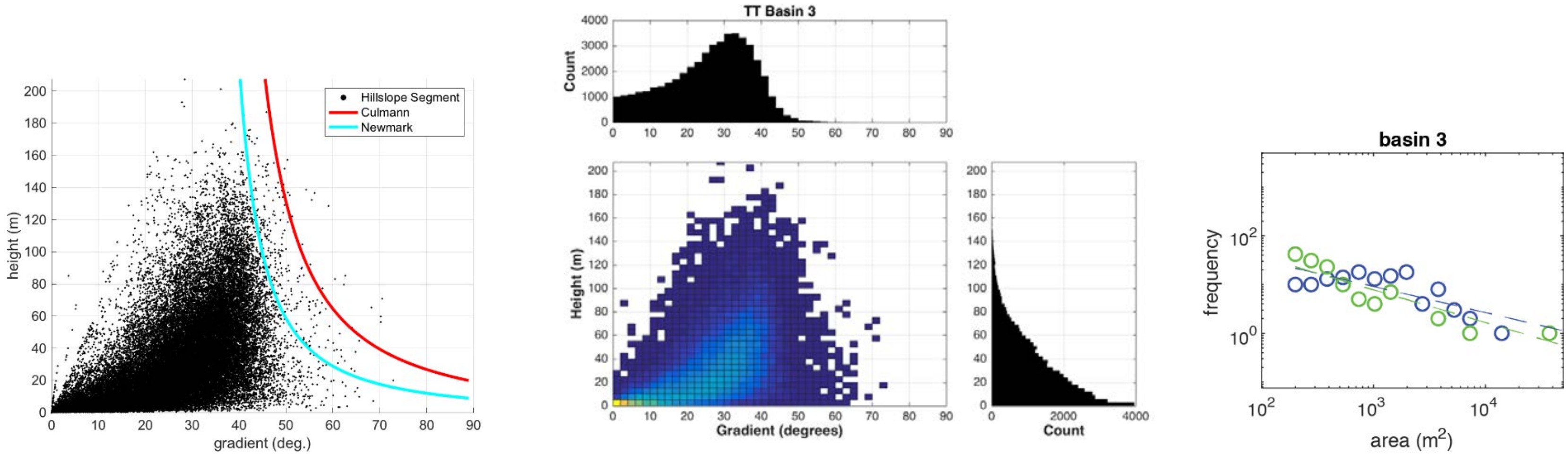

Appendix Figure A.7: (left) Basin 3 hillslope gradient-height scatter plot with Culmann and Newmark curves, (center) hillslope gradient-height density plot and histograms, (right) frequency-area plots of mapped (blue) and synthetic (green) landslide distributions.

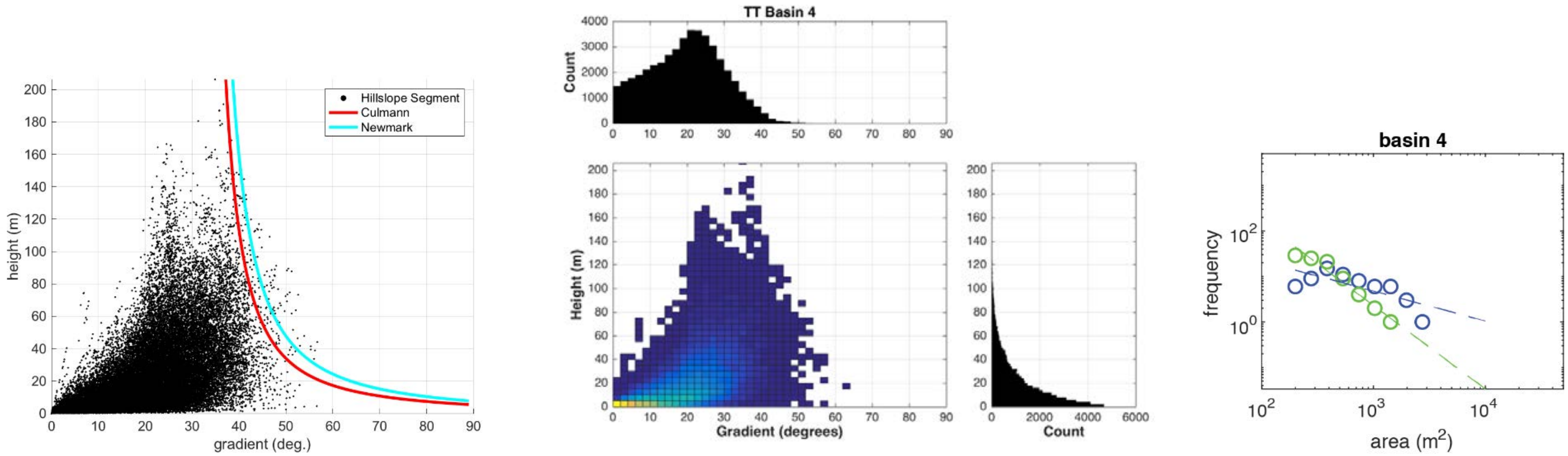

Appendix Figure A.8: (left) Basin 4 hillslope gradient-height scatter plot with Culmann and Newmark curves, (center) hillslope gradient-height density plot and histograms, (right) frequency-area plots of mapped (blue) and synthetic (green) landslide distributions.

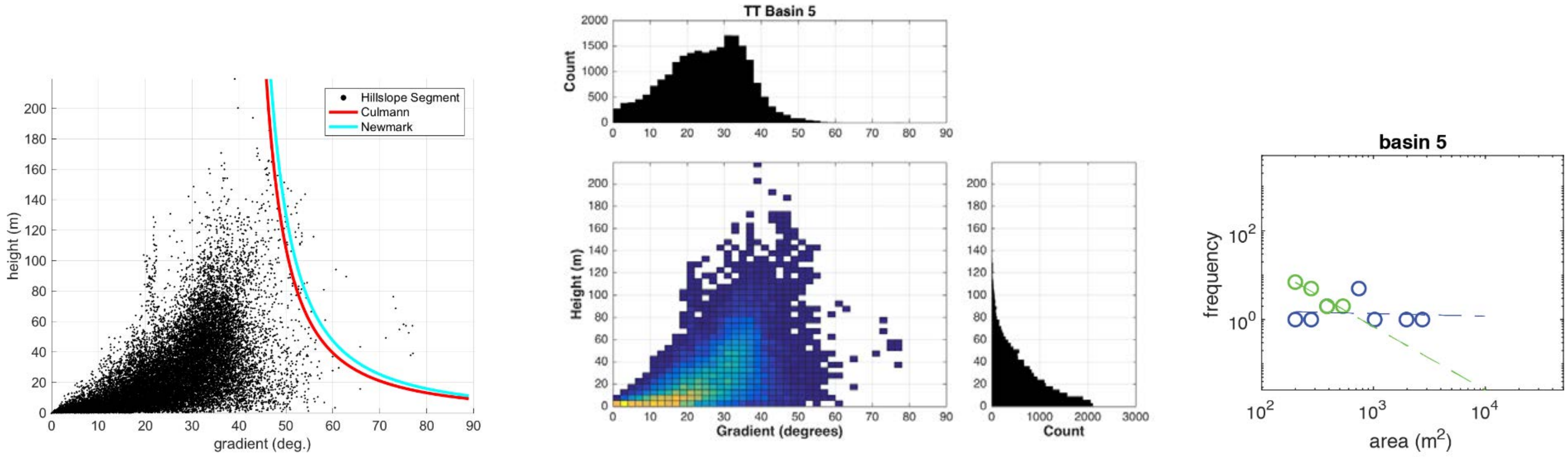

Appendix Figure A.9: (left) Basin 5 hillslope gradient-height scatter plot with Culmann and Newmark curves, (center) hillslope gradient-height density plot and histograms, (right) frequency-area plots of mapped (blue) and synthetic (green) landslide distributions.

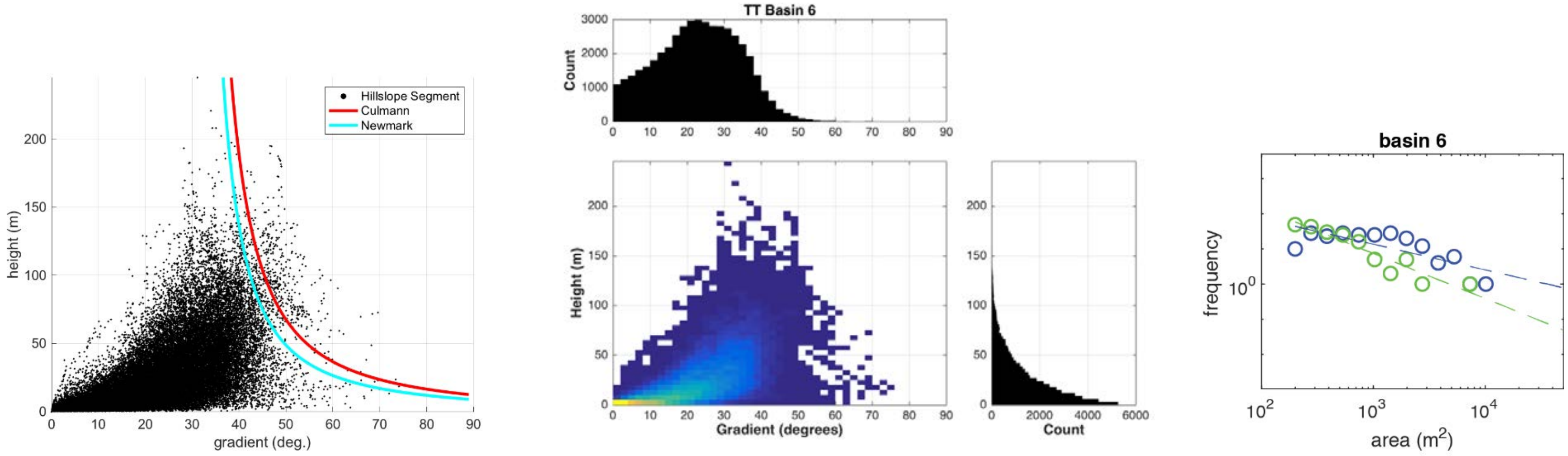

Appendix Figure A.10: (left) Basin 6 hillslope gradient-height scatter plot with Culmann and Newmark curves, (center) hillslope gradient-height density plot and histograms, (right) frequency-area plots of mapped (blue) and synthetic (green) landslide distributions.

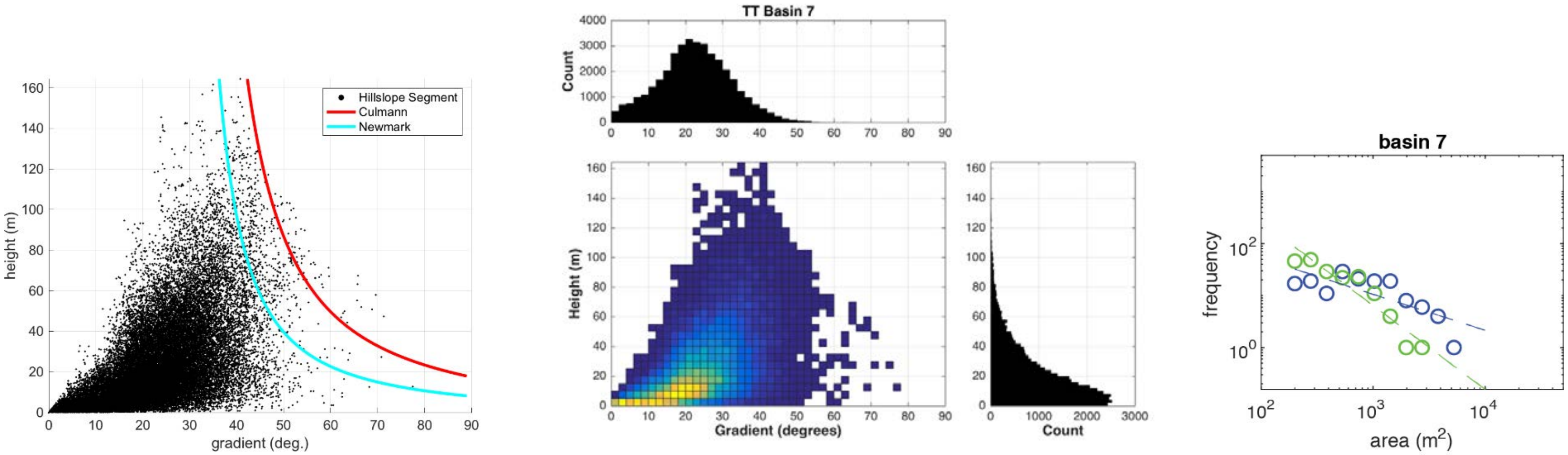

Appendix Figure A.11: (left) Basin 7 hillslope gradient-height scatter plot with Culmann and Newmark curves, (center) hillslope gradient-height density plot and histograms, (right) frequency-area plots of mapped (blue) and synthetic (green) landslide distributions.

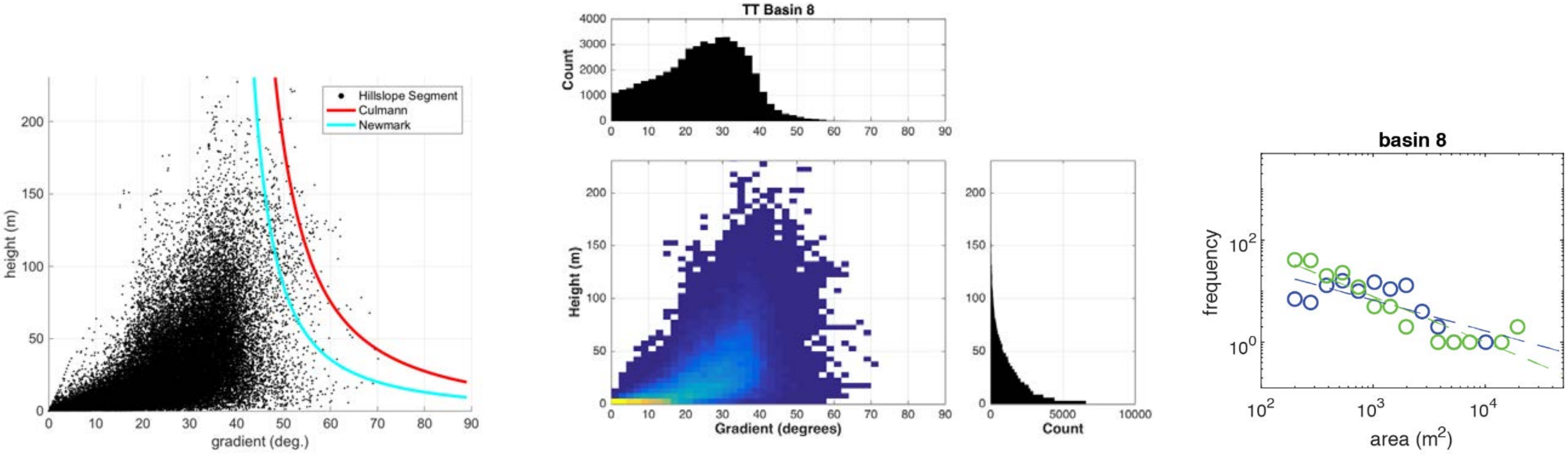

Appendix Figure A.12: (left) Basin 8 hillslope gradient-height scatter plot with Culmann and Newmark curves, (center) hillslope gradient-height density plot and histograms, (right) frequency-area plots of mapped (blue) and synthetic (green) landslide distributions.

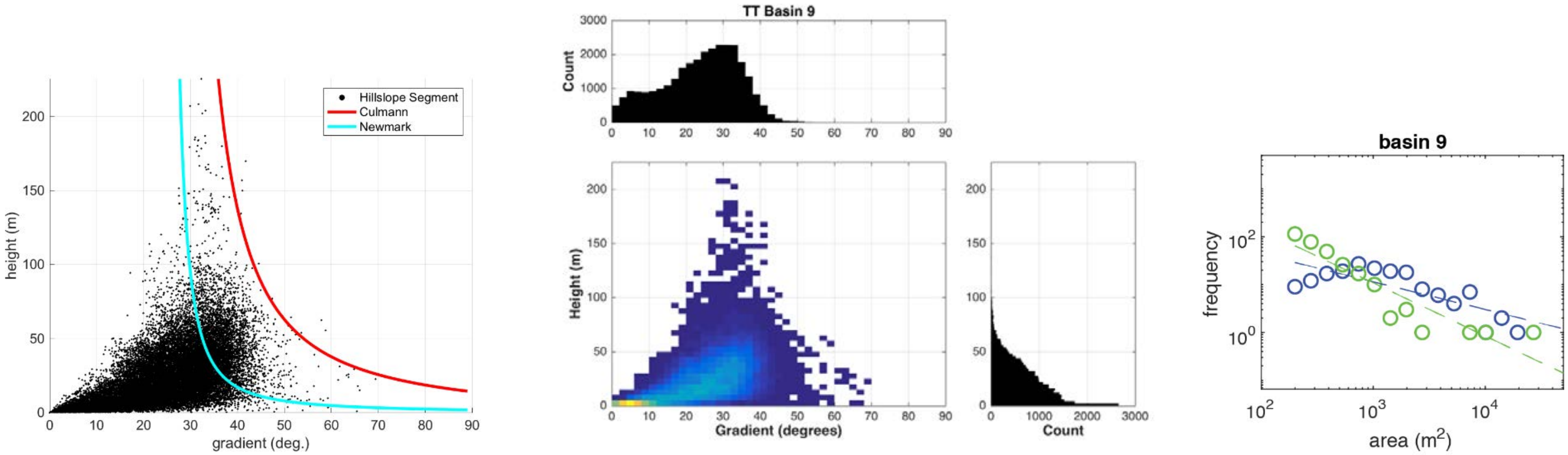

Appendix Figure A.13: (left) Basin 9 hillslope gradient-height scatter plot with Culmann and Newmark curves, (center) hillslope gradient-height density plot and histograms, (right) frequency-area plots of mapped (blue) and synthetic (green) landslide distributions.

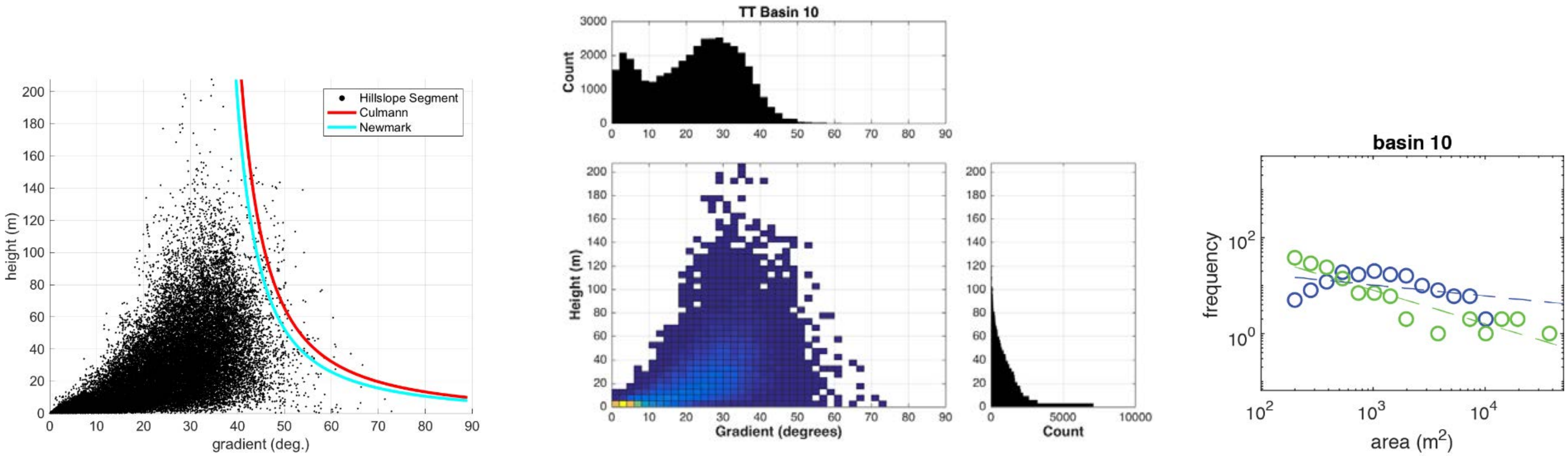

Appendix Figure A.14: (left) Basin 10 hillslope gradient-height scatter plot with Culmann and Newmark curves, (center) hillslope gradient-height density plot and histograms, (right) frequency-area plots of mapped (blue) and synthetic (green) landslide distributions.

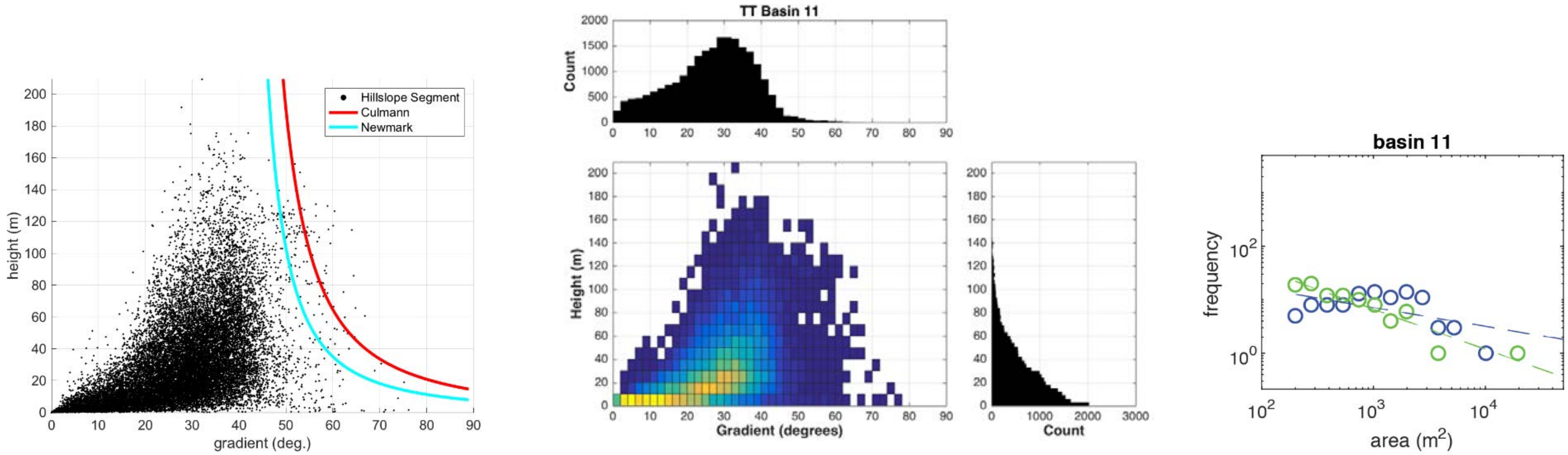

Appendix Figure A.15: (left) Basin 11 hillslope gradient-height scatter plot with Culmann and Newmark curves, (center) hillslope gradient-height density plot and histograms, (right) frequency-area plots of mapped (blue) and synthetic (green) landslide distributions.

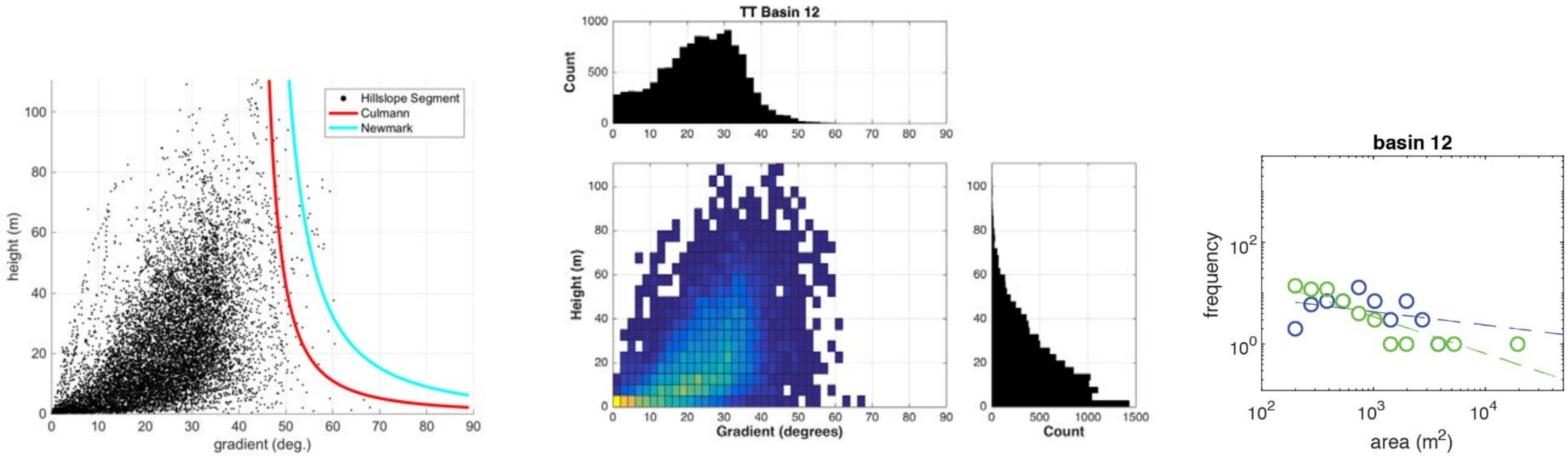

Appendix Figure A.16: (left) Basin 12 hillslope gradient-height scatter plot with Culmann and Newmark curves, (center) hillslope gradient-height density plot and histograms, (right) frequency-area plots of mapped (blue) and synthetic (green) landslide distributions.

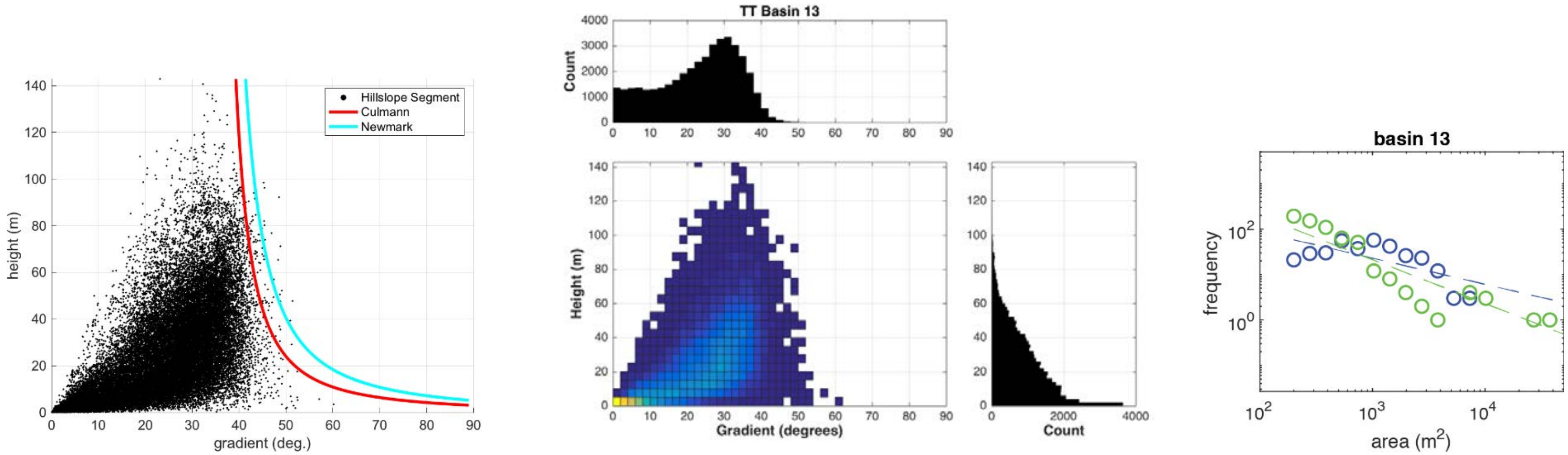

Appendix Figure A.17: (left) Basin 13 hillslope gradient-height scatter plot with Culmann and Newmark curves, (center) hillslope gradient-height density plot and histograms, (right) frequency-area plots of mapped (blue) and synthetic (green) landslide distributions.

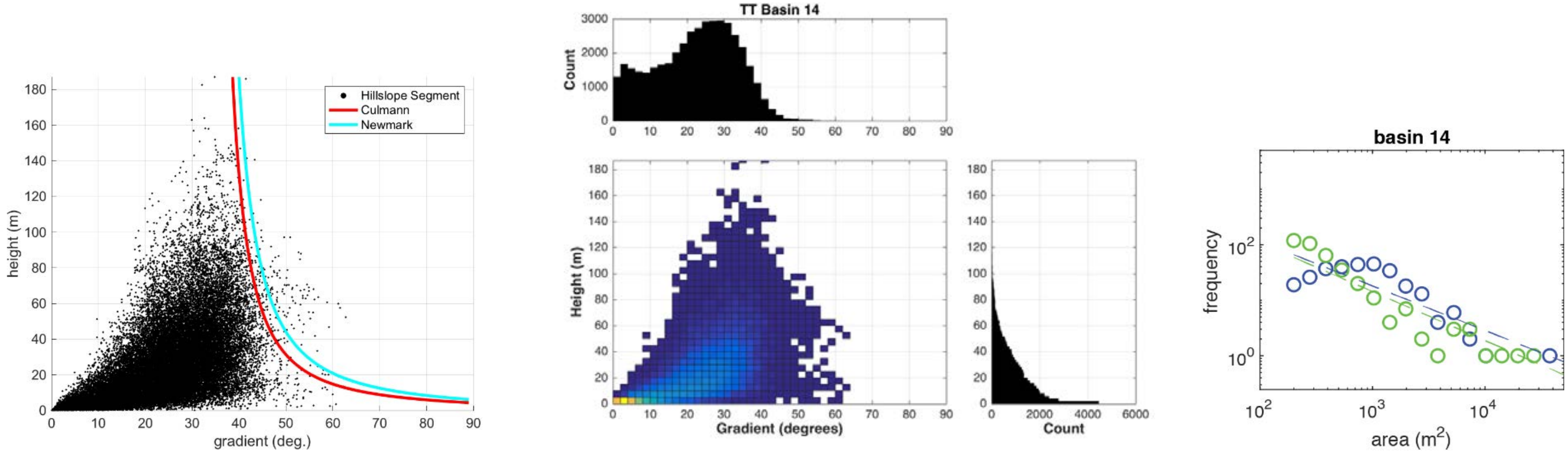

Appendix Figure A.18: (left) Basin 14 hillslope gradient-height scatter plot with Culmann and Newmark curves, (center) hillslope gradient-height density plot and histograms, (right) frequency-area plots of mapped (blue) and synthetic (green) landslide distributions.

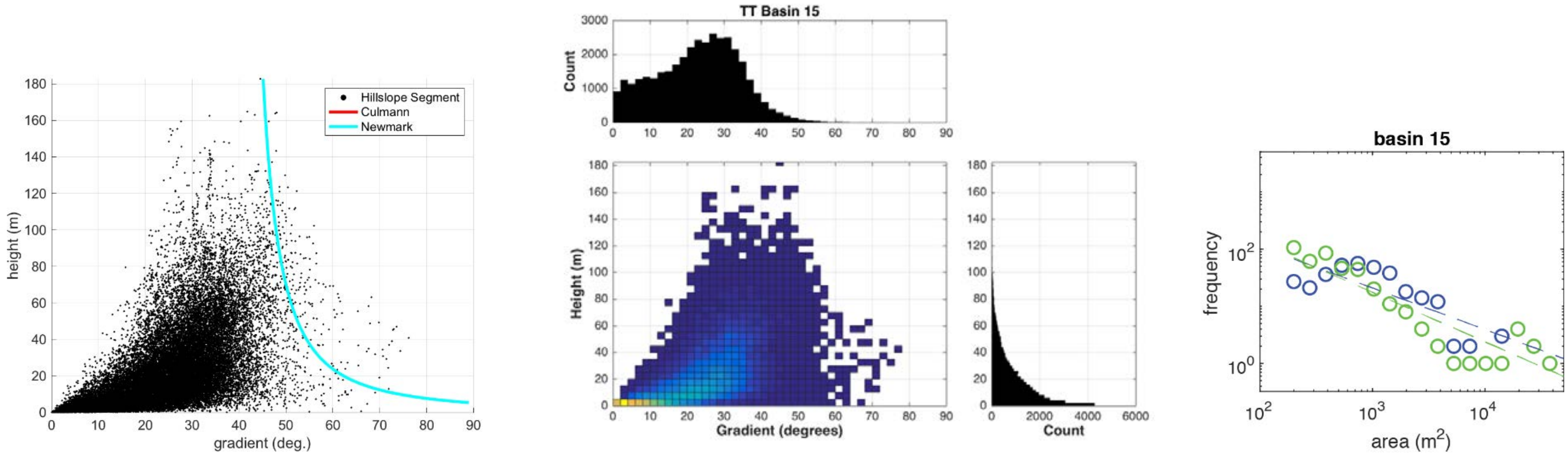

Appendix Figure A.19: (left) Basin 15 hillslope gradient-height scatter plot with Culmann and Newmark curves, (center) hillslope gradient-height density plot and histograms, (right) frequency-area plots of mapped (blue) and synthetic (green) landslide distributions.

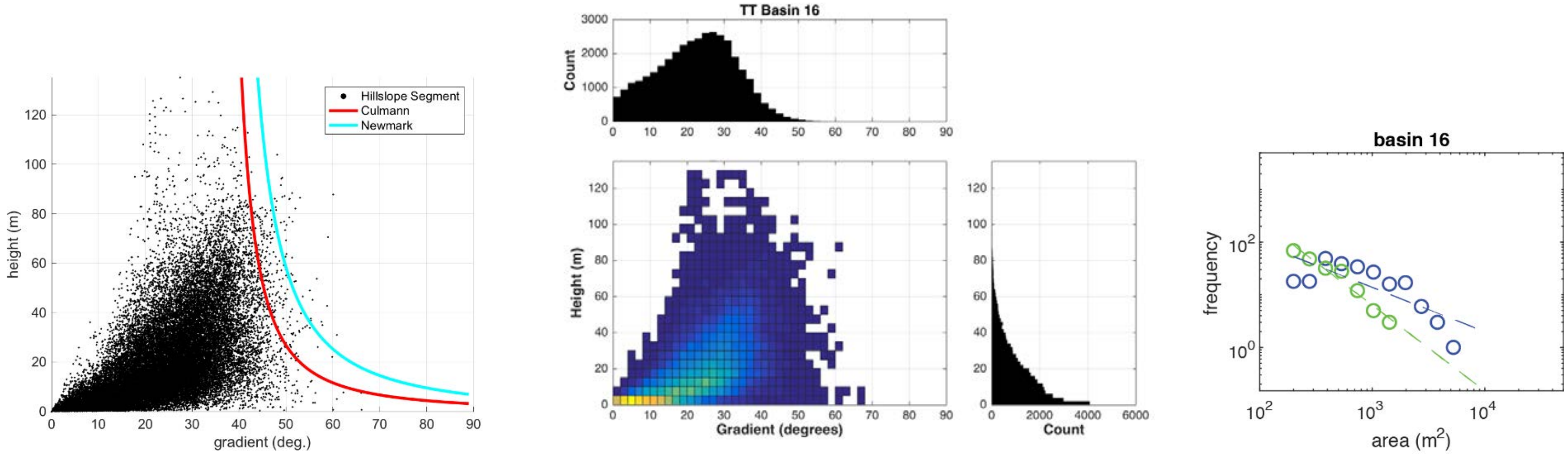

Appendix Figure A.20: (left) Basin 16 hillslope gradient-height scatter plot with Culmann and Newmark curves, (center) hillslope gradient-height density plot and histograms, (right) frequency-area plots of mapped (blue) and synthetic (green) landslide distributions.

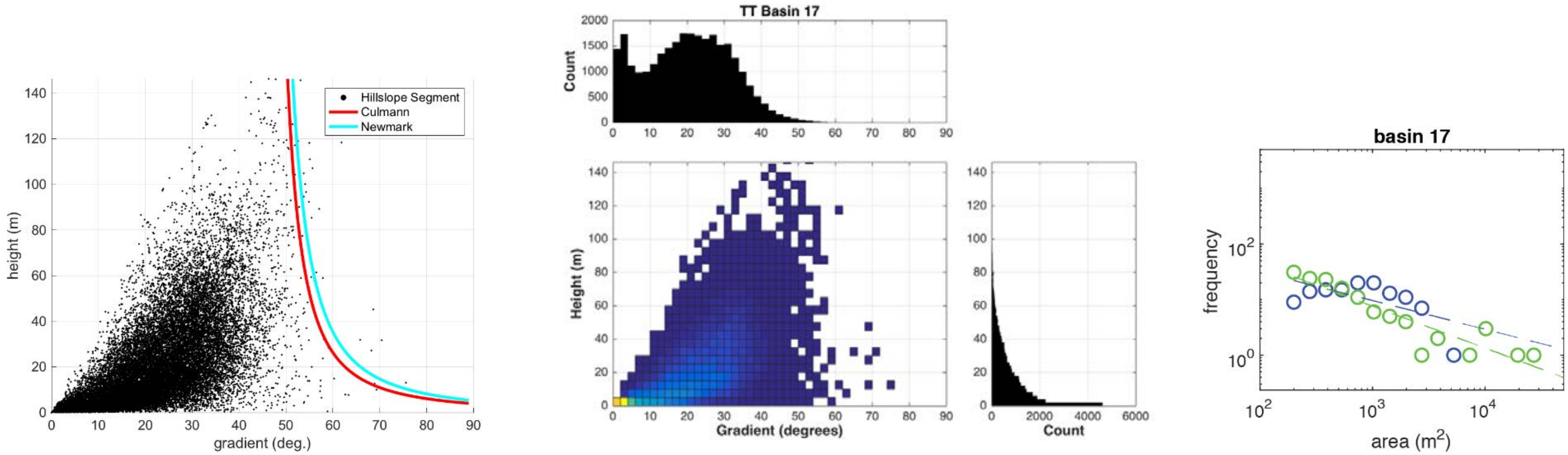

Appendix Figure A.21: (left) Basin 17 hillslope gradient-height scatter plot with Culmann and Newmark curves, (center) hillslope gradient-height density plot and histograms, (right) frequency-area plots of mapped (blue) and synthetic (green) landslide distributions.

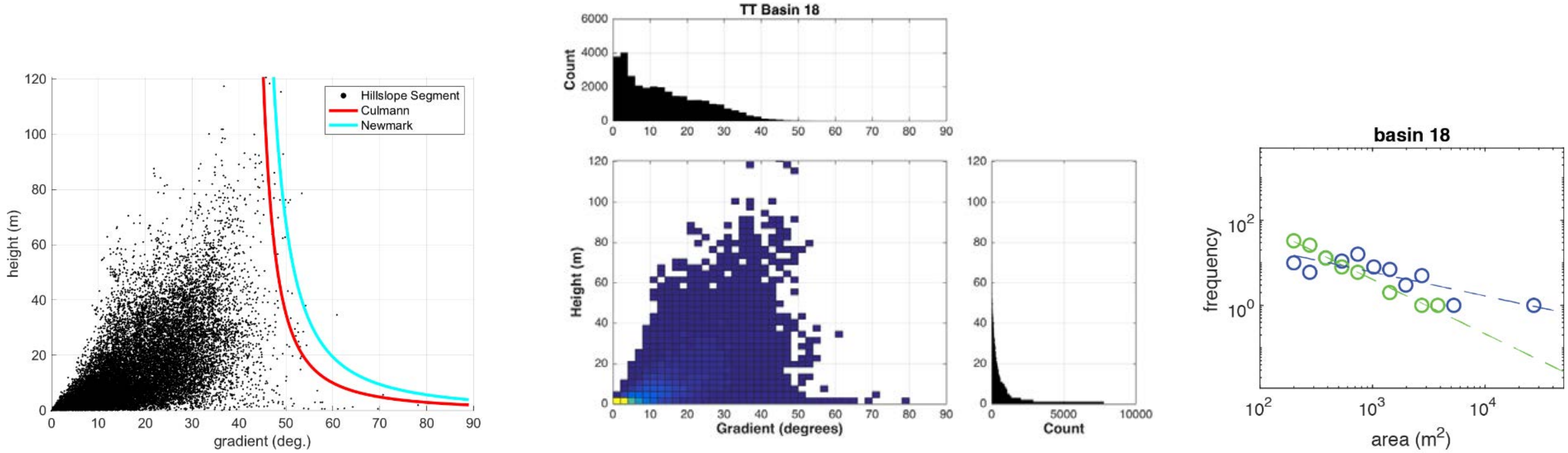

Appendix Figure A.22: (left) Basin 18 hillslope gradient-height scatter plot with Culmann and Newmark curves, (center) hillslope gradient-height density plot and histograms, (right) frequency-area plots of mapped (blue) and synthetic (green) landslide distributions.

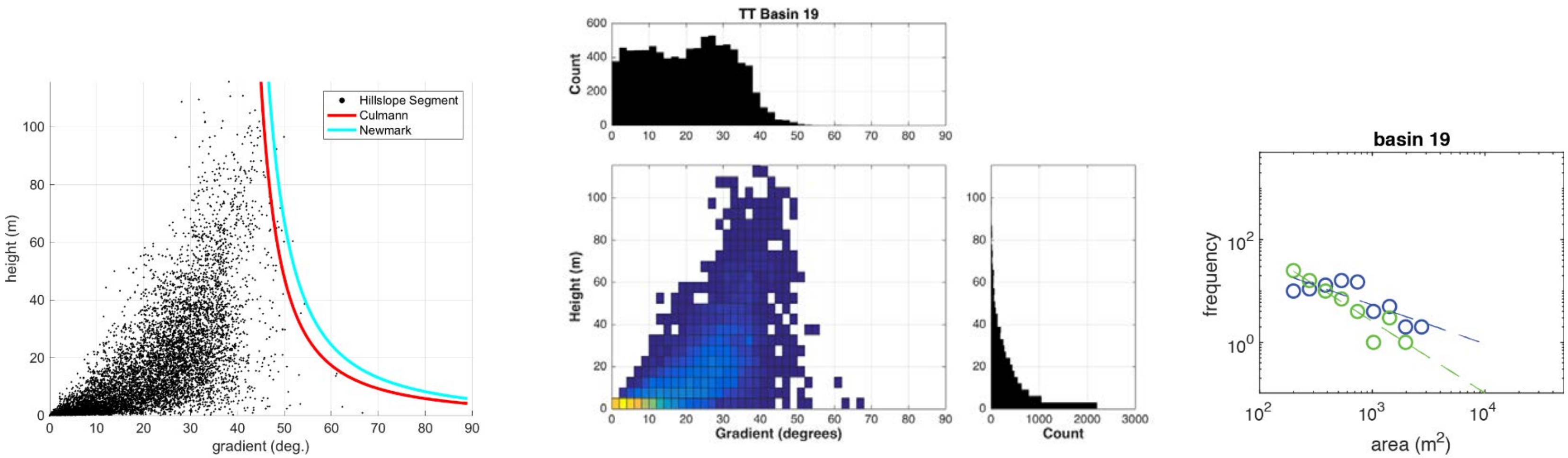

Appendix Figure A.23: (left) Basin 19 hillslope gradient-height scatter plot with Culmann and Newmark curves, (center) hillslope gradient-height density plot and histograms, (right) frequency-area plots of mapped (blue) and synthetic (green) landslide distributions.

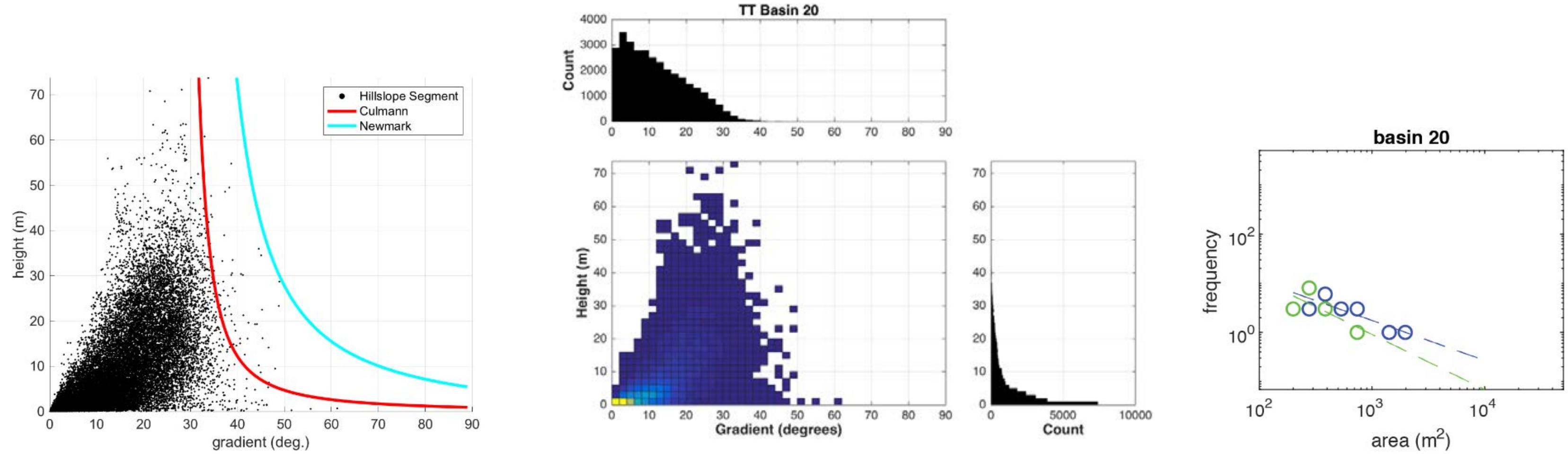

Appendix Figure A.24: (left) Basin 20 hillslope gradient-height scatter plot with Culmann and Newmark curves, (center) hillslope gradient-height density plot and histograms, (right) frequency-area plots of mapped (blue) and synthetic (green) landslide distributions.

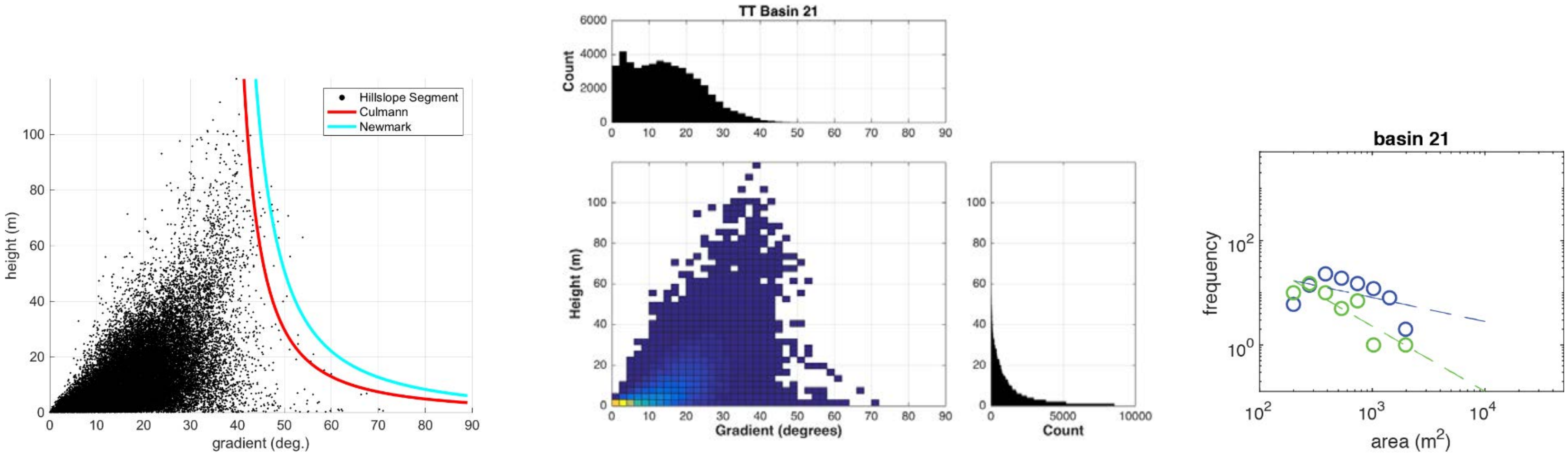

Appendix Figure A.25: (left) Basin 21 hillslope gradient-height scatter plot with Culmann and Newmark curves, (center) hillslope gradient-height density plot and histograms, (right) frequency-area plots of mapped (blue) and synthetic (green) landslide distributions.

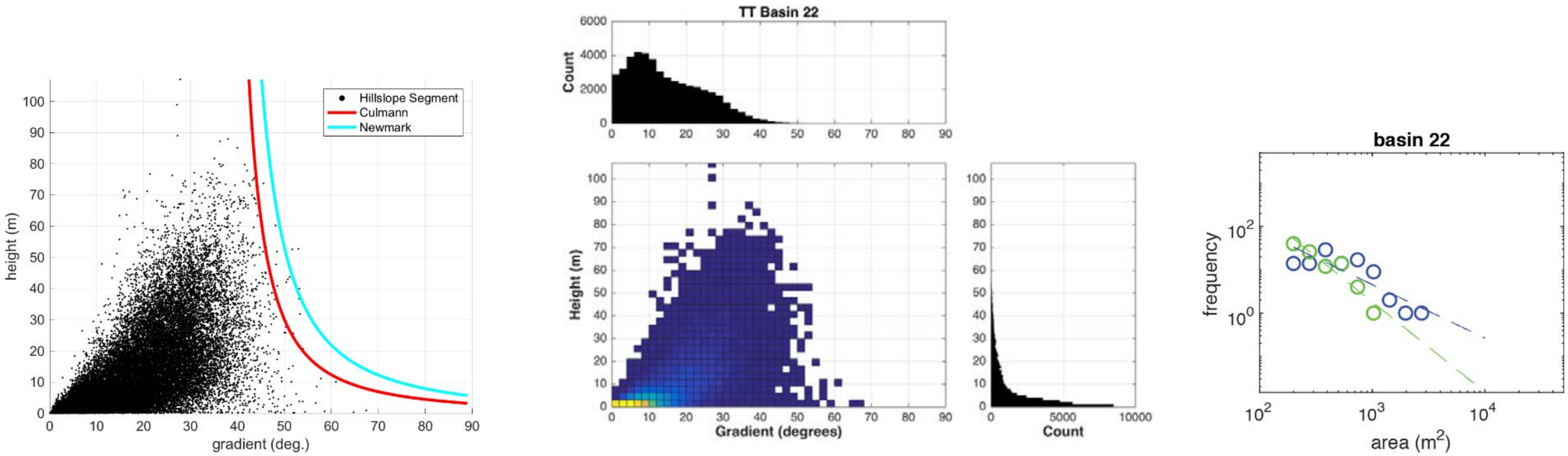

Appendix Figure A.26: (left) Basin 22 hillslope gradient-height scatter plot with Culmann and Newmark curves, (center) hillslope gradient-height density plot and histograms, (right) frequency-area plots of mapped (blue) and synthetic (green) landslide distributions.

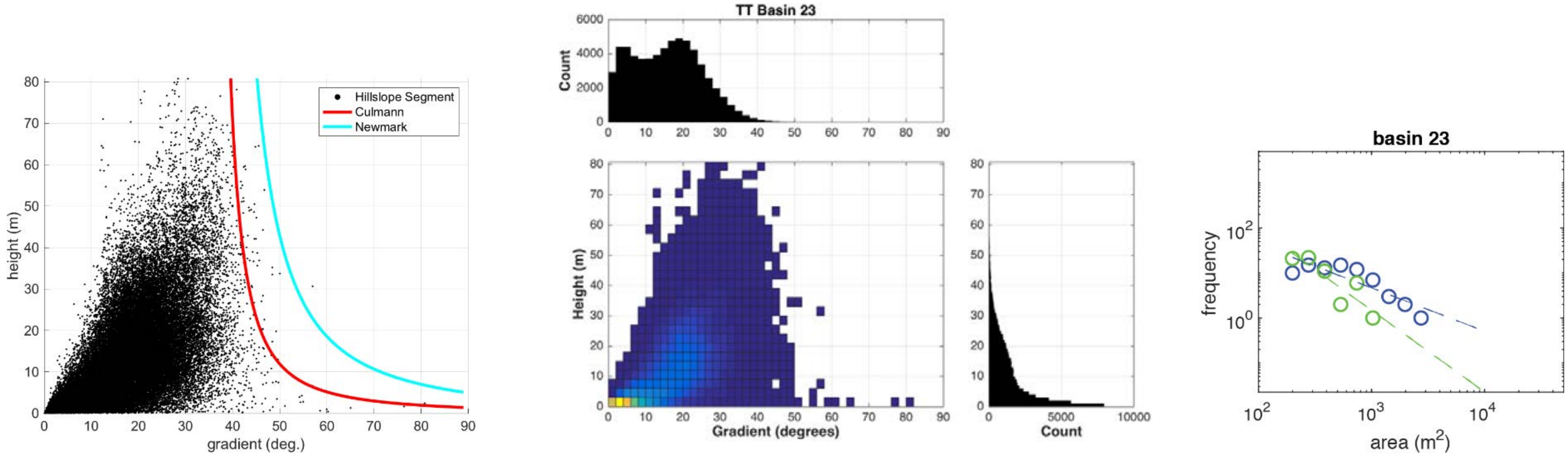

Appendix Figure A.27: (left) Basin 23 hillslope gradient-height scatter plot with Culmann and Newmark curves, (center) hillslope gradient-height density plot and histograms, (right) frequency-area plots of mapped (blue) and synthetic (green) landslide distributions.

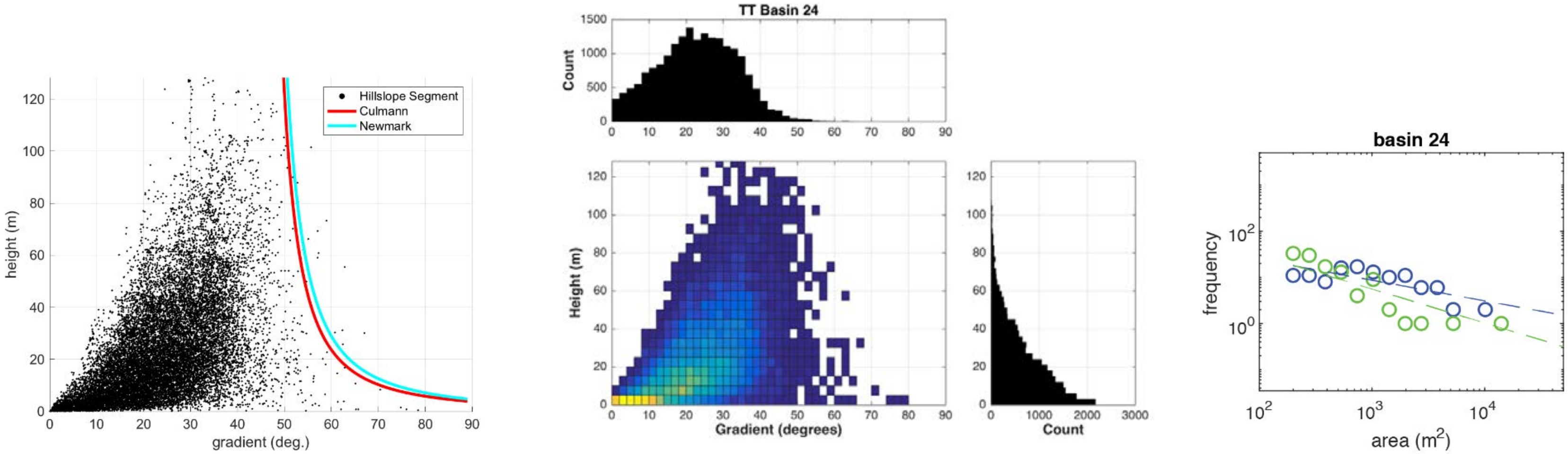

Appendix Figure A.28: (left) Basin 24 hillslope gradient-height scatter plot with Culmann and Newmark curves, (center) hillslope gradient-height density plot and histograms, (right) frequency-area plots of mapped (blue) and synthetic (green) landslide distributions.

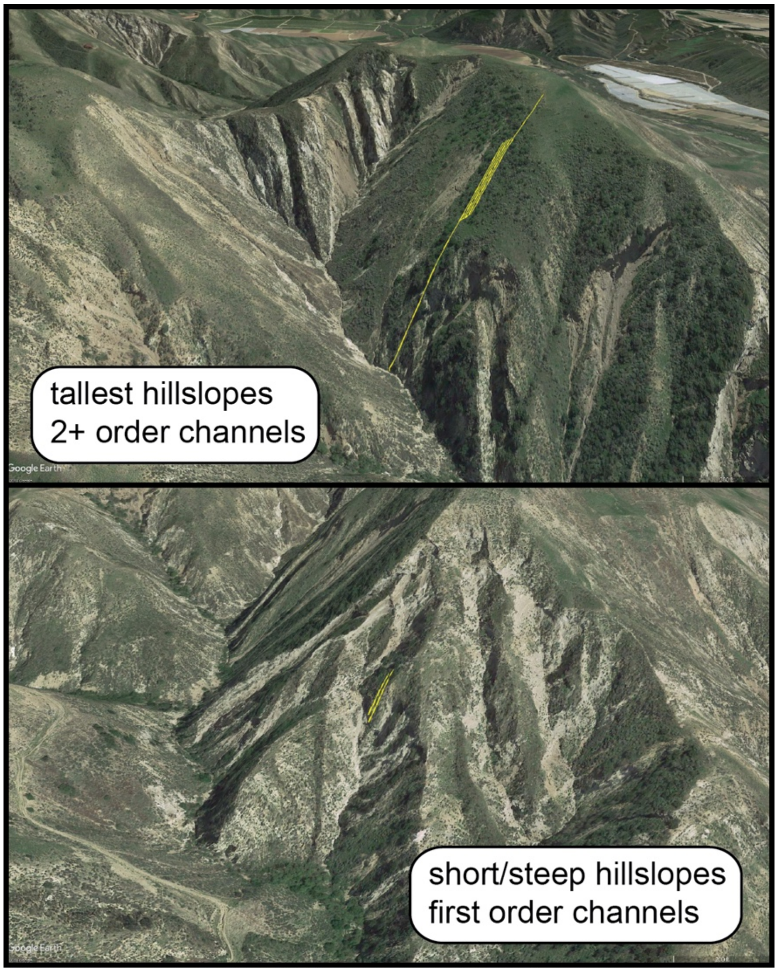

Appendix Figure A.29: Example locations of hillslopes in Basin 1. The tallest threshold hillslopes are generally located above second order and greater channels, while short/steep threshold hillslopes are typically located above first-order channels

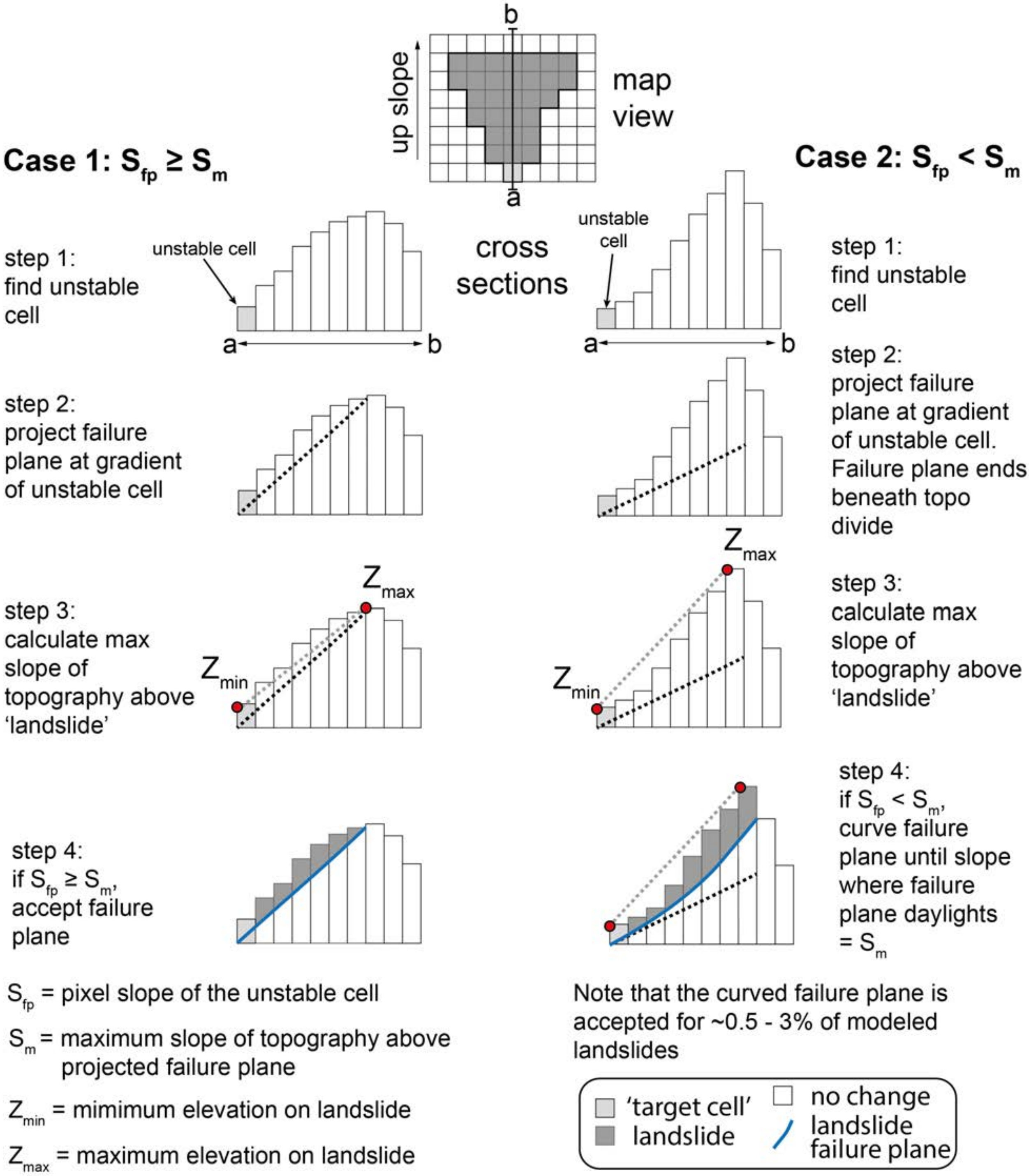

Appendix Figure A.30: Generalized method used to find the landslide failure plane projected upslope from Newmark failure cells in a digital landscape.

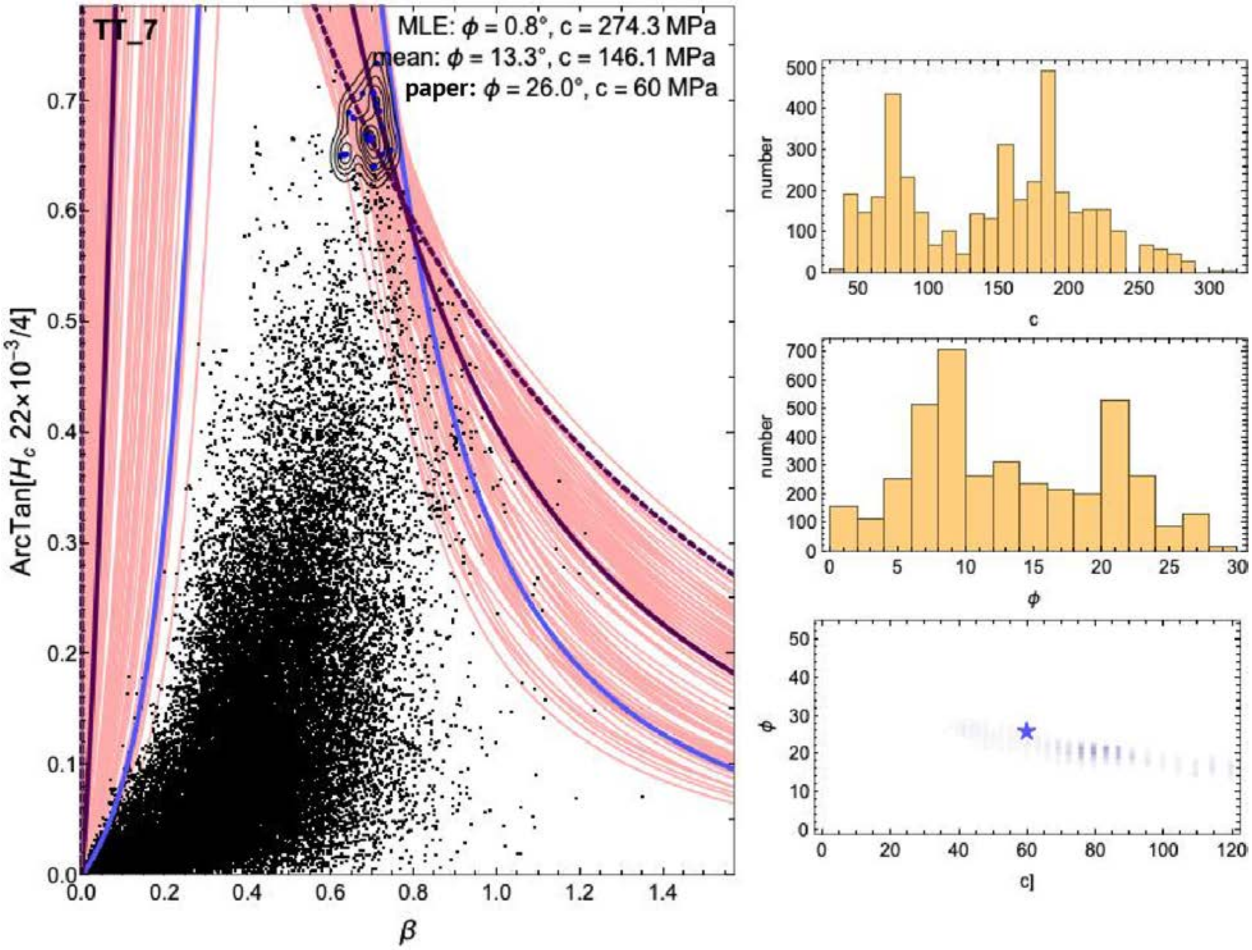

Appendix Figure A.31: Example of an attempted quantitative approach to fitting the Culmann model to the threshold of scatter data, with hillslope data from basin 7. The MCMC approach requires models pass through the tallest/steepest hillslopes by assigning a prior probability based on the density of data above 99.9% quantile in height, and 50% quantile in gradient at those heights, shown by PDF contours in the scatter plot. The MLE, and mean of posteriors, produce lower friction angle estimates than is characteristic of most earth materials. Histograms of posteriors demonstrate wide range of cohesion and friction angle estimates. Figure courtesy of Eric Hetland.

Appendix Table A.1: Sample locations and mean apatite (U-Th)/He ages. Sample locations are also shown in Figures 2.1 and A.1

Sample	**Longitude (°W)**	**Latitude (°N)**	**Elevation (m)**	**Mean Age[1] (Ma)**
16-PC-1	118.7612	34.46701	344	-- [2]
16-PC-3	118.7597	34.47153	347	-- [3]
16-PC-4	118.7557	34.46217	365	3.9 ± 1.2

[1] Mean age includes 2-sigma standard error

[2] One-sigma standard deviation of bedrock replicate analyses after outlier removal is greater than 45 percent of mean age. No mean age is reported.

[3] Replicate ages are older than the depositional age of the formation, indicating that ages are inherited and do not reflect cooling of the host rock. No mean age is reported.

Appendix Table A.2: Single-grain apatite (U-Th-Sm)/He analyses

Name	U ppm (ppm)	U SD (ppm)	Th (ppm)	Th SD (ppm)	Sm (ppm)	Sm SD (ppm)	He (ncc)	He error (ncc)	He (ncc/g)	Shape[1]	Effective Uranium (eU) (ppm)	Mass (mg)	FT[2]	Radius (um)	Length (um)	Uncorrected Age	Corrected Age (Ma)	Age Error[3]
16-PC-01a	12.35	0.18	27.40	0.43	31.24	0.50	0.0343	0.00022	14991.093	pp	18.92	0.0023	0.76	56.3	89.7	6.2	8.07	0.08
16-PC-01b	20.11	0.29	41.40	0.60	331.25	5.04	0.0173	0.00016	13918.051	nn	31.45	0.0012	0.70	40.4	94.6	3.3	4.79	0.05
16-PC-01c	39.27	0.56	41.07	0.59	240.54	3.59	0.2930	0.00058	110617.591	np	50.09	0.0026	0.76	51.0	126.4	18.4	24.26	0.22
16-PC-01d	7.96	0.12	11.02	0.16	34.38	0.58	0.0276	0.00009	11498.488	np	10.71	0.0024	0.75	49.3	122.8	8.3	11.02	0.10
16-PC-03a	27.47	0.39	32.34	0.47	54.62	0.89	0.1572	0.00025	65222.872	np	35.31	0.0024	0.74	44.8	148.8	15.1	20.50	0.18
16-PC-03b†	3.47	0.06	12.77	0.20	97.36	1.52	0.0380	0.00013	18432.188	pp	6.94	0.0021	0.71	40.2	158.1	21.8	30.47	0.25
16-PC-03c	8.25	0.12	23.92	0.34	92.03	1.43	0.0735	0.00017	31206.602	np	14.31	0.0024	0.74	47.0	132.1	17.9	23.99	0.19
16-PC-03d	19.57	0.28	11.95	0.17	220.10	3.24	0.2668	0.00054	99839.500	pp	23.47	0.0027	0.74	45.1	163.4	36.1	48.68	0.46
16-PC-04a‡	42.26	0.61	36.85	0.56	98.16	1.47	0.1284	0.00050	118772.223	pp	51.37	0.0011	0.70	43.3	71.6	18.9	27.04	0.24
16-PC-04b	11.87	0.17	15.78	0.23	25.25	0.48	0.0095	0.00012	4924.689	pp	15.69	0.0019	0.72	41.1	141.3	2.0	2.83	0.03
16-PC-04d	15.67	0.23	14.31	0.21	23.41	0.43	0.0210	0.00014	7714.107	np	19.14	0.0027	0.76	49.5	138.3	3.0	3.98	0.04
16-PC-04e	17.19	0.25	13.90	0.20	49.08	0.73	0.0468	0.00025	10146.815	nn	20.67	0.0046	0.80	59.6	161.2	3.9	4.91	0.05

† Age excluded from calculation of mean age due to and standard error due to low Uranium content (<5ppm).

‡ Age identified as an outlier by the statistical test of Dean and Dixon (1951) at the 90 percent confidence interval and excluded from calculation of mean age and standard error.

[1] The Following terms refer to the morphology of apatite grains: nn = a grain with two unbroken euhedral tips; pp = a grain with both tips broken such that they are roughly perpendicular to the c-axis; np = a grain with one unbroken tip and one tip broken roughly perpendicular to the c-axis; multigrain = multiple apatite grains degassed for 4He within one packet due to low single-grain 4He yield.

[2] Ft is alpha-ejection correction after Farley et al., (1996).

[3] The age error reported for single grained ages represents the propagated one-sigma uncertainty based on the analytical error in measuring He, U, Th and Sm.

Appendix Table A.3: Basin-averaged strength and topographic measurements

Basin #	Culmann C (kPa)	Culmann Phi (deg.)	Newmark C[1] (kPa)	Newmark C/t[2] (kPa/m)	Basin Area (km^2)	Max Hillslope Height (m)	Mean Hillslope Height (m)	Max Pixel Slope (deg.)	Mean Pixel Slope (deg.)	STD Pixel Slope (deg.)	Landslide Count	Average Newmark Landslide Thickness (m)	Average Culmann Landslide Thickness[3] (m)	Average Threshold Landslide Thickness[4] (m)	Geologic Unit[5]
1	21	33	22.2	10.2	12.0	233.8	29.5	75.0	28.6	12.3	451	2.6	1.9	3.8	Tm
2	41	29	26.3	12.1	12.5	261.5	33.5	78.6	29.8	12.0	341	3.0	2.7	6.7	Tm
3	60	31	26.8	12.3	12.1	207.4	33.2	81.7	30.7	11.1	134	3.1	2.2	8.7	Tm
4	17	30	23.9	11.0	10.8	206.2	22.1	76.5	24.3	10.2	73	2.4	1.6	3.2	Tm
5	25	37	30.1	13.9	5.5	219.3	27.3	81.4	28.5	11.4	12	8.2	1.4	4.3	Tm
6	40	28	28.9	13.3	10.9	245	26.8	84.4	27.7	11.4	230	3.8	2.5	6.5	Tm
7	60	26	27.4	12.6	8.5	164.3	23.1	77.8	25.5	10.5	168	3.2	2.1	8.3	Tm
8	55	35	25.9	11.9	12.2	230.7	28.6	81.8	27.8	12.1	106	5.3	1.8	8.1	Tm
9	50	24	6.2	2.86	6.5	225.2	23.5	70.6	25.9	11.1	182	1.8	2.1	7.7	Tp
10	30	31	24.0	11.0	9.6	207.5	25.4	72.4	25.2	11.9	158	3.0	1.7	5.0	Tp
11	38	38	20.6	9.5	5.7	209.4	30.5	79.9	28.8	11.7	105	6.4	1.4	6.0	Tm
12	5	41	14.8	6.8	3.0	110.6	21.5	72.2	23.2	13.1	59	3.1	1.1	1.0	Tp
13	9	33	15.2	7.0	9.6	135.7	24.6	66.9	24.7	11.4	378	1.6	1.0	1.7	Tp
14	13	32	18.3	8.4	10.5	165.2	24.9	72.2	25.0	11.1	309	2.0	1.3	2.5	Tp
15	14	38	14.0	6.4	8.1	164	22.5	78.4	26.2	11.7	362	2.7	1.3	2.6	Tp
16	9	34	19.6	9.0	7.8	131.6	19.8	72.5	24.7	11.4	254	2.8	1.1	1.7	Tp
17	9	44	12.1	5.6	6.2	146.4	19.9	76.9	23.5	12.1	141	3.4	1.3	1.7	Tp
18	5	40	9.7	4.5	6.3	120.6	10.7	73.3	15.8	11.5	94	2.1	0.8	1.0	QTs
19	11	37	15.5	7.1	1.8	115.6	16.7	69.9	23.8	12.7	90	1.9	1.1	2.0	Tp
20	3	27	17.8	8.2	5.5	73.8	7.4	59.1	13.8	9.6	20	1.8	0.5	0.6	QTs
21	10	34	17.1	7.9	9.0	119.9	9.8	75.7	16.8	10.3	108	2.1	0.8	1.8	QTs
22	9	35	15.9	7.3	8.3	107	9.6	70.1	17.7	11.4	117	2.2	0.7	1.7	QTs
23	4	34	14.4	6.6	12.4	80.8	11.7	60.0	17.6	9.5	94	1.7	0.6	0.8	QTs
24	9	43	11.0	5.1	4.6	128.2	23	75.1	24.5	11.6	125	2.8	0.9	1.7	Tp

[1] Calculated with Phi equal to the Culmann phi estimate

[2] Cohesion/(landslide thickness) model results. Values are multiplied by the median landslide thickness to produce estimates of cohesion in kPa.

[3] Culmann model estimates of landslide thickness were calculated using each hillslope gradient-height pair in a basin. Landslide failure angle is calculated as the geometric mean of the friction angle and hillslope gradient, i.e. $\theta = (\phi + \beta)/2$ (Lu and Godt, 2013). Thickness is calculated as the mean height of the resultant wedge, measured normal to the landslide failure plane.

[4] Threshold model estimates of landslide thickness were calculated with gradient-hillslope pairs that fall on the Culmann curve set by C and ϕ, in increments of 0.1 degrees. Landslide failure angle is calculated as the geometric mean of the friction angle and hillslope gradient, i.e. $\theta = (\phi + \beta)/2$ (Lu & Godt, 2013). Thickness is calculated as the mean height of the resultant wedge, measured normal to the landslide failure plane.

[5] Predominant geologic unit within each basin area. Tm = Monterey Formation, Tp = Pico Formation, and QTs = Saugus Formation. From Dibblee (1991, 1993) and Dibblee and Ehrenspeck (1996, 1997).

Appendix Table A.4: Burial depth of sedimentary rocks by basin

Basin #	Minimum Burial Depth (m)	Maximum Burial Depth (m)	Average Burial Depth (m)
1	3300	4000	3600
2	3300	4500	3900
3	4000	5300	4700
4	3300	4300	3800
5	4300	4800	4500
6	3300	4800	4000
7	4100	4900	4500
8	4100	4900	4500
9	1900	2900	2400
10	2900	3300	3100
11	3300	4200	3800
12	2900	3300	3100
13	2100	3000	2500
14	2100	3500	2800
15	1900	3300	2600
16	2100	3300	2700
17	2900	3500	3200
18	0	2200	1100
19	2100	2600	2300
20	500	2300	1400
21	1000	2200	1600
22	500	2100	1300
23	1300	2100	1700
24	2100	3300	2700

Appendix B: Supporting Information for Chapter 3. Profiles of Near-Surface Rock Mass Strength Across Gradients in Burial, Erosion, and Time

B.1 Introduction

This appendix contains eight supplemental figures to Chapter 3.

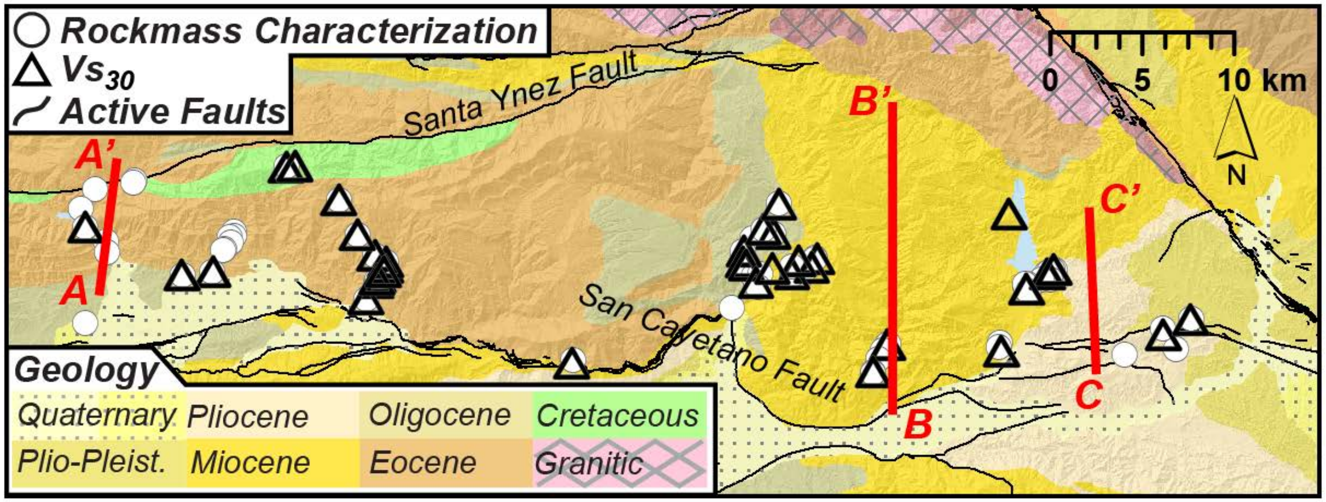

Appendix Figure B.1: Simplified geologic map of the Topatopa Mountains, with locations of cross section profiles A-A', B-B', and C-C'. Interpreted cross sections follow in subsequent figures.

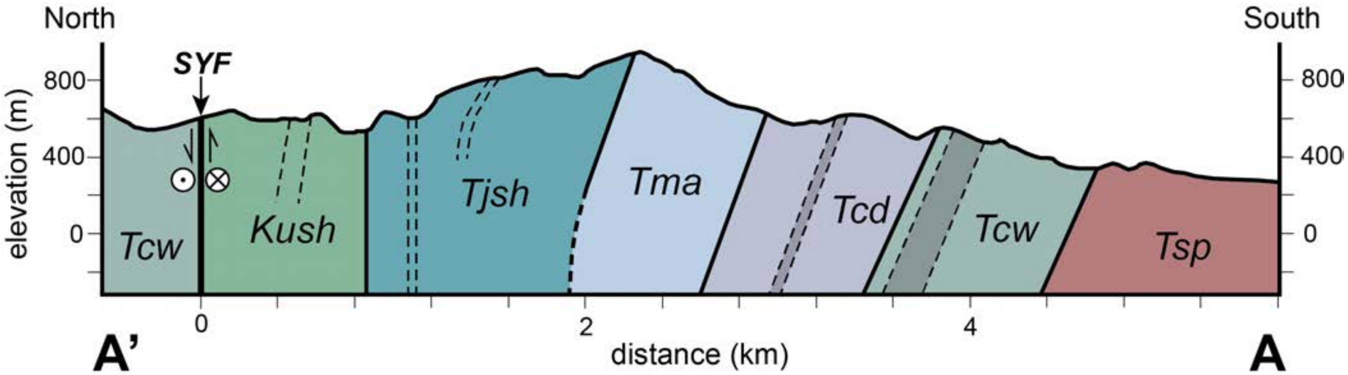

Appendix Figure B.2: Cross section through the western Topatopa Mountains at Matilija Canyon, profile A-A'(Figure B.1). Cross section interpreted from Dibblee (1987a). Note that Eocene (Tjsh, Tma, Tcd, Tcw) and Oligocene (Tsp) strata are overturned, and stratigraphic up is towards the south. Geologic unit abbreviations: Tsp–Sespe Formation, Tcw–Coldwater Sandstone, Tcd–Cozy Dell Shale, Tma–Matilija Sandstone, Tjsh–Juncal Formation, Kush–Unnamed Marine Strata, SYF–Santa Ynez Fault.

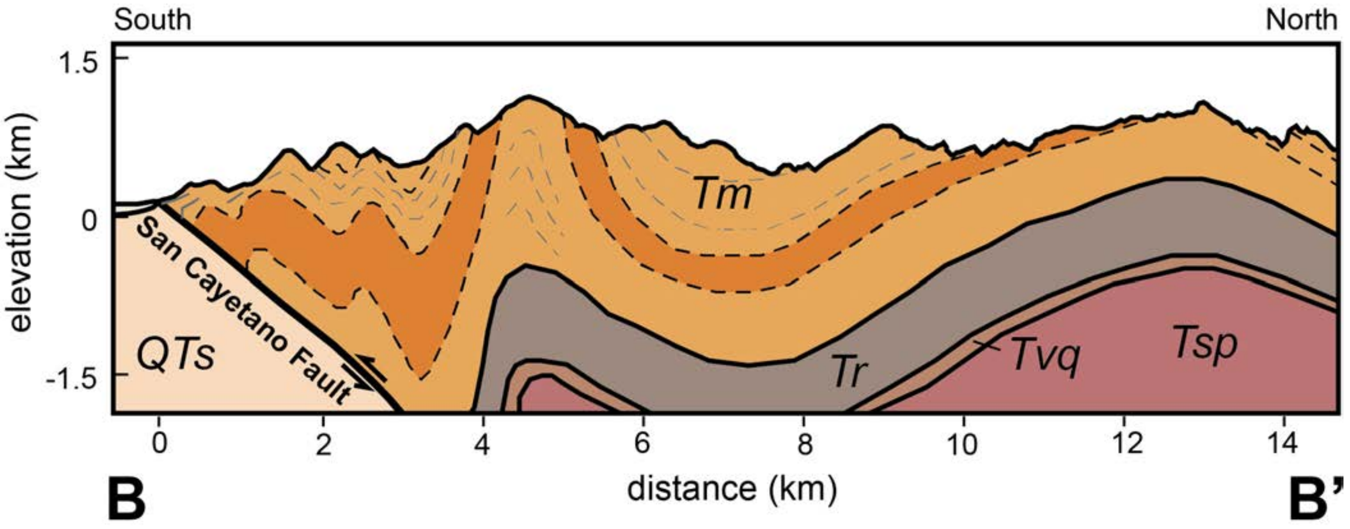

Appendix Figure B.3: Cross section through the Topatopa Mountains at Hopper Canyon, profile B-B' (Figure B.1). Modified from Dibblee (1991), Dibble and Ehrenspeck (1996), and Townsend et al. (2020). Geologic unit abbreviations: QTs–Saugus Formation, Tm–Monterey Formation, Tr–Rincon Shale, Tvq–Vaqueros Sandstone, Tsp–Sespe Formation.

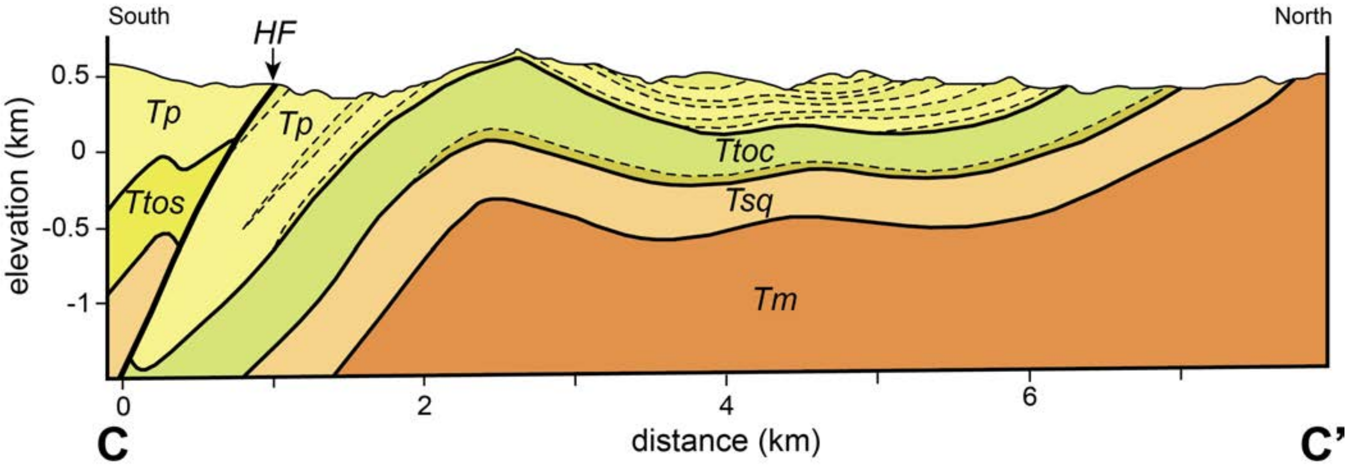

Appendix Figure B.4: Cross section through the eastern Topatopa Mountains at profile C-C'(Figure B.1). Modified from Dibblee (1993). Geologic unit abbreviations: Tp–Pico Formation, Ttoc/Ttos–Towsley Formation, Tsq–Sisquoc Formation, Tm–Monterey Formation, HF–Holser Fault. The Saugus Formation (QTs) is stratigraphically above the Pico Formation to the east of profile C-C'.

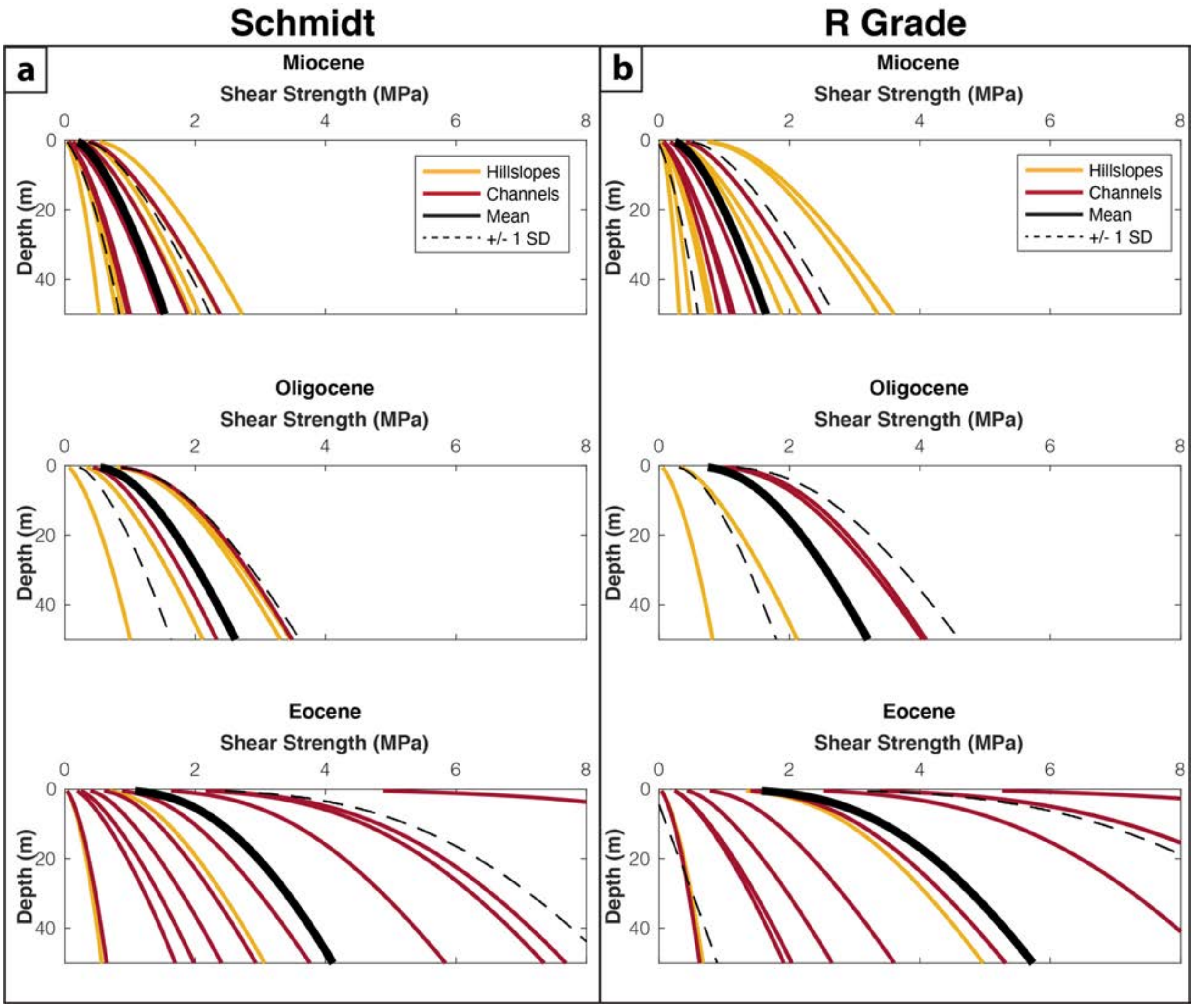

Appendix Figure B.5: Shear strength profiles of a subset of sites (n = 30) in the Western Transverse Ranges from which an R Grade observation was recorded, with a) σ_{ci} calculated with the Deere & Miller (1996) regression for UCS from Schmidt R values for this same subset of data, and b) σ_{ci} defined using R Grade values and Table 1 in Hoek et al., (1997). For each R Grade value, we defined UCS using the midpoint of the range reported in Table 1 of Hoek et al. (1997). For ranges of R Grade values (e.g. R1-R2), we used the UCS value on the Grade boundary. Mean values only differ by up to ~15% at the deepest part of the profiles, and the patterns in shear strength profiles are identical to those produced using Schmidt R and the Deere & Miller (1966) regression. Given this consistency between Schmidt R and R Grade values, we calculate shear strength profiles for the entire field inventory (n = 210) with intact strength defined using Schmidt R field measurements and the Deere & Miller (1966) regression.

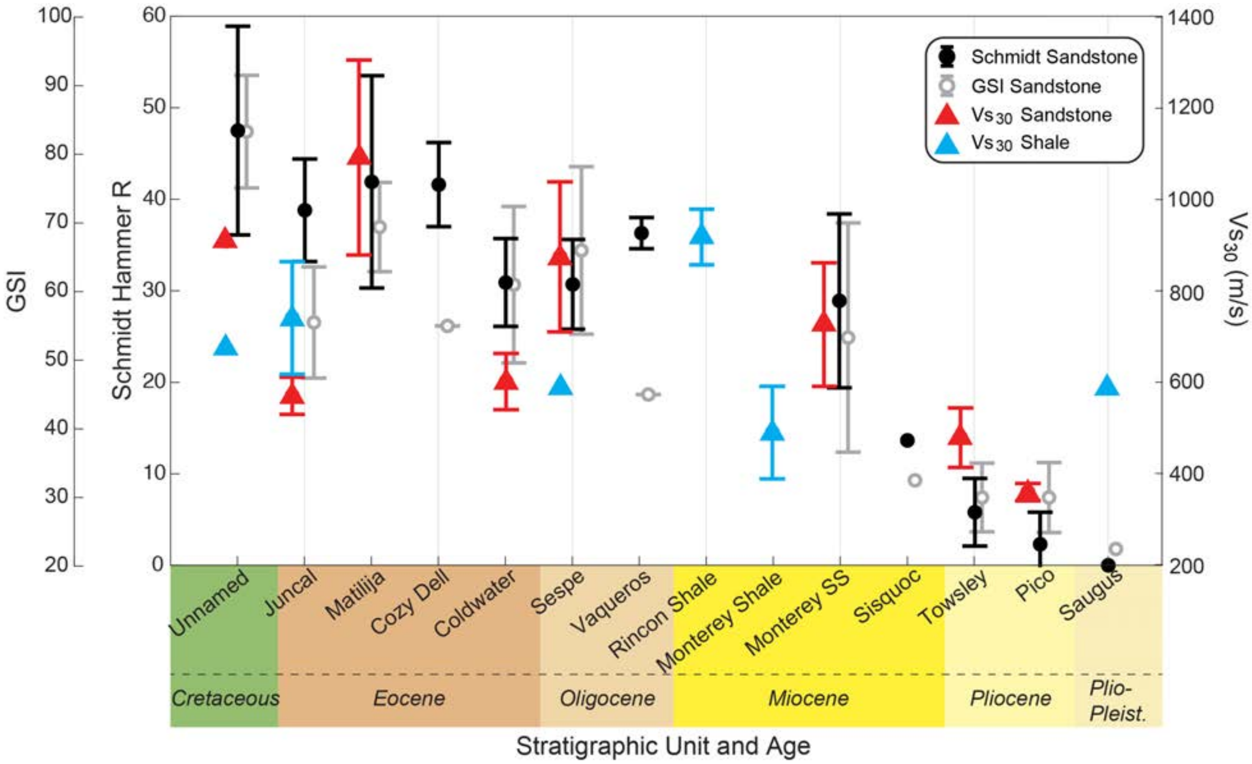

Appendix Figure B.6: Mean Schmidt hammer rebound values, mean GSI, and mean Vs_{30} by geologic unit in the Topatopa Mountains. This figure is identical to Figure 3.4 in Chapter 3, except that Vs_{30} of shale is included. Schmidt hammer R and GSI data were filtered to only include measurements on sandstones. Geologic units are arranged from youngest (Plio-Pleistocene) to oldest (Cretaceous). Mean Schmidt hammer rebound values, GSI, and Vs_{30} on sandstone increase with increasing age from Plio-Pleistocene (Saugus) to Oligocene (Sespe). Mean Schmidt hammer rebound values are largely the same for Eocene and Cretaceous units, whereas mean Vs_{30} is variable for these units.

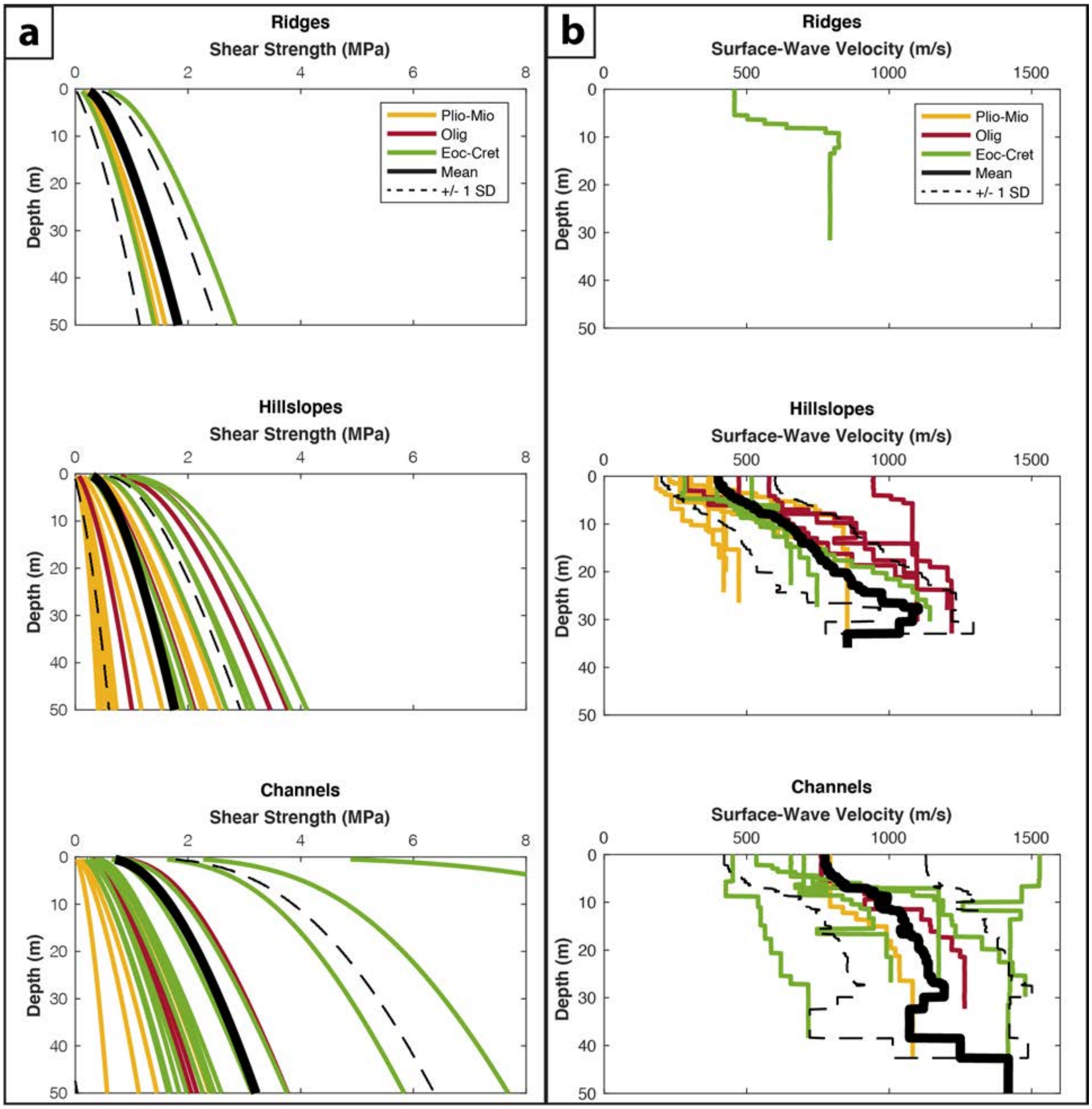

Appendix Figure B.7: a) Shear strength profiles, and b) S-wave velocity profiles of sandstone units in the Topatopa Mountains, by topographic position. Colors of each profile indicates the stratigraphic age of the unit from which the data was collected. Mean profiles of ridge and hillslope sites are nearly the same, whereas the mean shear strength profile of channel sites is stronger for each depth interval. This is likely biased by sites from Eocene and Cretaceous units.

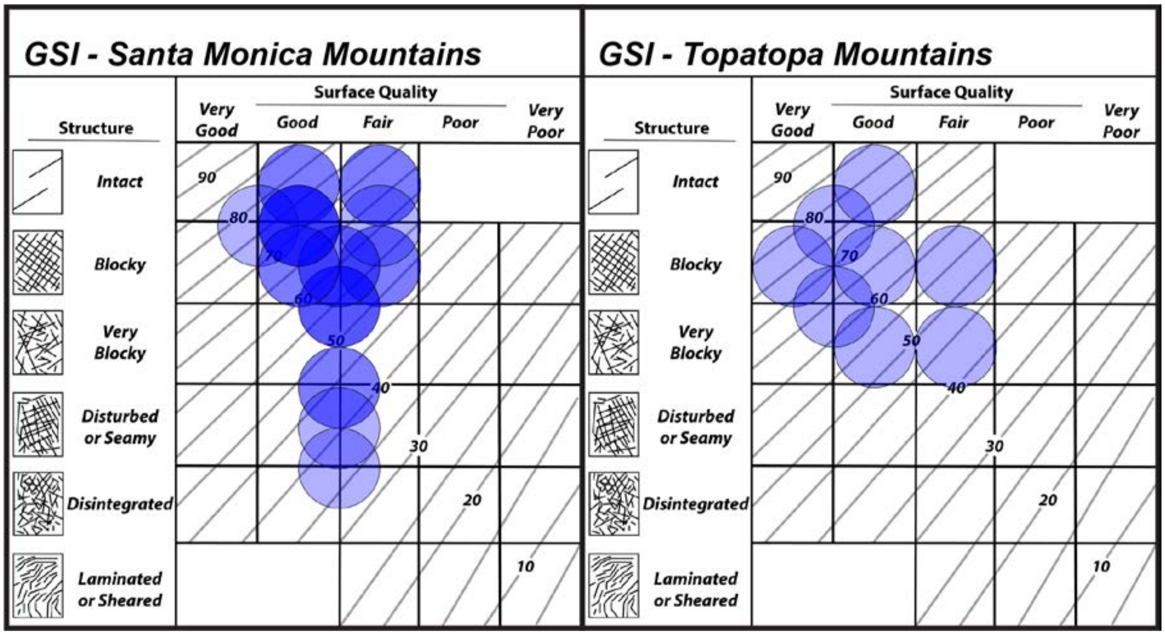

Appendix Figure B.8: GSI ranges from Sespe Formation sites with sandstone lithologic types in the Santa Monica Mountains and Topatopa Mountains.

Appendix C: Supporting Information for Chapter 4. Reverse Faulting within a Continental Plate Boundary Transform System

C.1 Introduction

This appendix contains a summary of laboratory and analytical protocols for analysis of apatite and zircon (U-Th-[Sm])/He thermochronometry, thermochronometric results for each transect, and descriptions of the pre-exhumation thermal histories as inferred from the thermal models and mapped geology. Fourteen supplemental figures showing geologic cross sections and full best-fit thermal histories are included.

C.2 Apatite (U-Th)/He Methods

Samples were crushed, sieved, and separated using standard methods to isolate apatite and zircon by exploiting differences in density and magnetic susceptibility. Individual mineral grains were hand-selected under a high-powered binocular microscope to screen for clarity, crystal morphology, and minimal inclusions of other potentially radiogenic minerals. Grains selected for analysis were measured along major and minor axes, photographed, packaged into individual Pt tubes, and analyzed for ^{4}He content using an Australian Scientific Instruments Helium Instrument (Alphachron) at the University of Michigan Thermochronology Laboratory. Apatite grains were heated for 5 minutes at 900°C, whereas zircon grains were heated for 10 minutes at 1200°C. Released ^{4}He was spiked with ^{3}He, and the ^{4}He /^{3}He ratio was measured on a Pfeiffer quadrupole mass spectrometer to determine the quantity of ^{4}He. Following this initial ^{4}He measurement, these analytical procedures were repeated to check for any additional extraction of ^{4}He that might be indicative of micro-inclusions of high-temperature radiogenic minerals that were not observed optically during grain selection. The Durango apatite age standard was also analyzed with our samples to ensure accuracy of measurements of unknown age. After measurement of ^{4}He, apatite grains were dissolved and analyzed for U, Th and Sm concentrations following standard procedures (Reiners & Nicolescu, 2006) using a Thermo Scientific Elements 2 ICP-MS at the University of Arizona Radiogenic Helium Dating

Laboratory. Zircon grains were dissolved in Parr bombs and analyzed for U and Th concentrations at the University of Arizona. Individual grain dates were solved for numerically using parent and daughter nuclide concentrations and the age equation, and analytical uncertainties were propagated through the age equation using Monte Carlo methods.

Individual grains were excluded from calculation of mean ages and thermal models following the criteria of Niemi & Clark (2018). Grains with low uranium concentrations are particularly susceptible to age biases that result from uranium-implantation from surrounding U-rich phases (Spiegel et al., 2009), so we exclude grains with uranium concentrations under 5 ppm from thermal models and calculation of mean ages. Outliers were identified using the Q-test at the 90% confidence interval. Using the remaining grain ages, we calculated mean apatite and zircon helium ages for each sample (Table 4.1 and 4.2). We do not report mean ages for samples with less than three grains remaining after low-U and outlier grains are removed (four ages). Because the observed variability in our (U-Th-[Sm])/He ages for individual samples is larger than the analytical error for single grains, we report mean ages for samples with uncertainty as the standard error of the mean for the multiple grains analyzed (Tables 4.1 and 4.2). We consider samples with a standard error greater than 1.0 Ma that is also greater than 20 percent of the mean age to have low reproducibility, and report ranges of individual grain ages instead of mean ages (nine ages). We do not identify any trends in grainsize and age or radiation damage (eU) and age, which can explain some of the variability in individual grain ages from some samples (Flowers et al., 2009; Guenthner et al., 2013; Reiners & Farley, 2001). We also report ranges of individual grain ages instead of mean ages for samples with grain ages that are older than the depositional age of the sedimentary rock from which they were collected, as these ages are likely inherited and do not reflect recent cooling of the sample (14 ages) (Tables 4.1 and 4.2).

C.3: Thermochronometry results by transect

Apatite and zircon helium results from each transect are described here. Results are first presented from the northern boundary from west to east, and second from the southern boundary from west to east.

C.3.1 San Cayetano Fault System

C.3.1.1 Rattlesnake Canyon Transect

The Rattlesnake Canyon transect is located just north of Santa Barbara, CA in the Santa Ynez Mountains (Figure 4.2a). The transect includes three samples that span 2,100 meters of stratigraphic separation in the hanging wall of the Santa Ynez Fault, with stratigraphic depth increasing with proximity to the fault (Figure C.1). Samples were collected from Cretaceous through Oligocene sandstones (Dibblee & Ehrenspeck, 1986), and AHe ages are 2.0 ± 0.1 Ma, 3.0 ± 0.1 Ma, and 3.8 ± 0.3 Ma (Table 4.1). These ages exhibit an age-stratigraphic depth trend, but not an age-elevation trend. ZHe analyses from the stratigraphically lowest sample (18-SBRC-7), closest to the Santa Ynez Fault, yielded a mean age of 15.3 ± 0.6 Ma (Table 4.1).

C.3.1.2 Matilija Canyon Transect

The Matilija Canyon transect is located along the Ventura River and North Fork Matilija Creek north of Ojai, CA, in the eastern Santa Ynez Mountains. The transect includes seven samples that span 3,500 meters of stratigraphic separation in the hanging wall of the Santa Ynez Fault, with stratigraphic depth increasing with proximity to the fault (Figure C.2). All samples were collected from Cretaceous through Oligocene sandstones (Dibblee, 1985, 1987a), and AHe ages range from 1.6 ± 0.2 Ma to 2.9 ± 0.3 Ma. ZHe analyses on five of these seven samples yield mean ages that range from 17.7 ± 3.1 Ma to 35.3 ± 0.7 Ma. ZHe analyses on the stratigraphically highest sample (16-OJ-1) yielded individual grain ages that range from 52.0 to 71.4 Ma, which are older than the Late-Eocene depositional age of the Coldwater Sandstone from which the sample was collected. Both the AHe and ZHe analyses demonstrate age-stratigraphic relationships, but no age-elevation trend (Table 4.1). White (1991) reports a mean apatite fission track age of 2.0 ± 1.2 Ma from sample WG2-90, which was collected from the sample outcrop as 17-OJ-7 (AHe age of 2.0 ± 0.5 Ma). The pooled apatite fission-track age and track length distribution of this samples was incorporated into the thermal models of this transect.

C.3.1.3 Sisar Canyon Transect

The Sisar Canyon transect is located northeast of Ojai, CA at the boundary between the Santa Ynez and Topatopa Mountains. Here the predominantly east-west striking, near-vertical homocline of the Santa Ynez Mountains and the generally north-south striking, gently east-dipping homocline of the Topatopa Mountains intersect in a structurally-complex series of plunging folds. Although maximum depth of exposure (Cretaceous) is higher in the Santa Ynez Mountains than the Topatopa Mountains, the Eocene through Miocene units are largely the same in both ranges. Due to the relatively complicated structural setting, samples were collected with elevation separation instead of stratigraphic separation. Four samples that span 1,200 meters of elevation separation were collected from Eocene sandstones in the hanging wall of the San Cayetano Fault (Dibblee, 1987b, 1990). AHe ages range from 2.1 ± 0.1 Ma to 3.4 ± 0.01 Ma and exhibit an age-elevation trend (Figure C.9). ZHe analyses conducted on the second-lowest sample (18-OSC-5) yielded individual grain ages ranging from 11.8 Ma to 40.5 Ma.

C.3.1.4 Santa Paula Canyon Transect

The Santa Paula Canyon transect is located in the Topatopa Mountains along Santa Paula Creek north of the community of Santa Paula, CA (Dibblee, 1990). The transect includes two samples collected from Eocene sandstones that span <500m of stratigraphic separation. Mean AHe sample ages are 2.3 ± 0.4 Ma (16-SP-1) and 2.1 ± 0.1 Ma (16-SP-3), and the mean ZHe age from sample 16-SP-3 is 56.3 ± 8.8 Ma (Tables 4.1 and 4.2). Due to the relatively complicated structural setting between strands of the San Cayetano Fault, only the AHe and ZHe data from 16-SP-3 were included in the thermal model.

C.3.1.5 Santa Paula Peak Transect

The Santa Paula Peak transect is located in the Topatopa Mountains northeast of Santa Paula, CA and northwest of Fillmore, CA. The transect includes three samples collected from the Eocene Matilija Sandstone, which is tightly folded due to fault-proximal deformation associated with slip on the San Cayetano Fault. These samples span 750 meters of elevation separation. AHe ages from two samples yield cooling ages of 1.3 ± 0.2 Ma (18-SPP-2) and 2.7 ± 0.3 Ma (18-SPP-3) and exhibit an age-elevation relationship. ZHe analyses from one sample near the base of the transect (18-SPP-6) yielded a mean age of 50.0 ± 7.8 Ma.

C.3.1.6 Hopper Mountain Transect

Hopper Mountain transect is located in the central Topatopa Mountains northeast of Fillmore, CA. The transect includes seven samples that span >1,100 meters of elevation separation. Samples were collected from Oligocene through Miocene sandstones and record AHe cooling ages of 1.6 ± 0.2 Ma to 3.3 ± 0.3 Ma. The lowest six samples on the transect yield cooling ages that are within one-sigma uncertainty of each other, and an age-elevation relationship is only apparent after adding the highest-elevation sample (18-FC-1, AHe age of 3.3 ± 0.3 Ma). ZHe analyses performed on four grains from the lowest elevation sample (16-FM-1) yield individual grain dates ranging from 52 to 72 Ma, which are older than the depositional age of the Oligocene Sespe Formation from which the sample was collected.

C.3.1.7 Piru Transect

The Piru transect is located north of Piru, CA in the eastern Topatopa Mountains. Five samples were collected at similar elevation but varying stratigraphic depth within the Miocene Monterey Formation (locally known as Modelo Formation; Dibblee, 1991b). Within rejection criteria, only one sample (16-PC-2) yielded a mean AHe cooling age younger than the depositional age of the Modelo Formation (5.9 ± 1.0 Ma). Individual grain ages of sample 16-PC-2 range from 1.8 to 27.3 Ma, which likely indicates partial resetting within the Helium partial retention zone. ZHe analyses were conducted on two samples, and resultant grain ages range from 75 to 89 Ma (16-PC-2) and 64 to 86 Ma (16-PC-4). These ZHe cooling ages are older than the depositional age of the formation, indicating that they do not record a cooling event related to recent exhumation. We were unable to solve for unique time-temperature histories with thermal modeling due to the lack of separation of AHe samples or reset ZHe ages. However, despite the high dispersion of in individual grains ages, young AHe grain ages of < 2.0 Ma in sample 16-PC-2 likely record both recent and rapid cooling due to exhumation.

C.3.2 Santa Monica-Channel Islands Fault System

C.3.2.1 Northern Channel Islands

Six samples were collected on a stratigraphic transect of Eocene through Miocene strata in the central and southern portions of Santa Rosa Island. Samples span 1,000 meters of stratigraphic separation, and AHe analyses on all but the stratigraphically highest sample yield mean ages ranging from 6.4 ± 0.1 to 9.6 ± 1.5 Ma. The stratigraphically highest sample (18-SRI-2) yielded grain ages ranging from 12.0 to 34.3 Ma, which are within the early-Miocene depositional age of the Rincon Formation from which it was collected, indicating that this sample was likely only partially reset during burial. Therefore, it was excluded from the thermal models. Sample 18-SCI-9 was also excluded from thermal modelling as it was collected from a fault-bounded block of South Point Sandstone with no marker horizons or unit contacts with which to place the sample in stratigraphic context. ZHe analyses from the stratigraphically lowest sample (18-SCI-6) yielded grain ages ranging from 51 to 85 Ma, which are older than the Middle-Eocene depositional age of the South Point Sandstone from which it was collected.

Seven samples were collected from the Paleocene through Miocene section of sedimentary rocks on the southwest end of Santa Cruz Island, to the east of Santa Rosa Island (Figures 4.1 and 4.3, Table 4.2). AHe analyses from one sample (18-PS-3) yielded a relatively young cooling age of 7.0 ± 0.6 Ma, which is consistent with cooling ages from Santa Rosa Island (Tables 4.1 and 4.2). Three samples (18-PS-1, 18-PS-7, and 18-PS-8) yielded cooling ages that are within or older than the depositional ages of the Miocene strata from which they were collected, indicating that they likely did not experience temperatures high enough during burial to reset the detrital thermal ages. AHe analyses from the Eocene and Paleocene strata yield cooling ages ranging from 18.2 ± 2.3 Ma to 29.5 ± 2.7 Ma. These samples do not exhibit age-stratigraphic depth or age-elevation relationships, and we therefore do not produce thermal models with these data.

C.3.2.2 Zuma Ridge and Las Flores Canyon Transects

AHe and ZHe data from the Las Flores Canyon and Zuma Ridge transects were produced by Niemi & Clark (2018). These transects span 1,600 meters (Las Flores Canyon) and 900 meters (Zuma Ridge) of stratigraphic separation and are located in the central Santa Monica Mountains near Malibu, CA. AHe ages of eight samples from Las Flores Canyon range from 2.3 to 11.5 Ma, and AHe ages of thirteen samples from Zuma Ridge range from 4.5 to 12.6 Ma. AHe ages exhibit both age-stratigraphic depth and age-elevation trends. ZHe ages from three samples on these transects range from 36 to 61 Ma.

C.3.2.3 Hollywood Transect

The Hollywood transect is located in the Hollywood Hills north of downtown Los Angeles, CA and spans 2,400 meters of stratigraphic separation. AHe analyses were conducted on two samples collected from a Cretaceous quartz diorite at the base of the transect, one sample collected from a Cretaceous sandstone that nonconformably overlies the quartz diorite, and four samples collected from Miocene sandstones and conglomerates that disconformably overlie the Cretaceous sandstone (Dibblee, 1991a). AHe ages from the basal quartz diorite and overlying Cretaceous strata range from 2.6 ± 0.4 Ma to 8.6 ± 1.3 Ma, and AHe ages from the Miocene section range from 7.1 ± 0.8 Ma to 20.4 ± 0.7 Ma. ZHe analyses conducted on the lowest sample yield a mean age of 22.1 ± 1.5 Ma. AHe data demonstrate an age-stratigraphic depth relationship, but mean AHe ages of samples collected from the Miocene strata are within the depositional age of these units. We included samples from Miocene rocks in the thermal model to produce predicted thermal histories, but these samples were not used in the inversion for most-likely thermal histories (Figure 4.4).

C.4 Post-Deposition Thermal Histories

Prior to late-Miocene time, thermal histories are mostly informed by the depositional history of the stratigraphic units from which samples were collected (Figures C.4-C.14). On the San Cayetano fault system, the Rattlesnake Canyon and Matilija Canyon transects record slow burial in Cretaceous through late-Eocene time (Figures C.4 and C.6). Thermal histories from the Sisar Canyon (Figure C.9), Santa Paula Canyon (Figure C.10), and Santa Paula Peak (Figure C.11) transects record rapid burial beginning in late-Eocene through late-Miocene time, which is consistent with deposition of the Juncal Formation, Matilija Sandstone, Cozy Dell Shale, and Coldwater Sandstone in middle- to late-Eocene time, the Sespe Formation in Oligocene time, and the Monterey Formation in Miocene-time. Oligocene to middle- to late-Miocene strata were sampled at Hopper Mountain, and the thermal history (Figure C.12) records relatively slow burial in Oligocene through middle-Miocene time, followed by rapid burial in late-Miocene through Pliocene time. This rapid burial is consistent with deposition of the Modelo Formation (time-equivalent of the Monterey Formation) in a localized transtensional basin (Gordon, 2014).

Sedimentation along the Santa Monica-Channel Islands fault system was interrupted by the development of regional unconformities. After initial cooling of the Cretaceous pluton at the base of the sampling transect in Hollywood (Figure C.13), the thermal history records cooling from Eocene through Early-Miocene time, which is likely a consequence of erosion of overlying strata and is reflected in the geologic record as a disconformable contact between the Cretaceous strata (Unnamed) and the overlying Miocene units (Middle and Upper Topanga Formations).

This phase of cooling was followed by rapid re-heating through late-Miocene time, which is consistent with deposition of the overlying middle- to late-Miocene strata. The Zuma ridge transect similarly records a cooling event from Eocene through Oligocene time, followed initially by slow reheating due to burial of Oligocene units, and more rapid reheating due to burial of Miocene strata (Niemi & Clark, 2018). However, the Las Flores Canyon transect record relatively constant heating due to burial from early-Eocene through latest-Miocene time (Niemi & Clark, 2018). The Santa Rosa Island transect records slow heating due to burial in Oligocene through early-Miocene time, followed by more rapid heating due to burial until late-Miocene time (Figure C.14).

C.5 References

Dibblee, T. W. (1985). *Geologic Map of the Wheeler Springs Quadrangle, Ventura County, California*. Santa Barbara, California: Dibblee Geological Foundation.

Dibblee, T. W. (1987a). *Geologic Map of the Matilija Quadrangle, Ventura County, California*. Santa Barbara, California: Dibblee Geological Foundation.

Dibblee, T. W. (1987b). *Geologic Map of the Ojai Quadrangle, Ventura County, California*. Santa Barbara, California: Dibblee Geological Foundation.

Dibblee, T. W. (1990). Geologic Map of the Santa Paula Peak Quadrangle. *Santa Barbara Museum of Natural History*.

Dibblee, T. W. (1991a). *Geologic Map of the Hollywood and South 1/2 Burbank Quadrangles*. Santa Barbara, California: Dibblee Geological Foundation.

Dibblee, T. W. (1991b). *Geologic Map of the Piru Quadrangle, Ventura County, California*. Santa Barbara, California: Dibblee Geological Foundation.

Dibblee, T. W., & Ehrenspeck, H. E. (1986). *Geologic map of the Santa Barbara quadrangle, Santa Barbara County, California*. Santa Barbara, California: Dibblee Geological Foundation.

Flowers, R. M., Ketcham, R. A., Shuster, D. L., & Farley, K. A. (2009). Apatite (U-Th)/He thermochronometry using a radiation damage accumulation and annealing model. *Geochimica et Cosmochimica Acta*, *73*(8), 2347–2365. https://doi.org/10.1016/j.gca.2009.01.015

Gordon, G. (2014). *Stratigraphic evolution and architectural analysis of structurally confined submarine fans: A tripartite outcrop-based study*. Colorado School of Mines.

Guenthner, W. R., Reiners, P. W., Ketcham, R. A., Nasdala, L., & Giester, G. (2013). Helium diffusion in natural zircon: radiation damage, anisotropy, and the interpretation of zircon (U-TH)/He thermochronology. *American Journal of Science*, *313*(3), 145–198. https://doi.org/10.2475/03.2013.01

Niemi, N. A., & Clark, M. K. (2018). Long-term exhumation rates exceed paleoseismic slip rates in the central Santa Monica Mountains, Los Angeles County, California. *Geology*, *46*(1), 63–66. https://doi.org/10.1130/G39388.1

Reiners, P. W., & Farley, K. A. (2001). Influence of crystal size on apatite (U-Th)/He thermochronology: An example from the Bighorn Mountains, Wyoming. *Earth and*

Planetary Science Letters, *188*(3–4), 413–420. https://doi.org/10.1016/S0012-821X(01)00341-7

Reiners, P. W., & Nicolescu, S. (2006). Measurement of parent nuclides for (U-Th)/He chronometry by solution sector ICP-Ms. *ARDHL Report 1*, (December 2006), 1–33. Retrieved from http://www.geo.arizona.edu/~reiners/arhdl/arhdl.html

Spiegel, C., Kohn, B., Belton, D., Berner, Z., & Gleadow, A. (2009). Apatite (U-Th-Sm)/He thermochronology of rapidly cooled samples: The effect of He implantation. *Earth and Planetary Science Letters*, *285*(1–2), 105–114. https://doi.org/10.1016/j.epsl.2009.05.045

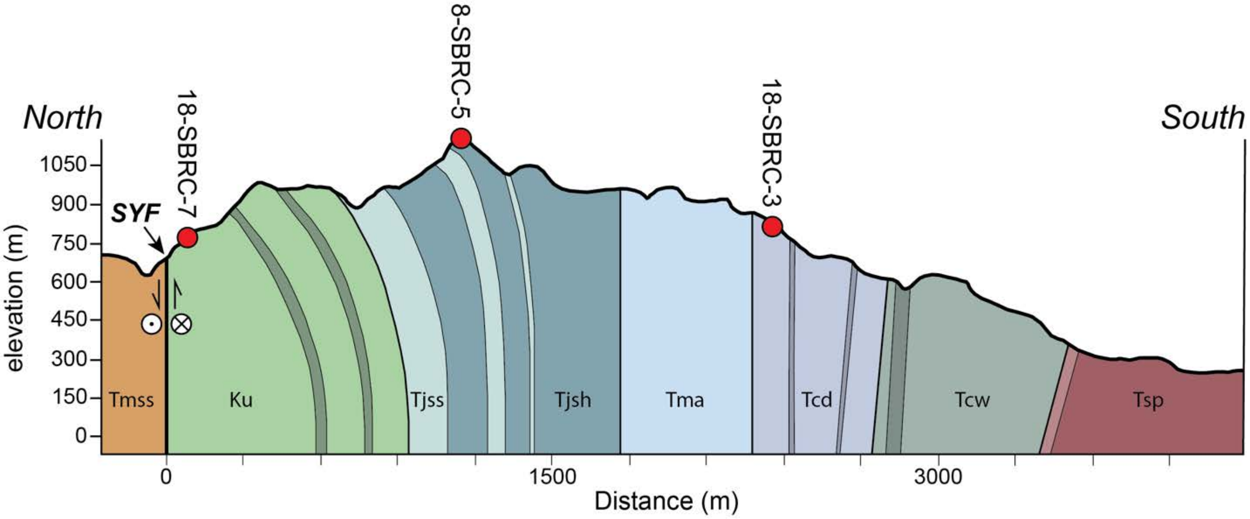

Appendix Figure C.1: Cross section through the Santa Ynez anticlinorium at the Rattlesnake Canyon transect. Red dots show sample locations. Cross section interpreted from Dibblee & Ehrenspeck (1986).

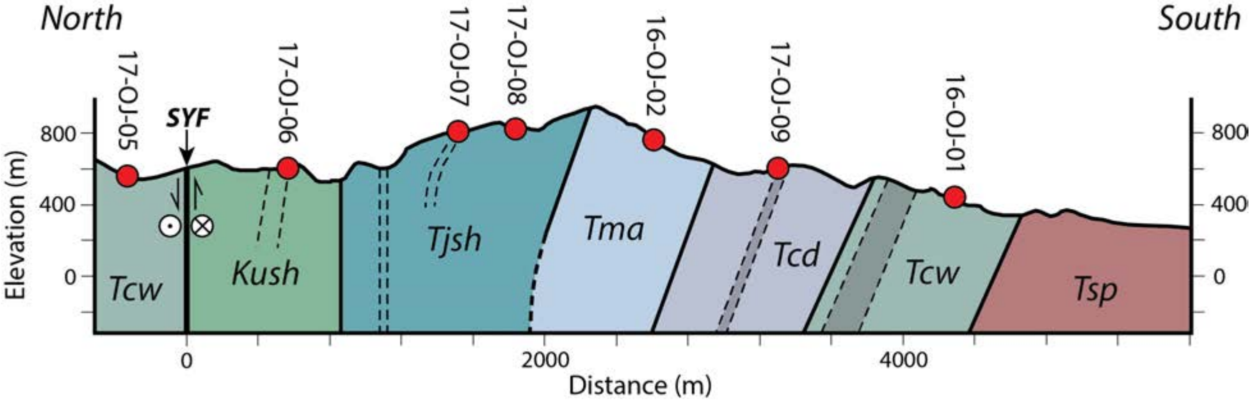

Appendix Figure C.2: Cross section through the Santa Ynez anticlinorium at the Matilija Canyon transect. Red dots show sample locations. Cross section interpreted from Dibblee (1987a).

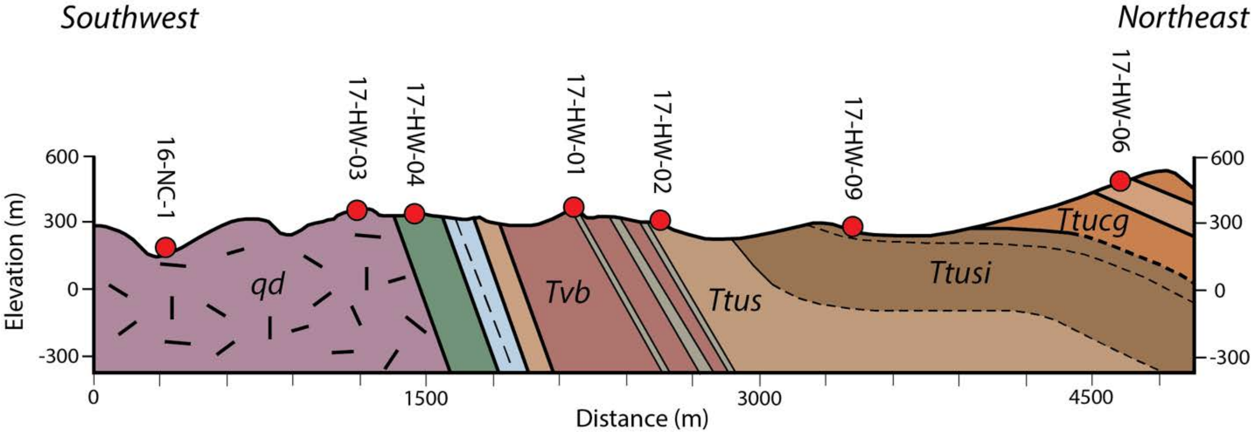

Appendix Figure C.3: Cross section through the Hollywood Hills at the Hollywood transect. Red dots show sample locations. Cross section interpreted from Dibblee (1991b).

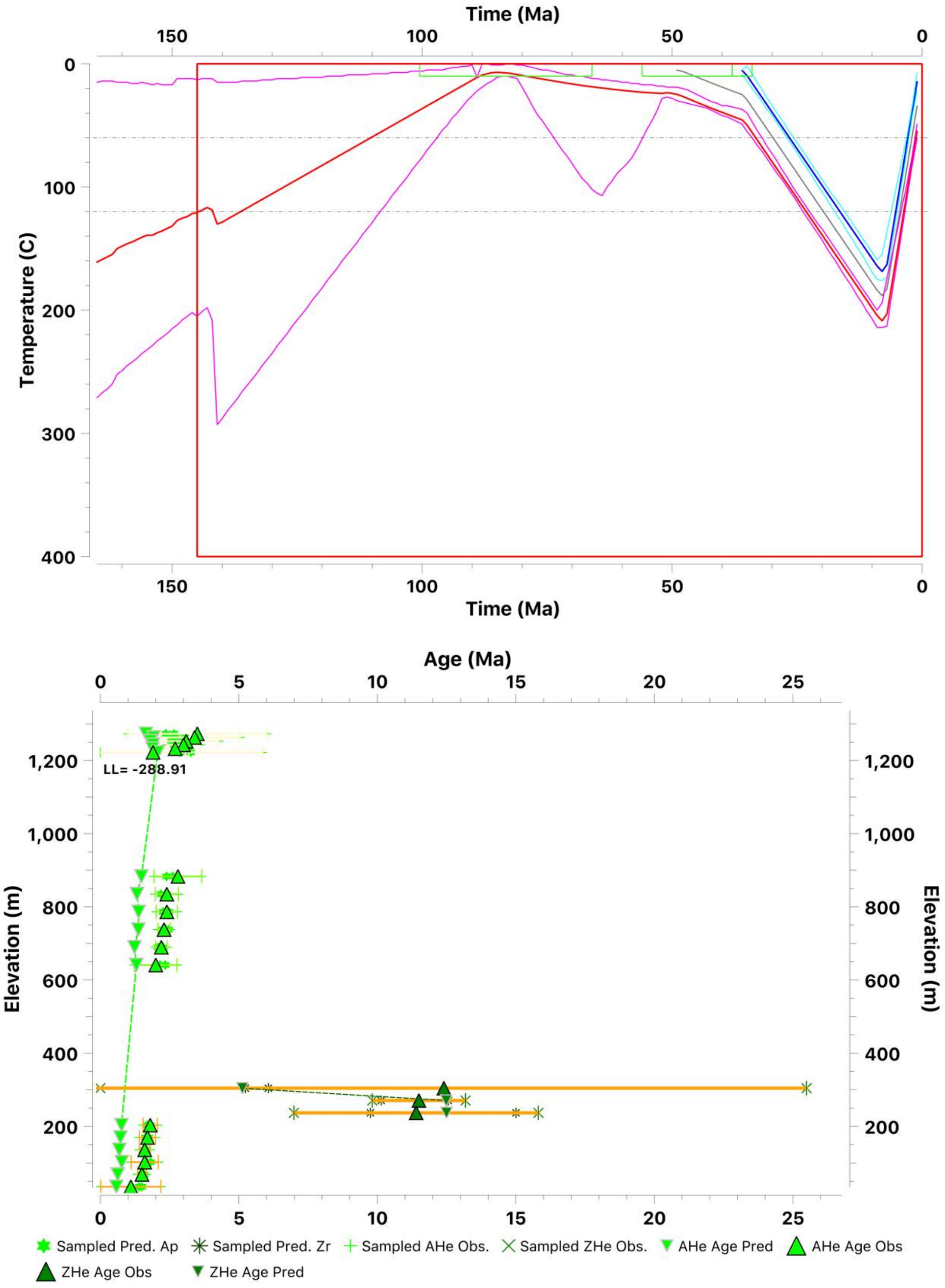

Appendix Figure C.4: Preferred thermal modelling results for the Rattlesnake Canyon transect data, with vertical sample separation defined by rotating the stratigraphic section back 55 degrees. Top: expected time-temperature history. The red box defines the range of time and temperatures explored in the MCMC. Bottom: Age-elevation plot of observed and predicted thermochronometry sample ages.

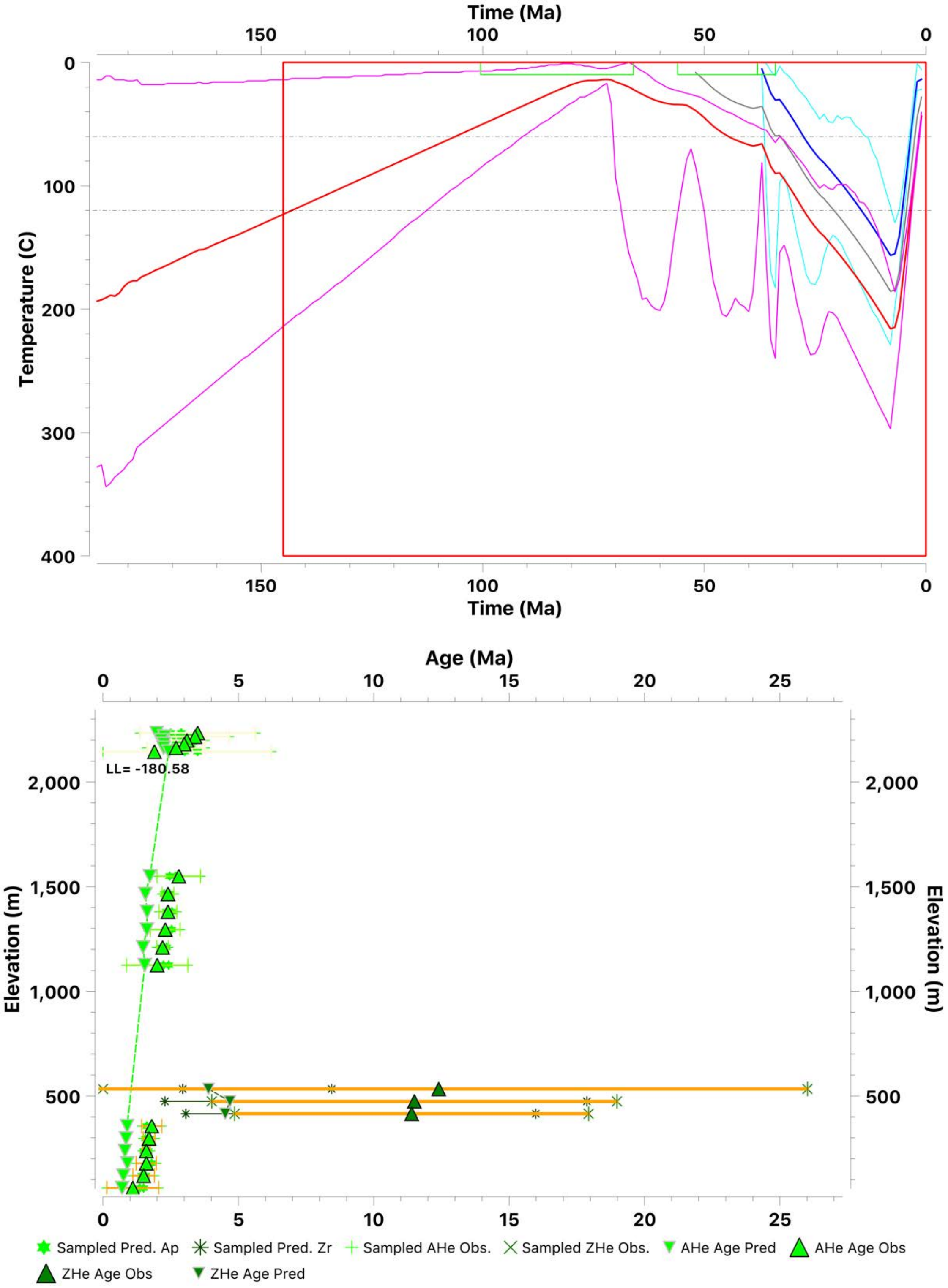

Appendix Figure C.5: Rattlesnake Canyon transect thermal modelling results with vertical sample separation defined by stratigraphic separation. Top: expected time-temperature history. The red box defines the range of time and temperatures explored in the MCMC. Bottom: Age-elevation plot of observed and predicted thermochronometry sample ages. Modelled ages of zircon thermochronometry samples underpredict observed ages.

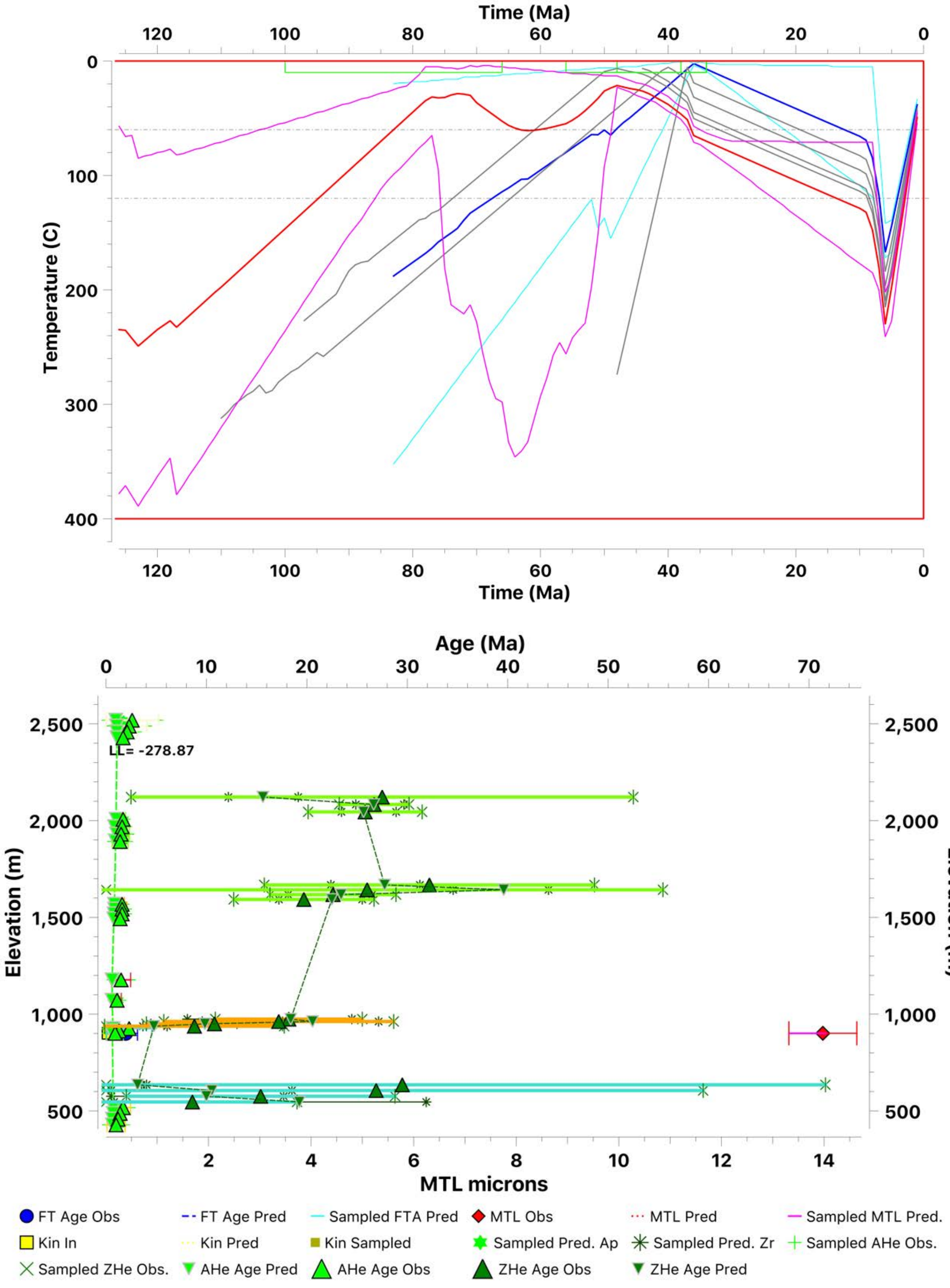

Appendix Figure C.6: Preferred thermal modelling results for the Matilija Canyon transect data, with vertical sample separation defined by rotating the stratigraphic section back 55 degrees. Top: expected time-temperature history. The red box defines the range of time and temperatures explored in the MCMC. Bottom: Age-elevation plot of observed and predicted thermochronometry sample ages.

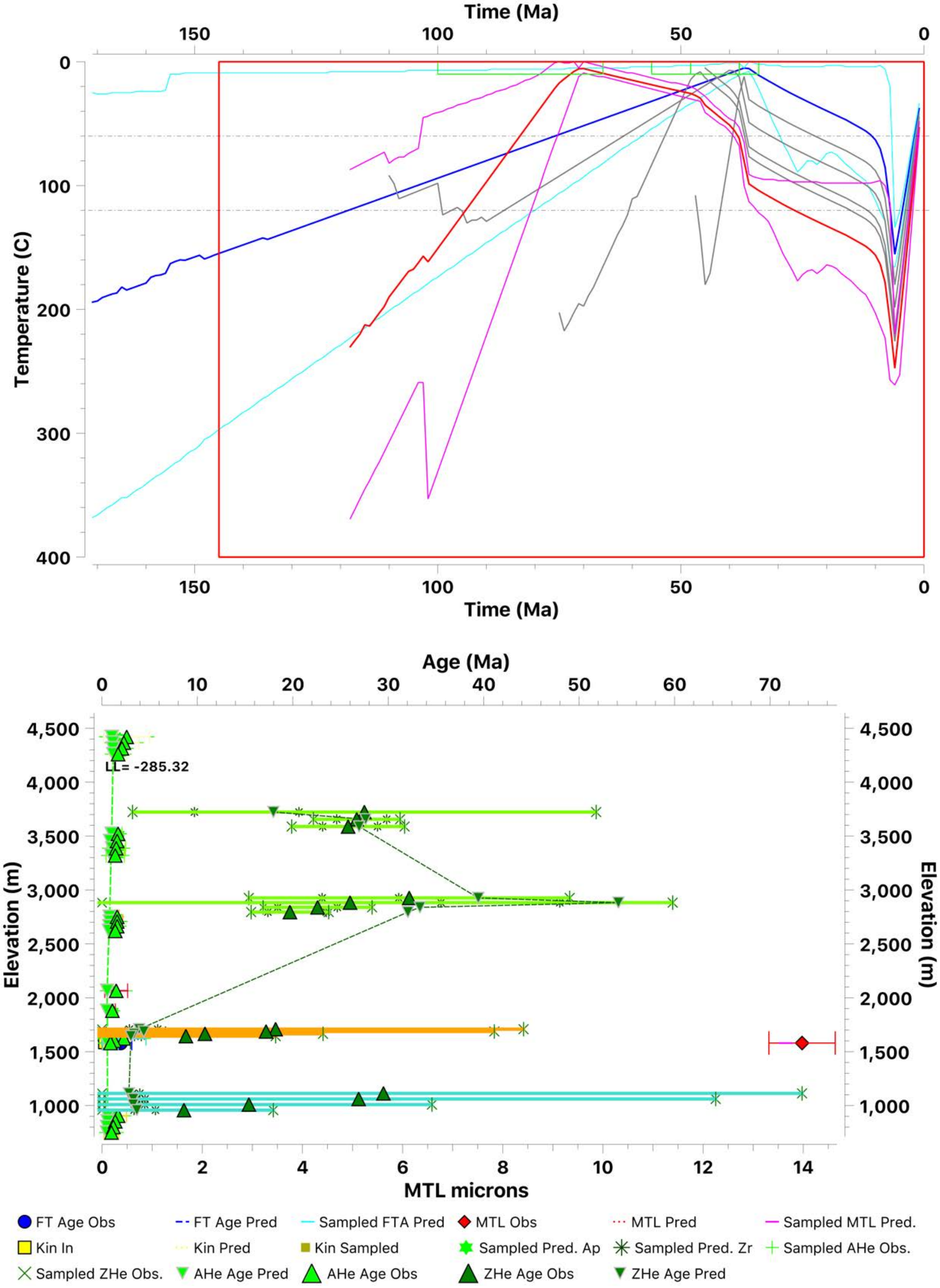

Appendix Figure C.7: Thermal modelling results for the Matilija Canyon transect data, with vertical spacing defined by stratigraphic separation. Top: expected time-temperature history. The red box defines the range of time and temperatures explored in the MCMC. Bottom: Age-elevation plot of observed and predicted thermochronometry sample ages. Modelled ages of lower two zircon thermochronometry samples underpredict observed ages.

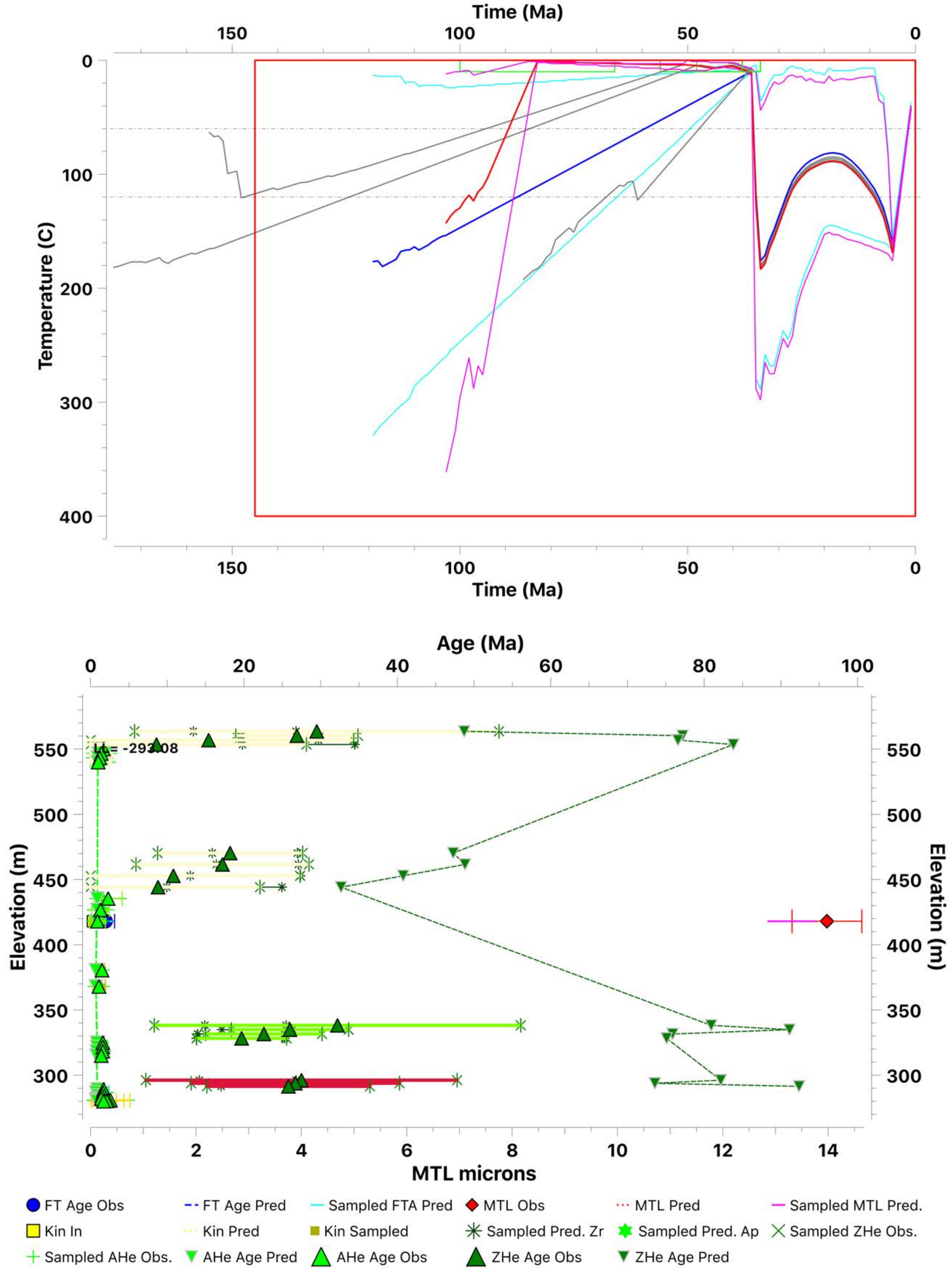

Appendix Figure C.8: Thermal modelling results for the Matilija Canyon transect data, with vertical spacing defined by elevation. Top: expected time-temperature history. The red box defines the range of time and temperatures explored in the MCMC. Bottom: Age-elevation plot of observed and predicted thermochronometry sample ages. Modelled zircon thermochronometry ages overpredict observed ages.

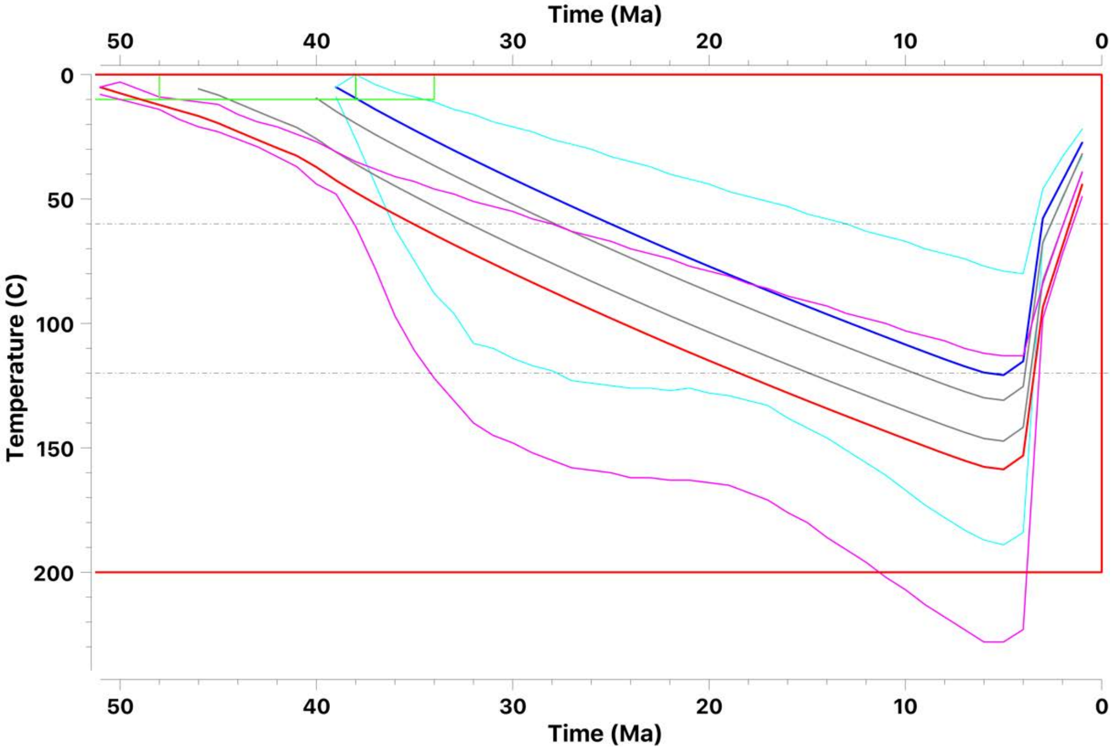

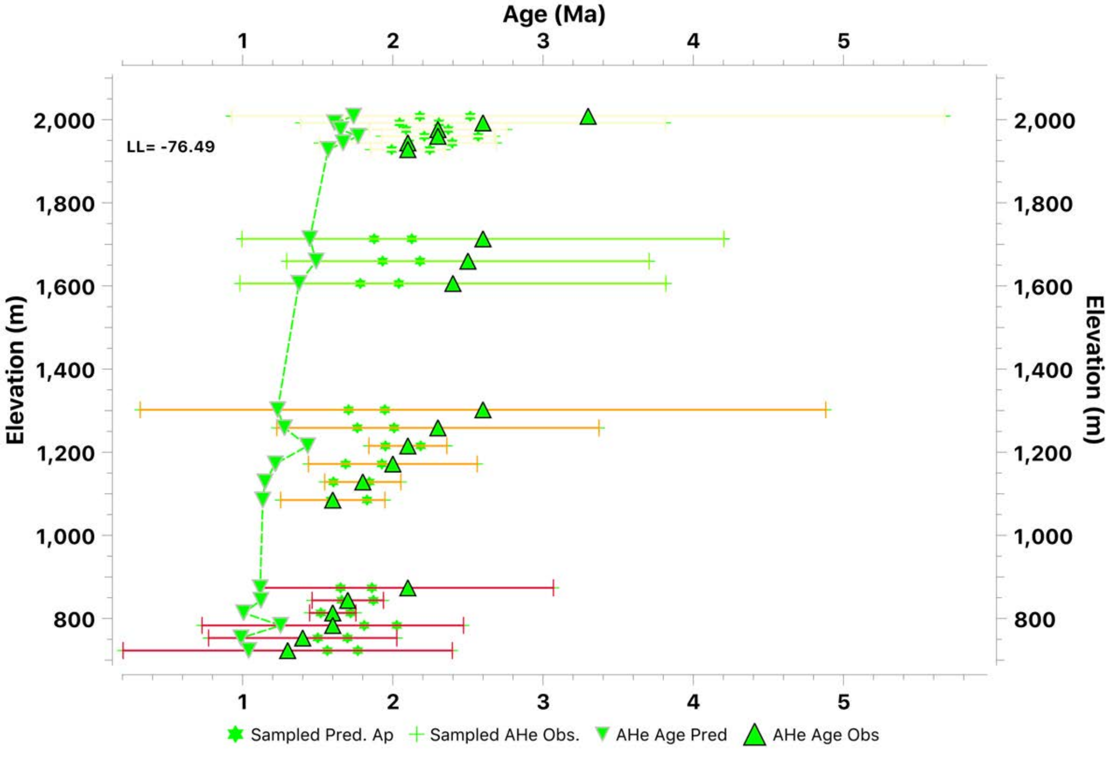

Appendix Figure C.9: Sisar Canyon transect thermal modelling results. Top: expected time-temperature history. The red box defines the range of time and temperatures explored in the MCMC. Bottom: Age-elevation plot of observed and predicted thermochronometry sample ages.

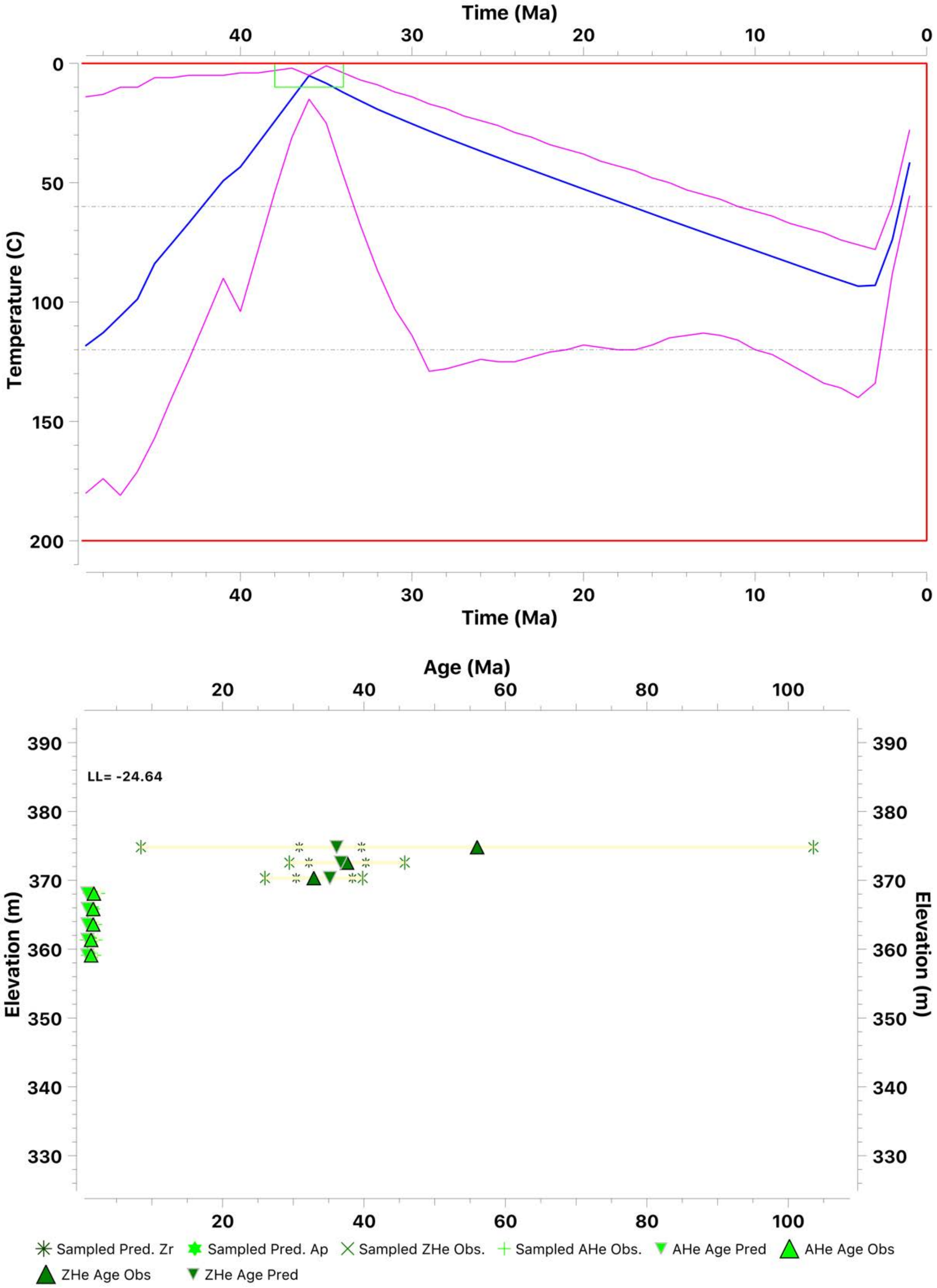

Appendix Figure C.10: Santa Paula Canyon transect thermal modelling results. Top: expected time-temperature history. The red box defines the range of time and temperatures explored in the MCMC. Bottom: Age-elevation plot of observed and predicted thermochronometry sample ages.

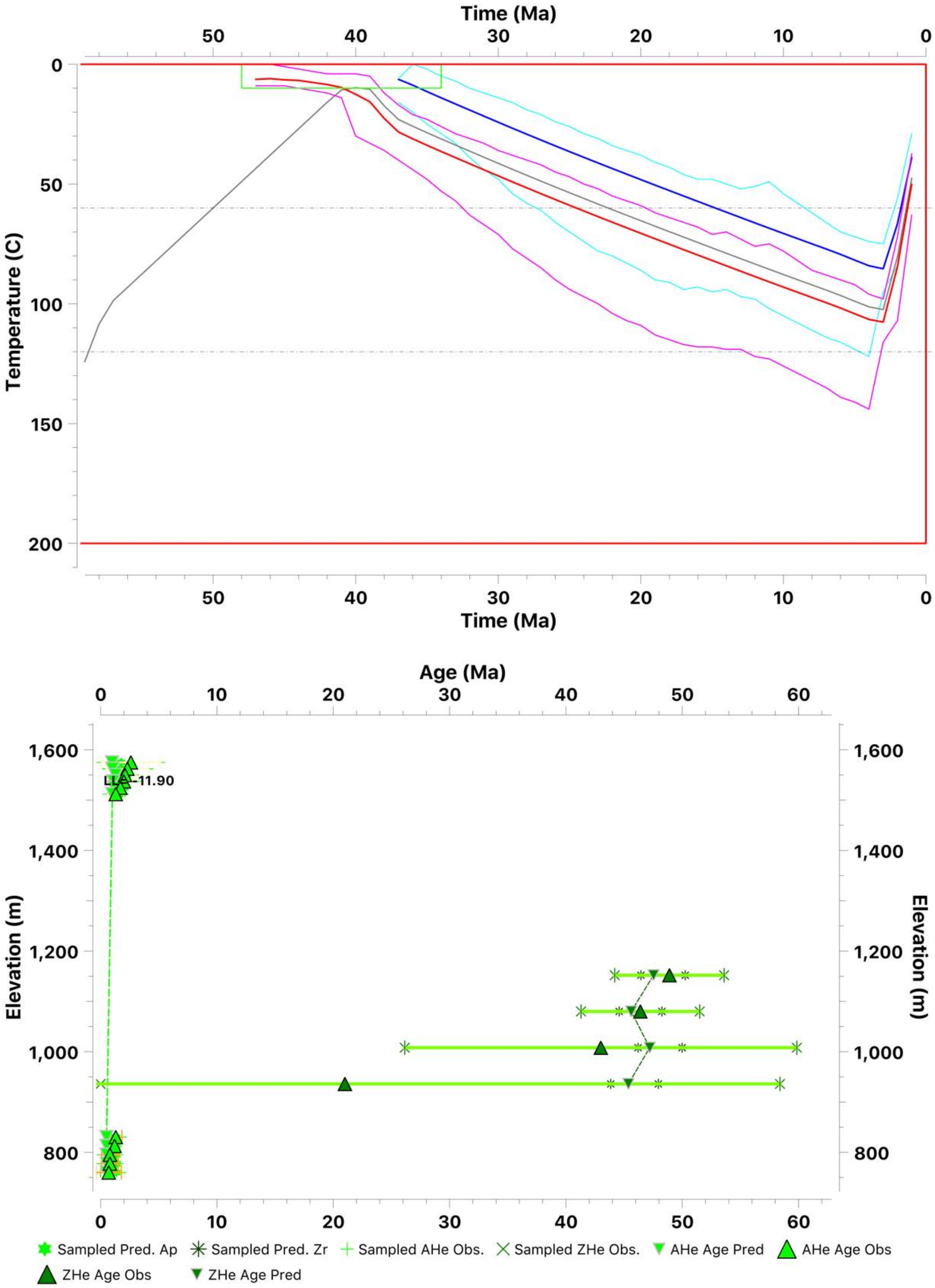

Appendix Figure C.11: Santa Paula Peak transect thermal modelling results. Top: expected time-temperature history. The red box defines the range of time and temperatures explored in the MCMC. Bottom: Age-elevation plot of observed and predicted thermochronometry sample ages.

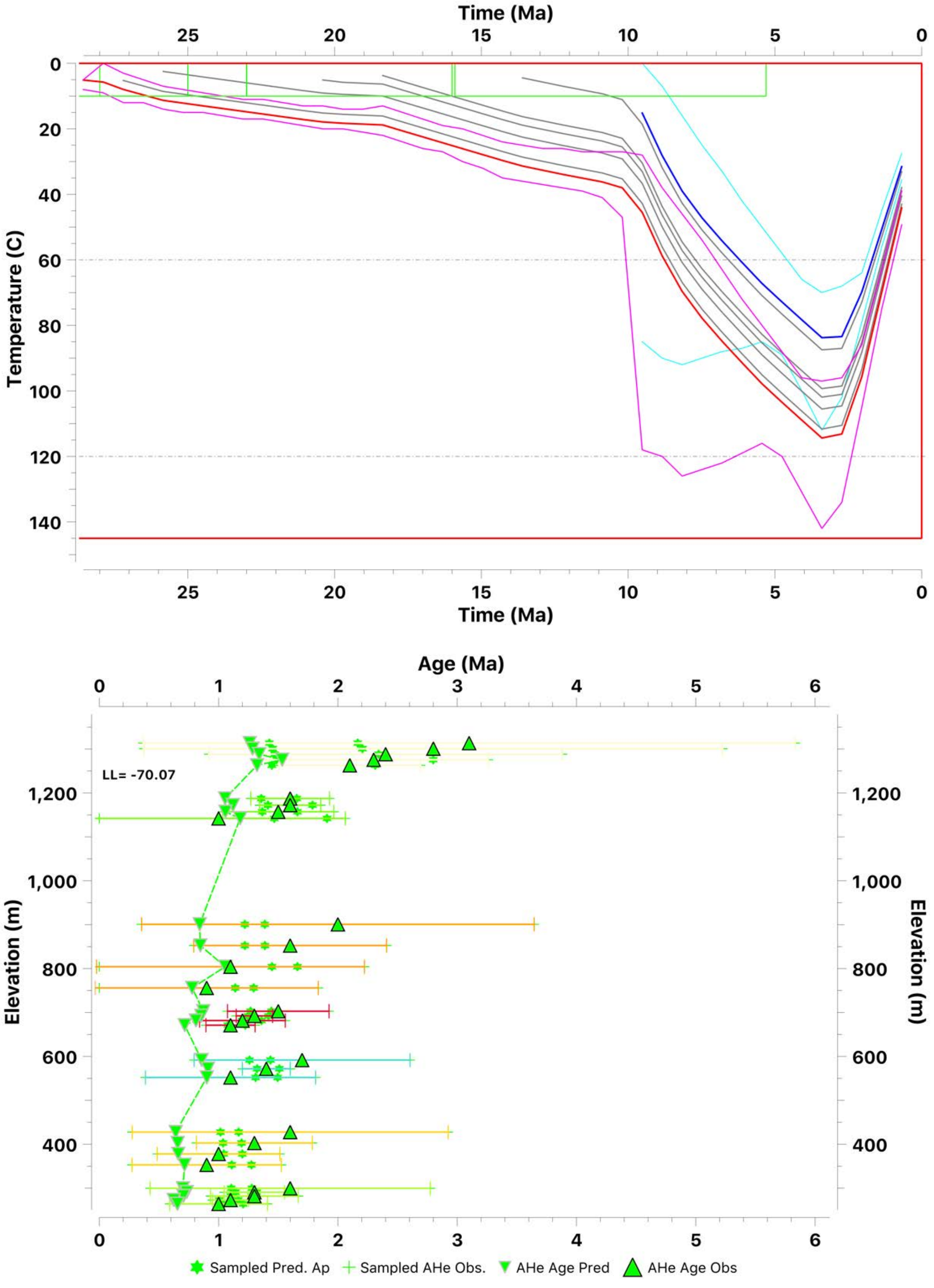

Appendix Figure C.12: Hopper Mountain transect thermal modelling results. Top: expected time-temperature history. The red box defines the range of time and temperatures explored in the MCMC. Bottom: Age-elevation plot of observed and predicted thermochronometry sample ages.

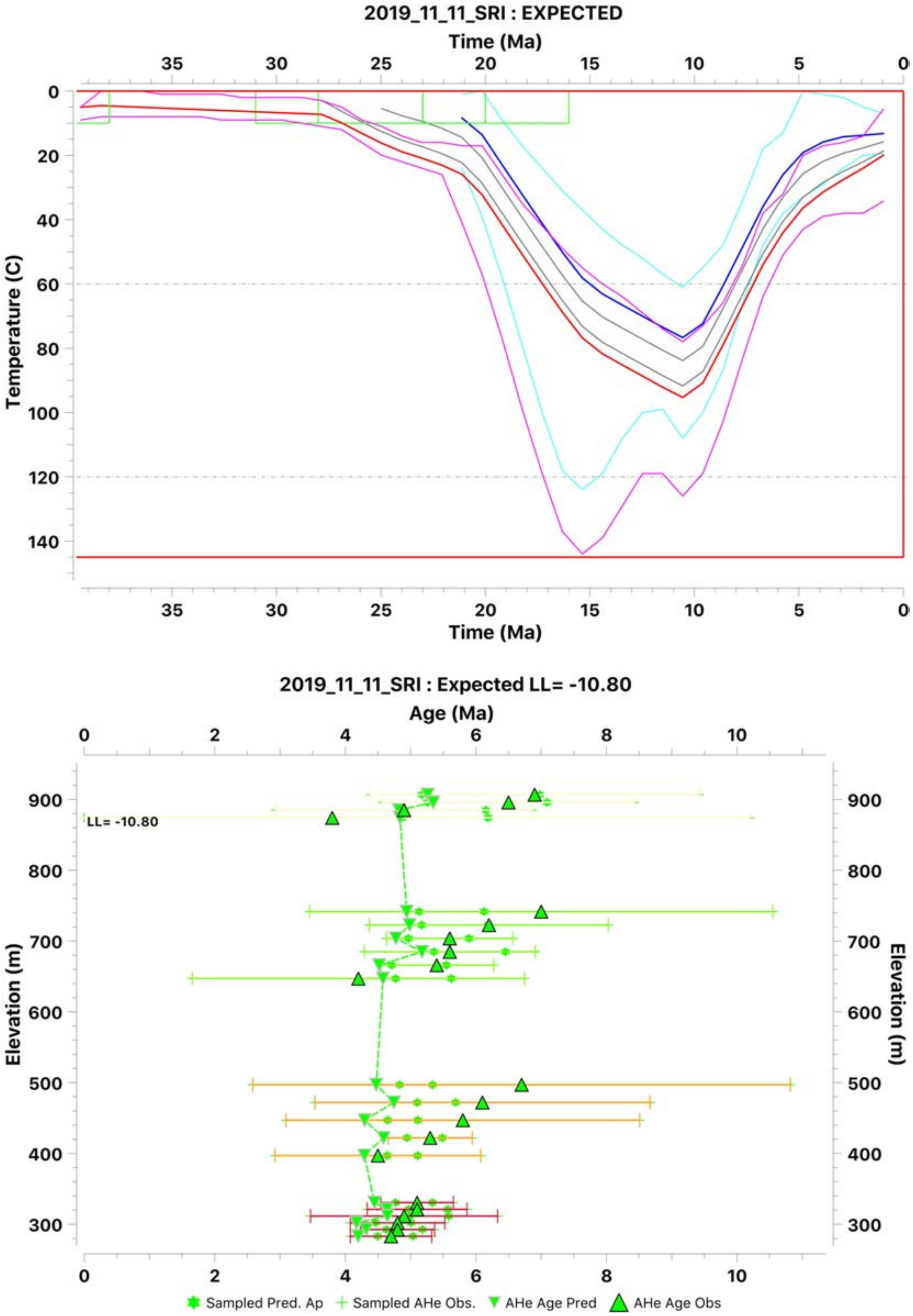

Appendix Figure C.13: Santa Rosa Island transect thermal modelling results. Top: expected time-temperature history. The red box defines the range of time and temperatures explored in the MCMC. Bottom: Age-elevation plot of observed and predicted thermochronometry sample ages.

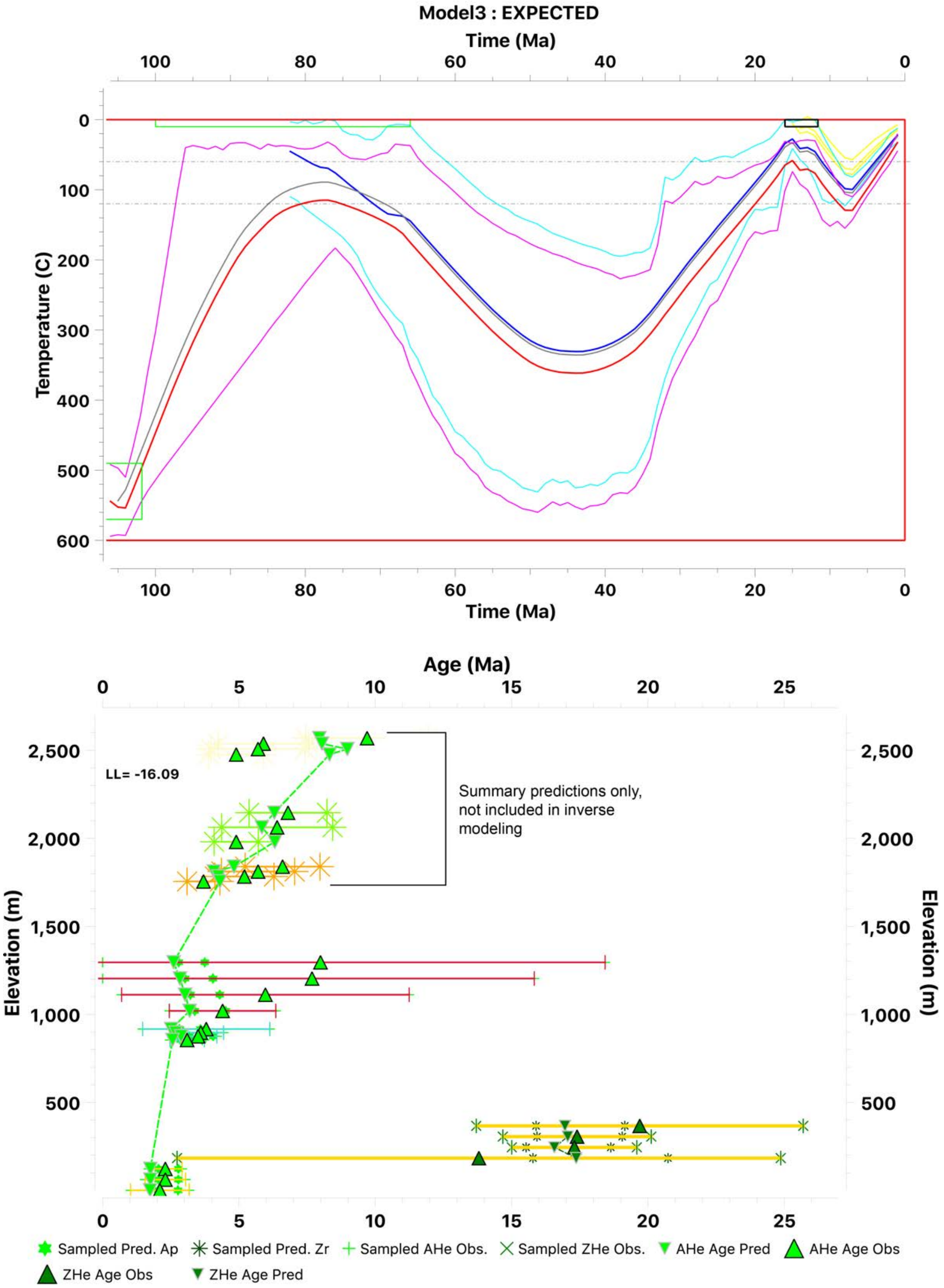

Appendix Figure C.14: Hollywood transect thermal modelling results. Top: expected time-temperature history. The red box defines the range of time and temperatures explored in the MCMC. The model was constrained to surface temperature in Middle-Miocene time due to the nonconformable contact between Cretaceous and overlying Miocene strata. Yellow lines show predicted thermal histories of three samples from the Middle-Miocene strata, which were not used in the inversion. Bottom: Age-elevation plot of observed and predicted thermochronometry sample ages. Predicted ages of Middle-Miocene strata are shown against observed ages.

Appendix D: Supporting Information for Chapter 5. The Scale-Dependent and Non-Linear Relationship Between Rock Strength and Topographic Metrics

D.1 Introduction

This appendix contains supplemental methods, Table D.2, and supplemental figures to Chapter 5.

D.2 Normalized Channel Steepness Methods

The normalized channel steepness (Ksn) of channel segments (Kirby and Whipple, 2012) was produced using the Topotoolbox set of topographic functions within MATLAB (Schwanghart & Scherler, 2014). Standard flow routing procedures were performed on a National Oceanographic and Atmospheric Administration (NOAA) Interferometric Synthetic Aperture Radio (IfSAR) 3-meter pixel resolution digital surface model (Office of Coastal Management, 2016). Filled DEM, flow-direction, and flow-accumulation rasters were produced, a minimum gradient of 0.001 was imposed, and a contributing area of 1,000 pixels (0.1 km^2) was set to define the channel network. Slope-area statistics were calculated for the entire region to determine the reference channel concavity of 0.37. Ksn was calculated for each segment by dividing channel gradient by the contributing area raised to the reference concavity, and the resulting values aggregated to channel lengths of 1000 meters. Stream segments were converted into raster datasets with pixel resolution equal to the resolution of the input DSM. Mean and $\pm 1\sigma$ were produced with zonal statistics using each stratigraphic age polygon as the input zone.

D.3 References

Kirby, E., & Whipple, K. X., 2012, Expression of active tectonics in erosional landscapes: *Journal of Structural Geology*, *44*, 54-75.

Office for Coastal Management, 2016: 2002/2003 IfSAR data for Southern California: Digital Elevation Model (NAVD88). *NOAA National Centers for Environmental Information*, https://inport.nmfs.noaa.gov/inport/item/48381.

Schwanghart, W., Scherler, D. (2014): TopoToolbox 2 – MATLAB-based software for topographic analysis and modeling in Earth surface sciences. Earth Surface Dynamics, 2, 1-7. [DOI: 10.5194/esurf-2-1-2014]

Appendix Table D.1: Mean strength and topographic metrics (±1σ) by stratigraphic age

Stratigraphic Age	Ksn [1]	Hillslope Relief [2] (m)	Local Relief [3] (m)	Slope [4] (°)	Schmidt [5] (R)	GSI [5] (of 100)	Vs_{30} [5] (m/s)	Intact Shear Strength [5] (MPa)	Outcrop Shear Strength [5] (MPa)
Plio-Pleistocene	3.7 ± 2.5	31.3 ± 22.7	185.5 ± 39.9	16.8 ± 10.4	0 ± 0	22.5 ± 0	- [6]	5.0 ± 0.0	0.15 ± 0.00
Pliocene	5.5 ± 3.0	59.5 ± 37.5	282.1 ± 59.5	24.8 ± 12.0	4.1 ± 4	28.9 ± 5.2	361 ± 19	6.3 ± 1.2	0.21 ± 0.04
Miocene	12.1 ± 6.4	75.9 ± 49.7	429.7 ± 107.6	26.7 ± 11.5	30.0 ± 10.1	52.2 ± 15.5	628 ± 165	22.0 ± 9.9	0.71 ± 0.27
Oligocene	14.2 ± 10.5	61.9 ± 55.0	441.6 ± 152.1	21.9 ± 11.3	30.9 ± 4.9	65.9 ± 12.2	875 ± 164	21.2 ± 4.6	1.22 ± 0.61
Eocene	18.4 ± 9.0	102.2 ± 70.0	590.0 ± 140.0	28.4 ± 10.7	39.0 ± 9.6	62.9 ± 10.1	840 ± 297	33.0 ± 12.9	1.28 ± 0.71
Cretaceous	16.3 ± 6.4	99.8 ± 56.6	552.4 ± 97.6	30.7 ± 9.0	47.7 ± 11.4	83.3 ± 8.2	679 [7]	51.0 ± 28.4	5.49 ± 3.66

[1] For reference concavity = 0.37

[2] Difference between highest and lowest elevations on hillslope flow paths, following Townsend et al. (2020) and Medwedeff et al. (2020).

[3] Calculated on a per-pixel basis within a circular moving window with radius of 1 km.

[4] Calculated on a per-pixel basis

[5] Data from Townsend et al. (2021)

[6] No data collected

[7] One survey, no standard deviation

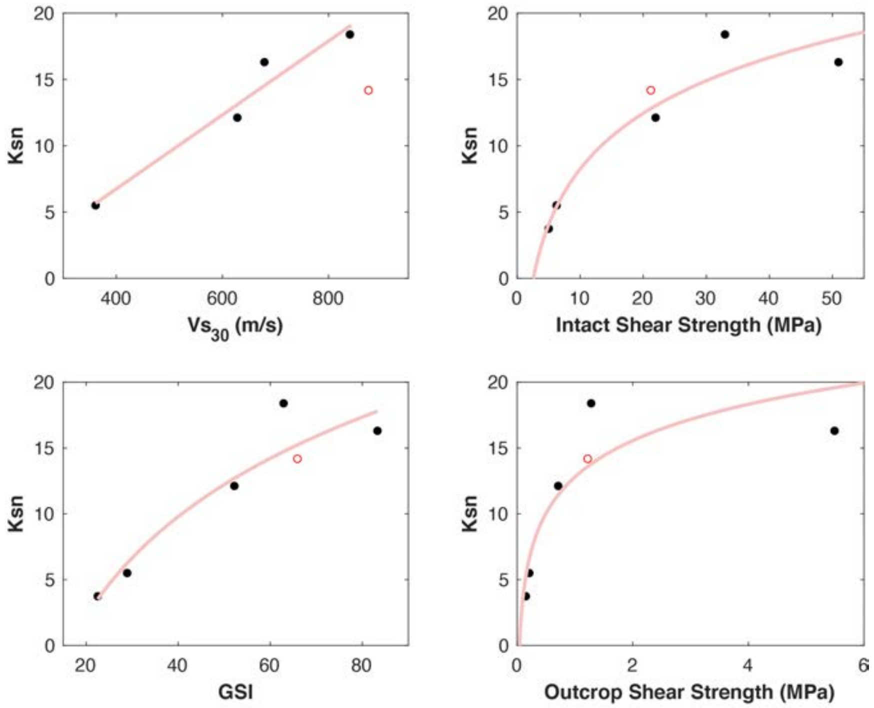

Appendix Figure D.1: Ksn plotted against Vs_{30}, Unconfined Compressive Strength (UCS), Geological Strength Index (GSI), and Shear Strength. Lines are best-fit regressions.

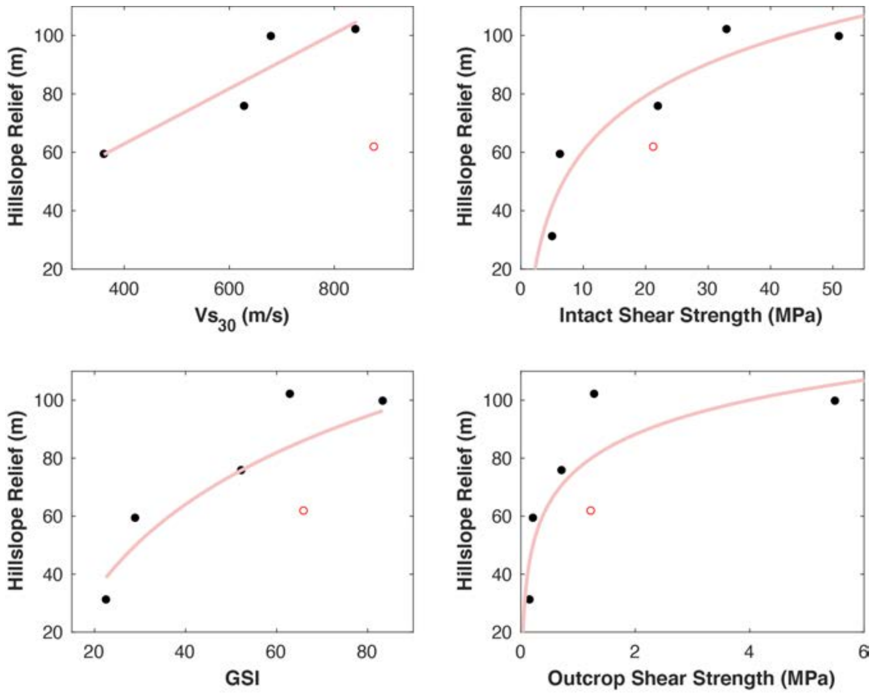

Appendix Figure D.2: Hillslope relief plotted against Vs30, Unconfined Compressive Strength (UCS), Geological Strength Index (GSI), and Shear Strength. Lines are best-fit regressions.

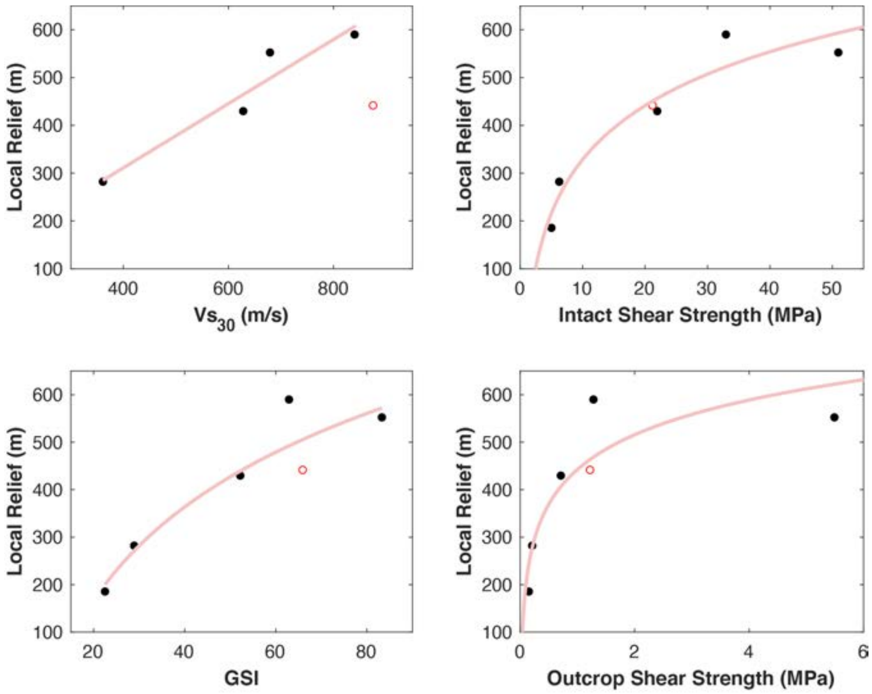

Appendix Figure D.3: Local relief within a circular moving window with 1-km radius, plotted against Vs$_{30}$, Unconfined Compressive Strength (UCS), Geological Strength Index (GSI), and Shear Strength. Lines are best-fit regressions.

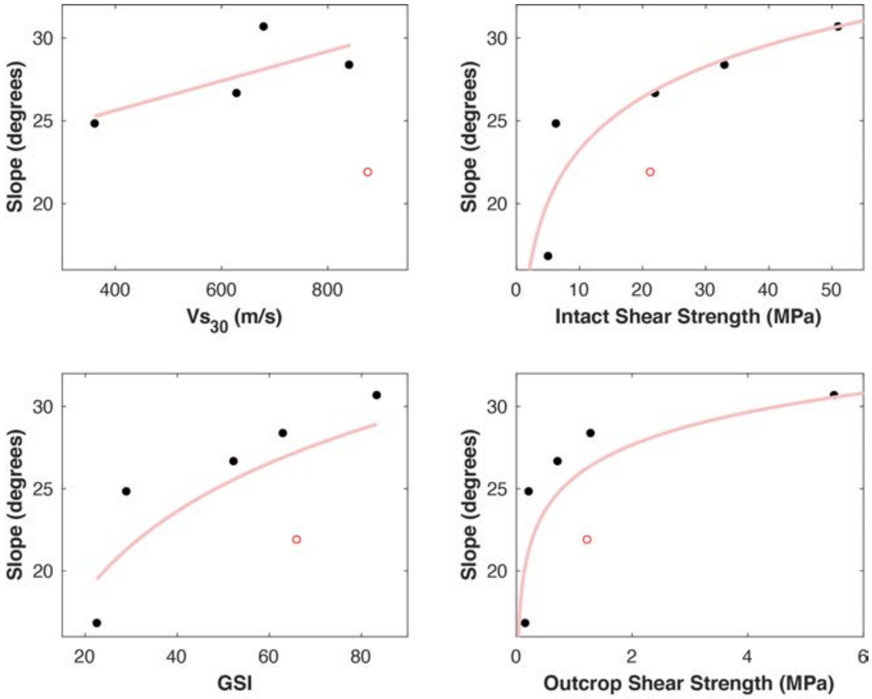

Appendix Figure D.4: Pixel slope plotted against Vs30, Unconfined Compressive Strength (UCS), Geological Strength Index (GSI), and Shear Strength. Lines are best-fit regressions.

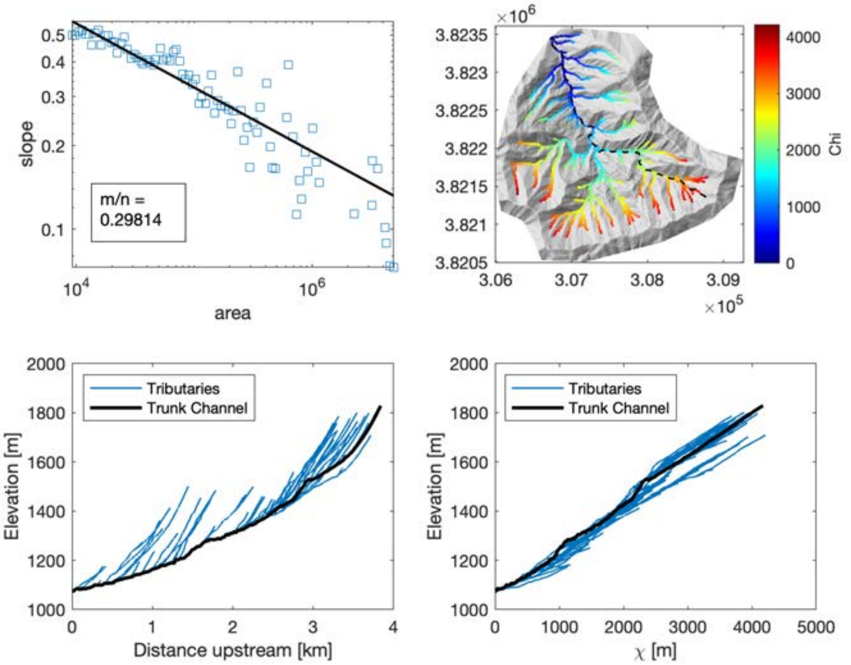

Appendix Figure D.5: Slope-area relationship, chi map (map units in meters, UTM Zone 11N), longitudinal profiles of trunk and tributary channels, and chi-transformed longitudinal profiles of trunk and tributary channels of a small watershed overlying Cretaceous sedimentary rocks in the Topatopa Mountains.

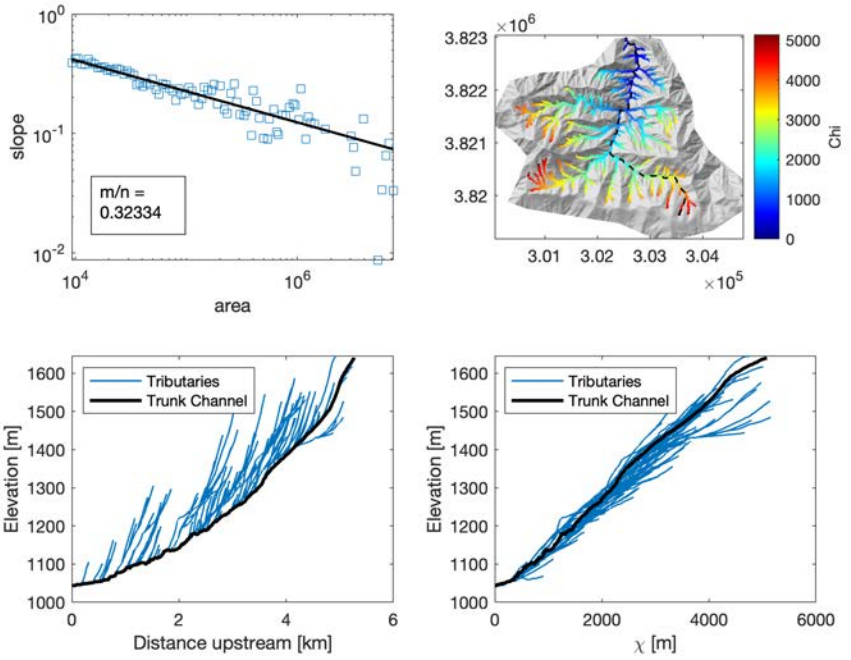

Appendix Figure D.6: Slope-area relationship, chi map (map units in meters, UTM Zone 11N), longitudinal profiles of trunk and tributary channels, and chi-transformed longitudinal profiles of trunk and tributary channels of a small watershed overlying Cretaceous sedimentary rocks in the Topatopa Mountains.

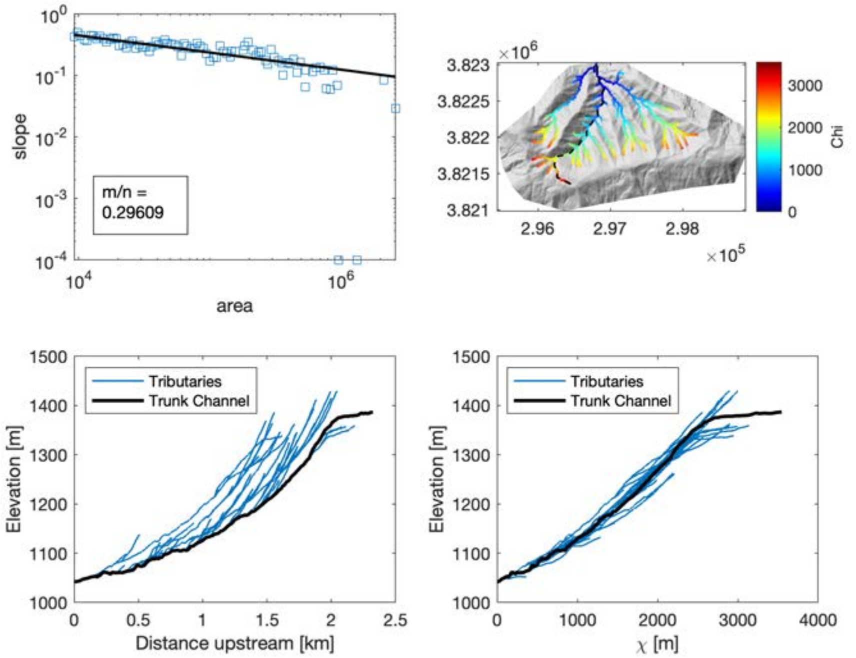

Appendix Figure D.7: Slope-area relationship, chi map (map units in meters, UTM Zone 11N), longitudinal profiles of trunk and tributary channels, and chi-transformed longitudinal profiles of trunk and tributary channels of a small watershed overlying Cretaceous sedimentary rocks in the Topatopa Mountains.

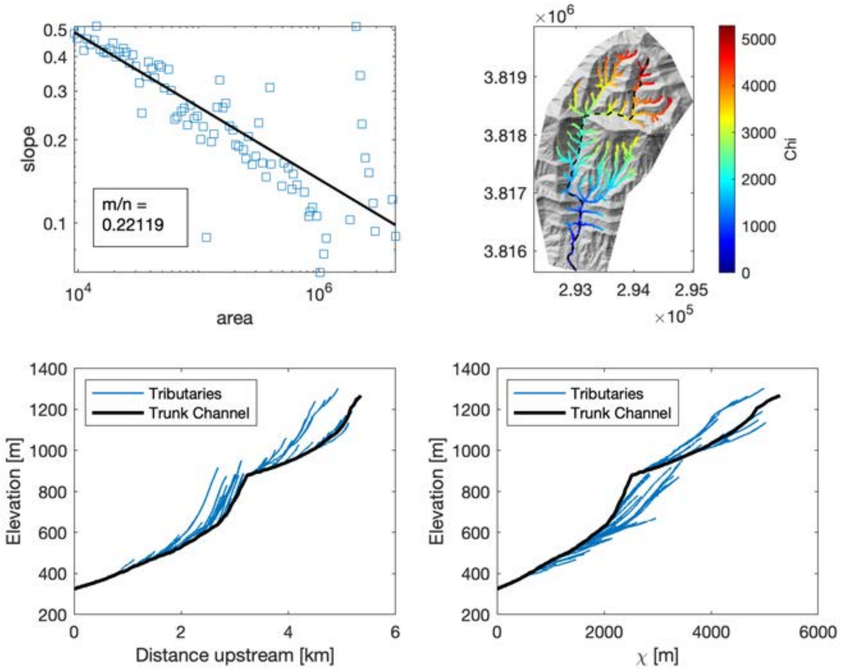

Appendix Figure D.8: Slope-area relationship, chi map (map units in meters, UTM Zone 11N), longitudinal profiles of trunk and tributary channels, and chi-transformed longitudinal profiles of trunk and tributary channels of a small watershed overlying Eocene sedimentary rocks in the Topatopa Mountains.

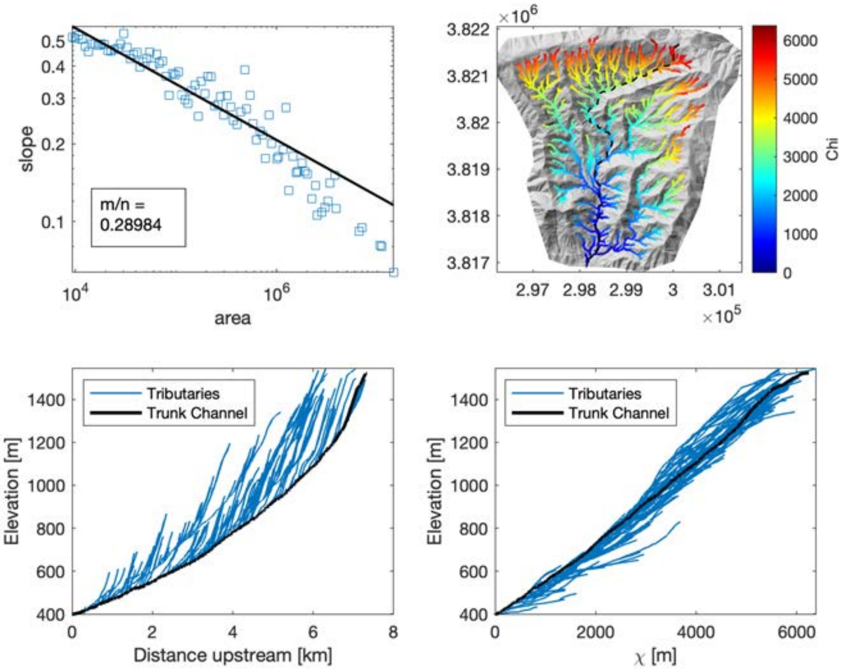

Appendix Figure D.9: Slope-area relationship, chi map (map units in meters, UTM Zone 11N), longitudinal profiles of trunk and tributary channels, and chi-transformed longitudinal profiles of trunk and tributary channels of the Senior Canyon watershed overlying Eocene sedimentary rocks in the Topatopa Mountains.

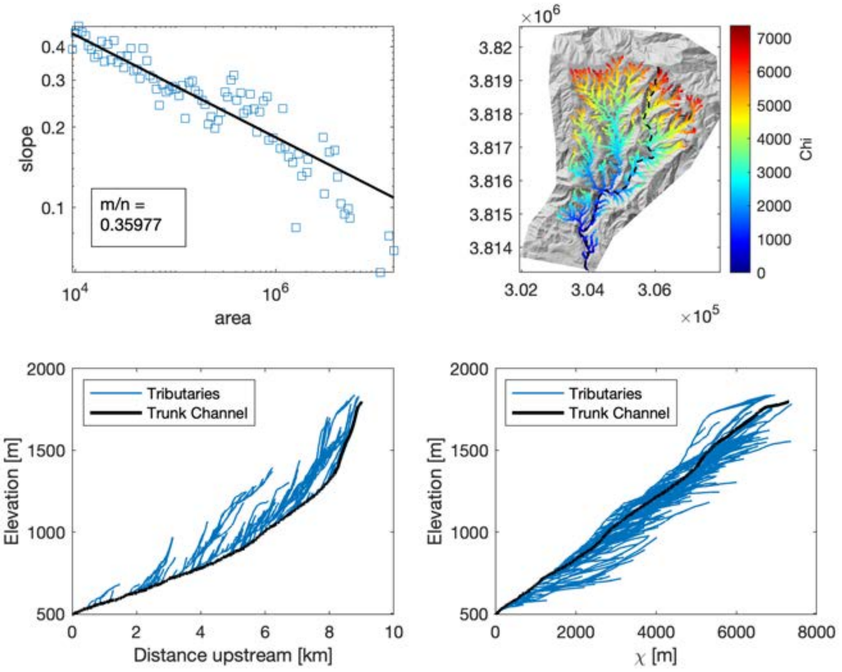

Appendix Figure D.10: Slope-area relationship, chi map (map units in meters, UTM Zone 11N), longitudinal profiles of trunk and tributary channels, and chi-transformed longitudinal profiles of trunk and tributary channels of a Sisar Creek watershed overlying Eocene sedimentary rocks in the Topatopa Mountains.

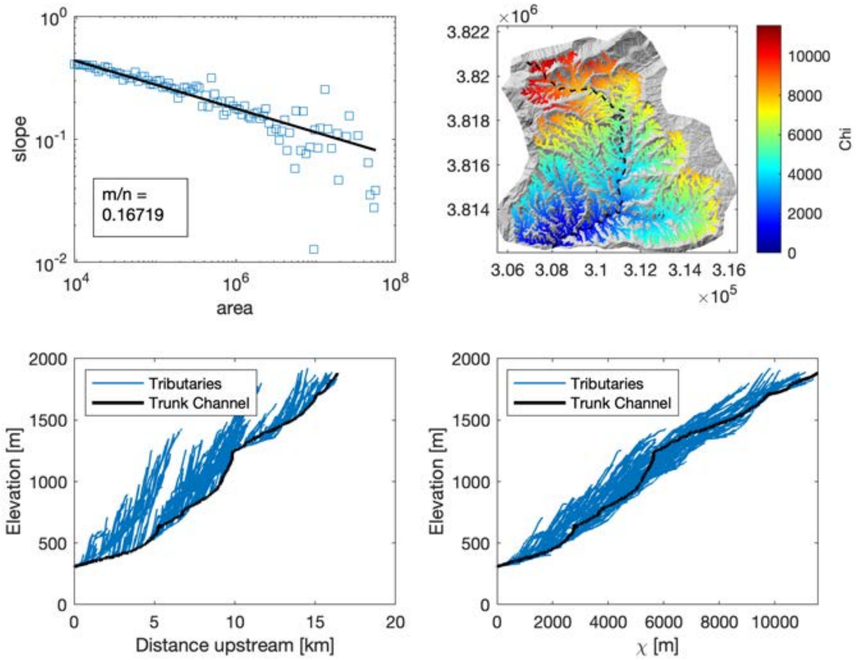

Appendix Figure D.11: Slope-area relationship, chi map (map units in meters, UTM Zone 11N), longitudinal profiles of trunk and tributary channels, and chi-transformed longitudinal profiles of trunk and tributary channels of the Santa Paula Creek watershed overlying Eocene sedimentary rocks in the Topatopa Mountains.

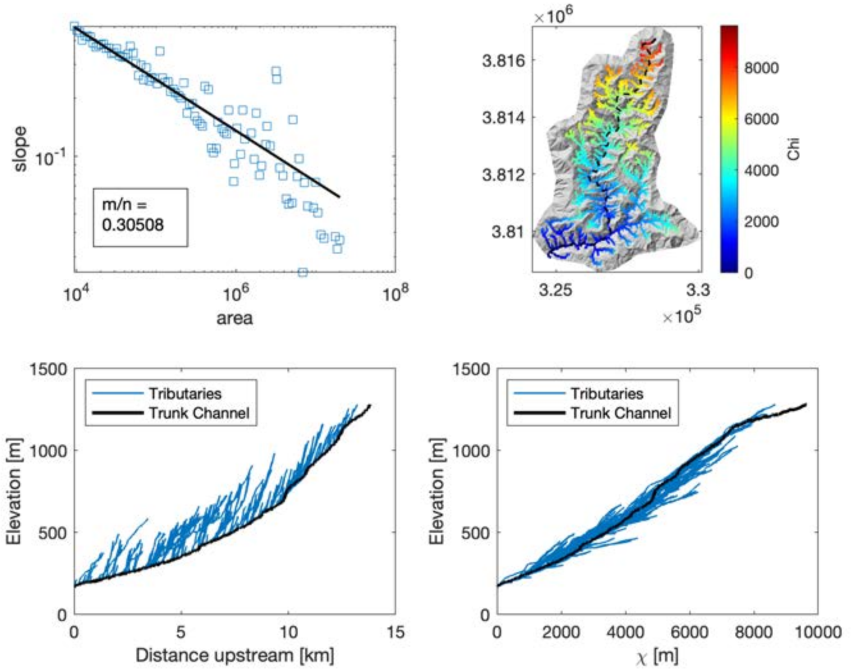

Appendix Figure D.12: Slope-area relationship, chi map (map units in meters, UTM Zone 11N), longitudinal profiles of trunk and tributary channels, and chi-transformed longitudinal profiles of trunk and tributary channels of the Pole Creek watershed overlying Miocene sedimentary rocks in the Topatopa Mountains.

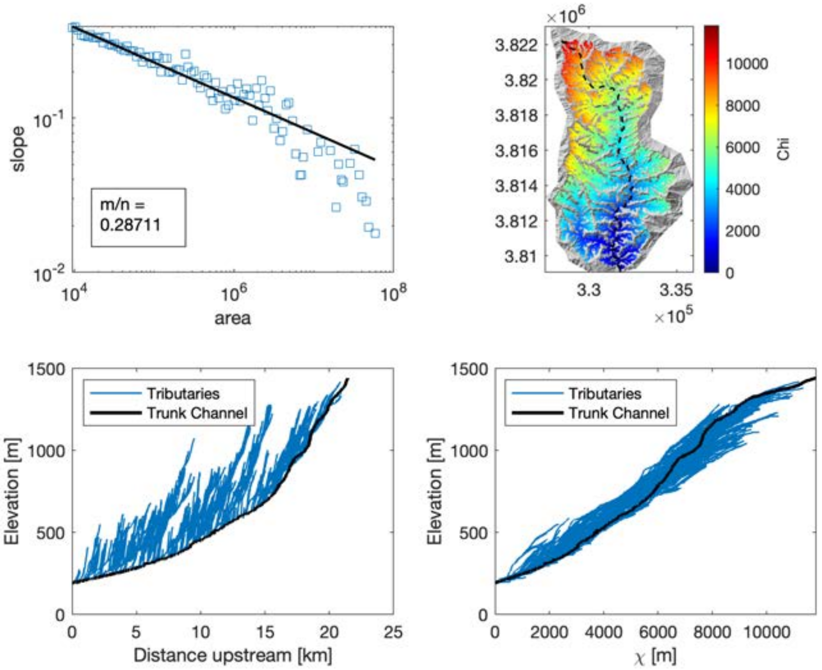

Appendix Figure D.13: Slope-area relationship, chi map (map units in meters, UTM Zone 11N), longitudinal profiles of trunk and tributary channels, and chi-transformed longitudinal profiles of trunk and tributary channels of the Hopper Creek watershed overlying Miocene sedimentary rocks in the Topatopa Mountains.

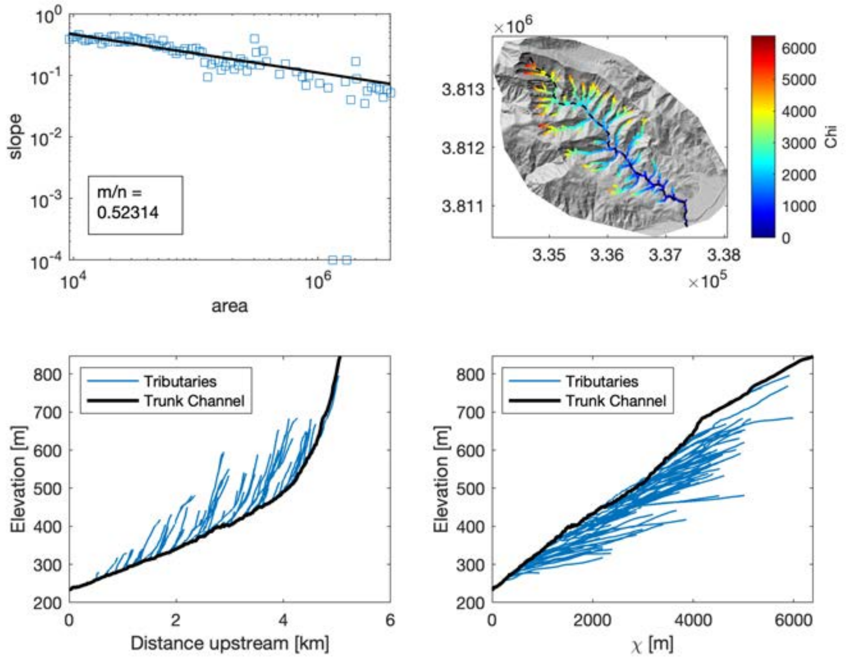

Appendix Figure D.14: Slope-area relationship, chi map (map units in meters, UTM Zone 11N), longitudinal profiles of trunk and tributary channels, and chi-transformed longitudinal profiles of trunk and tributary channels of a the Modelo Creek watershed overlying Miocene sedimentary rocks in the Topatopa Mountains.

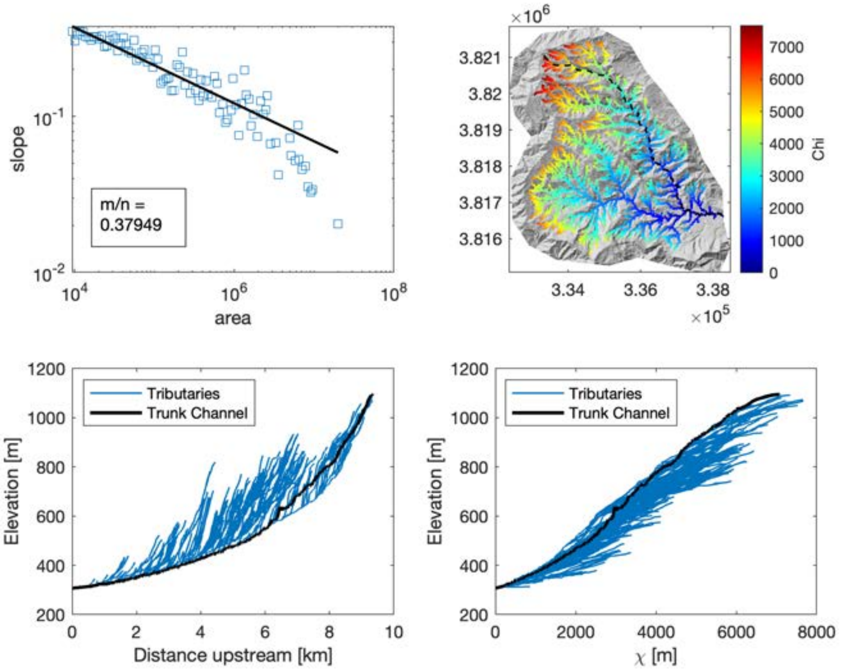

Appendix Figure D.15: Slope-area relationship, chi map (map units in meters, UTM Zone 11N), longitudinal profiles of trunk and tributary channels, and chi-transformed longitudinal profiles of trunk and tributary channels of a small watershed overlying Miocene sedimentary rocks in the Topatopa Mountains.

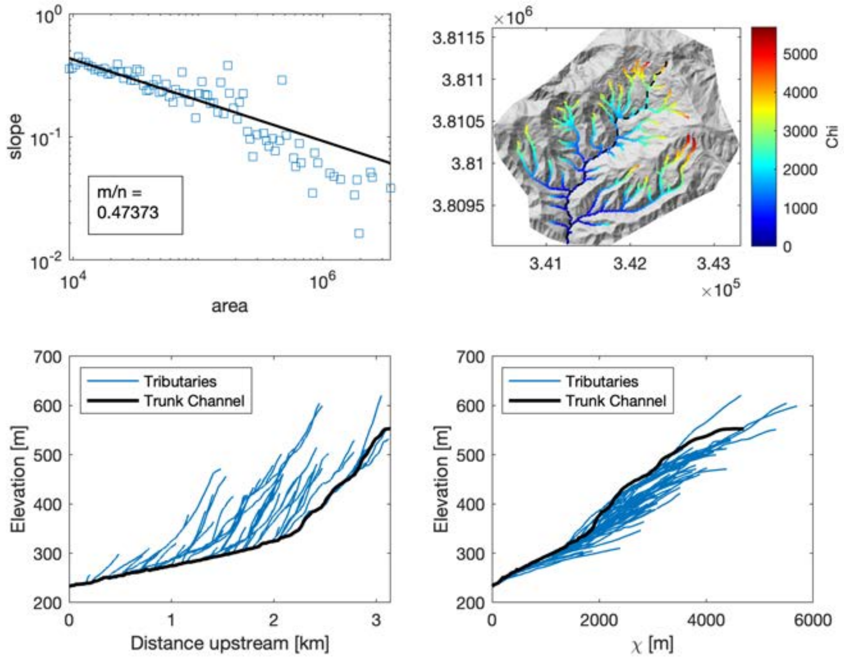

Appendix Figure D.16: Slope-area relationship, chi map (map units in meters, UTM Zone 11N), longitudinal profiles of trunk and tributary channels, and chi-transformed longitudinal profiles of trunk and tributary channels of a small watershed overlying Pliocene sedimentary rocks in the Topatopa Mountains.

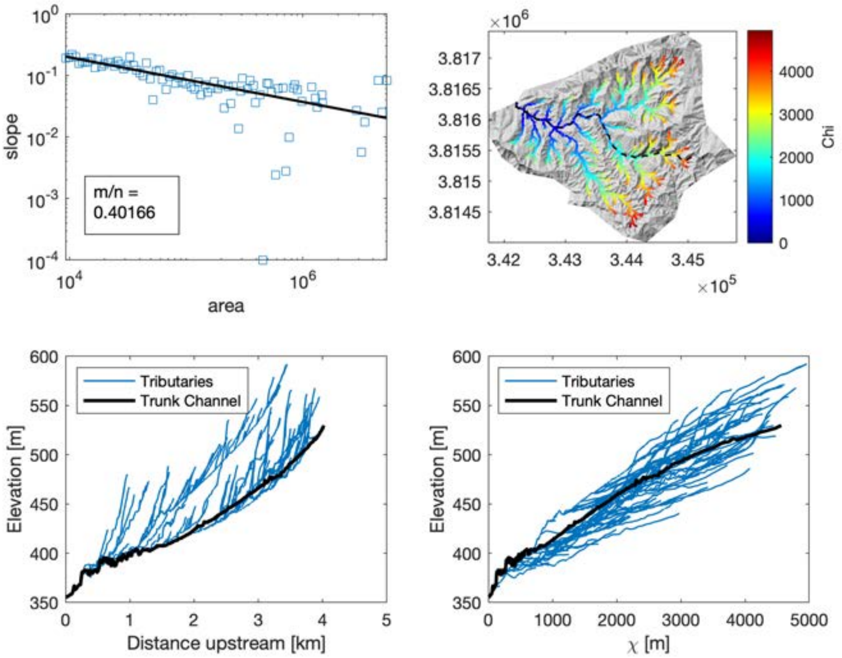

Appendix Figure D.17: Slope-area relationship, chi map (map units in meters, UTM Zone 11N), longitudinal profiles of trunk and tributary channels, and chi-transformed longitudinal profiles of trunk and tributary channels of a small watershed overlying Pliocene sedimentary rocks in the Topatopa Mountains.

Appendix E: Supporting Information for Chapter 6. The Contribution of Rock-Mass Strength to Post-Wildfire Erosion, Santa Monica Mountains, Southern California, USA

E.1 Introduction

This appendix contains supplemental text and figures to Chapter 6.

E.2 Soils Description

Soils within the study are dominated by Mipolomol, Topanga, Boades, Cotharin, and Talepop series, with rock outcrop exposed in 5-15% of maps area polygons. Soils orders are generally thin Mollisols and Entisols. Soils are generally thin and poorly developed, with ~30cm thick A horizons overlying weathered rock comprising ~70% of map areas polygons and more developed soils of ~1 m thickness comprising ~15% of map area polygons (Natural Resources Conservation Service, 2021).

E.3 Detailed Methods

E.3.1 LiDAR Acquisition and Processing

We obtained repeat airborne-LIDAR datasets within the study region in the central Santa Monica Mountains. Airborne LiDAR was collected prior to the wildfire by the Los Angeles Region Imagery Acquisition Consortium (LARIAC) between July 27, 2015 and October 18, 2016. Following the wildfire and storms, the National Center for Airborne Laser Mapping (NCALM) flew a repeat airborne-LIDAR survey on September 25, 2019.

The pre-fire LiDAR point cloud produced by LARIAC was obtained from Open Topography in the NAD83 UTM Zone 11n coordinate system, and the post-fire LiDAR point cloud was provided by NCLAM in the WGS84 UTM Zone 11n coordinate system. We used the National Oceanic and Atmospheric Administration's vertical datum transformation tool, (VDatum) to convert the vertical coordinate system of the post-fire point cloud from NCALM from WGS84 to NAVD88 with GEOID 12b. Following this conversion, we recognized a systematic horizontal offset of ~0.5 m between the two point clouds. To align the two datasets, we performed an Iterative Closest Point (ICP) registration in CloudCompare with the pre-fire

LARIAC point cloud as the reference dataset and the post-fire NCALM point cloud as the registered dataset. We required the root mean square (RMS) difference between successive iterations of the registration to fall below $1.0\text{x}10^{-7}$, and we set the theoretical final overlap between the two datasets to 75%. We deactivated the point subsampling optimization scheme, thereby requiring the ICP registration tool to use all points within both point clouds. After achieving a final RMS of 0.34, we extracted points along six transects perpendicular to paved roads, using two roads within the Zuma Creek watershed (Encinal Canyon Road and Mulholland Highway) and two roads outside the watershed (Kanan Dume Road and W Newton Canyon Road) (e.g. Figure E.10). The difference between the pre- and post-fire points at stable locations on these roads was used to estimate the level of detection (LOD) at 20 cm.

Many points in the post-fire NCALM dataset on bedrock outcrops and boulders that mantle hillslopes were not classified as ground returns, but points from these locations in the pre-fire LARIAC data are classified as ground returns. To ensure consistency in classification, we reclassified both point clouds.

We focus our analysis on vertical changes in the channel network, as the vertical change on hillslopes is lower and likely within the LOD. Further, vegetation regrowth on hillslopes between the Woolsey Fire and post-wildfire LiDAR survey obscures change due to the Woolsey Fire (Figure E.8-E.9). We define the channel network as pixels with upstream contributing areas exceeding 500 m^2. For each geologic unit, we sum the per-pixel vertical change to quantify volumes of material removed. We normalize eroded volumes by the aerial extent of each geologic unit within the channel network to quantify sediment fluxes from each unit in units of m^3/m^2. We also quantify sediment flux by aspect and slope.

E.3.2 Detailed Rock Mass Strength Methods

Rock strength is quantified in-situ using three field geotechnical approaches that average mechanical properties of rock masses over differing spatial scales. Field data were collected between November 2016 and August 2019, and were originally reported in Townsend et al. (2021). At the smallest spatial scale, we use a Schmidt hammer to measure the hardness of intact rock blocks between fractures (Original Schmidt, type N, manufactured by Proceq). This spring-loaded device measures rebound values that scale with laboratory measurements of uniaxial compressive strength of unfractured rock masses (Aydin & Basu, 2005; Deere & Miller, 1966; Selby, 1993). Due to the analytical variability of the Schmidt hammer and typical heterogeneities in rock masses, we collected 20 rebound measurements (*R*) from the least fractured rock surface at each site. We calculate and report the mean *R* values of these 20 measurements for each site. The Schmidt hammer was oriented horizontally for all measurements, so we do not correct for hammer orientation (Townsend et al., 2021).

At progressively larger spatial scales, the strength of rock masses is limited by the presence of discontinuities (fractures, bedding planes), which produce detached rock blocks and provide pathways for fluid flow and weathering (Gallen et al., 2015; Hoek & Brown, 1980). In a fractured rock mass, the ability of rock blocks to move relative to each other within a given stress state is controlled by the shape of the blocks and the degree of weathering on the surfaces separating the blocks (Hoek & Brown, 1997). At each field site, we describe these outcrop-scale fracture characteristics using the Geologic Strength Index (GSI) of (Hoek & Marinos, 2000). GSI is a framework with which rock masses are ranked on a scale of 0-100 based on five classes of discontinuity surface conditions and six classes of rock structure, with high values describing unfractured, unweathered rock masses, and low values describing highly fractured to sheared rock masses with weathered discontinuities. We record GSI observations within a range of ±5 (Townsend et al., 2021).

To aggregate the contributions of both the intact strength of the unfractured rock blocks, as well as the outcrop-scale fracture characteristics, we used the (Hoek & Brown, 1997) criterion to outcrop-scale rock mass shear strength (Townsend et al., 2021). Shear strength describes the maximum shear stress that at outcrop can sustain before failure, which varies as a function of confining stress. The Hoek & Brown criterion is an empirical framework designed to reduce the intact strength of the unfractured rock mass by the outcrop fracture structure and surface weathering. We use an empirical relationship (Deere & Miller, 1966) to convert Schmidt hammer R values to unconfined compressive strength, which we use as the intact strength input into the Hoek et. al (2002) series of equations for outcrop-scale shear strength calculations. Additional details on the methodology are available in (Townsend et al., 2021).

E.4 References

Aydin, A., & Basu, A. (2005). The Schmidt hammer in rock material characterization. *Engineering Geology*, *81*(1), 1–14. https://doi.org/10.1016/j.enggeo.2005.06.006

Borcherdt, R. D. (2012). VS30 – A Site-Characterization Parameter for Use in Paper Title Line Simplified Building Codes, Earthquake Resistant Design, GMPEs, and ShakeMaps. In *15th*

World Conference on Earthquake Engineering, Lisbon Portugal (Vol. 10).

Deere, D., & Miller, R. (1966). *Engineering classification and index properties for intact rock.*

Gallen, S. F., Clark, M. K., & Godt, J. W. (2015). Coseismic landslides reveal near-surface rock strength in a highrelief, tectonically active setting. *Geology*, *43*(1), 11–14. https://doi.org/10.1130/G36080.1

Hoek, E., & Brown, E. (1980). Empirical Strength Criterion for Rock Masses. *Journal of the Geotechnical Engineering Division*. https://doi.org/10.1016/0148-9062(81)90766-X

Hoek, E., & Brown, E. (1997). Practical estimates of rock mass strength. *International Journal of Rock Mechanics and Mining Sciences*, *34*(8), 1165–1186. https://doi.org/10.1016/S1365-1609(97)80069-X

Hoek, E., & Marinos, P. (2000). Predicting tunnel squeezing problems in weak heterogeneous rock masses. *Tunnels and Tunnelling International*, *Part 1-2*(November), 1–20. Retrieved from https://www.rocscience.com/documents/hoek/references/H2000d.pdf%0Ahttp://www.rockscience.com/hoek/references/H2000d.pdf

MesoWest. (2021). Surface Weather Maps-California.

Natural Resources Conservation Service, U. S. D. of A. (2021). Web Soil Survey.

NOAA. (2020). Weather and Climate Toolkit. Retrieved March 15, 2021, from https://www.ncdc.noaa.gov/wct/

Park, C. B., Miller, R. D., & Xia, J. (1999). Multichannel analysis of surface waves. *Geophysics*, *64*(3), 800–808. https://doi.org/10.1190/1.1444590

Park, C. B., Miller, R. D., Xia, J., & Ivanov, J. (2000). Multichannel seismic surface-wave methods for geotechnical applications. *Proc. of the First Int. Conf. on the App …*. Retrieved from http://www.kgs.ku.edu/Geophysics2/Pubs/Pubs/PAR-00-03.pdf

Selby, M. J. (1993). *Hillslope materials and processes*. Oxford University Press.

Townsend, K. F., Clark, M. K., & Zekkos, D. (2021). Profiles of near-surface rock mass strength across gradients in burial, erosion, and time. *Journal of Geophysical Research: Earth Surface*, *126*(e2020JF005694). Retrieved from https://doi.org/10.1029/2020JF005694

Wunderground. (2021). WunderMap Precipitation Summaries.

Appendix Figure E.1: Coarsening-upwards debris flow levee on side channel to Zuma Creek. Red backpack for scale. Image location: 34.0449° N 118.8138° W. Image date: June 3, 2021.

Appendix Figure E.2: Coarsening-upwards debris flow levee on side channel to Zuma Creek. Field iPad in blue case for scale. Image location: 34.0449° N 118.8138° W. Image date: June 3, 2021.

Appendix Figure E.3: Bedrock channel exposed along tributary drainage to Zuma Creek. Red backpack for scale. Image location: 34.0451° N 118.8133° W. Image date: June 3, 2021.

Appendix Figure E.4: Recent sediment deposition on an alluvial fan adjacent to Zuma Creek following the first post-wildfire rainfall event for which sediment-laden flows were documented. Image location: 34.0451° N 118.8133° W. Image date: December 28, 2018.

Appendix Figure E.5: Images from Arroyo Sequit, Leo Carrillo State Park, before and after the Woolsey Fire and November 29, 2018 storm a) Pre-fire image captured in spring, 2018. b) Post-fire image collected in December, 2018 showing channel aggradation. Images courtesy Rosi Dagit, Resource Conservation District of the Santa Monica Mountains.

Appendix Figure E.6: Images from Arroyo Sequit, Leo Carrillo State Park, before and after the Woolsey Fire and November 29, 2018 storm a) Pre-fire image captured in spring, 2018. b) Post-fire image collected in December, 2018 showing channel aggradation. Images courtesy Rosi Dagit, Resource Conservation District of the Santa Monica Mountains.

Appendix Figure E.7: Images from Bulldog Spring, Malibu Creek State Park, before and after the Woolsey Fire and November 29, 2018 storm a) Pre-fire image captured in spring, 2018. b) Post-fire image collected in December, 2018 showing channel aggradation. Images courtesy Rosi Dagit, Resource Conservation District of the Santa Monica Mountains.

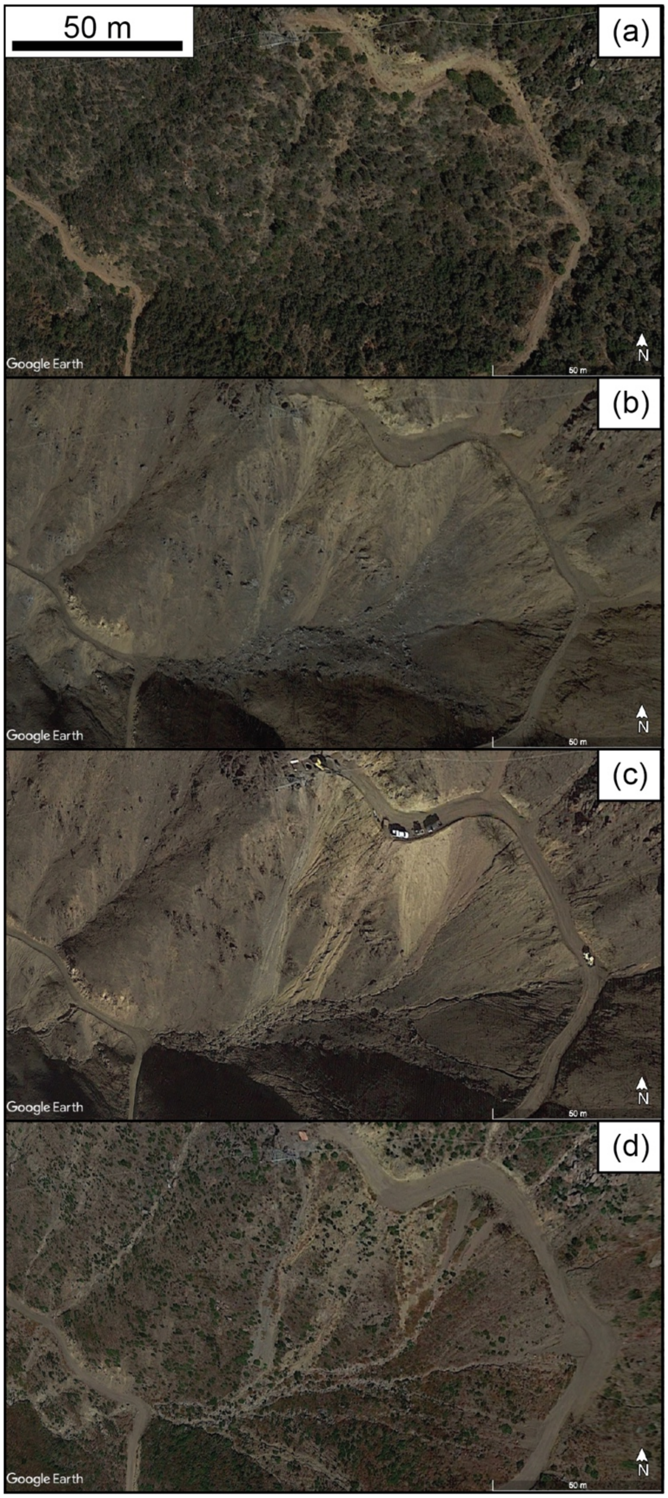

Appendix Figure E.8: Time series of Google Earth satellite images showing geomorphic change following the Woolsey Fire. a) Pre-fire image from August 12, 2018. b) Post-fire but pre-rain image from November 19, 2018. Note ravel cones on roadbed in upper-right corner of image c) Image from January 3, 2019, after the first storm. Rilling and gullying are evident. Note road maintenance equipment in the image. d) Image on August 19, 2019, following all three storms and preceding the post-fire airborne LiDAR survey by 37 days. Note vegetation regrowth. Image center 34.0593° N 118.8122° W.

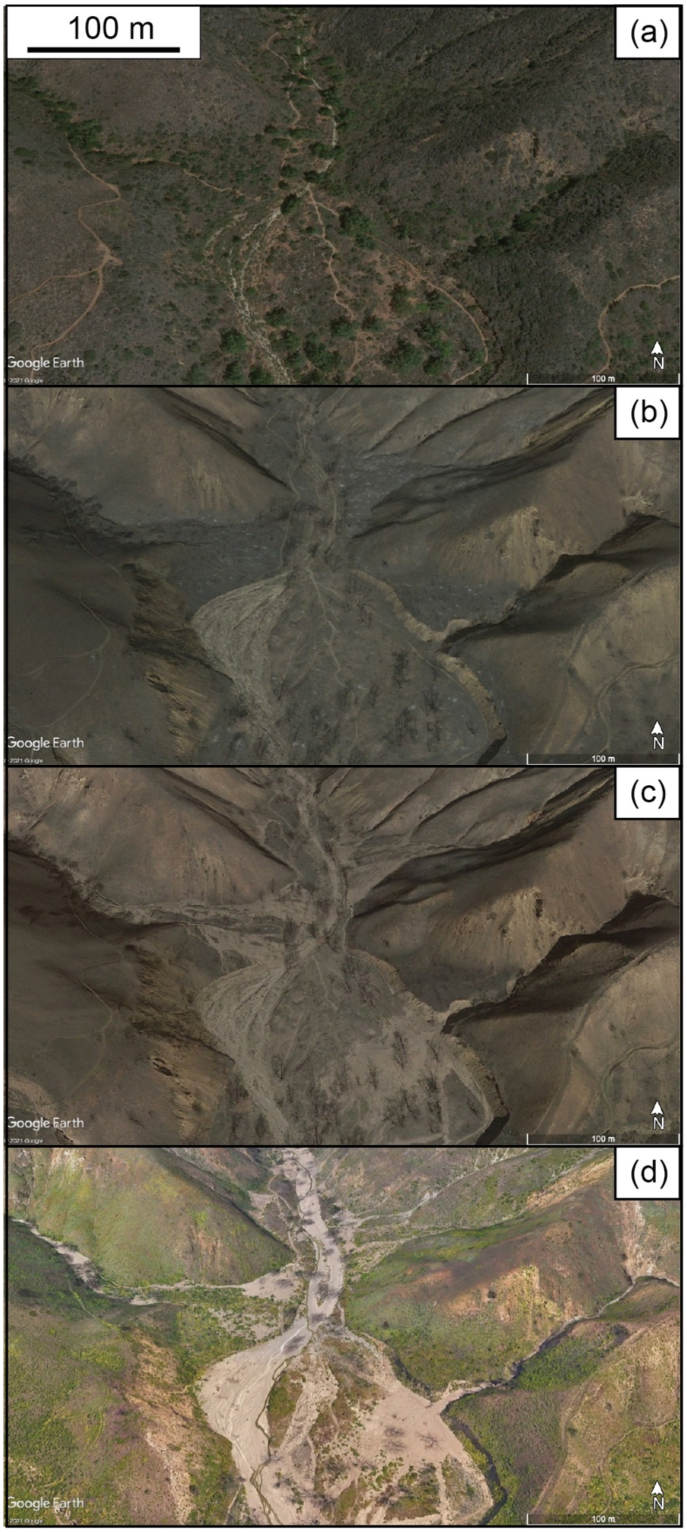

Appendix Figure E.9: Time series of Google Earth satellite images showing geomorphic change in Zuma Creek following the Woolsey Fire. a) Pre-fire image from August 12, 2018. b) Post-fire but pre-rain image from November 19, 2018. c) Image from January 3, 2019, after the first storm. Recent sedimentation is evident. d) Image on April 16, 2019, following all three storms and preceding the post-fire airborne LiDAR survey by five months. Note aggraded channels and vegetation regrowth. Image center 34.0402° N 118.8143° W.

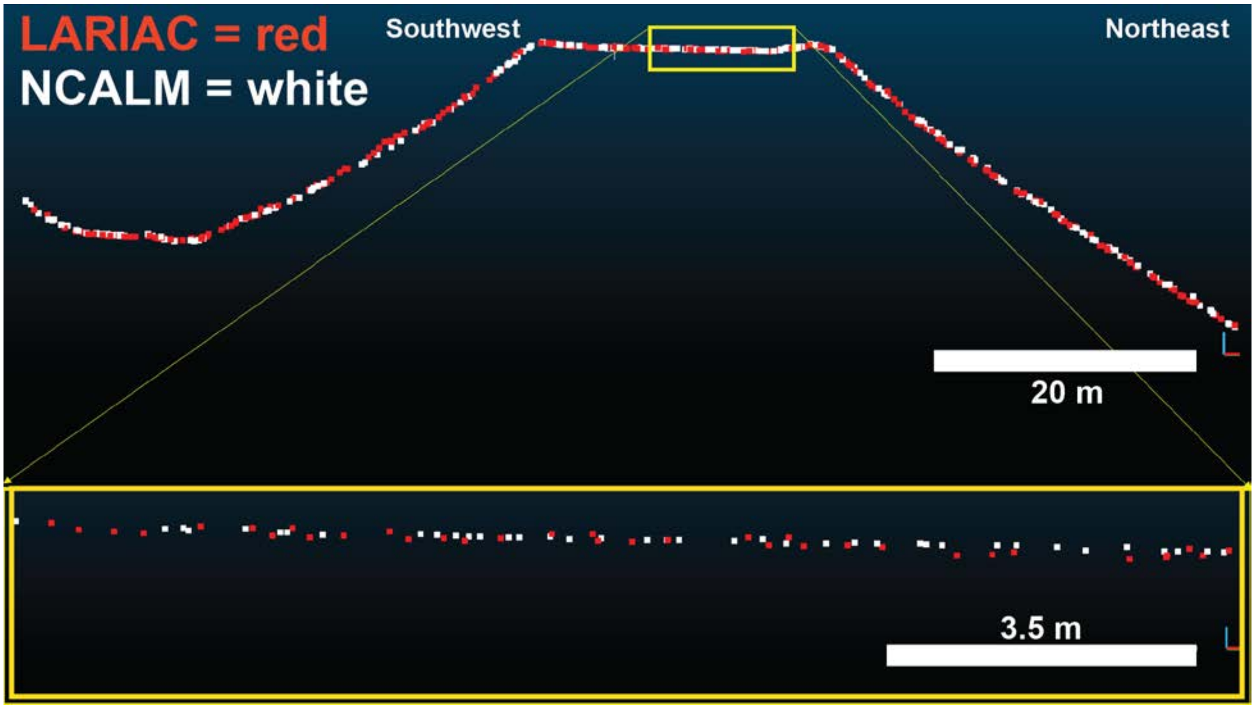

Appendix Figure E.10: Cross section of airborne-LiDAR ground-classified points across paved Kanan Dume road and adjacent road embankments after datum conversion and ICP registration. Ground return points from stable and flat surfaces, including the inset profile shown here, were used to determine a LOD of 20cm.

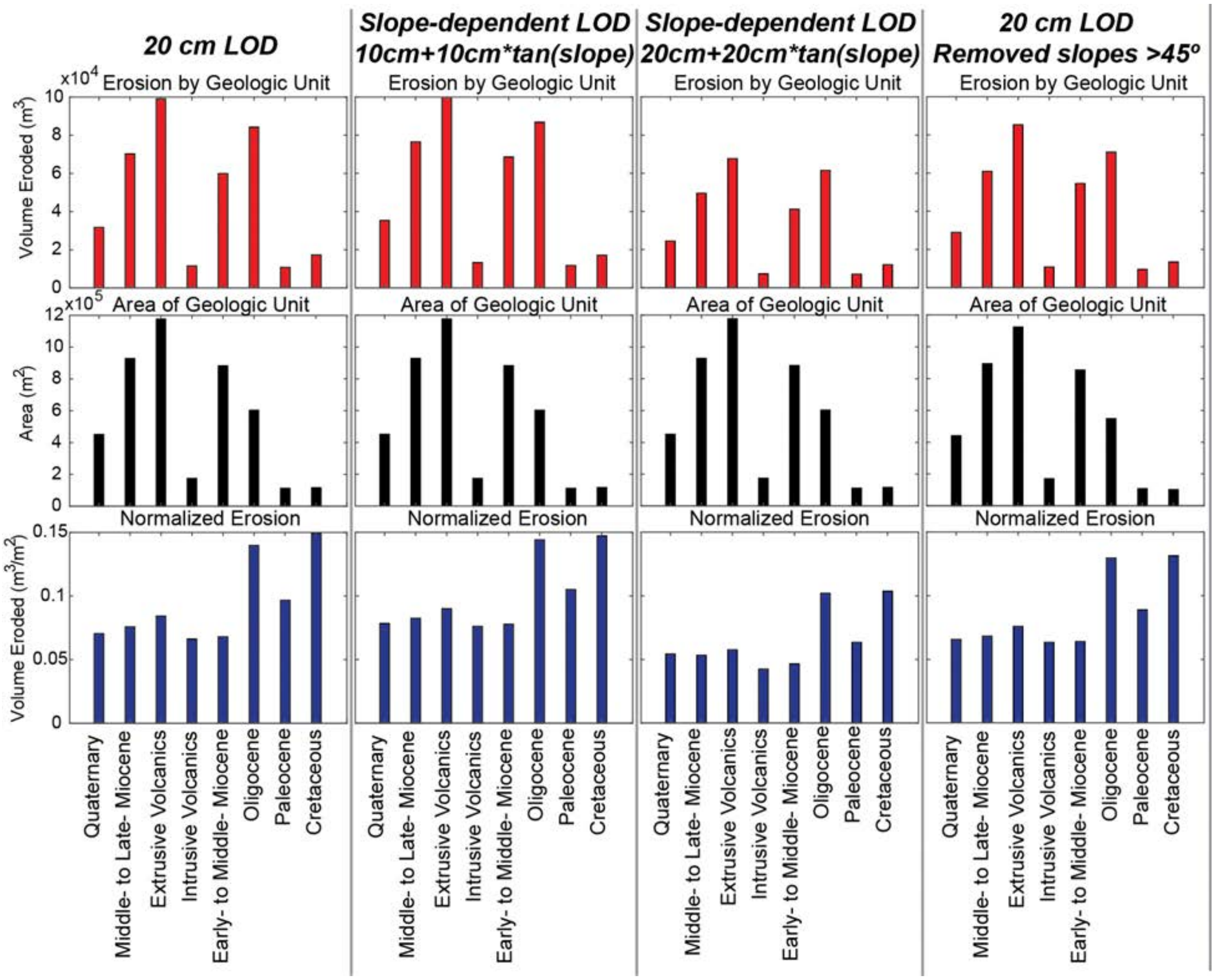

Appendix Figure E.11: Sensitivity of LiDAR-derived volumes of erosion by geologic age category with differing criteria for the level of detection (LOD). Upper plots show the total volume of material eroded from the channel network by geologic age category. Middle plots show the total areal extent of each geologic age category. Lower plots show the erosional flux (volumes normalized by area, or mean depth) from each geologic age category in units of m^3/m^2. 20cm LOD indicates that all elevation change falling below 20cm was removed from volume calculations. In the slope-dependent LOD calculations, the LOD of each individual pixel was increased based on the local slope by adding LOD*tan(slope) on top of either a 10cm or 20cm LOD. A slope-dependent LOD may be justified where the horizontal registration of the two LiDAR point clouds is variable. In the far-right column, a standard 20cm LOD was imposed across the study area, and all pixels with slopes >45° were removed. Results are consistent despite the chosen LOD. Our preferred results use the 20cm LOD with slopes >45° removed.

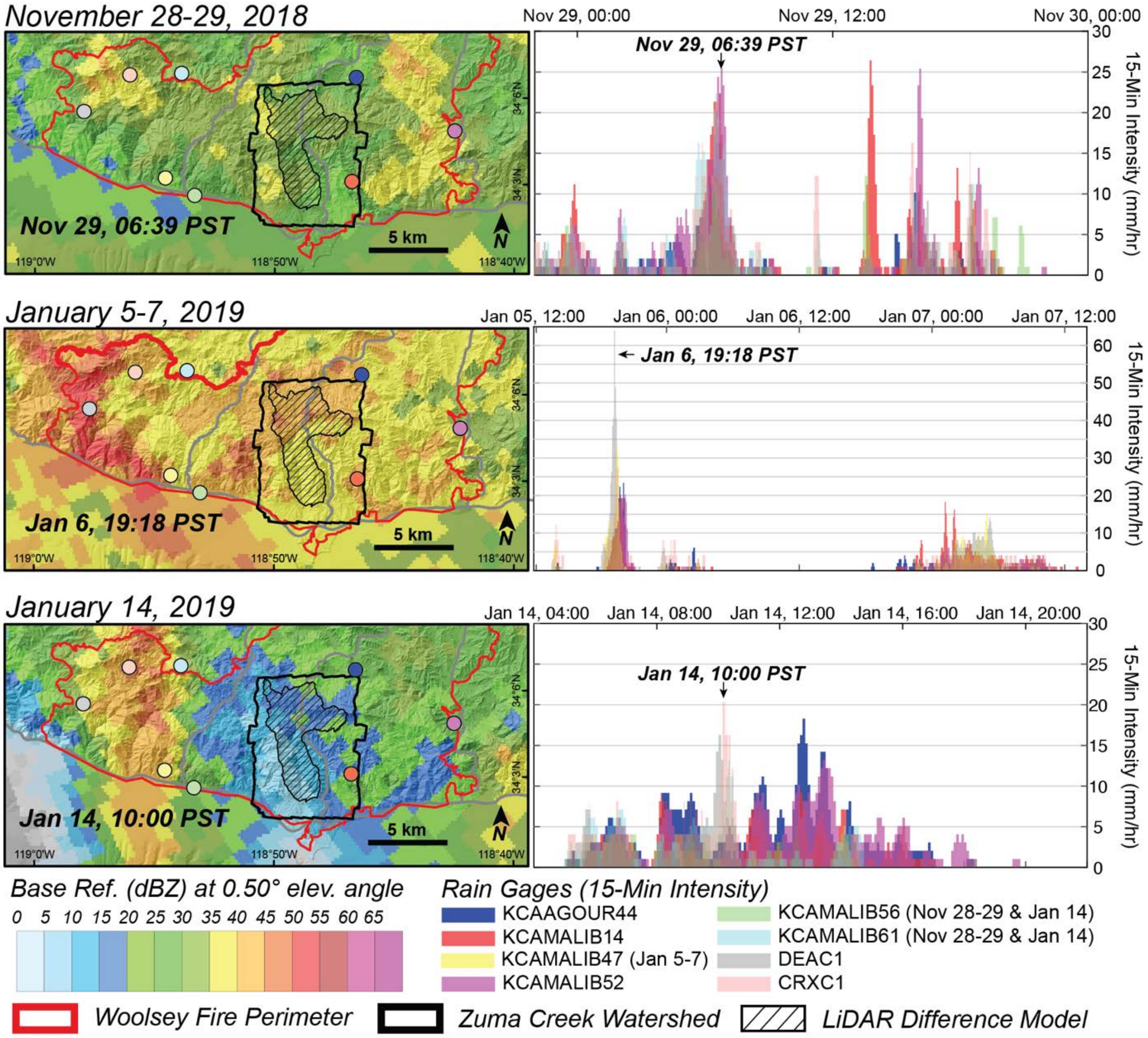

Appendix Figure E.12: (left) Maps of weather radar base reflectivity at peak 15-minute rainfall intensities during the three storms with known debris flows. Colored circles indicate rain gage locations, and colors correspond with stations in 15-minute rainfall intensities bar chart (right).

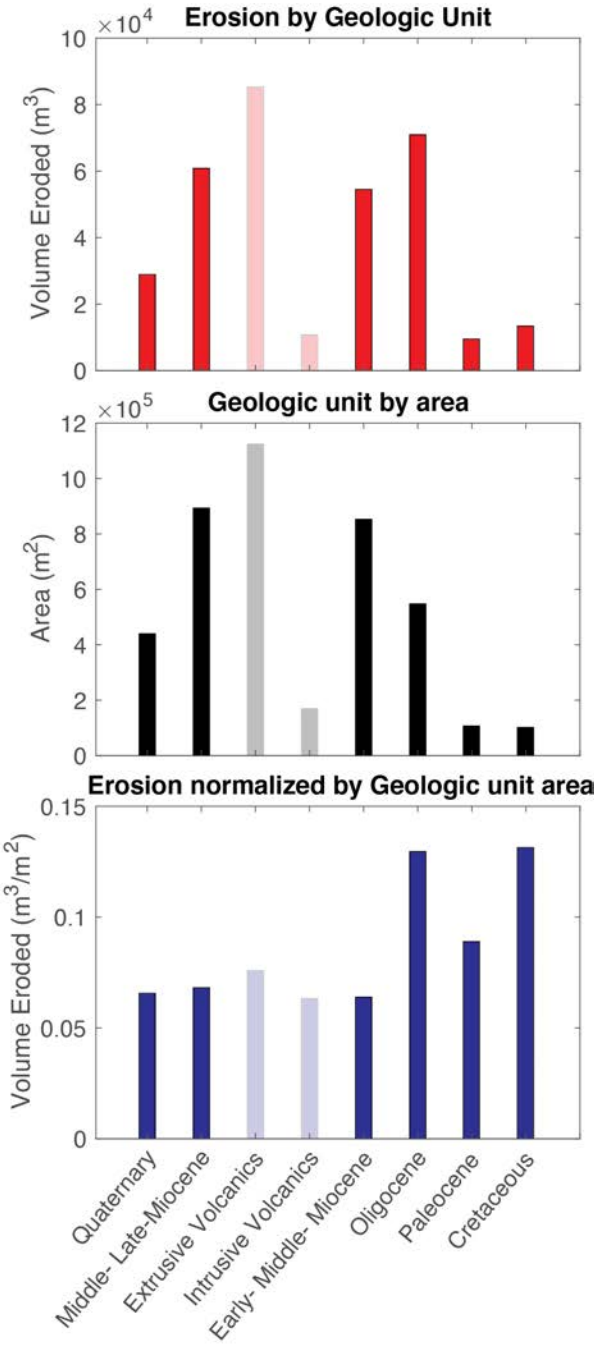

Appendix Figure E.13: Erosion by geologic unit as inferred from the LiDAR-derived difference model. Upper plot shows the total volume of material eroded from the channel network by geologic unit. Middle plot shows the total areal extent of each geologic unit. Lower plot shows the erosional flux (volumes normalized by area, or mean depth) from each geologic category in units of m^3/m^2.

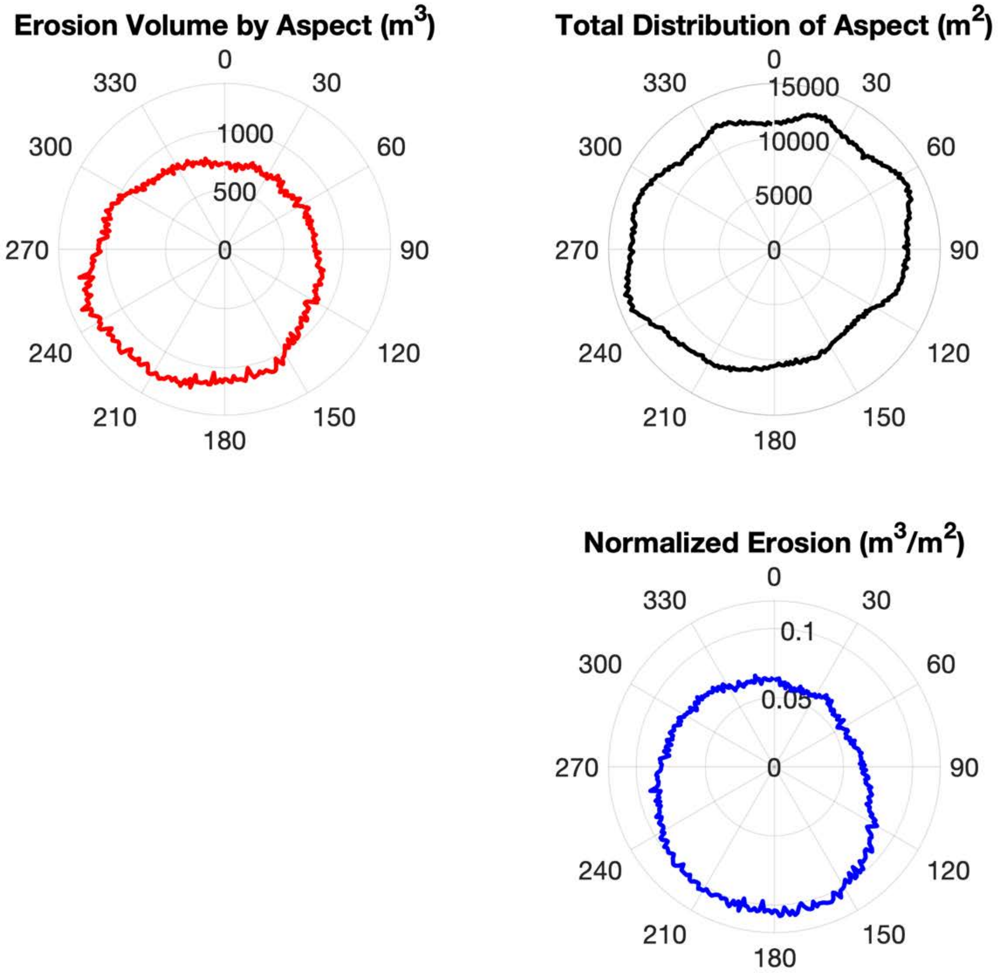

Appendix Figure E.14: Erosion by aspect as inferred from the LiDAR-derived difference model. Upper left plot shows the total volume of material eroded from the channel network by aspect. Upper right plot shows the total areal extent of aspect within the channel network. Lower right plot shows the erosional flux (volumes normalized by area, or mean depth) of each aspect value in units of m^3/m^2.

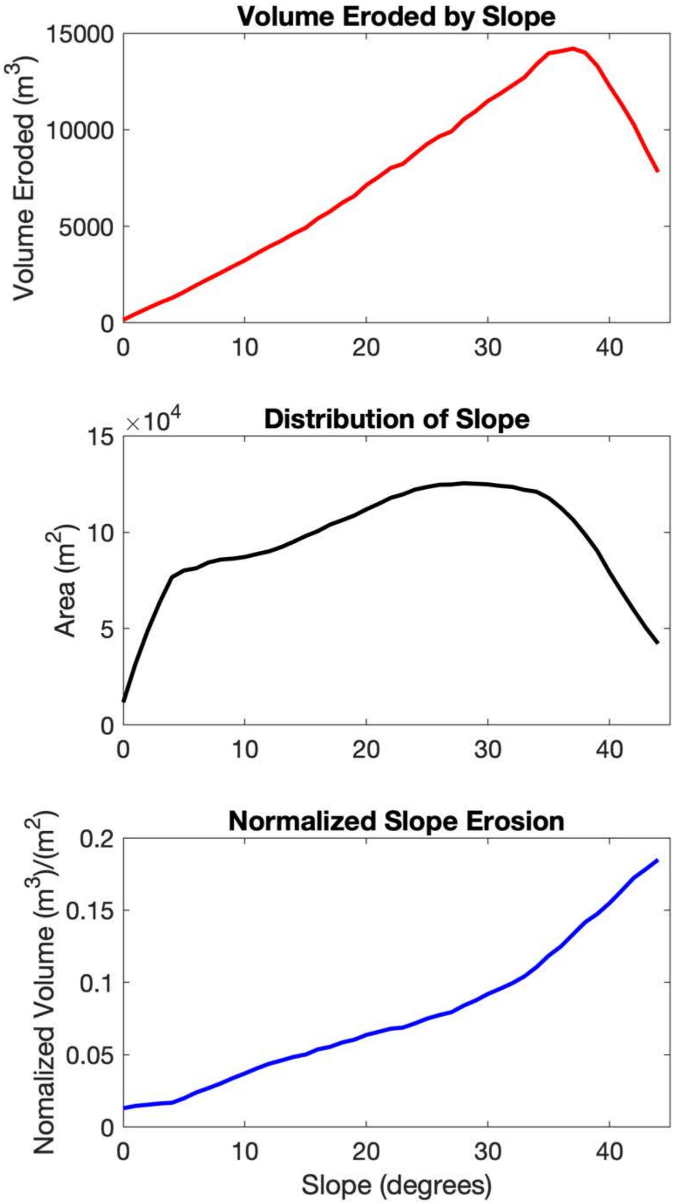

Appendix Figure E.15: Erosion by slope as inferred from the LiDAR-derived difference model. Upper plot shows the total volume of material eroded from the channel network by slope. Middle plot shows the total areal extent of slope within the channel network. Lower plot shows the erosional flux (volumes normalized by area, or mean depth) of each slope value in units of m^3/m^2. Note that all slopes >45 degrees were excluded.